Observer Based Engine Air Charge Characterisation

Rapid Observer Assisted Engine Air Charge Characterisation Using A Dynamic Dual-Ramp Testing Method

Peter Schaal

Submitted for the degree of

Doctor of Philosophy

Department of Aeronautical and Automotive Engineering

Loughborough University

2018

Abstract

Characterisation of modern complex powertrains is a time consuming and expensive process. Little effort has been made to improve the efficiency of testing methodologies used to obtain data for this purpose.

Steady-state engine testing is still regarded as the golden standard, where approximately 90% of testing time is wasted waiting for the engine to stabilize. Rapid dynamic engine testing, as a replacement for the conventional steady-state method, has the potential to significantly reduce the time required for characterisation. However, even by using state of the art measurement equipment, dynamic engine testing introduces the problem that certain variables are not directly measurable due to the excitation of the system dynamics. Consequently, it is necessary to develop methods that allow the observation of not directly measurable quantities during transient engine testing.

Engine testing for the characterisation of the engine air-path is specifically affected by this problem since the air mass flow entering the cylinder is not directly measurable by any sensor during transient operation. This dissertation presents a comprehensive methodology for engine air charge characterisation using dynamic test data. An observer is developed, which allows observation of the actual air mass flow into the engine during transient operation. The observer is integrated into a dual-ramp testing procedure, which allows the elimination of unaccounted dynamic effects by averaging over the resulting hysteresis.

A simulation study on a 1-D gas dynamic engine model investigates the accuracy of the developed methodology. The simulation results show a trade-off between time saving and accuracy. Experimental test result confirm a time saving of 95% compared to conventional steady-state testing and at least 65% compared to quasi steady-state testing while maintaining the accuracy and repeatability of conventional steady-state testing.

Keywords: Air-Path Observer, Rapid Engine Characterisation, Dynamic / Transient Engine Testing, Test Time Reduction, Joint State and Parameter Estimation, Unknown Input Estimation, Mean Value Engine Model, 1-D Engine Model, Dynamic Compensation, Dual-Ramp Averaging

Acknowledgements

I would like to express my deep gratitude to my Ph.D. supervisors, Dr. Byron Mason and Professor Kambiz Ebrahimi, for the support and encouragement during my time as a Ph.D. student.

Special thanks to Professor Mark Cary from Ford Motor Company for the immeasurable amount of help and guidance on this project.

To my friends and to my family, Susanne, Roland and Johannes, thank you for your support and encouragement. It is amazing what you can accomplish when the most important people in your life stand behind you.

And Natia, all this would have never been possible without you, thank you for patience and support during the most challenging time of my life. This work is dedicated to you…

Peter Schaal

February 2018

Contents

List of Figures

List of Tables

Nomenclature

General Symbols

A	m^2	Cross-sectional area
$A_{e,th}$	m^2	Effective throttle open area
A_{th}	m^2	Physical throttle open area
A_{WG}	m^2	Waste gate open area
c_p	J/K	Specific heat at constant pressure
c_v	J/K	Specific heat at constant volume
c_t	-	Turbine friction coefficient
C_d	-	Throttle discharge coefficient
CO	Vol.%	Carbon monoxide
CO_2	kg	Carbon dioxide
CO_2/km	kg/km	Vehicle CO_2 output per kilometre
CO_{2-eq}/km	kg/km	CO_2 equivalent output per kilometre of a BEV
e	- | %	Error
e_M	%	Measurement error
e_{M_IC}	%	Measurement error intercooler
e_{M_IM}	%	Measurement error intake manifold
e_{M_IV}	%	Measurement error intake volume
e_{M_tot}	%	Total measurement error (entire intake system)
e_{OBS}	%	Observation error
e_{OBS_IC}	%	Observation error intercooler
e_{OBS_IM}	%	Observation error intake manifold
e_{OBS_IV}	%	Observation error intake volume
e_{OBS_tot}	%	Total observation error (entire intake system)

E	J	Intrinsic internal energy
f_c	Hz	Filter cut-off frequency
h	J/kg | $\frac{W}{m^2K}$	Specific enthalpy / Heat transfer coefficient
h_0	J/kg	Stagnation enthalpy at zero velocity
H	J	Enthalpy
$\dot{H}$	W	Enthalpy flow
$\dot{H}_{in}$	W	Enthalpy inflow
$\dot{H}_{out}$	W	Enthalpy outflow
HC	ppm	Hydro carbons
J_t	$kg * m^2$	Turbine mass of inertia
k	-	Specific sample
k_f	-	Wall friction coefficient
k_r	-	Gain of recursive parameter estimation
k_t	-	Temperature correction factor
K	-	Kalman Gain
L	-	Gain of nonlinear observer
m	kg	Mass
$\dot{m}$	kg/s	Mass flow
$\dot{m}_c$	kg/s	Compressor mass flow
m_{cyl}	kg	Air mass inside the cylinder
$m_{cyl,d}$	kg	Demanded air mass inside the cylinder
$m_{cyl,r}$	kg	Air mass inside the cylinder at reference conditions
$\dot{m}_{ev}$	kg/s	Mass flow through the exhaust valve
$\dot{m}_{in}$	kg/s	Mass flow into a system
m_{IC}	kg	Air mass inside the intercooler

m_{IM}	kg	Air mass inside the intake manifold
m_{IV}	kg	Air mass inside the intake volume
$\dot{m}_{iv}$	kg/s	Mass flow through the intake valve
$m_{iv,IM}$	kg	Air mass inside cylinder based on intake manifold conditions
$\dot{m}_{maf}$	kg/s	Mass flow at MAF sensor location
$\dot{m}_{out}$	kg/s	Mass flow out of a system
$\dot{m}_{th}$	kg/s	Mass flow at throttle plate
M_a	-	Mach number
M_d	Nm	Friction torque
M_{eng}	Nm	Actual engine torque output
$M_{f,t}$	Nm	Turbine friction torque
M_i	Nm	Inner engine torque
$M_{i,c}$	Nm	Corrected inner engine torque
N	-	Number of samples
N_e	rpm	Engine speed
N_t	rpm	Turbine speed
NO_x	ppm	Nitrogen oxides
P	Pa	Pressure / Augmented Covariance Matrix (AEKF)
P_0	Pa	Stagnation pressure
$P_{c,in}$	Pa	Compressor inlet pressure
$P_{c,out}$	Pa	Compressor outlet pressure
P_{crit}	-	Critical pressure ratio for sonic flow
P_{cyl}	Pa	Pressure inside cylinder
P_{DP}	Pa	Down pipe pressure (turbine outlet)
P_{EM}	Pa	Exhaust manifold pressure

P_{ev}	Pa	Pressure at exhaust valve
P_{iv}	Pa	Pressure at intake valve
P_{IC}	Pa	Pressure inside the intercooler
$P_{IC,d}$	Pa	Demanded pressure inside the intercooler
$P_{IC,tgt}$	Pa	Target Intercooler outlet pressure
P_{IM}	Pa	Intake manifold pressure
$P_{IM,min}$	Pa	Minimum intake manifold pressure
$P_{IM,max}$	Pa	Maximum intake manifold pressure
$P_{IM,tgt}$	Pa	Target intake manifold pressure
$P_{IM,d}$	Pa	Demanded intake manifold pressure
P_{IV}	Pa	Intake volume pressure
$P_{t,in}$	Pa	Pressure upstream the throttle
$P_{t,out}$	Pa	Pressure downstream the throttle
pr_c	-	Compressor pressure ratio
PWR_c	W	Compressor power
PWR_t	W	Turbine power
$\dot{Q}$	W	Heat transfer rate
$\dot{Q}_h$	W	Heat transfer from cylinder head
$\dot{Q}_w$	W	Heat transfer from cylinder wall
R	$\frac{J}{kg \times K}$	Specific gas constant for dry air
R_m	-	Measurement covariance matrix
R_p	-	Process covariance matrix
t_{ramp}	s	Ramp time
t_{ramp_SDS}	s	Ramp time of a SDS test
t_{save}	s	Total time saving

t_{SS_high}	s	Steady-state period at $P_{IM,max}$
t_{SS_low}	s	Steady-state period at $P_{IM,min}$
t_{SS_TP}	s	Total test time for a steady-state test point
T	K	Temperature
$T_{c,in}$	K	Compressor inlet temperature
$T_{c,out}$	K	Compressor outlet temperature
T_{cyl}	K	Temperature inside cylinder
T_{ev}	K	Temperature at exhaust valve
T_{EM}	K	Exhaust manifold temperature
T_g	K	Gas temperature
T_{IC}	K	Intercooler outlet temperature
T_{in}	T	Inlet Temperature
T_{IM}	K	Intake manifold temperature
$T_{IM,ref}$	K	Reference intake manifold temperature
T_{iv}	K	Temperature at intake valve
T_{IV}	K	Intake volume temperature
T_m	K	Measured temperature
T_s	s	Sample time
T_w	K	Wall Temperature
$T_{w,ref}$	K	Reference engine coolant temperature
TP_{DP}	Pa	Pressure difference across the throttle plate
u	-	System input
v_m	-	Measurement noise
v_p	-	Process noise
V	m^3	Volume

V_{cyl}	m^3	Volume of one specific cylinder
V_d	m^3	Engine displacement volume
V_{IC}	m^3	Intercooler volume
V_{IM}	m^3	Intake manifold volume
V_{IV}	m^3	Intake volume
V_l	m^3	Lumped volume
V_{pi}	m^3	Volume of pipe
V_{pl}	m^3	Volume of plenum
w	m/s	Velocity
wg_d	%	Demanded waste gate duty cycle
x	-	System state
γ	-	System output
y_f	-	Filtered system output
z	-	Unknown system input

Greek letters

α_{th}	deg	Throttle angle
γ	-	Specific heat ratio
$\eta_{\varphi i}$	-	Torque correction due to spark advance
η_λ	-	Torque correction due to λ
η_c	-	Compressor efficiency
η_t	-	Turbine efficiency
η_v	-	Actual volumetric efficiency
η_{v_MAF}	-	MAF-based volumetric efficiency
η_{v_OBS}	-	Observed volumetric efficiency

η_{v_SS}	-	Steady-state volumetric efficiency
ϑ	-	Adaptive parameter
λ	-	Relative AFR
ρ	kg/m^3	Density
σ	-	Standard deviation
σ_x^2	-	System process covariance
σ_ϑ^2	-	Adaptive parameter process covariance
$\sigma_{\vartheta,des}^2$	-	Desired covariance of adaptive parameter
σ_{tr}^2	-	Convergence threshold for adaptive parameter covariance
τ	s	Time constant
τ_f	s	Filter time constant
φ_i	deg	Spark advance
ω_t	rad/s	Turbine rotational speed

Mathematical Operations

$\frac{d}{dt}$	Derivative with respect to time
$\dot{\ }$	Short form of time derivative
∂	Partial derivative
$f(\ \ )$	Function of

Abbreviations

0D	Zero Dimensional
1D	One Dimensional
AEKF	Augmented Extended Kalman Filter
AFR	Air to Fuel Ratio

AMPRBS	Amplitude Modulated Pseudo Random Binary Signals
ARX	Auto-Regressive with eXogenous input model
BEV	Battery Electric Vehicle
DCT	Dual Clutch Transmission
deg	Degree
DI	Direct Injection
DoE	Design of Experiment
DOR	Dynamic Offset Ramp
DRA	Dual Ramp Averaging
GDI	Gasoline Direct Injection
GTDI	Gasoline Turbocharged Direct Injection
ECU	Engine Control Unit
EGR	Exhaust Gas Recirculation
EKF	Extended Kalman Filter
EPV	Extended Parametric Voltera series
EU	European Union
EU28	All 28 member states of the European Union
GHG	Green House Gas
IC	Internal Combustion
ICV	Internal Combustion engine Vehicle
J	Joule
JSPE	Joint State and Parameter Estimation
K	Kelvin
kg	Kilogram
LCA	Life Cycle Assessment

LDV	Light Duty Vehicle
LOLIMOT	LOcal LInear MOdel Tree
MAD	Median Absolut Deviation
MAE	Maximum Absolute Error
MAF	Mass Air Flow
MAP	Manifold Absolute Pressure (intake manifold)
MVEM	Mean Value Engine Model
Nm	Newton meter
NSST	Non Steady State Testing
Pa	Pascal
PCM	Powertrain Control Module
PDF	Probability Distribution Function
PID	Proportional-Integral-Derivative
ppm	Parts Per Million
rad	Radians
RMSE	Root Mean Square Error
rpm	Revolutions per minute
PRBS	Pseudo Random Binary Signals
s	Seconds
SDS	Slow Dynamic Slope
SVT	Settled Value Testing
TTW	Tank To Wheel
UEGO	Universal Exhaust Gas Oxygen
UIE	Unknown Input Estimation
UVT	Unsettled Value Testing

VVT	Variable Valve Timing
W	Watt
WG	Waste Gate
WTT	Well To Tank

Chapter 1 Introduction

The success story of the internal combustion engine started 1876 in Germany where Nikolaus August Otto developed the world's first four-stroke engine. Thousands of engineers all over the world have continuously improved his original design. Increasing fuel prices and stricter legislation for emissions force engine developers to focus their research on the reduction of fuel consumption and emissions.

1.1 Contribution of Road Transportation on Greenhouse Gas Emissions

The latest study of Eurostat [1] on greenhouse gas (GHG) emissions shows that in 2015 the combined member states of the EU produced a total of 4452 Mt CO_2. Figure 1.1 shows the contribution to this number by sector.

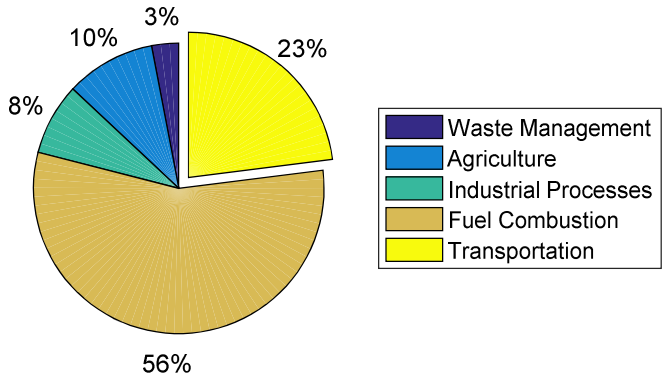

Figure 1.1: EU28 GHG emissions by sector
Values adopted from [1]

Figure 1.1 highlights that transportation is responsible for almost a quarter of the total GHG emissions. Note that "Fuel Combustion" in Figure 1.1 does not include the fuel used in road transportation. According to the European Commission [2], transportation is the main cause of air pollution in cities. A closer look at the study reveals that road transportation is the largest emitter, causing more than 70% of the total transportation GHG emissions as shown in Figure 1.2.

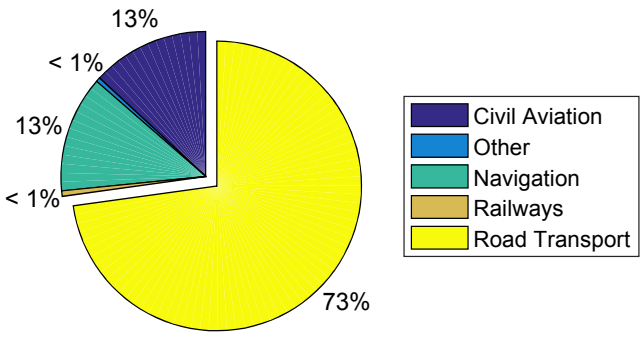

Figure 1.2: EU28 GHG emissions from transportation by mode
Values adopted from [2]

Combining the percentages in Figure 1.1 and Figure 1.2 reveals that in 2015, road transportation was responsible for 17% of the total GHG emissions in the EU. The fact that road transportation is such a significant contributor highlights the importance of research into improved efficiency of future powertrain systems.

Politicians and researchers around the world advertise Battery Electric Vehicles (BEV) as the solution to reduce GHG emissions caused by road transportation [3]. Yet, it has to be mentioned that BEVs are also not emission-free since most countries around the world produce a large percentage of their electricity from fossil fuels. A direct comparison of the total GHG emissions between BEVs and Internal Combustion Vehicles (ICVs) is difficult since a large number of factors have to be considered (car production, fuel production, car use and car disassembly and recovery). Consequently there is a large controversy about the lifecycle environmental impacts of BEVs, which according to Messagie [4] originates from biased publications and misused reports.

A publication by Verbeek *et al* [5] has recently been used in a Report of the European Environment Agency [6] to highlight the advantages and disadvantages of BEVs. Verbeek compares the CO_2 emissions of ICVs and BEVs in a vehicle Life Cycle Assessment (LCA). The LCA is used for environmental assessment of vehicle technologies and allows to compare the average CO_2/km output of an ICE vehicle to a CO_2 equivalent per kilometre of an BEV ($CO_{2-\mathrm{eq}}/\mathrm{km}$). The study published by Verbeek considers the following three main parts for the LCA:

- **Well-To-Tank (WTT)**: Fuel supply chain from source to tank
- **Tank-To-Wheel (TTW)**: Energy conversion in the vehicle

- **Vehicle production and disposal**:
    - Glider: Manufacturing, maintenance and recycling of the vehicle without the powertrain
    - Powertrain: Manufacturing the motor and electronics
    - Lithium Battery: Manufacturing and replacement of battery

The most important factor which determines the $\mathrm{CO}_{2-\mathrm{eq}}/\mathrm{km}$ of a BEV is the WTT stage. Consequently, countries, which have a low carbon footprint, achieve a low $\mathrm{CO}_{2-\mathrm{eq}}/\mathrm{km}$ for BEVs while countries with a large carbon footprint end up with relatively high $\mathrm{CO}_{2-\mathrm{eq}}/\mathrm{km}$ values. The reader should be referred to [4] for a $\mathrm{CO}_{2-\mathrm{eq}}/\mathrm{km}$ list per country.

Figure 1.3 shows the results from Verbeek's study [5] which compares the average $\mathrm{CO}_2/\mathrm{km}$ output of a reference ICV to the $\mathrm{CO}_{2-\mathrm{eq}}/\mathrm{km}$ of a BEV using different energy sources.

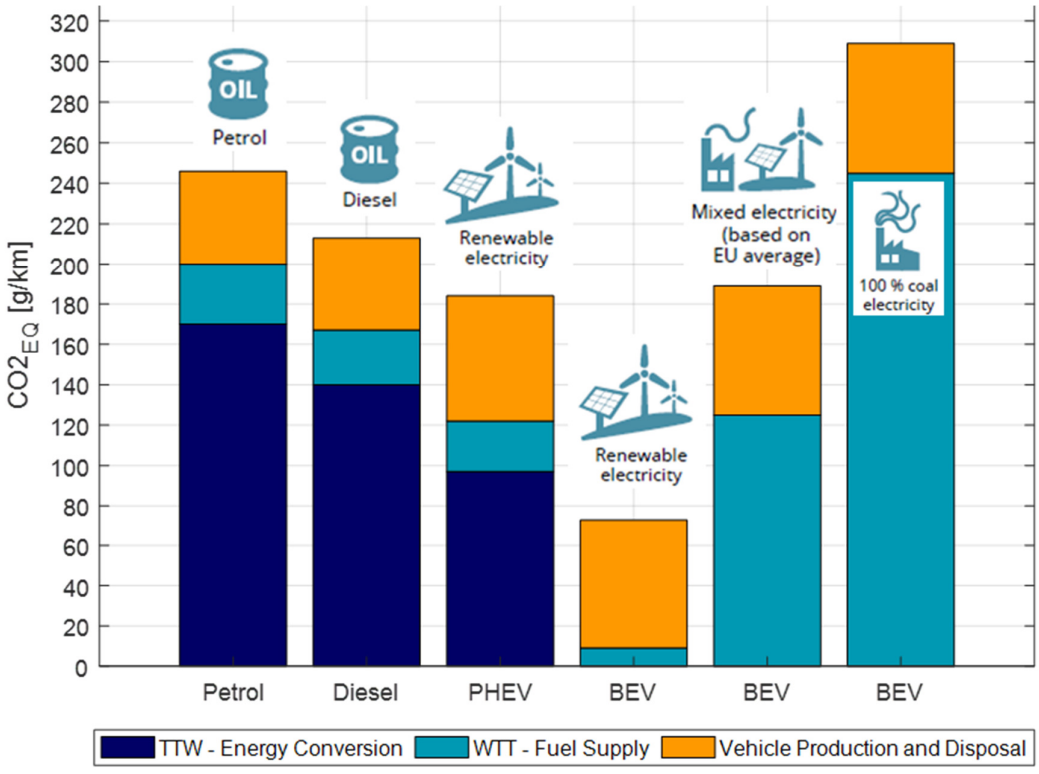

Figure 1.3: Range of life-cycle CO_2 emissions for different vehicle and fuel types

Values adopted from [5] and [6]

Verbeek's results [5] show that BEVs using renewable energy emit about 70% less CO_2 emissions than a mid-sized petrol car. However, comparing the BEV

using the EU28 mixed electricity to the petrol ICV shows that in this case the BEV emits only 25% less $\mathrm{CO_2/km}$. A closer look at Figure 1.3 shows that a $\mathrm{CO_2}$ output of 170g $\mathrm{CO_2/km}$ was used in the study for the petrol ICV, which without any question, is a reasonable average for mid-sized petrol cars. However, state of the art petrol cars such as the Ford Fiesta B479 [7] are advertised with only 97g $\mathrm{CO_2/km}$. It is widely known that these advertised values are too small. According to Fontaras *et al* [8], a factor of 1.3 has to be used to correct for real-world driving conditions. This would lead to 126g $\mathrm{CO_2/km}$. Using this value as a reference would change the LCA results of the petrol ICV from 245g $\mathrm{CO_2/km}$ down to 201g $\mathrm{CO_2/km}$. Consequently, one could argue that BEVs do not contribute significantly in reducing the carbon footprint of the road transportation sector.

On the other hand, as shown in a report by the European Commission [9], EU countries have committed to drastically reduce their carbon footprint until 2050. Therefore, the $\mathrm{CO_{2-eq}/km}$ of BEVs will drop significantly over the upcoming years. Consequently, it can be said that BEVs are definitely the long-term solution for reducing GHG emissions caused by road transportation.

However, the transformation from ICVs to BEVs will not happen overnight. A study from Bloomberg New Energy Finance [10] predicts that by 2040, 1.8 billion cars will be on the road.

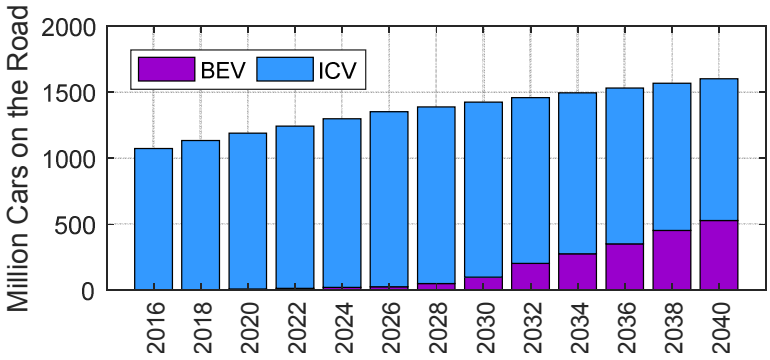

Figure 1.4: Global light-duty fleet predictions

Values adopted from [10]

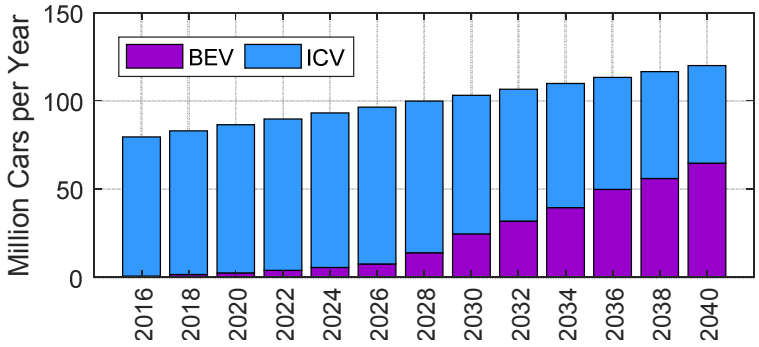

Figure 1.5: Global annual light-duty vehicle sales predictions

Values adopted from [10]

According to the study, by 2040, 33% of all cars will be BEVs and 54% of all new sales will be BEVs. This indicates that the IC engine plays an important role until 2040 and beyond. Consequently, research in IC engines with the aim to reduce fuel consumption and improve exhaust emissions is vital in the future decades to reduce the GHG emission footprint of road transportation.

1.2 Improving the Internal Combustion Engine

According to a study on the future of light-duty vehicles (LDV) by Heywood [11], naturally aspirated spark ignition engines were the most used and sold engine type for LDVs all over the world in 2015. Using this engine type as a reference, Heywood suggests that the following advanced engine technologies can significantly improve the fuel consumption of gasoline engines.

Table 1.1: Future improvements for gasoline engines
Table adopted from [11]

Promising Improvement Areas	Fuel Consumption Reduction
1. Further spread of recent innovations e.g. VVT, DCT	3%
2. Improved synthetic lubricants for lower friction	1%
3. Additional friction reduction opportunities	3%
4. Cylinder deactivation at lighter loads	4%
5. Variable valve control at full and part load	5%
6. Increased compression ratio	3%
7. Smart cooling system for improved heat loss	2%
8. Direct (gasoline) injection	2%
9. Stratified GDI engine operation: Lean NOx catalyst	6%
10. Turbocharged and downsized GDI engines	8% - 12%
11. Engine plus battery system in hybrid (mild/strong)	15% - 30%
12. Stop/start (engine off at idle)	4%
13. Higher expansion ratio engines (hybrids)	3%
14. More gears (7-9); improved transmission efficiency	≤10%

Heywood suggests that if all technologies listed are implemented, a realistic improvement of 17.5% in overall fuel efficiency can be achieved by 2030 compared to a naturally aspirated SI engine. However, current state of the art engines such as the Ford Fox 1.0 litre EcoBoost [12] already incorporate roughly half of the technology improvements from Table 1.1. Consequently, the possible reduction in fuel consumption is lower than 17.5% for state of the art gasoline engines.

However, as mentioned in [11], the difficulty is not to put the already available technologies from Table 1.1 onto new engines but to control them appropriately in real world driving conditions. The combination of multiple advanced technologies such as VVT, turbocharging, EGR and cylinder deactivation massively increase the complexity of the required control strategy. The following section provides a short insight into modern spark ignition (SI) engine control strategies.

1.3 Background - Modern SI Engine control

The objective of a modern Engine Control Unit (ECU) is to deliver the torque output demanded from the driver via the accelerator pedal [13]. The main aim is to generate the requested torque with a minimum fuel consumption while operating within the legal emission limitations. In addition, the driver expects low noise and good drivability such as direct response of the car to a change in pedal position [14]. The demand for higher fuel efficiency and increasingly stricter emission legislation have led to the use of new technologies such as variable valve timing (VVT), turbocharging, exhaust gas recirculation (EGR) and direct injection [11]. The combination of these technologies have turned the engine into a very complex system that requires highly advanced control strategies to ensure safe, robust and fuel efficient engine operation [14]. The interactions and cross couplings between the high number of inputs and outputs require a central coordination of all engine actuators. Isermann [13], Reif [15], Guzella and Onder [16] describe torque-oriented strategies which have become the standard for mass production SI engines since about 2000. This allows the direct request of a specific torque from the engine, which enables advanced driver assistance systems such as cruise control.

1.3.1 SI Engine Torque Control

The torque produced by a gasoline engine is directly proportional to the mass flow of air through it. In addition, engine speed, air-fuel ratio and the angle at which the mixture is ignited influence the torque output [13]. Consequently, the torque output at a certain engine speed has to be managed by controlling the cylinder air charge, the injected fuel quantity and the spark advance. To establish a precise control strategy with such a high number of inputs requires an invertible stationary torque model, which includes all variables that influence torque [16]. Unfortunately, there is no cost-effective and reliable way to directly measure the engine torque output on a vehicle. For this reason, the overall torque control is based on a feedforward strategy. The inversion of the static torque model forms the core of the feedforward control system. However, since a model with four inputs is not directly invertible, it is necessary to represent the multi-dimensional model with a combination of one- and two-dimensional look-up tables [13]. The structure of this model is defined by the hierarchical importance of the inputs,

which can be explained by having a look at the combustion process of the gasoline engine.

The combustion process requires an Air to Fuel Ratio (AFR) close to the stoichiometric ratio. The relative AFR, λ, which is defined as actual AFR divided by the stoichiometric AFR is commonly used in literature to define whether the combustion is rich, stoichiometric or lean [17]. A stable combustion is achieved between $0.8 < \lambda < 1.4$ and within this range; exhaust gas emissions such as Hydro Carbons (HC), Nitrogen Oxides (NOx) and Carbon Monoxides (CO) are affected as demonstrated in Figure 1.6.

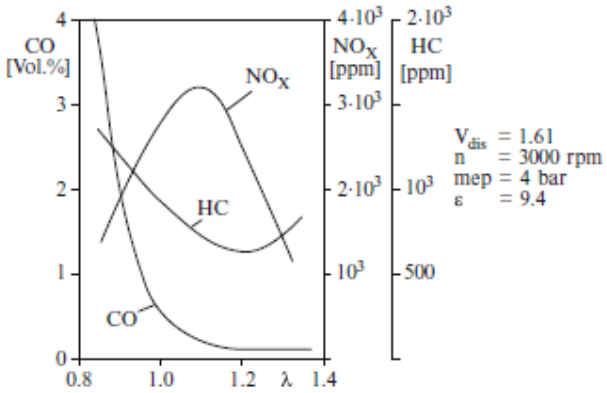

Figure 1.6: Pollutant formation as a function of the equivalence ratio

Adopted form [17]

To achieve current and future emission legislation the use of a three-way catalyst is currently unavoidable. However, the conversion efficiency of each specific emission is strongly dependent on the λ value as shown in Figure 1.7.

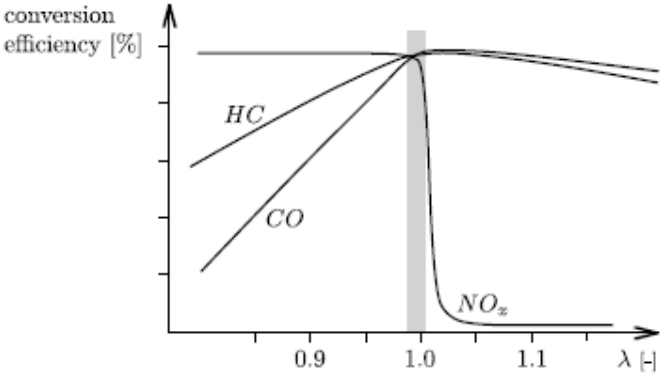

Figure 1.7: Conversion efficiency of a TWC

Adopted from [16]

Figure 1.7 clarifies that a precise AFR between $0.98 < \lambda < 1.02$ is required for the three-way catalyst to significantly reduce all three exhaust gas emissions. Combining the tight AFR operating window with the fact that the highest fuel efficiency is achieved at maximum brake torque (MBT) shows that the engine torque is ideally produced at $\lambda = 1$ and spark advance at MBT. Consequently, cylinder air charge is the main control variable for the engine torque output. The following structure for the engine torque model is commonly used in today's mass production ECUs.

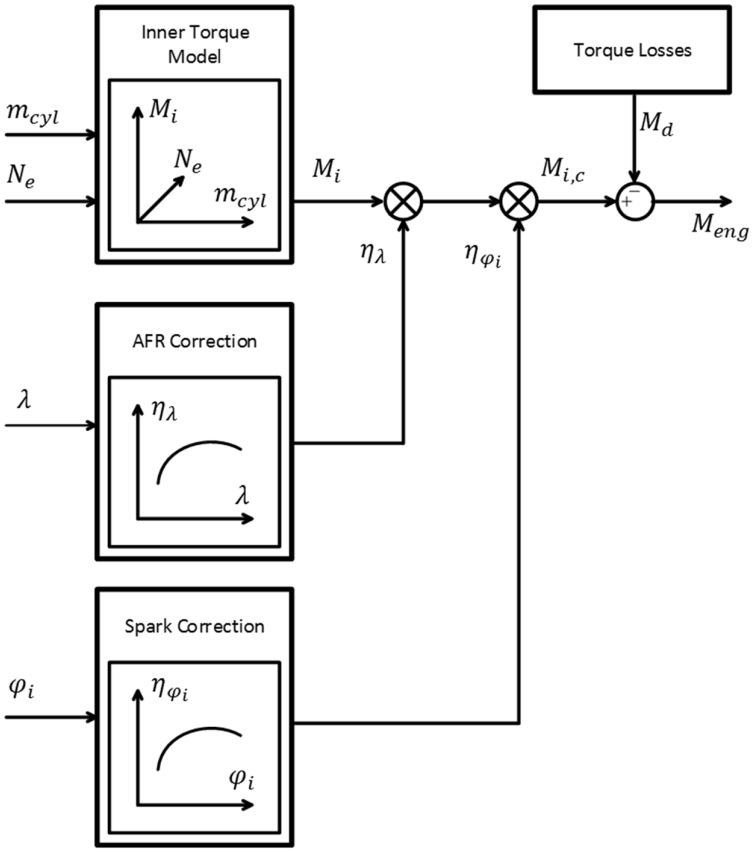

Figure 1.8: ECU torque model

Adopted from [13]

The inner torque model M_i is a two-dimensional map, which describes the engine torque dependency on the cylinder air charge m_{cyl} and engine speed N_{eng} when the engine operates at $\lambda = 1$ and with a spark advance φ_{spk} at MBT. Two additional one dimensional maps then describe how the inner torque varies with a change in AFR and spark advance leads to the corrected inner torque $M_{i,corr}$. Finally, the friction torque is removed to estimate the actual engine torque output M_{eng}. When the driver demands a certain torque from the engine, the torque

demand can be converted into desired air charge and a desired ignition angle. This process is known as torque conversion and inverts the torque structure described in Figure 1.8.

The ignition angle is set by the ECU and closed loop control using a knock senor is used to retard the spark in case the engine is knocking. In order to achieve the desired cylinder air charge, an air charge control strategy is required which is described in the following subsection.

1.3.2 SI Engine Air Charge Control

The cylinder air charge in a gasoline engine with a turbocharger is controlled through the position of the throttle and the waste gate (WG) [18]. The throttle position predominantly affects the intake manifold pressure and is used to restrict the air mass flow into the engine. The waste gate position affects the exhaust back pressure and the boost pressure, which allows an increase in air mass flow into the engine. The task of air charge control can be divided into the coordination between throttle and WG position and the actual control of the desired actuator positions.

a) Actuator Coordination

The coordination of throttle and WG position is a trade-off between transient response and fuel efficiency as shown by Eriksson *et al* [18]. The highest fuel efficiency is achieved if the WG is kept as open as possible to meet a specific air charge demand. Any increase in exhaust gas pressure increases the pumping work during the exhaust stroke and consequently reduces the fuel efficiency. However, as demonstrated by Gorzelic *et al* [19] the response of air charge to a change in WG position is much slower compared to a change in throttle position, which makes a smooth transition from throttled into boosted operating mode extremely difficult. The slow response to the WG actuator can be explained by the inertia of the turbocharger as well as by the filling and emptying of the intake and exhaust system, which further delay the build-up of boost pressure. The best response can be achieved if the WG is kept as closed as possible to meet a specific air charge demand. In this case, the WG is only used to limit the maximum boost pressure and the throttle is used to control the intake manifold pressure. However, the higher the boost pressure during throttled engine operation, the higher the penalty in fuel efficiency due to the increased pumping

work. A good compromise between fast response and high fuel efficiency can be achieved with the use of a boost buffer as shown by Beckman *et al* [20]. The aim of such a strategy is to build up a specific boost pressure when the intake manifold pressure is below ambient pressure and to maintain a specific pressure difference across the throttle once the intake manifold pressure exceeds ambient pressure. This allows a smooth transition from the throttled into the boosted operating range as well as a fast air charge response at high load.

Since most modern SI engines are equipped with a Mass Air Flow (MAF) sensor, it is theoretically possible to control throttle and WG position with a simple Proportional-Integral-Derivative (PID) controller. However, this would result in a very slow and poor response of the desired air charge [13]. To achieve a highly responsive but robust system, a more advanced control structure is required. In literature, a wider range of approaches with different complexity is available. The simplest methods combine feedback with static feedforward control as shown in Thomasson *et al* [21], Wakeman and Wright [22] or Iserman [13]. Replacing the static feed forward model with a linearized dynamic feed forward model, as shown by Colin *et al* [23], Kranik *et al* [24], Kalabic *et al* [25], Moulin *et al* [26] and Leroy *et al* [27], can further improve the transient response. The most advanced solutions, as presented by Cieslar [28] and Colin *et al* [29] make use of model predictive control which theoretically allows a close to optimal operation.

b) Actuator Position Control

All advanced control structures mentioned above require a static or dynamic model of the air-path. The most common solution for air charge control is the combination of feedforward and feedback control as shown in Isermann [13]. The engine air charge of a SI engine at a specific engine speed is mainly dependent on the intake manifold pressure. Therefore, a two-dimensional map, which describes how the air charge depends on intake manifold pressure and engine speed, forms the core of such a control strategy as shown by Colin [29]. The air charge model is multiplied by a one-dimensional map, which describes how the air charge is affected by the intake manifold temperature as illustrated in Figure 1.9. The inversion of this model allows converting the desired air charge into a desired intake manifold pressure as shown in Figure 1.10.

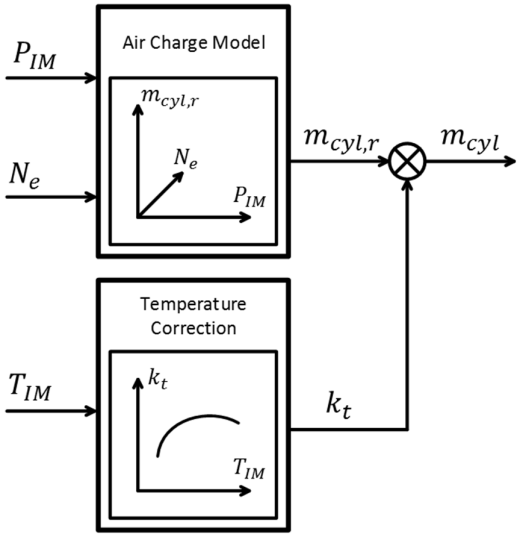

Figure 1.9: ECU air charge model

Adopted from [13]

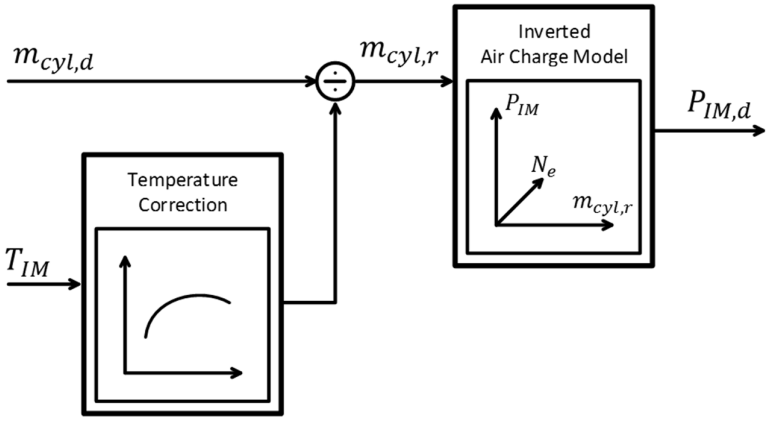

Figure 1.10: ECU air charge model inversion

Adopted from [13]

Combining the desired intake manifold pressure with the desired delta throttle pressure allows an estimate of desired boost pressure. The throttle is then used to control the intake manifold pressure, and the waste gate is used to control the boost pressure. Using the interconnected control structure, throttle and WG can be controlled as demonstrated in Figure 1.11 and Figure 1.12.

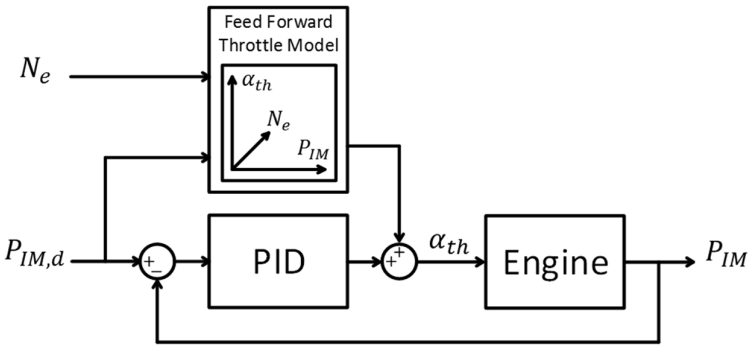

Figure 1.11: ECU throttle controller

Adopted from [13]

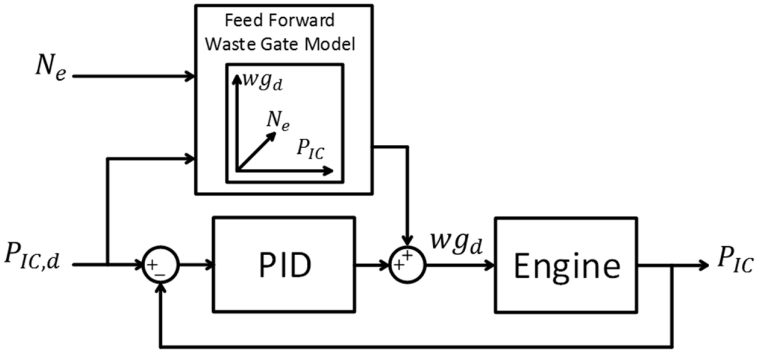

Figure 1.12: ECU waste gate controller

Adopted from [13]

The feedforward controller can be either a simple inverted stationary model or a linearised inverted dynamic model. The complete air charge control strategy is summarised in Figure 1.13.

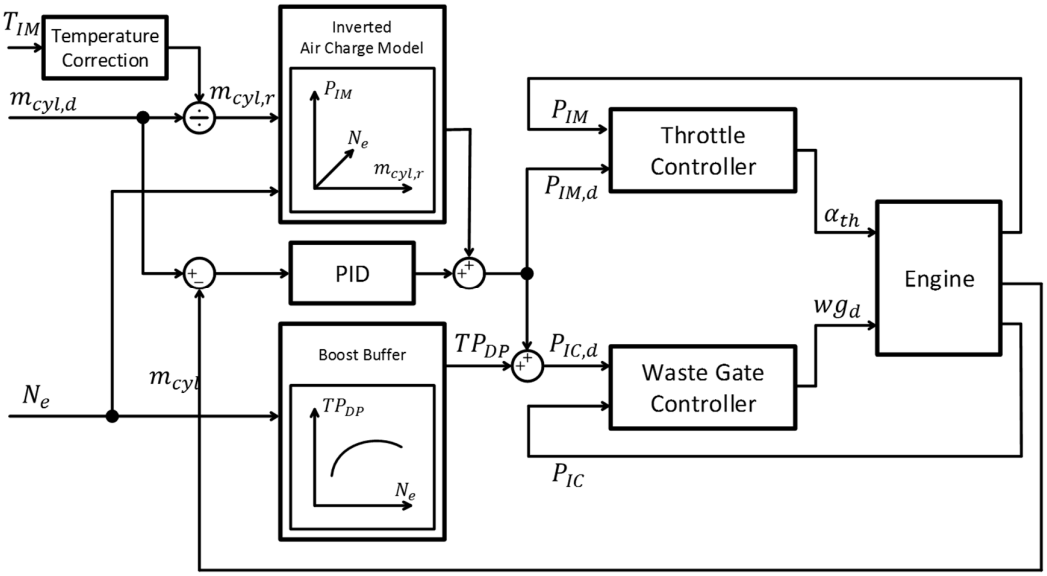

Figure 1.13: ECU air charge control strategy

Adopted from [13]

Feedforward torque based engine control strategies rely on a number of invertible stationary models. Generating these models is called the engine calibration process and requires a large amount of test data, which cover the entire engine operating range [14]. It is crucial that the calibration is performed with steady-state test data. In case the models do not describe the engine at steady-state conditions, accurate and fast responsive torque control is not possible, and thus the car will have very poor drivability as well as a poor fuel consumption and high emissions.

1.3.3 Mapping, Calibration, and Engine Testing

Improvements in fuel economy and reduction of emissions can only be achieved by using advanced engine technology [11]. However, in order to benefit from these technologies, advanced control strategies are required to control the actuators of each technology [13]. More advanced control strategies require an exponentially increasing amount of data to parameterise the models which form the core of the control strategy.

The required steady-state test data for engine calibration have to be generated on an engine test-bed. The increasing amount of ECU look-up tables demands an exponential increase in the required amount of test data [13]. Future engine technology with even more engine actuators could lead to a situation where the calibration process becomes the bottleneck in the engine development process. Conventional engine testing methodologies are too inefficient to provide the amount of test data which will be required for the calibration of future engine control strategies. The only solution to provide the enormous amount of data in the future is to significantly increase the efficiency of the engine testing process on the test-bed. This can be achieved by replacing the conventional steady-state testing method with dynamic engine testing which theoretically allows to save up to 80% of the testing time [30]. The main reason why dynamic engine testing methodologies are not implemented yet is, because engine data, which are recorded during transient engine operation, are affected by the dynamic behaviour of the entire engine system [13]. The direct use of transient test data without any dynamic compensation for ECU calibration would end up in catastrophic behaviour of the engine in terms of fuel consumption, emissions, power and drivability.

1.4 Problem Statement

With modern complex engine designs, the inefficiency of conventional steady-state testing methods has effectively created a bottleneck in the engine development process. This potentially limits the implementation of new technologies and improvement in fuel consumption and engine out emissions. In such an advanced system, the definition of the optimal schedules for all actuators would require a prohibitively large amount of steady-state test data. This is because the time needed to provide this data increases exponentially with the addition of each new engine actuator. Consequently, engine testing for ECU calibration has become a significant burden for the entire engine development process. Increased commercial pressures to bring new products to market require vehicle OEMs to significantly increase the efficiency of their calibration processes.

Currently, steady-state testing wastes around 90% of the testing time on actuator adjustment and parameter settling. Hence, the process is inherently inefficient and thus, not well suited to provide the data load required for the calibration of modern and future engines. Therefore, a rapid test methodology, which delivers time efficient engine characterisation, is required. Transient test methods offer one possibility, but the data includes the influence of the dynamic behaviour of the engine. Since the ECU base calibration requires steady-state data, it is necessary to develop tools, which allow the conversion of dynamic data into equivalent steady-state data or to compensate for excited dynamic effects.

The primary focus of this thesis is on the development and implementation of a practical transient data collection method, sufficient to support the calibration of the ECU air charge control strategy. At steady-state, in cylinder air charge measures can be made directly using a MAF sensor, or can be calculated from measurements of fuel flow and AFR.

During transient operation, significant transport and sensor response delays for a wideband universal exhaust gas oxygen (UEGO) AFR sensor complicate airflow estimates [31]. Similar remarks typically apply to the fuel measurement system. Consequently, dynamic air mass estimates are not sufficiently accurate.

Recently available ultrasonic air mass flow meters are highly accurate and have high band width [32]. Due to its size, the sensor must be installed before the air filter inlet tube. Consequently, especially for turbocharged engines, large

distances exist between the meter and the intake valve. During steady-state engine operation, this is not an issue since the air mass flow measured at the location of the sensor is identical to the air mass flow into the cylinder on a cycle average basis. However, during dynamic testing where the pressure in the intake system changes rapidly, measured and actual air mass flow into the cylinder are not identical anymore, due to the existence of filling and emptying dynamics associated with the intake system volumes. These filling and emptying phenomena can be described by relatively simple physics based equations. This facilitates the development of schemes to compensate for these dynamic phenomena. Consequently, it is possible to observe the instantaneous or cycle averaged airflow into the cylinder during transient engine operation.

1.5 Aims and Objectives

The aim of this research is to deliver a significant reduction in engine testing time required for air charge characterisation of a modern GTDI engine using transient test data. To achieve this aim, the following objectives were set:

1. Develop a sufficiently accurate physics based model, which describes the filling and emptying dynamics along the engine air-path.
2. Compare alternative observer principles to determine the most suitable estimator for the study.
3. Derive an observer for the entire air-path by combining the physics based filling and emptying model with the selected observation method, which accurately observes the airflow into the cylinder.
4. Validate the observer, by applying the observer to a higher fidelity 1D engine model and compare the observed air mass flow into the cylinder with the actual air mass flow into the cylinder.
5. Validate the observer experimentally by comparing the observed volumetric efficiency with corresponding steady-state values.

1.6 Major Contributions

The major contributions of this thesis are:

- **Methodology that leads to the reduction of engine testing time**: The main contribution of this thesis is the successful development and implementation of a rapid, observer based engine air charge

characterisation methodology. The experimental validation results demonstrate approximately a 95% reduction in required test time, compared to conventional steady state methods. Compared to state of the art quasi steady-state approaches, based on slow dynamic slopes (SDS), the observer-based method is at least 68% faster.

- **Air-path observer for a modern GTDI engine**: An air-path observer is developed which compensates for the filling and emptying dynamics along the entire intake air-path. Existing methods apply the theory only to one volume.
- **Mass based observer**: Existing work utilises pressure or pressure and temperature as the observer system states. Both approaches rely on thermodynamic assumptions, and these approximations may limit the accuracy of the observer outflow estimation. Here, the developed observer uses the mass inside the volume as system state. This approach eliminates the need for any thermodynamic process assumptions, without adding complexity to the observer design.
- **Observer accuracy**: To the best of the author's knowledge, currently no literature exists investigating the accuracy of an air-path observer in observing the volume outflow. The mean value model used in the observer neglects gas dynamic effects. Simulation studies illustrate that for sufficiently low intensity excitation the impact of these neglected gas dynamics is small. Observer accuracy is also shown to depend on the geometry of the volume as well as the intensity of dynamic excitation.
- **Steady-state versus transient volumetric efficiency**: Existing literature suggests that transient volumetric efficiency is identical to steady-state volumetric efficiency. Conduced simulation studies based on a 1D crank angle resolved model contradict this assertion. The magnitude of the reported differences depends on the intensity of the transient.
- **Trade-off between time saving and accuracy**: Two statistical measures are applied to the accuracy of the dynamic test results which allow to establish a relation between time saving and data accuracy.
- **Dual ramp averaging**: System dynamics are excited by ramping the intake manifold pressure from low to high and *vice versa*, as a prescribed rate. A novel implementation of a dual-ramp averaging procedure is developed. The algorithm incorporates an engine controller, which delivers

the symmetrical up-ramp and down-ramp required as a perquisite by the dual ramp averaging method. This ensures system dynamics are excited similarly on the up and down ramps, avoiding unintentional bias to either ramp.

1.7 Thesis Organisation

The thesis is divided into 10 chapters. The air charge estimation problem is introduced in Chapter 1 and set against the context of the ever-increasing data collection demands of modern complex engine control units. In addition, the primary aims and objectives of the thesis are presented. This is followed by a brief review of the major contributions resulting from the work.

Chapter 2 reviews the Literature. The review covers all relevant areas explored in the thesis. Section 2.1 presents a historical retrospective of various engine test protocols used in previous investigations. This includes conventional steady-state testing, quasi steady-state testing and dynamic testing. Section 2.2 is focused on dynamic compensation tools, which are required to produce equivalent steady-state test results from a dynamic engine test. In Section 2.3 a selection of different dynamic engine modelling approaches are compared and contrasted. Section 2.4 is specifically dedicated to mean value engine models as this model type forms the basis of all observers. Different methods for air charge observation are considered in Section 2.5. Having reviewed the relevant literature, Section 2.6 identifies a research gap, which this thesis attempts to fill.

Chapter 3 provides all important background information for dynamic engine air-path modelling of a turbocharged SI engine. The equations presented in this chapter provide the physics based modelling techniques required in Chapter 5 to develop the air-path observer. Air-path modelling is divided into restrictions, turbocharger and volumes, which are discussed in Sections 3.1, 3.2 and 3.3 respectively. Section 3.4 is focused on the cylinder model where a clear distinction between crank angle resolved and cycle average modelling is made.

Chapter 4 compares two different solution for the observation method which is required to solve the air-path observation problem. A simplified but representative problem is used to carry out a case study which compares the two methods. Based on the results of the case study, the appropriate method for this project is selected.

Chapter 5 combines the knowledge about dynamic air-path modelling and system state observation to develop the air-path observer, which is used to solve the main problem of this project. Two versions of the air-path observer are presented, one for offline applications and one for online, real-time applications.

Chapter 6 is focused on the implementation of the rapid air charge characterisation project. Section 6.1 discusses the inputs required for an air charge characterisation which is sufficient for engine control applications. Section 6.2 gives an overview over the entire test process in the engine test cell and Section 6.3 is focused on observer tuning to achieve the best possible results. The exact engine test procedure used in this project is defined in Section 6.4. A suitable engine air-path controller, which allows controlling the engine during the specified test, is developed in Section 6.5. Data processing and dual ramp averaging are treated in Sections 6.6 and 6.7 respectively.

Chapter 7 introduces the simulation platform which was developed to validate the developed air-path observer. Purpose of this chapter is to provide all important details of the simulation platform, since the simulation based validation in Chapter 8 is a crucial part of this thesis. The details of the virtual simulation platform are provided in Section 7.1. The 1D engine model is validated against experimental test results in Section 7.2 to prove that the model used for method validation is an accurate representation of the real system. Section 7.3 compares the two proposed engine air-path controllers to highlight the advantages and disadvantages of each method.

Chapter 8 uses the simulation platform to validate the accuracy of the developed air-path observer. Section 8.2 investigates if the volumetric efficiency of the engine is identical during steady-state and dynamic engine operation. This investigation is crucial, since it determines whether it is possible at all to characterise steady-state engine air charge behaviour from dynamic engine data. Section 8.3 investigates the impact of assumptions in the dynamic model of the observer on the accuracy of air charge observation. The results of this section indicate how accurate the observer works during transient engine operation and therefore gives an indication of how much time can be saved with the developed method. Finally, the entire developed methodology is validated in Section 8.4. Here the observed air charge values are compared to steady-state data to judge the accuracy of the developed method.

Chapter 9 provides the experimental validation of the methodology on a real engine. The state of the art engine test cell is introduced in Section 9.1. Section 9.2 provides the details of the experimental data collection which includes conventional steady-state testing, quasi steady-state testing and dynamic testing. Based on the repeatability of conventional steady-state testing, a measure of success is established in Section 9.3, which is used in the following sections to judge the accuracy of the methodology. Section 9.4 compares the observed air charge values from the dynamic engine test to steady-state data. Different ramp rates are used to produce a trade-off between time saving compared to steady-state testing and accuracy of the measurement results. Finally, Section 9.5 provides the time saving in engine testing time that has been achieve through this research. The results of this section determine whether the main aim of this thesis, to achieve a significant reduction in engine testing time for air charge characterisation, has been achieved.

Chapter 10 provides a summary, conclusions and future work. Section 10.1 summarises the work undertaken in each chapter. Section 10.2 presents the conclusions of this work. At first, the key conclusions / major contributions are listed in Subsection 10.2.1, followed by the conclusions of each individual chapter in Subsection 10.2.2. Ideas for future work are proposed in Section 10.3 based on the presented results, conclusions and remaining challenges.

Chapter 2 Literature Review & Background Information

This chapter present a review of literature and background information of all topics that are relevant to this work. Section 2.1 is focused on engine testing to clarify the inefficiency of conventional steady-state testing and to point out the potential of dynamic testing methodologies. Section 2.2 reviews dynamic compensation tools, which are required to produce equivalent steady-state data from dynamic test results. Section 2.3 is focused on dynamic engine modelling and Section 2.4 provides a detailed review of mean value engine modelling. Air charge observers are reviewed in Section 2.5. Based on the literature review, the research gap is identified in Section 2.6, which justifies the effort of the research conducted and clarifies the contribution of this work.

2.1 Engine Testing

This section reviews three fundamental different engine testing methodologies. Subsection 2.1.1 is focused on conventional stead-state testing, Subsection 2.1.2 covers quasi steady-state testing and Subsection 2.1.3 reviews dynamic testing methodologies.

2.1.1 Conventional Steady-State Testing

Conventional steady-state testing is currently seen as the golden standard for experimental engine testing [13]. It can be described by the following three steps, illustrated in Figure 2.1 [33]:

1. **Iterative adjustment of engine actuators**: A controller adjusts one or more actuators until the engine operates at the desired operating point.
2. **Engine stabilisation**: All engine actuators are kept in position for a certain amount of time until all engine responses have settled.
3. **Measurement**: Actuator settings and engine responses are recorded over a certain amount of time and the average value of each response is calculated. This is done in order to eliminate any disturbance of the measured signal caused by noise or other fluctuations.

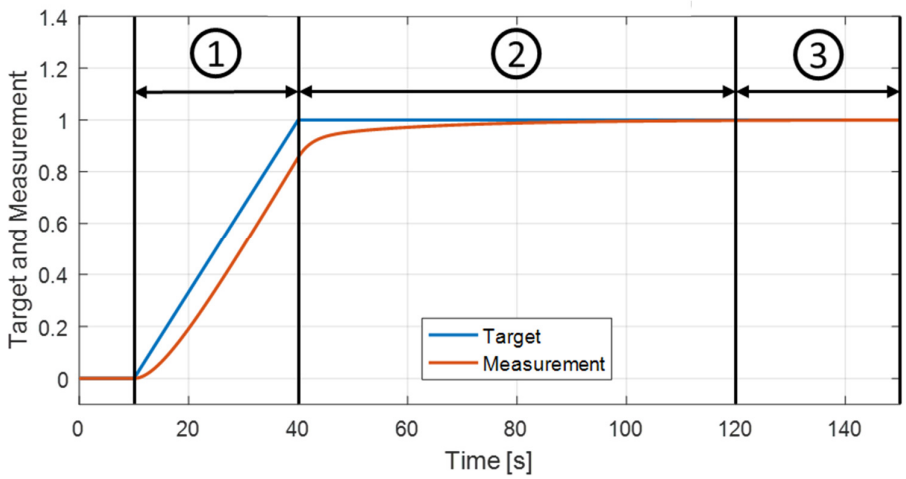

Figure 2.1: Conventional steady-state testing procedure

Adopted from [33]

The main characteristic of steady-state testing is that data are only recorded once all engine variables have settled. For this reason, the method is also known as settled value testing (SVT). The time used for engine stabilisation is dependent on the settling time of the desired engine response. Consequently, the time required for engine stabilisation depends on the purpose of the engine test as shown by Berger [33]. The overall process time for one test point typically varies between two and three minutes [13] but can be up to five minutes [33] if variables with extremely long settling times are involved. However, the actual recording time usually takes no longer than thirty seconds which means that up to 90% of the testing time is wasted.

The simplest and most traditional way to apply steady-state testing is to use a test plan with a full factorial regular grid [33]. The engine is tested at each point of the grid with the method described above. However, as described by Toepfer [34], a full factorial regular grid suffers from the ‘curse of dimensionality’, which basically means that the number of test points increases exponentially with the number of inputs. For current and future engines with 6-8 actuators, this method cannot provide the required data in any economical way [13].

The first attempt to reduce the overall engine testing time used Design of Experiment (DoE) methods which allow significant reduction in the number of test points by making use of some pre knowledge of the system as described by Fischer and Roepke [35]. According to Boehme [36] a reduction of testing points of up to 70% is possible if enough information about the sensitivity and nonlinearity of the system is known. This method aims to reduce testing time by

increasing the information content about the system of each test point. However, if the engine under test is not just a slight modification of an already existing engine, this means that the required pre-knowledge is not available and consequently the possible reduction of testing points is limited.

To improve the efficiency and reduce the cost of the engine mapping process, new test methodologies have to be developed. Huge improvements could be achieved by eliminating the wasted testing time required for actuator adjustment and response stabilisation. This would also allow the recording of data continuously, which massively increases the information quantity. Replacing a small amount of test points and very high information content with a high number of test points which cover the information content through the quantity of test points offers a significant advantage in the model building process during the calibration stage [36]. The possibility to save a significant amount of testing time combined with a massive increase in recorded test points indicates the tremendous potential of dynamic testing in the future.

2.1.2 Quasi Steady-State Testing

An intermediate step between conventional steady-state testing and dynamic testing is the quasi steady-state method [13]. The idea is to change one or more input variables continuously but extremely slowly to avoid significant excitation of relevant dynamics. Such an actuator input signal is also known as ‘slow ramp’ since the input signal changes linearly from its minimum to maximum value. For this reason, the method is also known as the slow dynamic slope (SDS) method. The data are recorded continuously with a high sampling rate and as many points as necessary can be selected within the ramp [13]. Figure 2.2 illustrates the difference between steady-state and quasi steady-state testing.

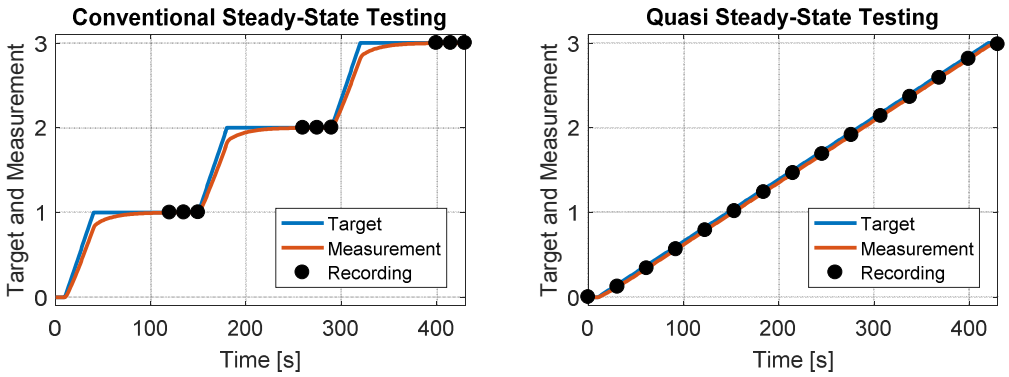

Figure 2.2: Comparison between conventional steady-state testing and quasi steady-state testing

Adopted from [13]

SDS testing is the simplest method to save engine testing time since it does not excite any dynamics and consequently requires no methodology for compensation. However, the slope of the ramp has to be defined by the largest time constant of the relevant engine dynamics to avoid any significant dynamic excitation [13]. Consequently, the ramp rate is strongly dependent on the response variable of interest. This leads to the conclusion that the methodology is unsuitable for testing which involves variables with long settling times such as exhaust gas temperature. The method was first applied by Hislop [37] in 1974 for the characterisation of the engine power curve. The author demonstrates that for low ramp rates, no difference between slow dynamic slope and steady-state testing is noticeable. In addition, it is shown that the error increases exponentially with increasing ramp rate. Fehl [38] makes use of a linear dynamic system model to limit the error caused by dynamic system excitation to a certain level. Boehme [36], [39] applied the testing method for air charge characterisation of a naturally aspirated SI engine. He inverted a physics based dynamic model of the intake manifold to limit the dynamic excitation by controlling the throttle appropriately. Murakami [40] applied the SDS method to the entire testing process of a stratified gasoline engine with nine degrees of freedom. A time reduction of more than 40% is reported. Keuth [41] used the methodology for air charge and torque characterisation of a turbocharged gasoline engine. A time saving of 36% was achieved. Leitgoeb [42] characterised the air charge behaviour of a gasoline engine with variable valve timing with a time saving of 50%.

2.1.3 Dynamic Testing

Dynamic engine testing can be performed in many ways which means that there is no standard method available as it is for conventional steady-state testing. Generally, dynamic testing can be characterised by the fact that some values *e.g.* actuator setting or a specific engine response have not settled and are changing over time. Therefore, dynamic testing is also known in literature as unsettled value testing (UVT) or non-steady-state testing (NSST). Dynamic engine testing can be divided into Dynamic Offset Ramp (DOR) testing and rapid step testing due to the significant difference in the actuator input signal.

a) Dynamic Offset Ramp

The input value of the actuator is ramped up quickly which causes a dynamic excitation of the system. If the system is linear the system response will show only a constant offset value compared to its steady-state value as illustrated in Figure 2.3.

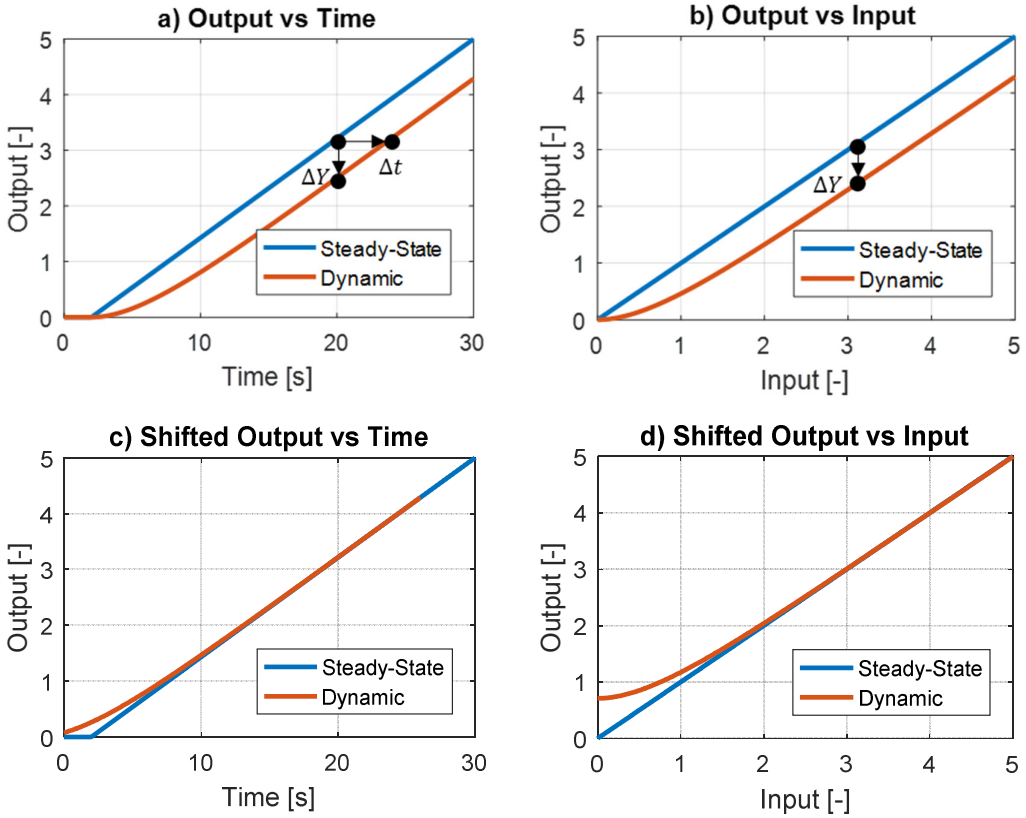

Figure 2.3: Dynamic offset ramp testing

Adopted from [13]

For linear systems, it is possible to identify the constant offset and correct the dynamic data by simply shifting them in time [13]. If the system is nonlinear, the dynamic offset is not constant. Unfortunately, almost any engine response has a nonlinear behaviour, which means that the offset is not constant and more complex methods are required to compensate for this fact. Methods for dynamic offset compensation are reviewed in Subsection 2.2.1. The aim of this dynamic testing methodology is to excite the system constantly to a specific level by using a ramp input. If the system is strongly nonlinear, the input eventually has to be modified in order to produce a ramp in the system response. This can be achieved by using an approximation of the dynamic system behaviour as shown in Boehme [36]. This method does not try to avoid dynamic excitation, in fact, the level of excitation is not limited. The higher the slope of the ramp, the stronger the excitation during the ramp. A constant excitation is desirable since it allows to use simple but effective compensation tools such as dual ramp averaging as described in Subsection 2.2.1.

b) Rapid Step Testing

Rapid step testing uses aggressive actuator input signal such as Pseudo Random Binary Signals (PRBS) or Amplitude Modulated Pseudo Random Binary Signals (AMPRBS) [13]. These input signals strongly excite the engine dynamics and the position of the actuator changes before the system has settled, as shown in Figure 2.4:

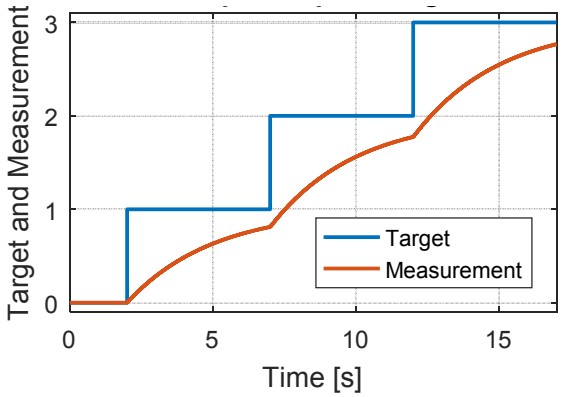

Figure 2.4: Rapid step testing procedure
Adopted from [30]

The idea behind this testing method is that an empirical dynamic engine model (also known as black-box model) is parameterised with the dynamic test data and the dynamic model is later used to predict the steady-state values [30]. Steady-

state prediction is reviewed in Subsection 2.2.2. This testing method is clearly different from the dynamic offset ramp. The aim of this method is to excite the dynamics as much as possible in order to characterise the dynamic behaviour as accurately as possible.

2.2 Dynamic Compensation Tools

As mentioned in Subsection 2.1.1, steady-state engine experiments are essential for the calibration of the ECU control strategy. On the other hand, significant reduction in engine testing time can only be achieved with dynamic testing methods as described in Subsection 2.1.3. The disadvantage of these testing methodologies is that the entire engine system is in a dynamic state, which makes it impossible to directly obtain the required steady-state data. This issue can be subdivided into three problems namely excitation of dynamic states, measurability of specific quantities and sensor response delays.

- **Excitation of dynamic states**: Some engine responses such as torque or exhaust gas temperature respond dynamically to a change in actuator settings such as spark advance. Consequently, during dynamic testing these engine states are not settled. In order to obtain steady-state measurement data for these engine variables, it is either necessary to compensate for the dynamic excitation or predict where these variables would have settled [30]. Dynamic offset compensation and steady-state prediction are treated in Subsections 2.2.1 and 2.2.2 respectively. The selection of the dynamic test methodology determines which compensation method has to be used. For clarification: Dynamic offset ramp testing requires dynamic offset compensation while rapid step testing requires the use of steady-state prediction.
- **Measurability of specific quantities**: Due to the size of some sensors and the geometry of the engine, some variables cannot be measured at the correct location. The most popular example for this problem is the measurement of the air mass flow into the cylinder. The MAF sensor can only be mounted in front of the air filter. This causes the problem that during dynamic testing which excites the filling and emptying dynamics of the intake system, measured air mass flow at the location of the sensor and actual air mass flow into the cylinder are not identical [43]. In order to measure the air mass flow into the cylinder during dynamic engine testing,

an observer is required. Air charge observers are specifically addressed in Section 2.5.

- **Sensor response delays**: Some sensors used to measure the engine response variables have a significant response delay. Thermocouples as well as emission measurement systems suffer in particular from this problem [44]. Due to the response delay a measurement error is introduced if a dynamic signal is measured. To ensure accurate measurement of the response variables during dynamic testing, input reconstruction methodologies have to be used which allow to compensate for the response delay of the sensor.

2.2.1 Dynamic Offset Compensation

As described in Subsection 2.1.3, dynamic offset ramp testing requires a methodology which compensates for the dynamic offset in order to produce the required steady-state data. This subsection reviews three available methods.

a) Dual Ramp Averaging:

A simple but effective method to compensate for the dynamic offset during fast ramps is the dual ramp averaging method (DRA) [45]. In order to apply this compensation method, it is required to ramp the actuator input up and down during the experimental test. This produces a hysteresis in the recorded engine responses [13]. The mean value of the hysteresis is then used to approximate the steady-state engine behaviour as illustrated in Figure 2.5.

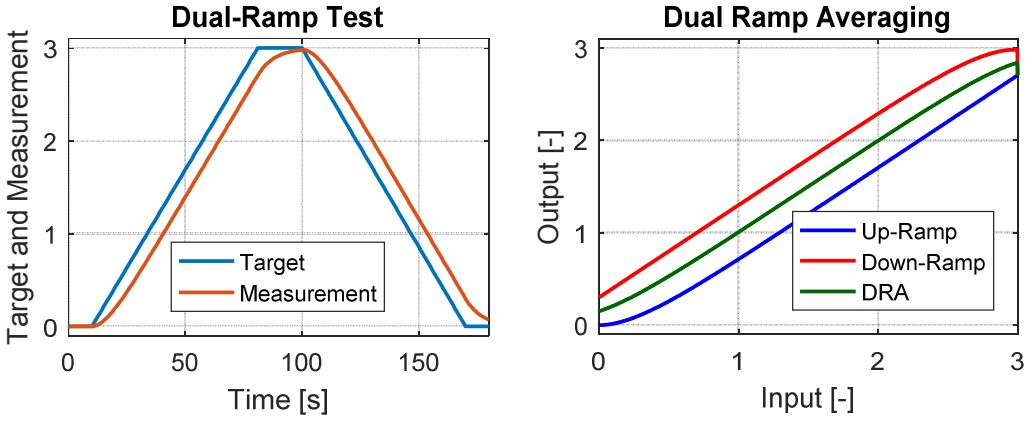

Figure 2.5: Dual ramp averaging procedure
Adopted from [13]

For this method, it is essential that the system dynamics get identically excited on the up-ramp and the down-ramp, otherwise the averaging does not lead to the correct steady-state values. The method was first suggested by Hislop [37], however, no detailed information about the achievable accuracy is given. Goulburn *et al* [46] continued Hislop's work and showed that the ramp rate can be significantly increased with this method while maintaining steady-state accuracy. Ward *et al* [45] applied the method for the characterisation of NO_x emissions, exhaust gas temperature and air charge. The results show that the averaging works well even for significant system excitations. However, it is also shown that the error compared to steady-state data increases with an increasing ramp rate. Schwarte [47] and Leitgoeb [42] show that DRA is a powerful tool since it can compensate for any dynamics as long as they are excited to an identical level during the up-ramp and the down-ramp. This requires symmetry in the system input signals between the up-ramp and the down-ramp.

b) Data Shifting

Another method to compensate for a dynamic offset is to simply shift the data in time. A ramp input into a linear system produces a constant dynamic offset compared to the steady-state response of the system. Shifting the dynamic data by the size of the time constant as shown in [13] theoretically allows to compensate for the dynamic offset. Ward *et al* [45] used this method for the characterisation of NO_x emissions. A constant transport delay was used to account for the location of the emission analyser. To account for the response delay of the emission analyser, a second order model was characterised to describe the settling time. The presented results show an improved accuracy compared with the dual ramp averaging method. However, the author also mentions a significant issue in terms of accuracy especially during the beginning and the end of the ramp where the excitation is not yet constant.

c) Model based Dynamic Compensation

The most advanced method to compensate for a dynamic offset is to make use of a dynamic system model. The idea behind this method is to use either a physics based model or an empirical model to describe the dynamic behaviour of the system. The model is then inverted to compensate for any dynamic system excitation. This method can handle linear and nonlinear systems. For linear systems, where the time constant is accurately known, the compensation is

straight forward [13]. An application to a nonlinear system, however, requires a nonlinear model to compensate for the excited dynamics. Sugita *et al* [48] applied the method to exhaust gas temperature testing. Firstly, an experimental dynamic model is identified, which describes the dynamic behaviour of the exhaust gas temperature to a change in spark advance at different air mass flow rates. The model is later inverted to correct the exhaust gas temperature during fast spark ramps at constant engine speed.

2.2.2 Steady-State Prediction

As described in Subsection 2.1.3, rapid step testing requires the identification of a dynamic model, which is then used to predict the steady-state response of the engine [30]. The idea behind steady-state prediction is to parameterise a dynamic model, which describes the dynamic response behaviour of a specific variable to an input change. This model is then used to predict where the variable would have settled if the input would have been kept constant [30]. The key factor in this method is that only a short but intensive excitation of the system is required to parameterise the model using system identification methods. This process is illustrated in Figure 2.6.

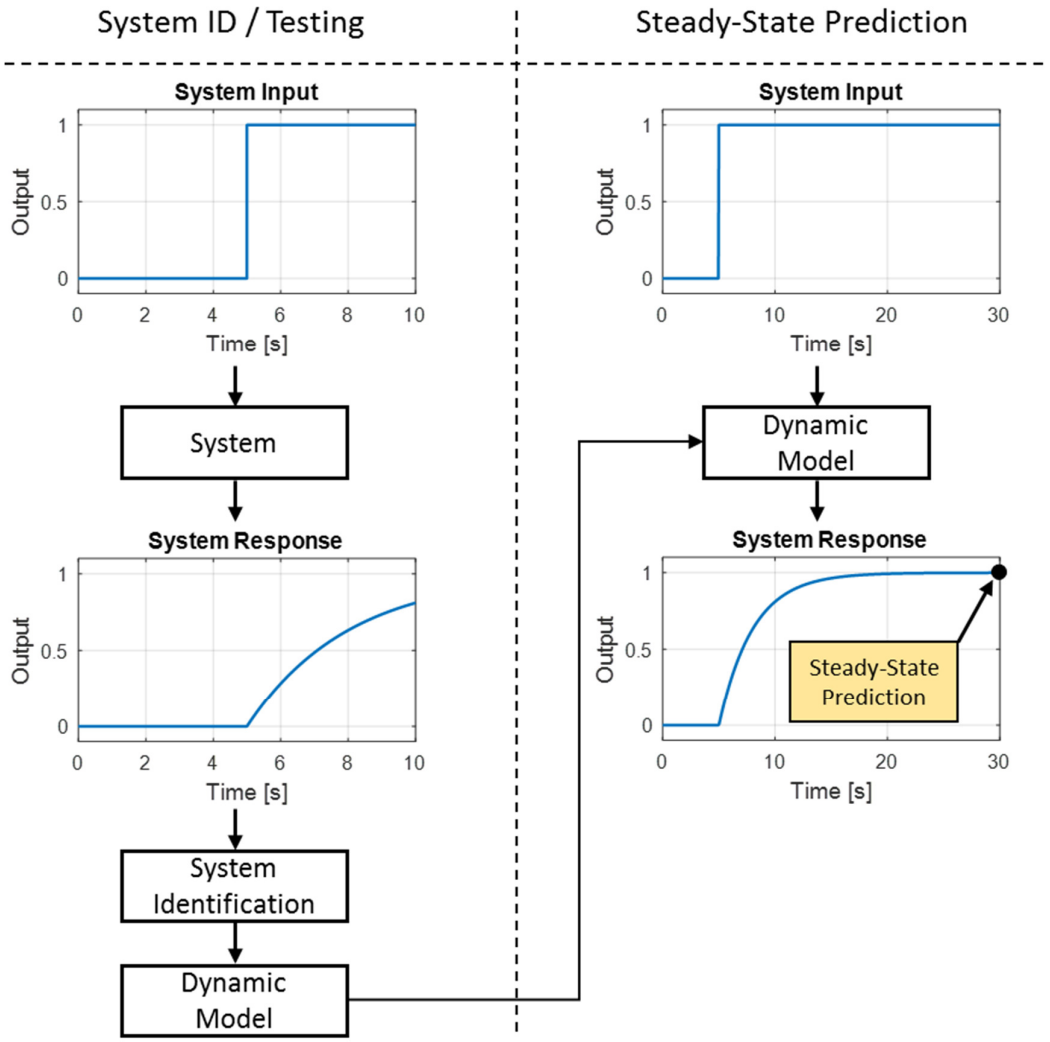

Figure 2.6: Rapid step testing and steady-state prediction

Figure 2.6 clarifies the steady-state prediction process. At first the system is tested using an aggressive input signal which causes a dynamic system excitation. As time goes towards infinity, any stable system asymptotically approaches a new steady-state value. However, as illustrated by Figure 2.6, only a small percentage of the dynamic system response is required to identify a dynamic model of the system. This model can later be used for steady state prediction. Therefore, the identified model is simulated with the same input signal, however, the model can now predict where the response will settle if the input signal were to remain constant for time towards infinity. It is important to note that this methodology is only applicable to asymptotically stable systems. In addition, it is also required that the dynamic model is an accurate representation of the dynamic system response, otherwise the predicted steady-state will defer significantly from the real steady-state value. Consequently, finding the

appropriate model which describes the dynamic behaviour is a key step in this process.

Hafner and Isermann [49], [50] were among the first researches who attempted to predict steady-state engine data from a dynamic model. A local linear model tree (LOLIMOT) was used to model the dynamic response of NO_x and opacity. Both models were trained with AMPRBS signals. The authors specifically mention a trade-off between dynamic and steady-state accuracy of the model. The accuracy of the steady-state prediction can be significantly increased if a certain number of steady-state measurement points are included in the model training data. However, the increase in steady-state accuracy causes a decrease in the accuracy of the dynamic representation and increases the required testing time. According to the authors, overall the model achieved an error smaller than 10% compared to steady-state data. However, for some measurement points, the predicted steady-state data shows an error of up to 50%.

More recently, Sugita *et al* [30] used an Auto-Regressive with eXogenous input (ARX) model to describe the dynamic settling behaviour of exhaust gas temperature. The model is parameterized using an AMPRBS spark input. After that, the engine was tested with step changes in spark advance by only a few degrees every ten seconds. The ARX model was then used to predict where the step changes would have settled. The authors claim that an accuracy of $\pm$0.75% was achieved compared with conventional steady-state test results.

Röpke *et al* [51], [52] used an Extended Parametric Voltera Series (EPV) to predict settled values for exhaust gas temperature, HC and NO_x emissions. The authors do not comment on the exact accuracy for each response but they claim that a disadvantage of 1% in fuel consumption was caused when the predicted data were used for calibration optimisation. However, no details about the test itself are given which makes it difficult to judge the presented results.

Boehme's [36] work is state of the art; he used a local linear model tree (LOLIMOT) model for the rapid identification of an exhaust gas temperature model. The testing process was assisted with an intelligent online DoE to further reduce the required testing time. Only dynamic data were used to train the model and the steady-state values were later predicted as described above. These values were then used to parameterise an exhaust gas temperature model of a modern ECU. According to the author, the accuracy achieved was more than

sufficient to use the methodology in order to replace conventional steady-state testing.

2.2.3 Input Reconstruction

As mentioned above, the response delay of specific sensors and measurement systems complicate accurate measurement of dynamic signals. During steady-state testing, response delays can be neglected, however the higher the excitation of the system dynamics during dynamic testing, the higher is the introduced measurement error [44]. This problem is illustrated in Figure 2.7.

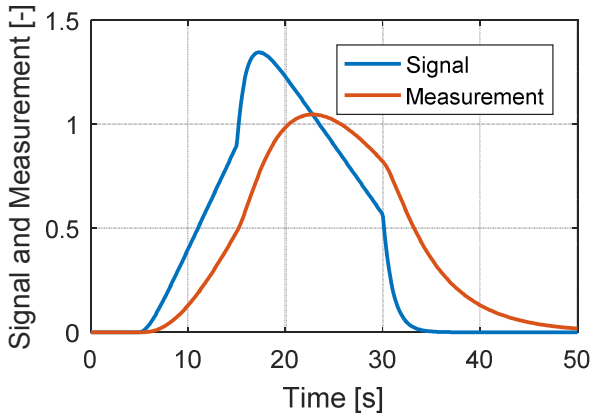

Figure 2.7: Sensor response delay

Figure 2.7 clarifies that significant measurement errors can occur, specifically when the signal to be measured changes very rapidly. However, it is possible to compensate for this response delay by using input reconstruction [44]. This methodology makes use of a dynamic sensor model which describes the measurement response of the sensor to a change in the sensor input.

Temperature measurement where usually shielded thermocouple sensors are used suffer in particular from this problem, since they have a relatively large response time constant compared to other sensors such as pressure transducers. For this reason, compensation for the response delay of a thermocouple is a well-known topic in literature. As shown by Zimmerschied [44], two different methods are available to reconstruct the true gas temperature once an accurate model of the thermocouple is available. The easiest way is to simply invert the dynamic model which requires the approximation of the state derivative (See Subsection 2.5.2). This is recommended for offline applications as shown by Schaal *et al* [53]. For online applications, Zimmerschied recommends the use

of an Augmented Extended Kalman Filter (AEKF) to cope with measurement noise. (The reader is referred to Subsections 2.5.3 and 2.5.4 for more detailed information about this topic).

As mentioned by Schaal *et al* [53], key for an accurate reconstruction of the original signal is a highly accurate sensor model. In fact, the accuracy of the reconstructed signal is directly related to the accuracy of the sensor model. Consequently, the identification or parameterisation of the sensor model has to be done with highest precision. The response behaviour of a thermocouple can be represented by a first order differential equation as shown by Tagawa *et al* [54]. However, as shown by Forney [55], the time constant of the thermocouple does depend heavily on air mass flow due to the significant difference in heat transfer from the gas to the hot junction point of the thermocouple. Therefore, the time constant of the thermocouple has to be identified from experimental test results at different air mass flow rates. Schaal [53] developed a test rig specifically for this task, which allows fast and accurate identification of the time constant. The identification of the time constant requires the measurement of system input and output which is problematic since the input into the sensor, the real gas temperature, is not directly measurable during fast temperature changes. Therefore, a methodology which makes use of two thermocouples, each with a different diameter can be used to overcome this problem. Zimmerschied [44] gives a state of the art procedure for the required system identification.

2.2.4 Potential of Dynamic Testing Methodologies

A direct comparison of the different dynamic testing methodologies and their potential in terms of time saving is difficult, since the existing examples applied the testing methods to different response variables with different time constants. However, summarising the information about ramp times, ramp rates as well as amplitude intervals in [13], [33] and [35] - [50], the potential time saving can be roughly approximated by Table 2.1.

Table 2.1: Potential of dynamic testing methods

Testing Method	Time Saving [%]
Slow Dynamic Slope	30 - 70
Dual Ramp Average	60 - 80
Dynamic Offset Ramp	80 - 95
Dynamic Model Identification	60 - 95

Table 2.1 indicates that the more a testing method allows exciting the dynamics, the higher is the potential for time saving. However, a stronger excitation of the dynamics also increases the necessity as well as the complexity for the compensation of dynamic effects. Compensation for dynamic effects requires dynamic models of the engine. Section 2.3 reviews the different types of dynamic engine models.

2.3 Dynamic Engine Modelling

A model is a representation of reality using mathematical constructs [13]. Physics based models use a combination of physical first principles to approximate reality. Empirical models identify the parameters of mathematical equations using experimental test results [14]. Consequently, models can either be physics based, experimentally based or a combination of the two as shown in Figure 2.8.This allows the classification of models into White-Box Models, Grey-Box Models and Black-Box Models. White-Box models are purely physics based models where all parameters are known. Linear and nonlinear differential equations describe the dynamic system behaviour. Grey-Box models are a combination of physical and experimental models. Linear and nonlinear physics based differential equations describe the dynamic system behaviour but some or all model parameters are unknown and need to be estimated from experimental test results. Black-Box models are purely experimental based. A specific structure of the dynamic model is assumed *a priori* and all model parameters are identified from experimental results. As described by Souflas [56] and illustrated in Figure 2.8, the three model types show a significant difference in complexity, simulation speed, cost and model fidelity. White-Box models have, due to their physics based differential equations, a high complexity and a high fidelity. However, the differential equations often required advanced, iterative solvers which results in a very slow simulation speed compared to the other modelling approaches.

Black-Box models on the other hand, are very cost intensive, since they require a huge amount of test data. However, the low complexity allows a very high simulation speed. Grey-Box model offer a compromise between the two extremes.

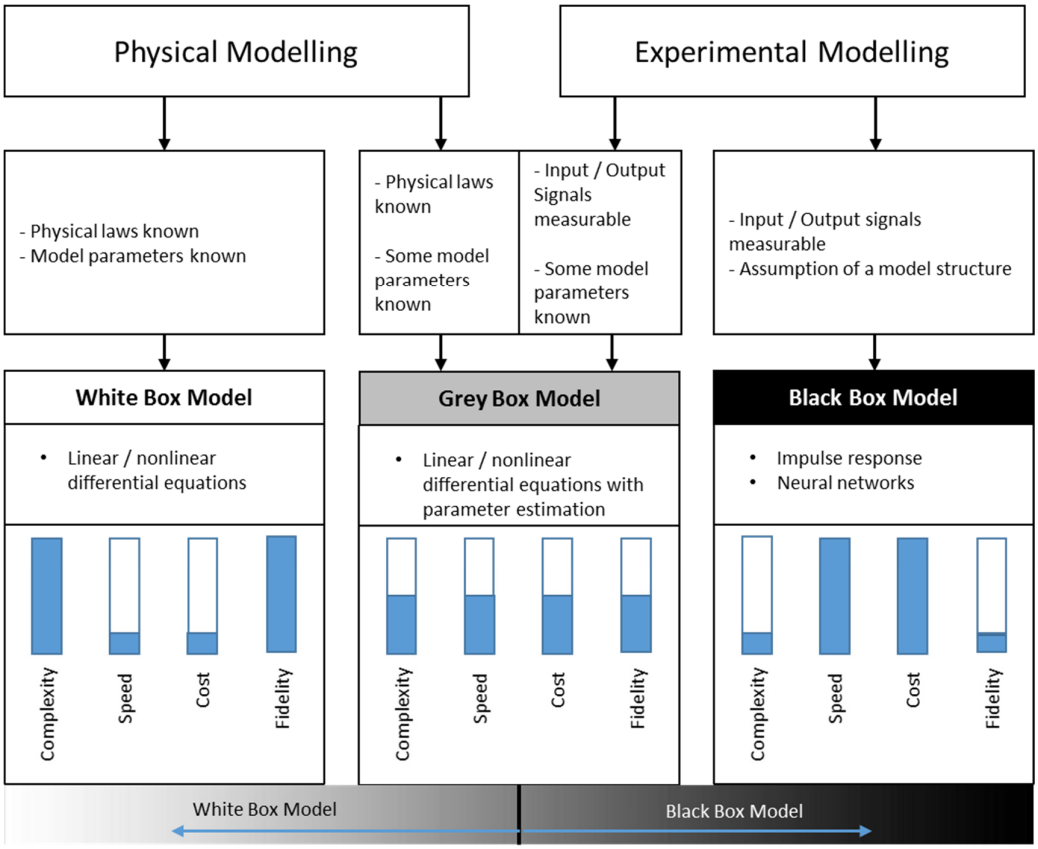

Figure 2.8: Classification of different dynamic engine model types
Adopted from [13] and [56]

In engine modelling it is common practice to divide the overall system model into an air-path and a cylinder model as shown by Wuerzenberger [57]. Air-path modelling means to model the pressures, temperatures and the air mass flows through the intake and exhaust system. Cylinder modelling includes everything that happens inside the cylinder such as torque production and exhaust gas temperature estimation. However, when a real system is described by physical equations, it is necessary to make some assumptions or simplifications of the system, which means that the air-path and the cylinder can be modelled with a different fidelity.

2.3.1 White-Box Models

The term “White-Box” refers to the fact that the entire model structure is visible which means that every equation used to describe a specific element of the system is based on physical principles. As described by Merker *et al* [17], the overall process of the internal combustion engine is very complex. In order to describe the overall process with physical equations, it is first of all necessary to break it down into partial problems which are physically describable and mathematically formulatable. Each problem is then solved by applying first principals from *e.g.* thermodynamics, fluid dynamics, chemical reactions, mechanics and kinematics. The overall process model is finally formed by connecting the individual solutions for each partial problem with each other.

A very logical way of breaking down the overall process was presented by Chow and Wyszynski [58] and Souflas [56]. The entire system can be represented as a combination of five elements, which are cylinder, plenum, pipe, restriction, and turbocharger. These elements can be modelled with different modelling techniques, depending on the desired model fidelity, complexity, simulation speed and cost for parameterisation as shown in Figure 2.9.

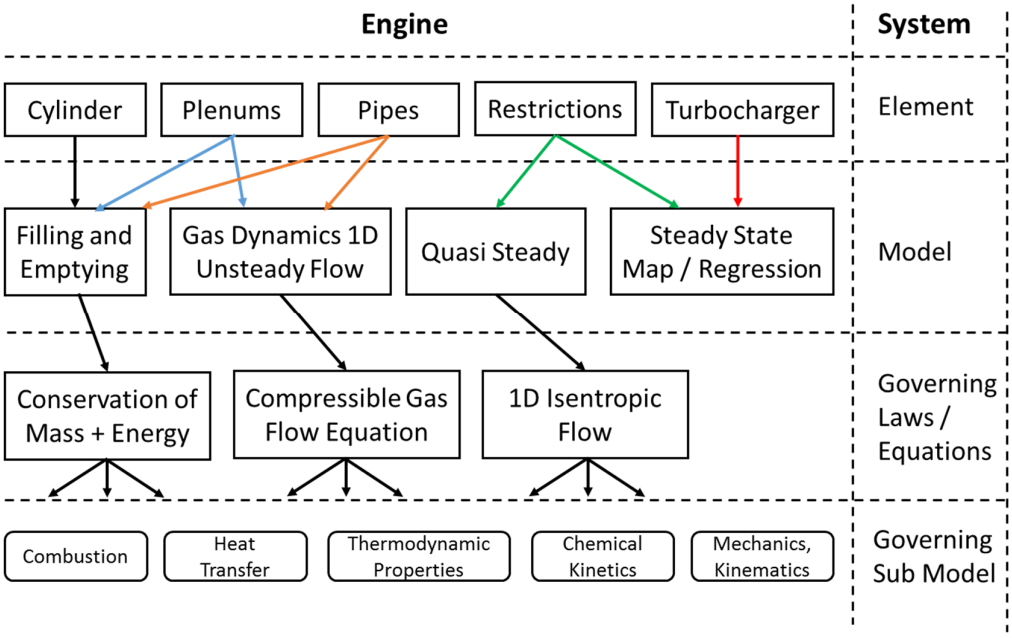

Figure 2.9: Top level structure of engine system models
Adapted from [56]

The choice of which modelling technique to use for a specific element determines the governing equations and sub models which finally lead to the fundamental

equations. In the following explanation, the details of each engine element including the different modelling techniques are reviewed.

- **Cylinder**: The cylinder element is modelled by applying the filling and emptying modelling technique, which can be derived by applying mass and energy balance for an open system to the cylinder. As described by Souflas [56], the complete cylinder model requires sub models for combustion [17], heat transfer [17], [59], [60], thermodynamic properties [59], [61] and kinematics and mechanics [59], [61], [62]. The reader is referred to Souflas [56] and references therein for a more detailed description and examples.
- **Plenum**: The plenum element represents the major volumes along the engine air path. This includes the intercooler, intake, and exhaust manifold as well as the catalyst and the silencers. Usually, plenums are modelled using filling and emptying dynamics, which means that the volumes are assumed to be zero dimensional. Two first order differential equations allow to model the dynamic behaviour of pressure and temperature inside the volumes. The required sub models are thermodynamics and heat transfer. The reader is referred to Isermann [13] and Guzzella and Onder [16] for more detailed information. Schaal *et all* [63] gives a detailed derivation as well as a review of different implementation methods.
- **Pipe**: The pipes which connect the main volumes along the air-path can be modelled in two different ways. The simple approach is to lump the pipes together with the plenums into big volumes [64]. *E.g.* lumping the intake runners together with the intake manifold into one volume. This approach allows to apply the filling and emptying dynamics. However, in order to capture the pressure wave propagation through the intake and exhaust system, the pipes have to be modelled using one dimensional gas dynamic modelling techniques [57]. One dimensional flow is derived from the Navier-Stokes equation restricted to one dimension which combines the conservation of mass, energy, momentum, and species inside the pipes as shown in [17]. The challenge in finding a numerical solution is that the set of equations depends on space and time. Early numerical solutions by the mesh method of characteristics were presented by Benson [65], [66]. Current state of the art is to combine finite volume discretization with shock-capturing techniques where the pipes are divided

into many small sub volumes. Toro [67] gives detailed information about this method.

- **Restriction**: The restriction element represents all valves and orifices along the engine air path such as throttle plate, intake and exhaust valve as well as the waste gate. The mass flow through this restrictions is modelled using quasi steady models which are based on the equation for one dimensional isentropic flow. However, to achieve a highly accurate prediction of the mass flow though the valve it is necessary to include a model for the discharge coefficient which compensates for the fact that the flow is not fully isentropic as shown by Anderson [68] and Hendricks *et al* [64].
- **Turbocharger**: The turbocharger element can either be modelled using a purely physics based approach as shown by Mueller [69] or using experimental maps as shown in Moraal and Kolmanovsky [70]. However, due to the extremely nonlinear and complex system behaviour, purely physics based models struggle to provide the required accuracy [69]. The most advanced solutions combine the turbine maps with one dimensional gas dynamics as shown by Macek [71]. Each turbocharger manufacturers delivers high accurate test results about the performance of the turbocharger. These test results are also known as turbocharger maps and usually include values for mass flow, pressure ratio, efficiency and rotational speed. For the turbine and the compressor model a regression model is fitted to the experimental data. For this reason, the turbocharger model could be regarded as a Black-Box model. However, since the data for each turbocharger are available from the manufacturer, no additional experimental testing is required. Recent studies by Wurzenberger [72] show that the maps need to be slightly edited if the pipes are modelled using filling and emptying dynamics instead of gas dynamics. Since this modelling technique does not predict the pressure wave propagation, the efficiency maps of the compressor and the turbine need to be modified slightly to compensate for the loss in information. A common problem is that the turbine and compressor maps do not cover the entire operating range of the turbocharger. Therefore, extrapolation methods are needed to ensure correct trend wise extrapolation as presented by Galindo *et al* [73], Bellis *et al* [74] and Martin *et al* [75].

Crank angle resolved simulation of the intake and exhaust events in the cylinder combined with the 1D pressure wave propagation in the intake and exhaust system allow a highly accurate physics based modelling of the air mass flow along the air-path [57]. This results in highly accurate cylinder air charge predictions. The crank angle resolved combustion models combined with the highly accurate air charge prediction allows accurate estimation of trend wise engine torque and exhaust gas temperature without the need of any engine test results. The disadvantage is that even the latest numerical solution methods are too time consuming to run in real time [14]. Only significant simplifications of the wave propagation models allow the models to be run in real time but with a loss in accuracy. 1D crank angle resolved engine models are usually used during a very early stage of engine development where no test results from a prototype engine are available. A common example is the design optimisation of the intake and exhaust system. To test the effect of intake runner lengths and diameters, valve sizes, camshaft profiles and many more geometrical aspects on the test bed is extremely time consuming. Models which simulate the air mass flow through the engine help the designers to find the optimum solution within the given design limits or tell the designers how to tune the components to achieve specific performance requirements. Specially to optimize full load performance engine simulation models are indispensable and routinely used by the industry. Hamilton *et al* [76], Piscaglia *et al* [77] and Yarsam *et al* [78] give some good examples.

In case the pipes are modelled with filling and emptying dynamics instead of 1D gas dynamics, the accuracy of air charge prediction is significantly reduced [57]. On the other hand, 0D model allow a significant increase in simulation speed compared to 1D models which enables the model to run in real time since no time consuming iterative numerical solutions are necessarily required. This significantly expands the application range of the model. Innovative solutions for real time running models were published by Wurzenberger *et al* [72], [79]. See Alix *et al* [80] and Chalet *et al* [81] for detailed information and a comparison with the 1D approach. 0D crank angle resolved models are mainly used during the early stages of engine development and/or for controls development. A common application is HIL (hardware in the loop) testing. One of the key parts in the engine development process is the control strategy development for transient engine control. A real ECU is connected in a loop with a real time running engine model.

The dynamic response of the model to changes in actuator settings allow tuning and testing of the control strategy. An example of this is shown by Pacitti *et al* [82], Corti *et al* [83], Wu *et al* [84] and Chen *et al* [85].

2.3.2 Black-Box Models

The term “Black-Box” indicates that the physical system behaviour is not directly visible from the mathematical equation which is used to represent the system process [13]. The models do not include any physical laws and a model of the process is obtained purely from measurements. As shown by Isermann [13], this model type is also known as system identification and the result of the identification process is an experimental model. Black-Box models can be divided into stationary and dynamic models.

- **Stationary models**: The simplest stationary experimental models are non-parametric models such as grid-based look-up tables. However, the data points increase exponentially with the number of systems inputs [13]. Consequently, map based models are only practical for systems with one or two inputs. A more advanced solution are parametric models like polynomials and splines, neural networks, and fuzzy models. The model parameters are identified from experimental data using parameter estimation techniques such as linear and nonlinear least squares and maximum likelihood method as described by Keesman [86] and Ljung [87].
- **Dynamic Models**: Experimental models for nonlinear dynamic systems can be separated into models with a special structure such as Hammerstein models, Wiener models, Volterra series and models with a general structure such as local linear models and multilayer perceptrons. The reader is referred to Isermann [13] for a detailed description of these models. The model parameters of the dynamic models are identified from experimental data with the parameter identification methods listed above.

Souflas [56] and Cary [88] summarised the development process of a black-box models by three consecutive steps:

1. **Design of Experiments & Data Collection**: The first step is the definition of the model inputs/outputs and the operating range of the engine that the model will have to be identified and validated. Once the inputs and outputs as well as the operating range is known, Design of Experiment (DoE)

methods can be applied to define the experimental engine operating test points. The purpose of DoE is to minimise the required number test points and maximise the information content of each test point. In other words, DoE allows an efficient estimation of the experimental model. Three popular DoE methods are used in engine testing which are classical / full factorial, space filling and optimal as described in Cary [88] and Roepke and von Essen [89].

2. **Data Modelling**: Once the experimental data are available, a suitable mathematical model is fitted to the data to explain the relation between the inputs and the outputs.
3. **Validation & Verification**: The final step of the model development process is the validation of the model. Several statistical measures such as root mean square error (RMSE) are used to determine the prediction accuracy of the model. It is important for the validation to use a set of experimental test points, which were not included in the data, used to fit the model. If the accuracy is not sufficient, the modelling process is repeated until the model achieves the desired results. Eventually additional experimental test data must be collected.

2.3.3 Grey-Box Models

Grey-Box models are the combination of White-Box and Black-Box models. In literature [13], they are also known as semi-physical models since they combine physics based models with experimental models. The combination of both modelling techniques allows a compromise between complexity, fidelity, cost, and simulation speed [57]. Highly complex subsystems, which require complicated and time intensive solvers can be replaced with experimental models [57]. On the other hand, making use of simple physics based equations to describe the general dynamic system behaviour means keeping the cost for parameterisation at an acceptable limit. The replacement of complex subsystems with experimental models also allows to increase the model accuracy of engine responses which are very difficult to model solely with physical equations such as exhaust gas emissions [14].

2.4 Mean Value Engine Modelling

The most popular way to model the dynamic behaviour of an engine is the Mean Value Engine Model (MVEM) approach. According to Hendricks *et al* [64], all engine variables are described as the mean over one engine cycle instead of on a crank angle basis. For this reason a MVEM is also called a cycle average model. The model is therefore only able to capture phenomena with a duration longer than one engine cycle (720 degree crank angle). Traditionally, mean value engine models can be classified as Grey-Box models since usually the entire cylinder is represented with experimental models. Although some examples do exist that allow a physical representation of the cycle average cylinder variables as shown by Kocher *et al* [90] in which case the model could also be seen as a White-Box type. However, pipes and plenums along the air path are lumped together into two to six main volumes, which are modelled using filling and emptying dynamics. Each volume is treated as a storage for mass and energy, which are defined by the levels of pressure and temperature inside the control volume. The volumes are considered to be zero-dimensional which means that it is assumed that all properties are homogenous over the entire volume. Restrictions are modelled using quasi steady 1D isentropic flow and the turbocharger is represented with a look-up table or a regression model. Isermann [13], Chevalier *et al* [91], Lee *et al* [92], and Müller [93], Hadef *et al* [94] and Anderson [68] give examples for state of the art models.

The experimental cylinder model is what really separates the mean value engine model from the 0D and 1D crank angle resolved White-Box models [57]. The air mass flow into the cylinder is modelled using a combination of simple physics corrected by an experimental model. The speed-density approach allows to estimate the cycle average air mass flow into the cylinder using the product of air density inside the intake manifold times volumetric flow rate of the engine which is estimated from engine speed and swept volume [95]. However, this simple equation does not include all aspects that influence the engine breathing performance. Therefore, the speed density equation is multiplied by the experimental volumetric efficiency model. A mathematical regression model based on test results is used to describe how pressure wave propagation, variable valve timing, engine speed, pressures in the intake and exhaust manifold and many more factors affect the aspiration of the cylinder [59]. An accurate

model over the entire engine operating range allows extremely accurate air charge predictions [96]. Engine torque and exhaust gas temperature are usually mathematical regression models based on experimental test results. The main disadvantage of this model type is that the complexity of the regression models grows exponentially with the engine complexity. Therefore, engines with high technology such as variable valve timing require a huge amount of test data in order to achieve accurate predictions of the response variables. Schulze *et al* [97] do a comparison of 0D crank angle resolved models and MVEMs.

2.4.1 Mean Value Engine Model Applications

The main application field of mean value engine models is the air-path control of modern engines during transient operation. MVEMs are often used as an observer for cylinder air charge estimation during transient engine operation [43], [98]. This area is specifically addressed in Section 2.5. Another application is to use a MVEM as open-loop prediction of intake manifold pressure and temperature and air mass flow during fast throttle transients as shown by Aquino [99], Hendricks [95], Chevalier *et al* [100]. This allows to avoid the response delay of pressure and temperature and MAF sensors during very fast transients. In addition, the predictor can be used to predict the air mass flow ahead of time for engines with electronically controlled throttle. This offers the advantage that the amount of fuel that has to be injected can be calculated in advance which was of particular importance for port fuel injected engines as demonstrated by Chevalier *et al* [100]. MVEMs can also be used in form of a Kalman Filter as shown by Chevalier *et al* [100] and Hendricks and Vesterholm [96], Jenson [101] and Chen *et al* [102] to filter the measurement signals such as intake manifold pressure and temperature. MVEMs are also crucial for advanced control strategies of complex air-path systems. Wang *et al* [103] uses a MVEM for dynamic feedback stabilisation control of a diesel air-path system. Jung *et al* [104] and Beckmann *et al* [20] establish a dynamic feedforward control by inverting the MVEM. Drews *et al* [105] uses a MVEM as an observer within a model predictive control strategy. Apart from control applications, MVEMs are also suitable for the use in HIL testing. Examples are given by Schuette and Ploeger [106], Papadimitiou *et al* [107] and Gambarotta [108].

2.4.2 Critical Analysis of Mean Value Engine Models

The validity of mean value models is critically evaluated by Hendricks and Vesterholm [96] with particular attention paid to the nonlinear behaviour of an internal combustion engine and the resulting challenges for control strategies. In addition, the model is compared with a wide range of test results proving the validity of MVEMs during steady-state and transient engine operation.

The literature [91], [109] discusses whether mean value engine models are fully valid during transient engine operation or not. This question arises as consequence of the fact that all of the empirical models of a MVEM are based on steady-state measurements. Three dynamic phenomena are discussed by Chevalier *et al* [91] which are not able to be modelled by a simple mean value engine model approach:

- **Inertial effects**: Pumping fluctuations continuously accelerate and decelerate the air mass inside the induction system. Therefore, during the acceleration, the gas inside the intake system has to acquire kinetic energy which is then later released during the deceleration of the gas [91]. This energy balance could affect the cylinder air charge at the end of the induction stroke depending on valve timing and engine operation point. During steady-state engine operation, this phenomenon is called inertial ramming. Steady-state volumetric efficiency maps account for this phenomenon. However, a tip-in theoretically should decrease induction ramming due to the momentum gained by the gas [91].
- **Wave effects**: Disturbances in the system initiated by the boundaries (*e.g.* intake valve closing) travel back and forwards through the induction system at the speed of sound and are reflected at open and closed pipes [91]. This phenomenon can be used to improve the engine breathing performance and is called the wave effect. It is assumed in literature that the waves build up after a few cycles of steady-state engine operation [91]. The volumetric efficiency maps of the mean value models account for that phenomenon but during transients, the waves do not have time to establish themselves, which in theory cause an error in the volumetric efficiency map [91].
- **Friction effects**: Mean value models only account for flow resistance which separate the main volumes of the air-path [91]. Flow resistance in

the pipes and especially in the junctions between plenum and runners are neglected in mean value engine models. During transient operation, these flow resistances could have an additional impact on the filling and emptying of the manifold state equations and therefore lead to errors in the predicted cylinder air mass flow [91].

Chevalier *et al* [91] use a carefully developed 1D crank angle resolved model in order to investigate these phenomena in detail. The results are then compared with a mean value model. The authors conclude that the impact of inertia and wave effects on the accuracy of steady-state based volumetric efficiency is extremely small and can be neglected at least for control applications. The phenomena mentioned above were also discussed by Smith [109] for engine speed transients under wide open throttle. A similar approach to Chevalier *et al* [91] was used (1-D model to investigate the phenomena). The author concludes that transient engine volumetric efficiency responds almost quasi-steadily for real-world rate changes in engine speed. Investigations were pushed to the limit with a simulation (1000 to 5000 rpm in 1 degree crank angle). The results show that even during such unreal changes in engine speed the actual volumetric efficiency does vary only a little from steady-state volumetric efficiency. The validity of mean value engine models during transient engine operation has been proven by Chevalier *et al* [91], Hendricks and Vesterholm [96] and Smith [109] for real-world rate of changes.

2.5 Air Charge Observers

The problem of transient cylinder air charge estimation is well known in literature for more than 35 years. Aquino [99] was one of the first researches who addressed this topic. Due to the size and the operational principle of the MAF sensor, it is not possible to directly measure air mass flow into the cylinder [110]. Consequently, the MAF sensor is either placed upstream from the throttle in naturally aspirated engines or upstream from the compressor in turbocharged engines. However, in both cases there is at least one volume with a considerable size between the MAF sensor and the cylinder. From a cycle-average point of view, pressure and temperature inside the volume are constant during steady-state engine operation. Under consideration of mass and energy balance, it follows that the cycle average inflow and outflow of the volume are identical. Consequently, during steady-state engine operation, the air mass flow measured

by the MAF sensor and actual air mass flow into the cylinder are identical [43]. However, during transient engine operation where the pressure and temperature inside the volume change, measured and actual air mass flow into the cylinder differ from each other due to the change in pressure and temperature inside the system [91]. This dynamic effect is associated with the filling and emptying of a volume and can be modelled with two first order differential equations [91]. Based on these simple equations, an observer can be established which allows estimation of the outflow of the volume, if the inflow as well as the pressure and temperature inside the volume are measurable [43]. The observer compensates for the filling and emptying dynamics of the volume and therefore allows observation of the actual air mass flow into the cylinder during transient engine operation [110].

Different authors arrive at different solutions for this problem. The existing literature can be divided into two main approaches, which are 'Unknown Input Estimation' and 'Joint State and Parameter Estimation'. Subsections 2.5.2 and 2.5.3 treat the solutions respectively. A fundamental question for both methods is how accurate the observer model needs to be which describes the filling and emptying dynamics of the volume. This is addressed in the following subsection.

2.5.1 Observer Model

As shown by Schaal *et al* [63], the derivation of the filling and emptying dynamics leads to two first order differential equations which describe the dynamic behaviour of pressure and temperature inside the volume. However, almost since the beginning of mean value engine modelling authors have been arguing whether it is possible to assume that the system is either fully isothermal or fully adiabatic. The reason for this discussion is that both assumptions allow a significant simplification of the original equation set. Assuming adiabatic conditions allows the neglect of the heat transfer which is always difficult to model accurately. Assuming isothermal conditions allows the reduction of the model down to only one equation. Guzzella and Onder [16] suggest the use of an isothermal model for small surface-to-volume ratios and the adiabatic model for large surface-to-volume ratios. Most available solution for transient air charge observers make use of the isothermal assumption. However, Schaal *et al* [63],[53], Mueller *et al* [69] as well as Chevalier *et al* [100] show that during fast throttle transients the temperature inside the volume is not constant and

consequently the isothermal assumption is not valid. Chevalier [91], Deur [111], [112] investigate the heat transfer in the intake manifold during fast throttle transients and conclude that the system is not adiabatic. Consequently, especially heavy transients are neither fully isothermal nor fully adiabatic. Stefanopoulou [43] has proposed an innovative solution to this problem. Directly observing the mass inside the volumes allows the observer to be based on a mass balance, which does not include any significant thermodynamic assumptions. However, since it is not possible to measure the mass directly, it is necessary to estimate the mass using the ideal gas law from measured pressure and temperature. Schaal *et al* [113] show a successful implementation of a mass based observer in combination with an ultra-fast temperature sensor and input reconstruction.

2.5.2 Unknown Input Estimation

Stotsky and Kolmanovsky [98] describes the frequent problem in automotive control applications where the input to a system has to be estimated from the system state measurement. In dynamic systems, the input and the system state are related by a first order differential equation. Therefore, it is not possible to estimate the input directly from the measured state. The solution to this problem requires the estimation or approximation of the state derivative. Once the derivative of the state is known, the unknown input can be estimated using the system state equation. However, it should be noted that this only allows the estimation of one unknown input. For offline applications, simple numerical differentiation can be used in combination with a zero-distortion filter. Online differentiation is always a trade-off between phase shift and noise amplification. Kolmanovsky presents three different methods for the online approximation of the state derivative. The simplest method is the derivative filter which can be derived by applying a stable first order low pas filter to a state derivative as shown in Kolmanovsky [98] and Young [114]. More advanced is the use of a high gain observer as described by Dabroom [115] and Vasiljevic *et al* [116]. A high gain observer is a simple Luenberger state observer as shown in [117], [118], with a very high gain on the difference between measured and observed state. An alternative to the high gain observer is the use of a sliding mode observer as shown by Fridman *et al* [119].

As described in Subsection 2.5.1, modelling the air-path volumes with an isothermal model allows representation of the filling and emptying dynamics with one simple differential equation for the pressure inside the volume. The inflow into the volume is measured by the MAF sensor and the state derivative is approximated with one of the solution listed above. Based on the inflow and the derivative of the pressure inside the volume it is possible to estimate the outflow using the state equation for pressure. As described in [98], the outflow can be estimated without any model of the outflow. However, the accuracy can be significantly increased if a model is available which approximates the volume outflow [98]. In this case the unknown input becomes the difference between the real and the approximated outflow. This allows a significant increase in accuracy especially during fast transients since the unknown input to be estimated by the unknown input estimator becomes much smaller. For the application to the intake manifold, the outflow can be approximated with the speed-density equation as described in Section 2.4. In case no volumetric efficiency model is available, the method also works if the volumetric efficiency is assumed to be one. Successful examples can be found in Stotsky and Kolmanovsky [98], [120], [121] and Liu and He [122]. A solution which includes EGR is given in [123]. Buckland *et al* [124] present an application where the observer is applied to two volumes on a turbocharge SI engine. The focus of the paper is to estimate the compressor air mass flow in case no MAF sensor is available. The air mass flow into the cylinder is estimated based on speed-density in combination with an accurate volumetric efficiency model. The observer compensates for the filling and emptying of the intake manifold and the intercooler to estimate the compressor air mass flow.

2.5.3 Joint State and Parameter Estimation

An alternative method to the unknown input estimation technique for transient engine air charge estimation is the joint state and parameter estimation technique [125]. This method combines a state observer with an adaptive parameter estimation method. A state observer is used to observe a measurable system state, *e.g.* the intake manifold pressure. The model used in the observer should include a model, which can approximate the outflow such as the speed-density equation for the intake manifold [126]. The outflow model must include an adaptive parameter, which is continuously identified online. In the speed-density equation, the volumetric efficiency is selected as the adaptive parameter. A

simple integration over the error between observed and measured state is then used to identify the adaptive parameter with the aim to drive the difference between measured and observed state to zero. Reale [127] provides a comparison of suitable observers for joint state and parameter estimation.

Storset *et al* [128] was one of the first authors who applied the joint state and parameter estimation technique to transient air charge estimation. A simple volumetric efficiency model is used which describes the breathing efficiency depending on engine speed and intake manifold pressure. The model is multiplied by an adaptive parameter which corrects the mapped volumetric efficiency for all unaccounted effects such as variable valve timing and exhaust manifold pressure. A simple Luenberger observer is used for the state observer and the gain of the adaptive law is adjusted depending on engine speed. The idea of Storset *et al* [128] was also used by Andersson [126]. Instead of multiplying the volumetric efficiency with a correction parameter, the author divided the volumetric efficiency into a known and an unknown part. The adaptive law is used to identify the unknown part. Stefanopoulou [43] presents an attempt to estimate cylinder air charge without a MAF sensor. However the presented results show a significant decrease in accuracy compared to [128]. Storset *et al* [129] investigate the impact of sensor inaccuracies of intercooler outlet pressure, intake manifold pressure and temperature on the accuracy of the estimated air charge during transient operation. Solutions which also include EGR can be found in Guillaume [130], Lee [131] and Zhao [132]. A solution with a sliding mode observer is presented by Monir *et al* [133].

Wang *et al* [125] provides a review of available transient engine air charge estimation methods including an experimental validation. The paper presents results for both methods, unknown input estimation and joint state and parameter estimation. Unfortunately, the author uses a different data set for each method. Consequently, it is not clear if any of the two methods offers a significant advantage in terms of accuracy. However, the author concludes that the joint state and parameter estimation method is less sensitive to measurement noise since better methods exist for observer tuning such as the extended Kalman filter. This issue is treated in the next subsection.

2.5.4 Observer Tuning / Augmented Extended Kalman Filter

As mentioned by Wang [125] and other authors [129], [122], [98] cyclic variations in air mass flow, pressure and temperature as well as measurement noise limit the tuning of the observer and consequently the convergence rate of the adaptive air charge estimation. According to Wang [125], specially the unknown input estimation method suffers from this problem due to the required state derivative approximation. In order to estimate an accurate state derivative during rapid transients, high gains are required on the observer error feedback term. On the other hand, the higher the gain the higher the amplification of measurement noise which can lead to massive errors in the approximated derivative [125]. Applying a filter on the state before estimating the derivative allows to reduce the noise however the lower the cut-off frequency of the filter, the higher the introduced phase shift, which does also lead to large errors in the approximated derivative [98]. The joint state and parameter estimation method suffers from the same problem. A fast adaption of the adaptive parameter during fast transients requires a high gain in the adaptive law. However, high gains cause the adaptive parameter to respond to measurement noise. Consequently, whether the unknown input observer or the joint state and parameter estimation method is used, tuning the observer is always a trade-off between fast convergence or noise amplification.

An intelligent solution for a trade-off can be found by solving the problem of joint state and parameter estimation using an augmented extended Kalman filter (AEKF). The AEKF is an extension to the Kalman filter [134] which is only applicable to linear systems. As demonstrated by Faragher [135], the Kalman filter allows the combination of information of prior knowledge of the system state, predictions from systems models and noisy measurements. The prediction accuracy of the model and the measurement noise are represented by Gaussian probability distribution functions (PDF), each with a specific variance [135]. The information about prediction accuracy and measurement noise can be fused by multiplying the two Gaussian PDFs. Based on this information, the Kalman gain can be estimated. This provides an optimal solution for the observer tuning, assuming that measurement noise and the model accuracy have a Gaussian distribution and that the variance of each PDF is known. The extended Kalman filter EKF as shown in [136] is an extension of the Kalman filter to nonlinear

systems. The EKF can be used for state estimation [136] as well as for parameter identification [56]. The AEKF is an augmentation of the EKF which allows joint state and parameter estimation, Hofland *et al* [137], Hassanzadeh [138] and Wenzel [139]. The measurement noise covariance can be estimated from the measurement data. The process noise covariance is then used to tune the convergence rate of the observer as shown by Zimmerscheid [44]. However, it is important to note that the AEKF does not achieve higher accuracy then using a Luenberger observer in combination with an error integral based parameter adaption law. The advantage is that the AEKF provides an optimal statistical trade-off between measurement noise and model accuracy. The resulting gain is based on an optimal statistical solution rather than a trial and error method, which significantly reduces the time effort for tuning. A second advantage is that the AEKF can handle the nonlinearity of the system. The gains automatically adjust to changes in system sensitivity. This avoids extensive tuning effort over the entire system operating range. Applications for air charge estimation can be found in Schaal [113], Andersson [140], Pavcovic [141] and Hoeckerdal [142].

2.6 Research Gap

Dynamic testing methodologies are without any question the future in engine testing for ECU mapping and calibration. The potential to reduce engine testing time by a factor of five or more gives the opportunity to significantly increase the efficiency of the entire mapping and calibration process. During the past ten years, quasi steady-state testing has been used by some automotive manufacturers to replace the extremely inefficient steady-state testing procedure [40]. The next step to further improve the efficiency of the engine testing process is to move to dynamic testing methodologies, which were introduced in Subsection 2.1.3. Dynamic testing methodologies have been applied for the characterisation of engine torque [37],[46], exhaust gas temperature [36],[45],[48],[30], emissions [45], [51], [49] and the turbochargers [143]. However, apart from Ward [45] no attempt has been made to use dynamic testing for the characterisation of the engine air-path model. Several authors have used the SDS method [39],[36],[42],[41]. Boehme [36] clarified that the slope of the ramp is limited to avoid any noticeable excitation of the filling and emptying dynamics of the intake system. No attempts were made to use a dynamic model to compensate for the excited dynamics. Ward [45] used faster ramps than

Boehme which cause a dynamic offset during the ramp. To compensate for the offset, Ward applied the duel ramp averaging method, which allows a significant increase in the slope of the ramp. However, the presented results show that the dual ramp averaging method cannot compensate for very fast ramps and suffers from the problem that the dynamics need to be excited identically during the up-ramp and the down-ramp. Apart from that, Ward [45] and Boehme [36] used a naturally aspirated engine for their research. Due to the small intake system, filling and emptying dynamics do not introduce a massive difference between measured and actual air mass flow into the cylinder. However, on turbocharge engines, the problem becomes much more complicated since turbocharged engines have a large intake system. Based on the available literature in the fields of dynamic engine testing, dynamic engine modelling and air charge observers, the research gap can be defined as follows:

The main factor which limits the time saving for engine air charge characterisation is the excitation of the filling and emptying dynamics in the intake system. Air charge observers which were reviewed in Section 2.5 allow the compensation of filling and emptying dynamics along the engine air-path. However, until today air charge observers have only been used on engine control applications and apart from Buckland *et al* [124] only for the compensation of one volume. An air-path observer, which compensates for the filling and emptying dynamics in all major volumes along the air-path of a turbocharged SI engine, could be used for rapid characterisation of the ECU air charge model. This has the potential to significantly reduce the testing time compared to any available methods since it would allow strong excitation of the filling and emptying dynamics. The required research for an observer based engine air charge characterisation methodology can be summarised by the following points:

- **Dynamic engine modelling**: Review available dynamic engine model types to find the most suitable model to for the observer
- **System observation**: Review and compare available observer principles to find the most suitable version for the implementation of an air-path observer
- **Modelling of filling and emptying dynamics**: Detailed analysis of the fundamental modelling principles of filling and emptying dynamics to

develop an observer which does not require thermodynamic assumption which could potentially affect the accuracy of the observed volume outflow

- **Observer accuracy**: Investigate the accuracy of the observer in observing the volume outflow. The observer can only compensate for filling and emptying dynamics in the volumes. An investigation is required to determine the impact of neglecting the gas dynamics on the observed volume outflow
- **Limit excitation of unaccounted dynamic effects**: If gas dynamic effects have a noticeable impact on the observation accuracy a suitable test procedure has to be developed which allows to limit the error to a specific value
- **Steady-state versus transient volumetric efficiency**: Investigate if transient volumetric efficiency is identical to volumetric efficiency at steady-state. If there is a noticeable difference, the intensity of the dynamic excitation during the test has to be limited to an acceptable error

2.7 Summary

Modern engine control strategies control the engine actuators using an invertible engine model. In order to achieve a desired air charge, an air-path model is inverted, which determines the settings for throttle angle, waste gate duty cycle and cam shaft timing. The parameterisation of such an engine model requires a massive amount of test data since it has to cover the entire engine operating range. Conventional steady-state testing is wasting approximately 90% of the testing time while waiting for the engine to settle. Dynamic engine testing has the potential to significantly reduce testing time; however, the excitation of engine dynamics leads to significant problems, which need to be solved. Some variables are not directly measurable due to the location of the sensor, others cannot be measured accurately due to sensor response delays and variables with long settling times require a steady-state prediction in order to be useful for engine mapping. Dynamic engine models can represent the dynamic behaviour of the engine with a high accuracy and can therefore form the platform to develop a methodology, which allows the compensation of all excited dynamics. Air charge observers make use of a mean value air-path model and allow the compensation of filling and emptying of the volumes along the air-path. Input reconstruction

allows compensation for any sensor response delays, however, the accuracy of the reconstructed signal relies on the accuracy of the identified sensor model.

Chapter 3 Dynamic Engine Air-Path Modelling

This chapter focuses on dynamic engine air-path modelling. The presented equations are used in Chapter 5 to develop the air-path observer. One section is dedicated to each fundamental element of an engine air-path model. Section 3.1 is focused on restrictions. Section 3.2 covers the turbocharger. Section 3.3 is focused on volumes and Section 3.4 presents the equations for the cylinder model.

3.1 Restrictions

Restrictions comprise all valves and orifices along the engine air-path [16]. Regardless, the mass flow through the device is modelled using quasi-steady state data. The primary inputs into such models are the pressure difference or pressure ratio, an input temperature and an orifice effective area. The exact nature of the static function describing the airflow across the restrictive element depends on the flow regime, which may be compressible or incompressible.

3.1.1 Compressible Flow

White [144] provides a practical test for when the effects of compressibility can be ignored. White provides a compelling argument for assuming that the flow can be considered to be compressible if the Mach number is less than or equal to 0.3. Using standard isentropic flow relations, this suggests:

$$\frac{p}{p_o} \leq \left[1+\frac{1}{2}(\gamma-1)M^2\right]^{\frac{\gamma}{1-\gamma}} \leq \left[1+\frac{1}{2}(\gamma-1)0.3^2\right]^{\frac{\gamma}{1-\gamma}} \leq 0.939 \qquad \textbf{3.1}$$

Alternatively, we can express the compressibility threshold, as the pressure drop across the device must be less than 6%. Practically speaking, this threshold is exceedingly limiting and consequently compressible flow principles must be used to model many air intake system components. For example, flow models for the throttle plate, intake valve, exhaust valve and waste gate are approached in this manner. These restrictions usually have a variable open area, which is approximated by a Laval nozzle with a variable throat diameter. The throat area is the projected cross sectional open area of the restriction. For example, Figure 3.1 illustrates the equivalent nozzle throat area for the throttle plate.

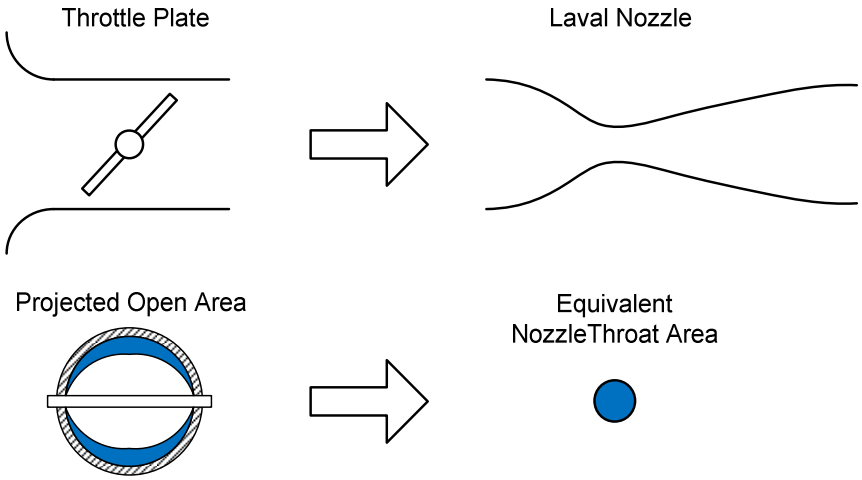

Figure 3.1: Throttle plate geometry

For small throttle openings, the velocity of the air across the restriction can reach the speed of sound [59]. This happens when the critical pressure ratio is reached.

$$P_{crit} = \left(\frac{2}{\gamma+1}\right)^{\frac{\gamma+1}{2(\gamma-1)}} \approx 0.528 \quad \text{for } \gamma = 1.4 \tag{3.2}$$

where γ is the ratio of specific heats. Therefore, it is necessary to distinguish between the subsonic and a sonic flow case. For the subsonic case, where $\left(\frac{P_{t,out}}{P_{t,in}}\right) > \left(\frac{2}{\gamma+1}\right)^{\frac{\gamma+1}{2(\gamma-1)}}$, the air mass flow is given by Equation 3.3 [59].

$$\dot{m} = \frac{C_d A_{th} P_{t,in}}{\sqrt{R T_{t,in}}} \left(\frac{P_{t,out}}{P_{t,in}}\right)^{\frac{1}{\gamma}} \left\{\frac{2\gamma}{\gamma-1}\left[1 - \left(\frac{P_{t,out}}{P_{t,in}}\right)^{\frac{(\gamma-1)}{\gamma}}\right]\right\}^{\frac{1}{2}} \tag{3.3}$$

where C_d is the throttle discharge coefficient and A_{th} is the physical throttle open area. For the sonic case with $\left(\frac{P_{t,out}}{P_{t,in}}\right) \leq \left(\frac{2}{\gamma+1}\right)^{\frac{\gamma+1}{2(\gamma-1)}}$, the velocity of the gas at the minimum throat reaches the speed of sound and cannot be further increased. Therefore, the mass flow becomes independent on the pressure ratio across the restriction and only depends on the upstream conditions and the throat area. Equation 3.4 gives the sonic air mass flow [59].

$$\dot{m} = \frac{C_d A_{th} P_{t,in}}{\sqrt{R T_{t,in}}} \sqrt{\gamma} \left(\frac{2}{\gamma+1}\right)^{\frac{\gamma+1}{2(\gamma-1)}} \tag{3.4}$$

The throat area A_t has to be described by a model which describes how the projected open area depends on the actual actuator position. Models for the

projected open area of throttle plate as well as intake and exhaust valves are provided in [17], [59] and [62].

Equations 3.3 and 3.4 are valid for frictionless, adiabatic flow through a smoothly convergent – divergent nozzle. However, this does not exactly correspond with reality. To compensate for this assumption, the throttle open area A_{th} is multiplied by a discharge coefficient C_d. Carlson [145] and Pursifull [146] provide a detailed analysis of discharge coefficient and model structures. The models are usually implemented in the form of a black box model, based on experimental or 3D CFD simulation data. A more detailed derivation for the compressible flow equation can be found in Appendix B.

3.1.2 Incompressible Flow

In some restrictions, such as in the air filter, the velocity of the gas is much smaller than the speed of sound. Such restrictions can be modelled using the incompressible flow equation as given by Equation 3.5 [59].

$$\dot{m} = C_d A_{th} \sqrt{\frac{2P_{t,in}\left(P_{t,in} - P_{t,out}\right)}{RT_{t,in}}} \qquad \textbf{3.5}$$

Detailed information about the derivation of Equation 3.5 can be found in Appendix C.

3.2 Turbocharger

The turbocharger element consists of three sub models. These are compressor, turbine and the shaft which connects the two with each other. Subsections 3.2.1, 3.2.2 and 3.2.3 gives the equations for each sub model respectively.

3.2.1 Compressor

The compressor outlet pressure is calculated from Equation 3.6 [59].

$$P_{c,out} = Pr_c P_{c,in} \qquad \textbf{3.6}$$

The compressor pressure ratio can be calculated by fitting a regression model on the pressure ratio map provided by the turbocharger manufacturer. The two-dimensional regression model has the following structure:

$$Pr_c = \mathrm{f}(N_t, \dot{m}_c) \tag{3.7}$$

The compressor outlet temperature can be calculated from Equation 3.8 [59]:

$$T_{c,out} = \left[\frac{\left(\frac{P_{c,out}}{P_{c,in}}\right)^{\frac{\gamma-1}{\gamma}} - 1}{\eta_c} + 1\right] T_{c,in} \tag{3.8}$$

The compressor efficiency can be calculated by fitting a regression model on the efficiency map. The following structure is used:

$$\eta_c = \mathrm{f}(Pr_c, \dot{m}_c) \tag{3.9}$$

Equation 3.10 calculates compressor power [59].

$$PWR_c = \frac{\dot{m}_c c_p T_{c,in}}{\eta_c}\left[\left(\frac{P_{c,out}}{P_{c,in}}\right)^{\frac{\gamma-1}{\gamma}} - 1\right] \tag{3.10}$$

3.2.2 Turbine

Equation 3.11 gives the turbine mass flow [59].

$$\dot{m}_t = \frac{\dot{m}_{t,corr} P_{EM}}{100\sqrt{T_{EM}}} \tag{3.11}$$

The corrected mass flow $\dot{m}_{T,corr}$ is provided in the form of a map by the turbocharger manufacturer. A regression model is fitted on the map with the following structure:

$$\dot{m}_{t,corr} = \mathrm{f}\left(\frac{P_{DP}}{P_{EM}}\right) \tag{3.12}$$

The turbine outlet temperature is calculated from Equation 3.13 [59].

$$T_{t,out} = \left[1 - \eta_t\left(1 - \left(\frac{P_{CP}}{P_{EM}}\right)^{\frac{\gamma-1}{\gamma}}\right)\right] T_{EM} \tag{3.13}$$

The turbine efficiency is obtained by fitting a regression model on the turbine efficiency map. The model has the following structure:

$$\eta_t = \mathrm{f}\left(\frac{P_{DP}}{P_{EM}}\right) \quad \textbf{3.14}$$

Turbine power can be calculated from Equation 3.15 [59].

$$PWR_t = \dot{m}_t c_p \eta_t T_{EM} \left[1 - \left(\frac{P_{CP}}{P_{EM}}\right)^{\frac{\gamma-1}{\gamma}}\right] \quad \textbf{3.15}$$

3.2.3 Shaft

The turbocharger shaft speed is solved by applying Newton's law of motion to the shaft, which connects the compressor and the turbine wheel [59].

$$\dot{\omega}_t = \frac{1}{J_t}\left(\frac{PWR_t}{\omega_t} - \frac{PWR_c}{\omega_t} - M_{f,t}\right) \quad \textbf{3.16}$$

The friction torque caused by the bearings can be approximated by a linear function of turbine rotational speed.

$$M_{f,t} = c_t \omega_t \quad \textbf{3.17}$$

3.3 Volumes

The volumes of the air-path can be separated into plenums and pipes. Plenums are the big receivers with a volume while pipes connect the plenums and restrictions.

3.3.1 Plenums

Large plenums such as the intake manifold can be represented by an open system of constant volume. The volume itself is assumed to be zero dimensional which means that all thermodynamic states of the system are homogenous throughout the entire volume. A schematic of the control volume subsystem is shown in Figure 3.2. Inputs are the enthalpy inflow $\dot{H}_{in}$ and heat transfer into the system, $\dot{Q}$. Output is the enthalpy outflow $\dot{H}_{out}$.

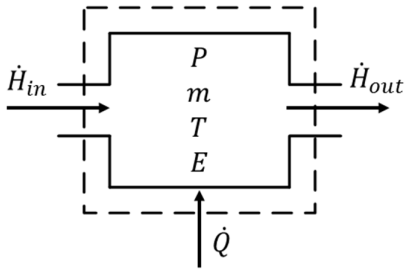

Figure 3.2: Control volume

The system itself can be seen as a storage for mass and energy, which are defined by the level of pressure and temperature. Therefore, pressure and temperature are the system state variables. The storage of mass and energy can be described by a mass and energy balance for the control volume:

- **Mass balance**: The rate of change in mass inside the control volume is equal to the difference in mass flow rate entering and leaving the control volume [16].

$$\frac{dm}{dt} = \dot{m}_{in} - \dot{m}_{out} \quad \textbf{3.18}$$

- **Energy balance**: Assuming shaft work inside the control volume to be zero, the rate of change in internal energy is equal to the difference in enthalpy flows plus heat transfer into the system as shown in Equation 3.19 [16].

$$\frac{dE}{dt} = \dot{m}_{in}h_{0\_in} - \dot{m}_{out}h_{0\_out} + \dot{Q} \quad \textbf{3.19}$$

Combining the Equations 3.2 and 3.3 with the ideal gas law [144]

$$m = \frac{PV}{RT} \quad \textbf{3.20}$$

and the first derivative of the ideal gas law

$$\frac{dm}{dt} = \frac{V}{RT}\frac{dP}{dt} - \frac{PV}{RT^2}\frac{dT}{dt} \quad \textbf{3.21}$$

the pressure and temperature state inside the control volume can be solved from Equations 3.22 and 3.23 [63].

$$\frac{dP}{dt} = \left[c_p\dot{m}_{in}T_{in} - c_p\dot{m}_{out}T + \frac{dQ}{dt}\right]\frac{R}{c_vV} \quad \textbf{3.22}$$

$$\frac{dT}{dt} = \left[c_p \dot{m}_{in} T_{in} - c_p \dot{m}_{out} T - c_v T \dot{m}_{in} + c_v T \dot{m}_{out} + \frac{dQ}{dt}\right] \frac{RT}{c_v PV} \quad \textbf{3.23}$$

Heat transfer into the system is given by Equation 3.24 [91].

$$\frac{dQ}{dt} = A_w h [T_w - T] \quad \textbf{3.24}$$

In order to represent the pressure and temperature inside a volume by Equations 3.22 and 3.23, a few assumptions have to be made. A detailed derivation including all assumptions can be found in Appendix A.

However, as mentioned in Subsection 2.5.1, further simplification are possible to reduce the complexity of the filling and empty dynamics represented by Equations 3.22, 3.23 and 3.24. Assuming that there is no heat transfer from the wall into the gas, the equation set reduces to the adiabatic filling and emptying model [63].

$$\frac{dP}{dt} = \left[c_p \dot{m}_{in} T_{in} - c_p \dot{m}_{out} T\right] \frac{R}{c_v V} \quad \textbf{3.25}$$

$$\frac{dT}{dt} = \left[c_p \dot{m}_{in} T_{in} - c_p \dot{m}_{out} T - c_v T \dot{m}_{in} + c_v T \dot{m}_{out}\right] \frac{RT}{c_v PV} \quad \textbf{3.26}$$

Assuming that the temperature inside the volume is constant, the model can be reduced to only one first order differential equation [63].

$$\frac{dP}{dt} = [\dot{m}_{in} - \dot{m}_{out}] \frac{RT}{V} \quad \textbf{3.27}$$

However, the adiabatic and the isothermal model make some significant thermodynamic assumptions about the system. As shown by Schaal *et al* [63],[53], Mueller *et al* [69] as well as Chevalier *et al* [100], in reality the system in neither fully adiabatic nor fully isothermal. For this reason, adiabatic or isothermal assumptions can lead to significant modelling errors, especially during fast transients such as throttle tip-in and tip-out where the pressure and temperature inside the volume changes rapidly.

3.3.2 Pipes

In order to model the gas dynamic behaviour including the pressure wave propagation, it is required to model the pipes with one-dimensional gas dynamics. This can be achieved by applying the Navier-Stokes equations restricted to only

one dimension and to neglect gravity to the pipe element as shown in [17]. The conservation equation can be expressed in vector form as shown in Equation 3.28.

$$\frac{\partial G(x,t)}{\partial t} + \frac{\partial F(x,t)}{\partial x} + C(x,t) = 0 \qquad \textbf{3.28}$$

The Vectors $G(x,t)$, $F(x,t)$ and $C(x,t)$ can be derived from the conservation of mass, momentum, and energy [17].

$$G(x,t) = \begin{bmatrix} \rho \\ \rho w \\ \rho\left(u + \frac{w^2}{2}\right) \end{bmatrix} \qquad \textbf{3.29}$$

$$F(x,t) = \begin{bmatrix} \rho w \\ \rho w^2 + P \\ w\rho\left(h + \frac{w^2}{2}\right) \end{bmatrix} \qquad \textbf{3.30}$$

$$C(x,t) = \begin{bmatrix} \rho w \\ \rho w^2 \\ w\rho\left(h + \frac{w^2}{2}\right) \end{bmatrix} \frac{d\ln(A)}{dx} + \begin{bmatrix} 0 \\ \rho k_f \\ -\dot{q} \end{bmatrix} \qquad \textbf{3.31}$$

Local density, local pressure and local velocity can be expressed as elements of $G(x,t)$ [91]. Therefore, Equation 3.28 is solved for $G(x,t)$ either with the Single-Step Lax-Wendroff Method or the Two-Step Lax-Wendroff Method as shown in [17]. Each pipe is therefore discretised into $N-1$ cells of size Δx giving N discretisation nodes at which Equation 3.28 has to be solved for $G(x,t)$. This indicates the computational effort of the modelling technique.

3.3.3 Lumped Volumes

A physics based air-path model is established by connecting restrictions, plenums, and pipes as illustrated in Figure 3.3.

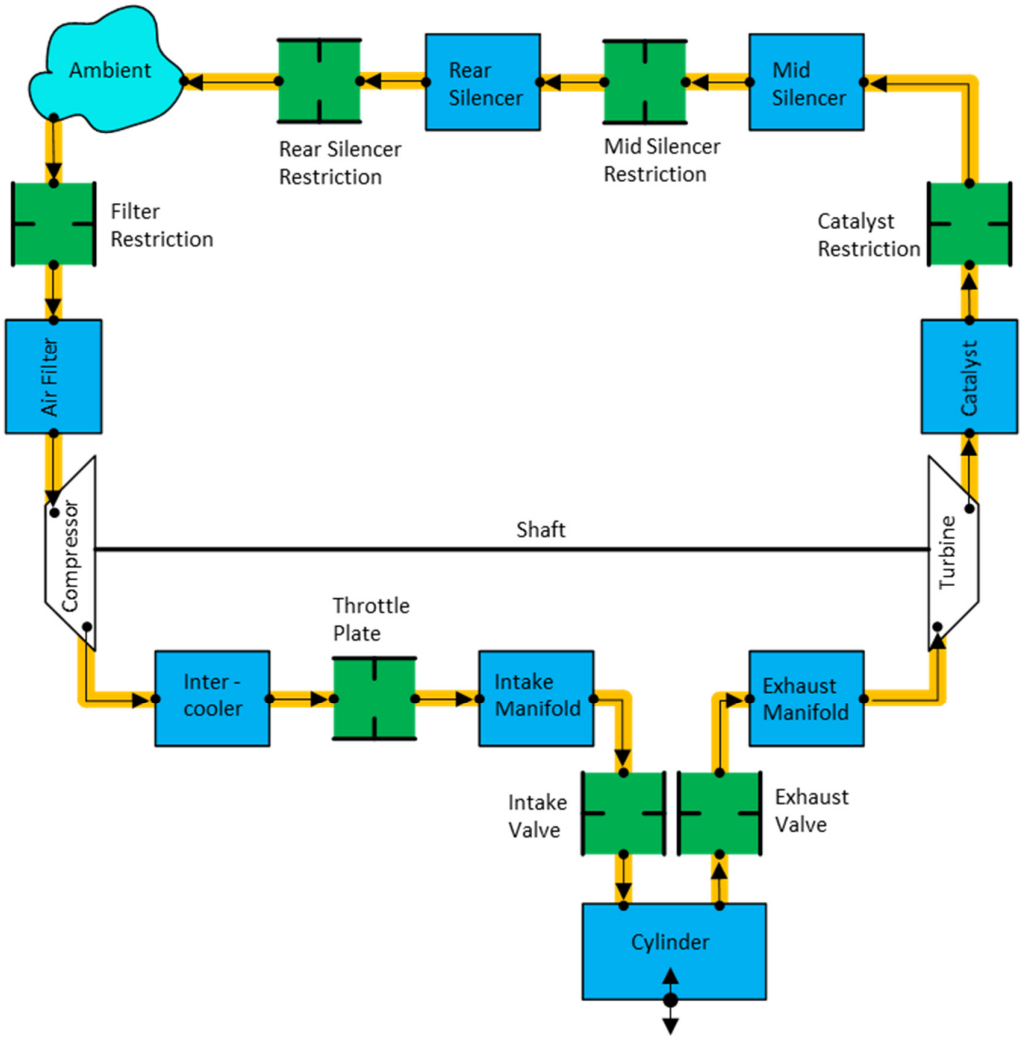

Figure 3.3: Distributed parameter engine model

The number of restriction, plenums and pipes used in the model depends on the design of the engine air-path system. However, as mentioned in Subsection 2.3.1, the complexity of a physics based model can be significantly reduced by lumping the pipes together with the plenums into major volumes along the air-path. This simplification is illustrated in Figure 3.4.

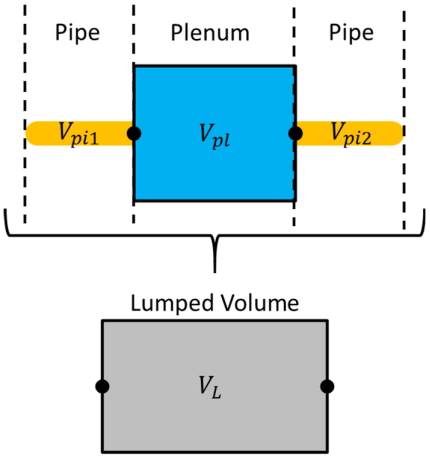

Figure 3.4: Lumped volume

When pipes with a specific volume V_{pi} and plenums with a volume V_{pl} are lumped together, the size of the lumped volume V_l is equal to the sum of all individual volumes as described by 3.32.

$$V_l = \sum V_{pi} + \sum V_{pl} \qquad \textbf{3.32}$$

For modelling, the lumped volume in Figure 3.4 is treated as a zero-dimensional volume such as the plenums in Subsection 3.3.1. Pressure and temperature inside the lumped volume are therefore modelled using Equations 3.22 and 3.23. However, this reduces the 1D gas dynamic air-path model to a model which only represent the filling and emptying dynamics of the air-path. Consequently, the resulting model is unable to represent the inertial behaviour of the gas inside the pipe as well as wave propagation phenomena. The reader is referred to Broome [147], [148], [149] for a detailed description of these effects. Neglecting these physical effects has a significant impact on the model's accuracy for cylinder air charge predictions, especially if the engine which is modelled includes long and thin pipes in the air-path as mentioned by [80]. On the other hand a significant simplification of the air-path model and a massive increase in simulation speed is achieved [57].

After lumping pipes and plenums into major volumes, the air-path model consists out of volumes and restrictions as indicated in Figure 3.5.

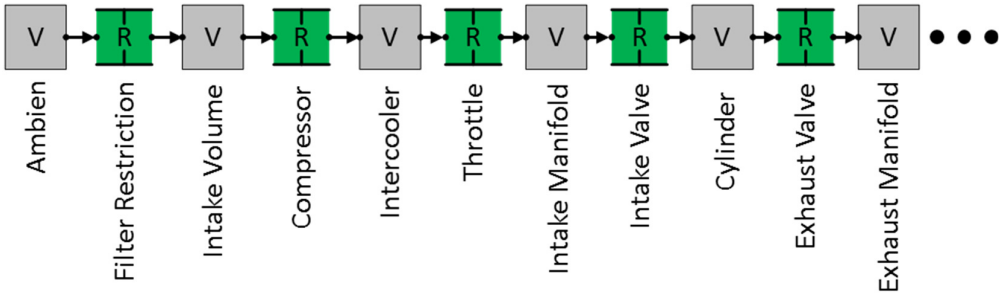

Figure 3.5: Filling and emptying based air-path modelling using lumped volumes

Adopted from [17]

3.4 Cylinder

The centre of every air-path model is the cylinder element since it is responsible for generating the mass flows through the intake and exhaust system [57]. At first, a purely physics based model is presented in Subsection 3.4.1, followed by the mean value modelling approach in Subsection 3.4.2.

3.4.1 Crank Angle Resolved - White Box Modelling

A purely physics based model to represent the gas exchange process of the cylinder can be established by applying the modelling techniques for restrictions and volumes [57]. Figure 3.6 illustrates all components which are relevant for the cylinder gas exchange process.

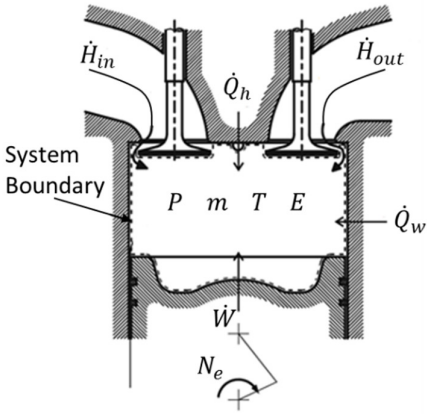

Figure 3.6: Physics based cylinder model

Adopted from [17]

The mass flows through the intake and exhaust valves are modelled by applying the equation set for compressible flow as defined by Equations 3.3 and 3.4. The Equation Set 3.33 gives the air mass flow across the intake valve [61]

$$\dot{m}_{iv} = \frac{C_d A_{th} P_{iv}}{\sqrt{RT_{iv}}} \left(\frac{P_{cyl}}{P_{iv}}\right)^{\frac{1}{\gamma}} \left\{\frac{2\gamma}{\gamma - 1}\left[1 - \left(\frac{P_{cyl}}{P_{iv}}\right)^{\frac{(\gamma-1)}{\gamma}}\right]\right\}^{\frac{1}{2}}$$

$$\dot{m}_{iv} = \frac{C_d A_t P_{cyl}}{\sqrt{RT_{iv}}} \sqrt{\gamma} \left(\frac{2}{\gamma + 1}\right)^{\frac{\gamma+1}{2(\gamma-1)}} \quad \textbf{3.33}$$

and the Equation Set 3.34 gives the mass flow from the cylinder into the exhaust system [61].

$$\dot{m}_{ev} = \frac{C_d A_{th} P_{cyl}}{\sqrt{RT_{cyl}}} \left(\frac{P_{ev}}{P_{cyl}}\right)^{\frac{1}{\gamma}} \left\{\frac{2\gamma}{\gamma - 1}\left[1 - \left(\frac{P_{ev}}{P_{cyl}}\right)^{\frac{(\gamma-1)}{\gamma}}\right]\right\}^{\frac{1}{2}}$$

$$\dot{m}_{ev} = \frac{C_d A_t P_{cyl}}{\sqrt{RT_{cyl}}} \sqrt{\gamma} \left(\frac{2}{\gamma + 1}\right)^{\frac{\gamma+1}{2(\gamma-1)}} \quad \textbf{3.34}$$

Temperature inside the cylinder is derived from energy balance as described by Equation 3.35 [61].

$$\frac{dT_{cyl}}{dt} = \left[c_p\left(\dot{m}_{iv}T_{iv} - \dot{m}_{ev}T_{cyl}\right) - c_v T_{cyl}(\dot{m}_{iv} - \dot{m}_{ev}) + Q_c - Q_w - P_{cyl}\frac{dV_{cyl}}{dt}\right] d\,\frac{RT_{cyl}}{c_v P_{cyl} V_{cyl}} \quad \textbf{3.35}$$

The mass inside the cylinder is solved from the mass balance, given by Equation 3.36 [17].

$$\frac{dm_{cyl}}{dt} = \dot{m}_{iv} - \dot{m}_{ev} \quad \textbf{3.36}$$

and pressure inside the cylinder is finally estimated from the ideal gas law as shown in Equation 3.37 [17].

$$P_{cyl} = \frac{m_{cyl} R T_{cyl}}{V_{cyl}} \quad \textbf{3.37}$$

In addition to the thermodynamic properties which are described by Equations 3.33 to 3.37, a complete physical cylinder model requires equations which

describe the kinematics of the piston, camshaft, and the valves. These equations deliver the required information of the actual cylinder volume V_{cyl}, its derivative $\frac{dV_{cyl}}{dt}$, as well as the physical open areas of the intake and exhaust valves A_{iv} and A_{ev} respectively. The required equations can be found in Heywood [59], Pezouvanis [62] and Ferguson [61].

Equations 3.33 to 3.37 describe the gas exchange process of the cylinder. The equation set indicates the complexity of the process and allows a technical analysis of all factors which have an influence. The equation set reveals that there are seven factors which have a direct influence on the final cylinder air charge at Intake Valve Closing (IVC). Those factors are discussed in the following:

- **Flow conditions upstream from the intake valve**: The pressure difference across the intake valve drives the air mass flow into the cylinder described by Equation 3.33. Consequently, pressure and temperature upstream from the intake valve have a very strong influence on the amount of fresh air inside the cylinder at IVC.
- **Flow conditions downstream from the exhaust valve**: The pressure difference across the exhaust valve drives the mass flow from the cylinder into the exhaust system as described by Equation 3.34. Consequently, the higher the back pressure in the exhaust system, the higher the pressure inside the cylinder at EVC. A higher in-cylinder pressure at IVO reduces the amount of fresh air that can be induced during the induction stroke.
- **Valve timing**: The timing of the intake and exhaust valve actuate the mass flows into and out of the cylinder. The profile of the camshaft and the timing with respect to the engine crankshaft determine the physical open area A_{iv} and A_{ev} in Equations 3.34 and 3.35 respectively. Valve lift, lift duration as well as the timing of EVO, EVC, IVO and IVC have a significant impact on the amount of fresh air inside the cylinder by the end of induction. The reader is referred to [59] for more detailed information about the impact of valve timing upon the gas exchange process.
    - **EVO**: Early exhaust valve opening helps emptying the cylinder from exhaust gases due to the high in-cylinder pressure. This allows reducing the mass of the residual gases.
    - **EVC**: The most important factor, which determines the amount of residual gases, is the Exhaust Valve Closing (EVC) event. A too

early EVC prohibits the exhaust gases from leaving the cylinder while a too late EVC causes exhaust gases to be sucked back into the cylinder as the piston moves from TDC to BDC.

- **IVO**: Intake valve opening has a very small impact on the air charge. However, early IVO causes overlap where intake and exhaust valves are open at the same time. This enables blow through of fresh air into the exhaust system or flow of residual gases into the intake manifold. Which phenomenon occurs depends on the current pressures P_{IM}, P_{cyl} and P_{EM}.
- **IVC**: Intake valve closing is the most important valve event for air charge. Late IVC can increase the cylinder filling at high engine speeds where P_{cyl} at BDC is still smaller than P_{IM} due to the flow restriction across the valves. However, at low engine speed late IVC causes backflow from the cylinder into the intake manifold as the piston moves from BDT to TDC.

- **Valve design**: The size and the geometry of the intake and exhaust valve affect the flow restriction of the valve. This determines the flow coefficient of each valve in Equations 3.34 and 3.35 respectively which directly affects the mass flows into and out of the cylinder.
- **Intake and exhaust system geometry**: The length of the intake and exhaust runners, as well as the size of the plenums in the intake and exhaust system, determine the propagation of the pressure waves through the air-path system. Tuning the length of the pipes in the exhaust system allows the reduction of pressure downstream from the exhaust valve to enhance emptying the cylinder. This is achieved if an expansion wave arrives at the exhaust valve just before EVC. Tuning of the intake system allows to increase the pressure upstream from the intake valve just before IVC which can significantly increase the cylinder air charge. This is achieved if a pressure wave arrives at the intake valve just before IVC. Tuning the length of the pipes is straightforward since the pressure waves always travel with the speed of sound.
- **Charge heating**: Heating of the air inside the cylinder during the intake stroke reduces the density of the air charge, which consequently reduces the amount of air inside the cylinder at IVC. Charge heating has two main causes:

- **Heat transfer**: Heat transfer from the cylinder walls and the piston into the air increase the in-cylinder temperature as described by Equation 3.35. This phenomenon is primarily dependent on cylinder wall temperature T_w and the temperature upstream the intake valve, T_{iv}. A higher wall temperature increases the in-cylinder heat transfer due to the increased temperature difference between T_{cyl} and T_w. A higher temperature T_{iv} reduces the heat transfer due to the reduced difference between T_{cyl} and T_w.
- **Mixing with residual gas**: The in-cylinder temperature at EVC defines the temperature of the residual gas which mixes with the fresh gas. The higher the temperature at EVC, the higher is the temperature of the mixed gas at IVC.

- **Engine speed**: The local velocities of the gases along the engine air-path are proportional to the mean piston speed [59]. Consequently, engine speed affects the cylinder air charge in a number of different ways.
  - **Charge heating**: The duration of the induction stroke is proportional to the speed of the engine. For this reason, the impact of charge heating reduces with increasing engine speed, since less time is available to heat the induced air in the cylinder.
  - **Friction losses**: The friction losses across valves increases as the square of the velocity. Specifically, at high engine speeds the flow at the end of the induction stroke becomes choked as described in Equations 3.33 and 3.34. Once this occurs, the air mass flow into the cylinder can only be increased by a higher pressure upstream the intake valve.
  - **Induction ram**: Since the pressure waves always propagate with the speed of sound, tuning of the intake and exhaust system is limited to a specific engine speed range. The length of the runners determines at which engine speed the pressure wave arrives just before IVC which increase the cylinder air charge. At other engine speeds this effect, which is also known as induction ram [147]–[149], is not present or might even have a negative effect in case an expansion wave arrives just before IVC.

The physics based cylinder model (Equations 3.33 to 3.37) allows accurate cylinder air charge predictions since it includes most physical effects. However, accurate predictions require accurate models for the flow coefficients of the intake and exhaust valve, as well as an accurate representation of the pressure wave propagation in the intake and exhaust systems which requires gas dynamic models. As mention in Subsection 3.3.2, this involves time consuming solvers and a small simulation step size.

3.4.2 Cycle Average - Black Box Modelling

An alternative to a physics based crank angle resolved model is a cycle average cylinder model [64]. Such a model uses the cycle average pressure and temperature inside the intake manifold to estimate the cycle average air mass flow through the intake valve. To model the cycle average air mass flow through the intake valve based on the cycle average intake manifold conditions, the well-known speed-density approach is used. The cylinder element is therefore treated as a reciprocating air pump with a swept volume identical to the displacement of the engine.

Let the total air mass induced thorough the intake valve over one engine cycle m_{iv} be defined as

$$m_{iv} = \int_0^{720} \dot{m}_{iv}\, \omega\, d\theta \qquad \textbf{3.38}$$

where ω is rotational speed and θ is the angular position of the crank shaft. Considering that a four-stroke engine has only one intake event every two revolutions, the cycle average air mass flow through the intake valve at a given engine speed N_e can be expressed by Equation 3.39.

$$\dot{m}_{iv} = m_{iv} \frac{N_e}{120} \qquad \textbf{3.39}$$

Assuming that IVC occurs at BDC, it is possible to fill the entire engine displacement volume V_d with fresh air. In this case, induced air mass can be expressed with the ideal gas law as shown in Equation 3.40.

$$m_{iv} = \frac{P_{cyl,IVC} V_d}{R T_{cyl,IVC}} \qquad \textbf{3.40}$$

Where $P_{cyl,IVC}$ and $T_{cyl,IVC}$ are the pressure and temperature inside the cylinder at IVC respectively. If the pressure and temperature inside the cylinder at IVC are identical with cycle average pressure and temperature inside the intake manifold, the induced air mass could theoretically be expressed in terms of intake manifold conditions as shown in Equation 3.41.

$$m_{iv,IM} = \frac{P_{IM} V_d}{R T_{IM}} \tag{3.41}$$

However, as mention in Subsection 3.4.1, there are several factors which affect the gas exchange process. Flow restriction as well as chocked flow through the valves may cause that $P_{cyl,IVC} \neq P_{IM}$. Charge heating causes that $T_{cyl,IVC} \neq T_{IM}$. Due to valve timing, IVC eventually occurs after BDC, which under certain operating conditions causes backflow into the intake manifold. In this case, it is not possible to fill the entire displacement volume with fresh air. It follows that intake manifold conditions on its own are insufficient to estimate a highly accurate cylinder air charge. To account for the fact that cylinder air charge cannot directly be expressed in terms of intake manifold pressure and temperature, the volumetric efficiency term is used. The volumetric efficiency is also known as the engine breathing efficiency and describes the effectiveness of the cylinder gas exchange process. It defines air mass induced per cycle through the intake valve compared to the amount of air mass that theoretically could be induced based on cycle average intake manifold conditions and is therefore defined as

$$\eta_v = \frac{m_{iv}}{m_{iv,IM}} = \frac{m_{iv}}{\frac{P_{IM} V_d}{R T_{IM}}} \tag{3.42}$$

Substituting Equation 3.42 into 3.39, the cycle average air mass flow through the intake valve can be estimated from Equation 3.43.

$$\dot{m}_{iv} = \frac{\eta_v P_{IM} V_d N_e}{120 R T_{IM}} \tag{3.43}$$

Since the complex gas exchange process is depending on a high number of variables, the volumetric efficiency must cover the effect of all important variables which influence the engine breathing efficiency. An analysis of the equations which describe the gas exchange process in Subsection 3.4.1 indicates that the volumetric efficiency depends on engine speed, intake manifold pressure,

exhaust manifold pressure, valve timing, intake manifold temperature, and engine coolant temperature.

3.5 Summary

Chapter 3 presents the fundamental equations required to model the air-path of a modern GTDI engine. Restrictions such as valves or the air filter are modelled using the equations for compressible and incompressible flow. The volumes of the air-path can be separated into the big plenums and pipes. Plenums are modelled using filling and emptying dynamics. The pipes can either be modelled assuming one-dimensional gas dynamics or can be lumped together with the plenums into big volumes which allows modelling with the filling and emptying technique. The cylinder element can be modelled on a crank angle resolved basis using filling and emptying dynamics and the equations for compressible flow for the intake and exhaust valves. Alternatively, it is possible to represent the cylinder on a cycle average basis, which allows modelling the cycle average air mass flow through the intake valve based on intake manifold conditions. However, this requires an accurate characterisation of the engine breathing efficiency, which depends on a high number of engine variables. The compressor and turbine are modelled by fitting regression models to the maps, which are provided by the manufacturers.

Chapter 4 System Observation & Parameter Identification

This chapter introduces two different methodologies, which can be used to solve the transient engine air charge problem. A case study is presented in Section 4.1, which is a simplified representation of the fundamental problem that needs to be solved. One solution is to treat the problem as an unknown input estimation problem. The second solution is to treat the problem as a joint state and parameter estimation problem. The two solutions are then applied to the simplified problem to evaluate their performance under 'noise-free' and 'noisy' conditions. Both observation principles are used in Chapter 5 to develop the air-path observer, which is required to solve the transient air charge estimation problem.

4.1 Simplified Problem

This section presents a simplified example of the transient engine air charge estimation problem, which requires an identical solution. This simplified problem is used to compare and evaluate the performance of available methods. Consider the following first order nonlinear differential equation.

$$\dot{x}(t) = x(t)\vartheta(t) + u(t) \tag{4.1}$$

where $x(t)$ is the system state, $u(t)$ is the system input and $\vartheta(t)$ is an unknown parameter which changes over time. Assume that $x(t)$ and $u(t)$ are measurable and the task is to continuously identify the unknown parameter $\vartheta(t)$ based on measurement of $x(t)$ and $u(t)$. Since the derivative of the state $\dot{x}(t)$ is not directly measurable, it is not possible to estimate $\vartheta(t)$ directly from Equation 4.1. This problem can be solved either by treating it as an unknown input estimation problem or a joint state and parameter estimation problem. The two solutions are treated in Section 4.2 and Section 4.3 respectively.

4.2 Unknown Input Estimation

The problem above can be converted into an unknown input estimation problem. Therefore, Equation 4.1 is rewritten into the following form.

$$\dot{x}(t) = z(t) + u(t) \tag{4.2}$$

where $z(t)$ is considered to be an unknown system input. The unknown input is estimated either by directly inverting Equation 4.2 or by using an unknown input observer. The unknown parameter is finally estimated from the approximation / observation of the unknown input, $\hat{z}(t)$. For the specific example given by Equation 4.1, $\hat{\vartheta}(t)$ is estimated from Equation 4.2.

$$\hat{\vartheta}(t) = \frac{\hat{z}(t)}{x(t)} \tag{4.3}$$

Two methods for unknown input estimation are presented in the following subsections.

4.2.1 Model Inversion

The simplest way to estimate the unknown input $z(t)$ is to directly invert Equation 4.2.

$$\hat{z}(t) = \dot{\hat{x}}(t) - u(t) \tag{4.4}$$

Equation 4.4 requires an estimation or approximation of the state derivative $\dot{\hat{x}}(t)$. Using the Euler backwards method [150], the derivative of a signal f at the sample k can be approximated by Equation 4.5.

$$\dot{f}(k) \approx \frac{f(k) - f(k-1)}{T_s} \tag{4.5}$$

where T_s is the sample time. Therefore, the state derivate can be approximated by

$$\dot{\hat{x}}(k) = \frac{x(k) - x(k-1)}{T_s} \tag{4.6}$$

The Euler backwards method is a very simple numerical differentiation method. However due to the direct difference operation $x(k) - x(k-1)$, this method is very sensitive to measurement noise [44]. Therefore, this method is only suitable for applications where noise-free measurement data are available. If the measurement data are corrupted with noise, the Unknown Input Observer (UIO) can be used.

4.2.2 Unknown Input Observer

The Unknown Input Observer which was developed by Kolmanovsky [98], is given by Equations 4.7 and 4.8.

$$\dot{\varepsilon}(t) = k^2 x(t) - k\varepsilon(t) + ku(t) \tag{4.7}$$

$$\hat{z}(t) = kx(t) - \varepsilon(t) \tag{4.8}$$

The two equations can be derived by applying a high gain observer to Equation 4.2. The reader is referred to Dabroom [115] and Vasiljevic *et al* [116] for more details about high gain observers. The UIO is less sensitive to measurement noise than the Euler derivative approximation. k is the gain of the UIO and defines how fast the estimated input $\hat{z}(t)$ converges to the real value of $z(t)$. However, tuning the gain is always a trade-off between fast response and noise amplification.

4.3 Joint State and Parameter Estimation

As mentioned in Section 4.1, the second solution to the simplified problem is the Joint State and Parameter Estimation (JSPE) technique. This method combines a system state observer with an adaptive parameter identification law to observe the unknown parameter in a differential equation [139]. State observation for a nonlinear system is discussed in Subsection 4.3.1 and adaptive parameter identification is treated in Subsection 4.3.2. A solution which can be applied to sampled measurement data is presented in Subsection 4.3.3.

4.3.1 Nonlinear State Observer

For the general nonlinear time invariant system represented by Equation 4.9

$$\begin{aligned} \dot{x}(t) &= f\big(x(t), u(t)\big) \\ y(t) &= g\big(x(t)\big) \end{aligned} \tag{4.9}$$

the nonlinear observer for the system state $x(t)$ is given by Equation 4.10 [151].

$$\dot{\hat{x}}(t) = f\big(\hat{x}(t), u(t)\big) + L\big[y(t) - g\big(\hat{x}(t)\big)\big] \quad \textbf{4.10}$$

The convergence rate of the observer can be controlled by tuning the gain L.

4.3.2 Adaptive Parameter identification

Adaptive or recursive parameter identification allows identification of a time varying parameter online from measured system input-output data. A nonlinear regression model with a possibly time varying parameter $\vartheta(t)$ is given by Equation 4.11.

$$y(t) = h\big(\phi(t), \vartheta(t)\big) + \epsilon(t) \quad \textbf{4.11}$$

Equation 4.12 gives the general form for recursive estimation of the adaptive parameter $\hat{\vartheta}(t)$ as shown in [152], where $y(t)$ is the system output and $\phi(t)$ are the explanatory variables.

$$\hat{\vartheta}(k) = \hat{\vartheta}(k-1) + k\left(y(k) - h\left(\phi(k), \hat{\vartheta}(k-1)\right)\right) \quad \textbf{4.12}$$

or for convenience in continuous time form:

$$\dot{\hat{\vartheta}}(t) = k\left(y(t) - h\left(\phi(t), \hat{\vartheta}(t)\right)\right) \quad \textbf{4.13}$$

Equation 4.12 identifies the adaptive parameter $\hat{\vartheta}$ by driving the prediction error $y(k) - h\left(\phi(k), \hat{\vartheta}(k-1)\right)$ to zero. The gain k determines how much the current prediction error affect the update of $\hat{\vartheta}$. There are a several different methods available to compute the gain of the adaptive identification. Solutions range from user defined *ad-hoc* values over recursive least squares and recursive least squares with forgetting factor to the Kalman filter and the Extended Kalman filter. The reader is referred to Souflas [56] for more detailed information.

However, if the adaptive parameter is part of a differential equation, Equations 4.12 or 4.13 cannot directly be used to identify the parameter. Consider the following nonlinear first order system.

$$\dot{x}(t) = f\big(x(t), u(t), \vartheta(t)\big) \quad \textbf{4.14}$$

$$y(t) = g\big(x(t)\big)$$

If $x(t)$ or $y(t)$ are measurable but $\dot{x}(t)$ is not available from measurements, the adaptive identification algorithm from Equation 4.13 cannot directly be used to identify the parameter $\vartheta(t)$ in the System 4.14. The reason for this is that the System 4.14 does not establish a direct algebraic relation between the measured system output and the adaptive parameter. One way to overcome this problem would be to approximate the state derivative using one of the methods presented in Section 4.2. However, in this case the resulting solution would be extremely similar to the unknown input estimation method. Alternatively, an observer can be used which produces an observation $\hat{y}$ based on the identified parameter $\hat{\vartheta}$ as shown in Equation 4.15.

$$\dot{\hat{x}}(t) = f\left(\hat{x}(t), u(t), \hat{\vartheta}(t)\right) + L\big[y(t) - g\big(\hat{x}(t)\big)\big]$$

$$\hat{y}(t) = g\big(\hat{x}(t)\big) \qquad \textbf{4.15}$$

The adaptive parameter is then identified from Equation 4.16 based on the difference between the measured and observed state.

$$\dot{\hat{\vartheta}}(t) = k\big(y(t) - \hat{y}(t)\big) \qquad \textbf{4.16}$$

The solution represented by Equations 4.15 and 4.16 is known as joint state and parameter estimation. The collaboration between state observer and parameter identification is illustrated in Figure 4.1.

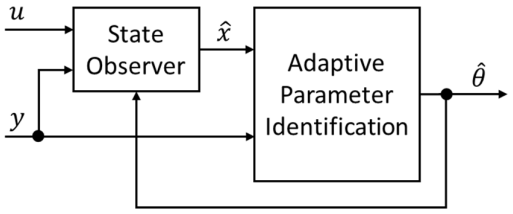

Figure 4.1: Joint state and parameter estimation principle

The state observer observes a measurable system state based on a model which describes the dynamic behaviour of the state. It is essential that the model used in the state observer includes an adaptive parameter. The adaptive parameter is then identified with an adaptive parameter identification law. The identification

law uses the difference between measured and observed system state to identify the adaptive parameter with the aim to drive the difference between measured and observed state to zero [129].

The convergence rate of the identified parameter $\hat{\vartheta}(t)$ as well as the sensitivity to measurement noise depends on the tuning of the gain L in the state observer and the gain k of the adaptive law. The simplest solution is to choose some *ad-hoc* values for the gains. A more advanced solution is to make use of the Kalman filter theory in the form of the Augmented Extended Kalman Filter (AEKF).

4.3.3 Augmented Extended Kalman Filter (AEKF)

The AEKF allows the application of the solution for joint state and parameter estimation represented by Equations 4.15 and 4.16 to sampled measurement data. In addition, the AEKF allows the computation of the gains of the state observer and the adaptive parameter identification by fusing the knowledge about prediction accuracy of the model and the level of measurement noise as described in Subsection 2.5.4. The state of the nonlinear system $x(k)$ is therefore augmented by the adaptive parameter $\vartheta(k)$ as shown by Equation 4.17, where $X(k)$ represents the augmented state [113], [138].

$$X(k) = \begin{bmatrix} x(k) \\ \vartheta(k) \end{bmatrix} = \begin{bmatrix} f\big(x(k-1), u(k), \vartheta(k-1)\big) + \nu_p \\ \vartheta(k-1) \end{bmatrix}$$
$$y(k) = g\big(x(t)\big) + \nu_m \qquad \textbf{4.17}$$

$u(k)$ is the system input, $y(k)$ the measured output and $\nu_p(k)$ and $\nu_m(k)$ are the process noise and measurement noise respectively. The Kalman filter algorithm for the augmented system 4.17 is represented by the Equation Set 4.18 [138].

$$\hat{X}(k|k-1) = f\left(\hat{x}(k-1|k-1), u(k), \hat{\vartheta}(k-1|k-1)\right)$$
$$P(k|k-1) = FP(k-1|k-1)F^{-1} + R_p$$
$$K(k) = P(k|k-1)H^T(k)[H(k)P(k|k-1)H^T(k) + R_m]^{-1} \qquad \textbf{4.18}$$
$$\hat{X}(k|k) = \hat{x}(k|k-1) + K(k)\big[y(k) - g\big(\hat{x}(k|k-1)\big)\big]$$
$$P(k|k) = \big(I - K(k)H(k)\big)P(k|k-1)$$

where P is the augmented covariance matrix, R_p is the process covariance matrix, R_m is the measurement covariance and K is the Kalman gain. R_p is given by

$$R_p = \begin{bmatrix} \sigma_x^2 & 0 \\ 0 & \sigma_\vartheta^2 \end{bmatrix} \quad \textbf{4.19}$$

where σ_x^2 is the process covariance of the system state model and σ_ϑ^2 is the process covariance of the adaptive parameter(s). σ_x^2 and σ_ϑ^2 are given by Equations 4.20 and 4.21 respectively.

$$\sigma_x^2 = diag[\sigma_{x1}^2 \quad \sigma_{x2}^2 \quad \dots \quad \sigma_{xn}^2] \quad \textbf{4.20}$$

$$\sigma_\vartheta^2 = diag[\sigma_{\vartheta 1}^2 \quad \sigma_{\vartheta 2}^2 \quad \dots \quad \sigma_{\vartheta n}^2] \quad \textbf{4.21}$$

whilst the measurement covariance matrix, R_m is given by Equation 4.22.

$$R_m = diag\left[\sigma_{y1}^2 \quad \sigma_{y2}^2 \quad \dots \quad \sigma_{yn}^2\right] \quad \textbf{4.22}$$

For the simplified problem presented in Section 4.1, the augmented state vector of the AEKF is given by the Equation Set 4.23.

$$\hat{X}(k) = \begin{bmatrix} \hat{x}(k) \\ \hat{\vartheta}(k) \end{bmatrix} = \begin{bmatrix} \hat{x}(k-1) + T_s\left(\hat{x}(k-1)\hat{\vartheta}(k-1) + u(k-1)\right) \\ \hat{\vartheta}(k-1) \end{bmatrix}$$
$$g(k) = \hat{x}(k) \quad \textbf{4.23}$$

4.4 Comparison

In this section, the UIE method and the JSPE method are applied to the simplified problem presented in Section 4.1. The performance of both methods is compared in an online and an offline case study to highlight the advantages and disadvantages of each method.

In both case studies, the unknown parameter $\vartheta(t)$ which needs to be identified is given by Equation 4.24.

$$\vartheta(t) = -[x(t) + 1] \quad \textbf{4.24}$$

Substituting Equation 4.24 into Equation 4.1 leads to Equation 4.25 which describes the system model used in both case studies.

$$\dot{x}(t) = u(t) - x(t)[x(t) + 1] \tag{4.25}$$

Note that Equations 4.24 and 4.25 are only used to produce the simulation data. A step input and a ramp signal are used to demonstrate the performance of both methods.

4.4.1 Offline Case Study

Offline applications allow to use a wider range of filters which can remove measurement noise without introducing any phase shift. Noise-free data are therefore used in the offline case study. As mentioned in Subsection 4.2.1, for noise free data, the unknown input can be estimated by directly inverting the model and approximating the state derivative with the Euler backwards method. In the AEKF the measurement noise covariance is set to $\sigma_{y1}^2 = 0$.

The input signal is shown in Figure 4.2 a) and the system state response in Figure 4.2 b). Figure 4.2 c) compares the real value of the unknown parameter with identified parameter using the UIO and the AEKF. Figure 4.2 d) represents the identification error in percent.

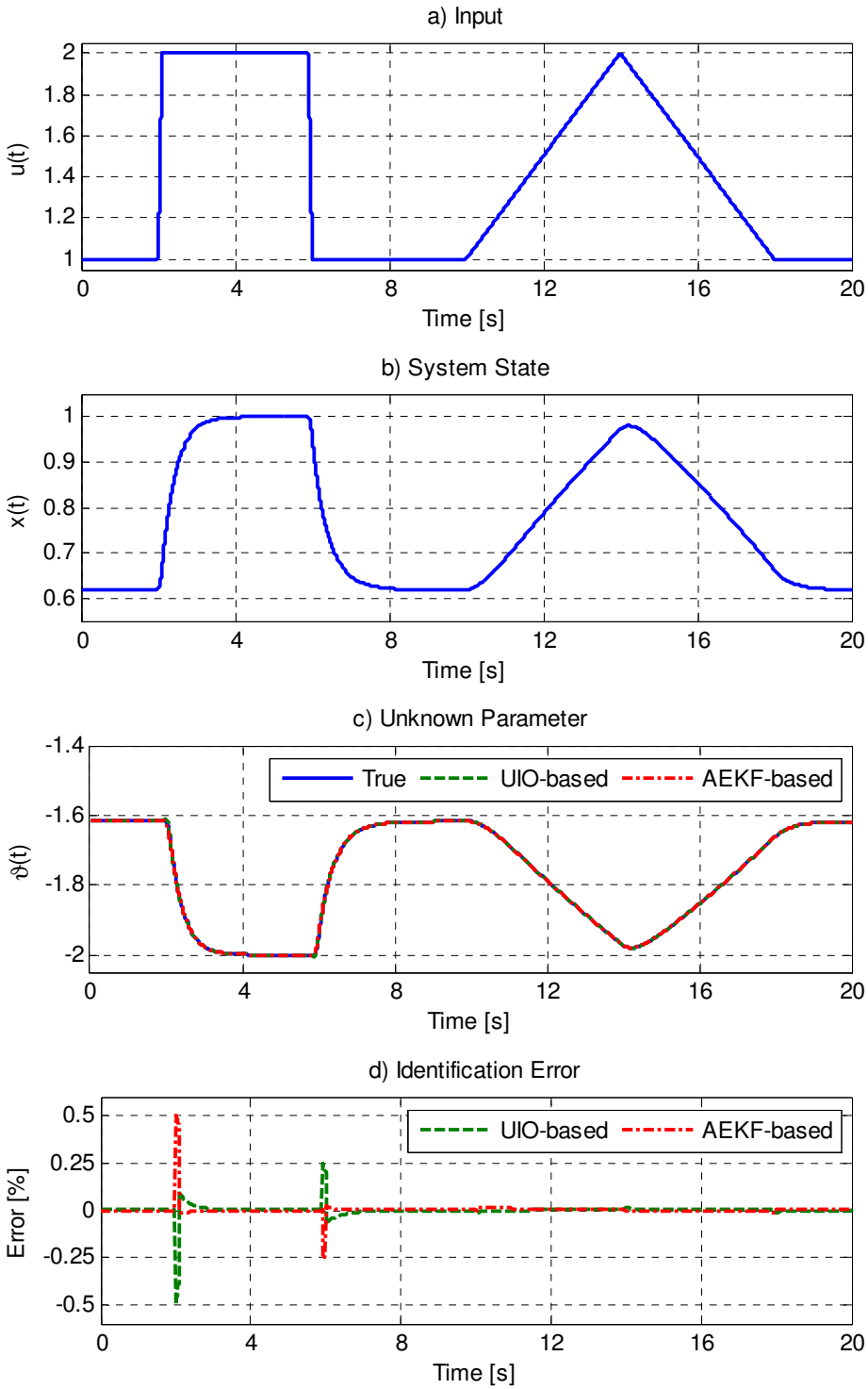

Figure 4.2: Offline case study results

Figure 4.2 c) shows that the identified parameters (green and red lines) are line on line with the true value of the unknown parameter (blue line). This proves that both methods allow a highly accurate identification of the unknown parameter if the data are noise free. The identification error in Figure 4.2 d) shows a maximum error of 0.5% during the step input. Therefore, it can be concluded that for offline

application where the measurement data are noise-free the UIE and the JSPE method achieve identical accuracy. These findings can be explained by analysing the algorithm of the AEKF in more detail. In case noise-free data are available, the measurement noise covariance σ_{y1}^2 is set to zero. Therefore, the AEKF algorithm assumes that perfect measurement data are available. If the process covariance of the state equation σ_x^2 is set to zero as well, the AEKF algorithm assumes that the system model used to describe the system state is 100% accurate. Consequently, the computed gain for the adaptive parameter becomes extremely high. The high gain makes the AEKF act similarly to a high gain observer, which approximates the derivative of a state as the gain goes to infinity.

The simulation results presented in Figure 4.2 lead to the conclusion that under noise-free conditions both methods achieve an identical accuracy. However, the UIE method in form of direct model inversion is easier to implement and requires les computational effort since no integration is involved. In addition, the UIE method is easier to use for analytical investigations due to its simple formulation. Consequently, the UIE method is definitely the simpler solution for offline applications.

4.4.2 Online Case Study

Online applications suffer from the problem that only certain filters can be implemented online and those filters usually lead to a phase shift in the filtered signal. Therefore, in the online case study, a measurement noise with a covariance of $\sigma_m^2 = 0.005$ was added to the measured system state as shown in Figure 4.3 b). The same input signal was used as in the offline case study above. The UIO with a gain of $k = 8$ is used to observe the unknown system input and the measurement covariance of the AEKF is stet to $\sigma_y^2 = \sigma_m^2$. Figure 4.3 c) compares the real value of the unknown parameter with identified parameter using the UIO and the AEKF. Figure 4.3 d) represents the identification error in percent.

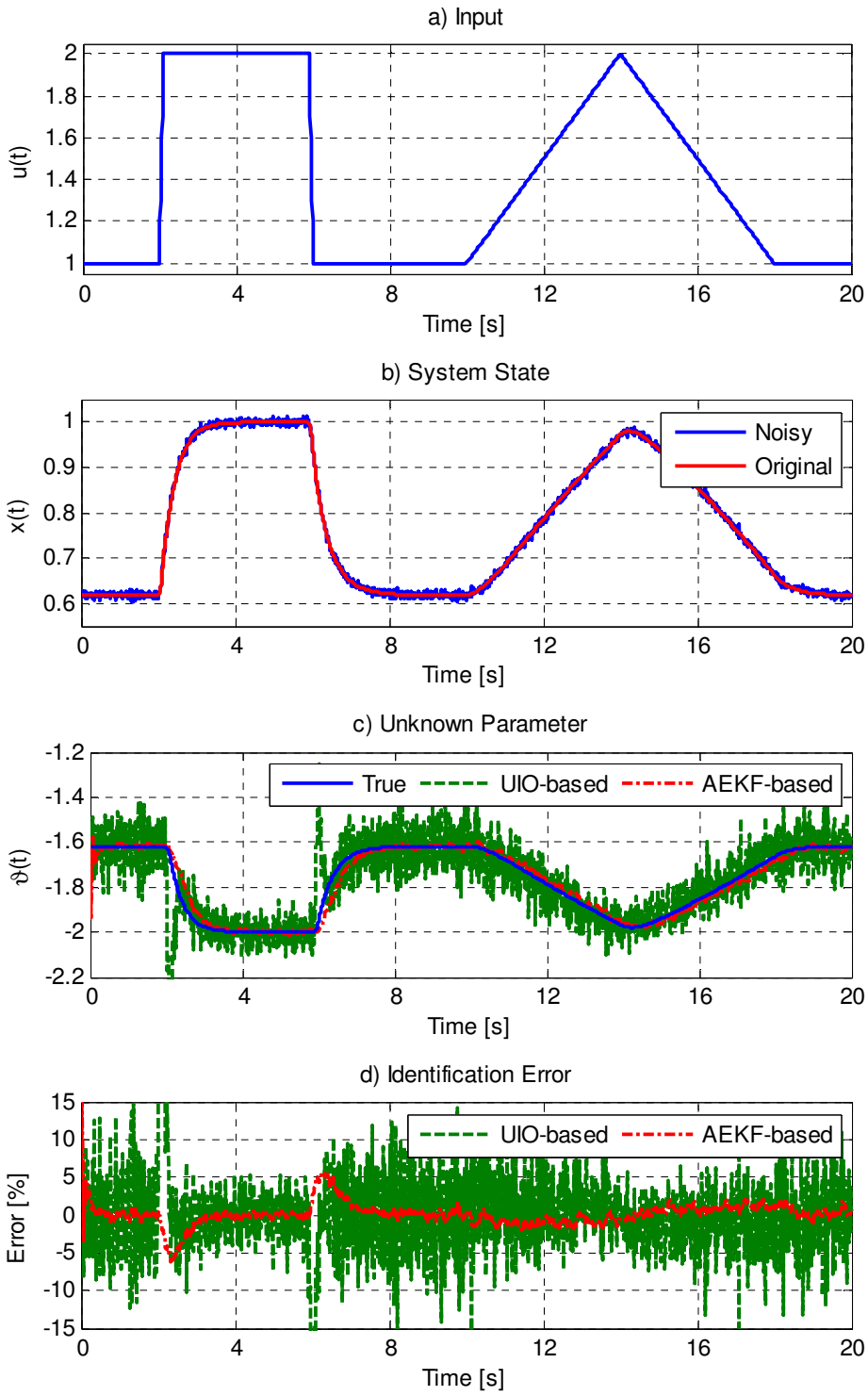

Figure 4.3: Online case study results

Figure 4.3 shows a significant difference in the performance between the two methods. Obviously, the AEKF estimates the unknown parameter with a much higher accuracy than the UIO. The results demonstrate the power of the Kalman filter and point out the weakness of the UIO method if the measurement data are corrupted with a significant level of noise. The main reason for the relatively high

accuracy of the AEKF is the collaboration between state and parameter estimation. The recursive estimation of the parameter $\hat{\vartheta}(t)$ ensures that the model used in the state observer $\hat{x}(t)$ is a very accurate description of the real system state $x(t)$. Consequently, the state observer filters out the measurement noise very effectively. This allows a much smoother adaption of the unknown parameter compared to the UIO. The main reason for the poor performance of the UIO is the weakness of the high gain observer. Although it provides a smoother estimate than the Euler backwards method, it still significantly amplifies the noise. This amplification could be reduced by reducing the gain, however, this would penalise the response to changes in the unknown parameter. The simulation results presented in Figure 4.3 lead to the conclusion that the AEKF achieves a higher identification accuracy then the UIO in online applications where the measurement data are corrupted with noise.

4.5 Summary

Chapter 4 presents two different methodologies which can be used to solve the transient engine air charge estimation problem. In the UIE method, the term of the equation which contains the unknown parameter is treated as an unknown system input. The unknown input is either estimated by approximating the state derivative or by using the unknown input observer. The unknown parameter is finally estimated from the unknown input. The JSPE method, on the other hand, combines a recursive parameter estimation technique with a system state observer to identify the unknown parameter. The model used in the state observer includes the adaptive parameter which is then identified by driving the error between measured and observed system state to zero. In the offline case study in which noise-free measurement data were used, both methods achieved an identical accuracy. In the online case study in which the measurement data were corrupted with noise, the JSPE method in form of the AEKF showed a more accurate identification of the unknown parameter. Following these results, it can be concluded that for offline applications the UIE method is more suitable since it is much easier to implement and achieves a high accuracy without tuning any parameters. For online applications, the JSPE method in the form of the AEKF has a significant advantage over the UIE method since it is much less affected by the presence of measurement noise.

Chapter 5 Engine Air-Path Observation

This chapter applies the UIE-method and the JSPE-method to a dynamic air-path model to establish an air-path observer, which allows the observation of the actual air mass flow through the intake valve. Section 5.1 justifies which model type should be chosen for the observer, in how many major volumes the air-path should be divided and which system state should be used in the observer. Section 5.2 presents the UIE based observer in form of the direct model inversion which is suitable for online applications. Section 5.3 presents the JSPE based observer in form of the AEKF which should be used for online applications. Input reconstruction for compensation of the thermocouple response delay is treated in Section 5.4.

5.1 Transient Engine Air Charge Estimation

The main problem of transient engine air charge estimation is that the state of the art sensors for air mass flow measurement are far too large to be installed anywhere close to the engine intake valves. Figure 5.1 shows the AVL FLOWSONIX [32] air mass flow sensor, which is currently one of the best air mass flow sensors available on the market in terms of accuracy and response time.

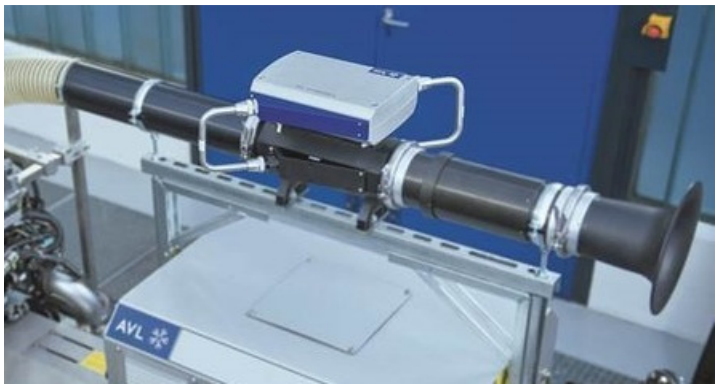

Figure 5.1: AVL FLOWSONOIX measurement device

The only practical way is to install the sensor in front of the air filter. During transient engine operation, the filling and emptying, as well as the gas dynamics of the engine intake system are excited. For this reason, the measured air mass flow at the location of the sensor and the actual air mass flow through the intake valve are not the same. This difference in air mass flow can be described with a dynamic air path model from Chapter 3. By combining such an air-path model

with one of the observation methods presented in Chapter 4, it is possible to observe the actual air mass flow through the intake valve.

5.1.1 Air-Path Model Type

To compensate for the differences between measured and the actual air mass flow through the intake valve, it is firstly necessary to model the dynamic behaviour of the air-path system. Several approaches were presented in Chapter 3, which allow modelling of the dynamic behaviour of the air-path system with different fidelity. Consequently, the first question is which model type is most suitable to establish the air-path observer.

A 1D crank angle resolve air-path model is theoretically capable of representing all major dynamic effects, which can cause a difference between measured and actual air mass flow into the cylinder. This includes the complex gas dynamics of the pipes as well as the much simpler filling and emptying dynamics of the plenums. However, the UIE-method as well as the JSPE-method require the measurement of each model state. Due to the discretisation of the pipes in the 1D approach, the final model has an incredibly high number of states. The number of pressure and temperature sensors that would be required is therefore uneconomical. In addition, most of the gas dynamic effects are extremely difficult to measure since they are extremely fast compared to the response time of pressure and temperature sensors. This suggests that the air-path model used in the observer should be established based on ‘lumped’ volumes as described in Subsection 3.3.3. However, neglecting the gas dynamics can lead to an error in the observed air mass flow. Consequently, the effect upon the accuracy of the observed air mass flow though the intake valve needs to be investigated. This investigation is carried out in Section 8.3.

The next question is whether the observation is crank angle resolved or on a cycle average basis. This obviously depends on the application of the observer. If the air mass flow through the intake valve needs to be known on a crank angle resolve basis, then a crank angle resolved model is required. An example for this could be the identification of the valve discharge coefficient. However, a crank angle resolved observer requires an in-cylinder pressure transducer, in addition to the sensors along the air-path. If a cycle average air mass flow into the cylinder is sufficient, a cycle average model should be used. Firstly, less instrumentation

is required for this approach since no in-cylinder pressure sensor is required. In addition, a crank angle resolved observer does not increase the accuracy of the cycle average air mass flow since the dynamic air-path behaviour in both cases is described with filling and emptying dynamics. Using a crank angle resolved observer for the observation of a cycle average air mass flow would unnecessarily complicate the solution.

The main task of this work is to characterise the volumetric efficiency of the engine. As described in Subsection 3.4.2, the volumetric efficiency is used to estimate a cycle average air mass flow into the cylinder based on intake manifold conditions. Consequently, a cycle average air mass flow into the cylinder is sufficient to characterise the engine's volumetric efficiency. Therefore, a cycle average air-path model using 'lumped volumes' is chosen for the air-path observer.

5.1.2 Air-Path Division

Subsection 5.1.1 shows that an air-path model where the pipes and the plenums along the air-path are lumped into major volumes is the most suitable model type for the air-path observer. Therefore, the intake system of a GTDI engine which is illustrated in Figure 3.3 has to be divided or lumped into a specific number of major volumes. Figure 3.5 shows how an air-path model is established based on volumes and restrictions. Each major volume has to be separated by a restriction. Consequently, the air-path was divided wherever a substantial pressure difference can occur. This leads to an air-path model which comprises three major volumes as illustrated by Figure 5.2.

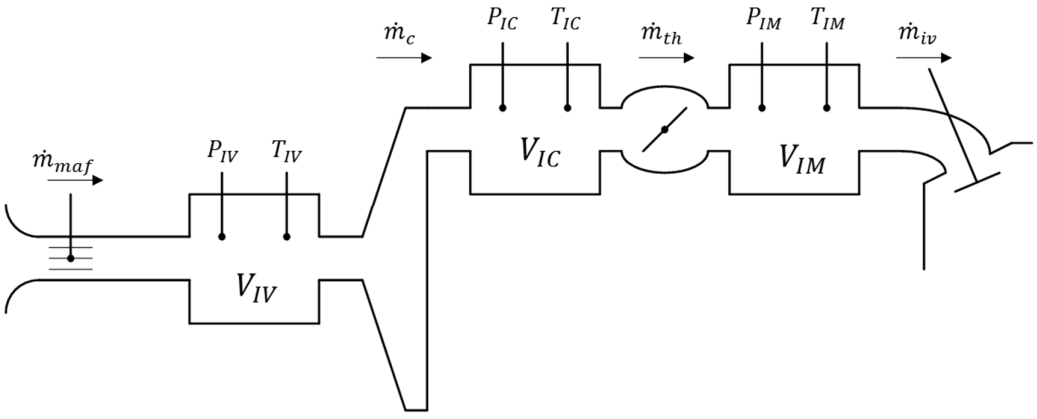

Figure 5.2: Air-path division into major volumes

Figure 5.2 shows the air-path model which is divided into the Intake Volume, V_{IV}, InterCooler V_{IC} and Intake Manifold V_{IM}. In the following sections, the air-path observer is established based on the model, which is illustrated in Figure 5.2. Consequently, the observer has to compensate for the filling and emptying dynamics of three big volumes in order to observe the actual air mass flow through the intake valve.

5.1.3 Observer State

The principal of an air-path observer is extremely similar to the abstract problem described in Section 4.1. Assume that for a specific volume, the air mass flow entering the volume as well as the pressure and temperature inside the volume are measurable, as illustrated in Figure 5.3.

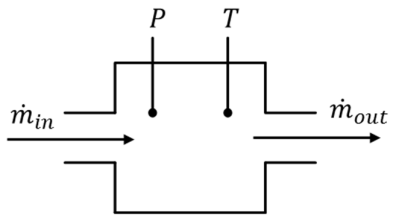

Figure 5.3: Measurement details for control volumes

By applying the UIE-method in form of direct model inversion to Equation 3.22, it is possible to estimate the volume outflow from Equation 5.1.

$$\dot{m}_{out} = \left[c_p \dot{m}_{in} T_{in} - \frac{dP}{dt}\frac{c_v V}{R} + \frac{dQ}{dt}\right]\frac{1}{c_p T} \qquad \textbf{5.1}$$

In this case, the volume outflow is basically the unknown input into the system which was represented by $z(t)$ in the simplified example. However, Equation 5.1 includes the heat transfer between the wall and the gas. Therefore, the estimated outflow depends on the accuracy of the heat transfer model. Unfortunately, heat transfer is very difficult to model since the heat transfer coefficient of Equation 3.24 depends on a high number of variables and parameters. For this reason, there is an ongoing dispute amongst researchers whether an isothermal or an adiabatic model should be used to represent the filling and emptying dynamics of the volumes along the air-path. Most researchers have used the simplified isothermal version of the model which is represented by Equation 3.27. By applying the UIE-method in the form of direct model inversion to Equation 3.27, it is possible to estimate the volume outflow from Equation 5.2.

$$\dot{m}_{out,ISO} = \dot{m}_{in} - \frac{V}{RT}\frac{dP}{dt} \quad \textbf{5.2}$$

However, due to the isothermal assumption an error is introduced. By substituting Equation 3.18 into 3.21 it can be shown that the error caused by the isothermal assumption is given by Equation 5.3.

$$e_{ISO} = -\frac{PV}{RT^2}\frac{dT}{dt} \quad \textbf{5.3}$$

During fast transients, such as throttle tip-in and tip-out, the isothermal assumption can cause an error in the outflow estimation of up to 15% [91]. This problem can be avoided by using the mass inside the volume as observation state rather than pressure. This means the observer can be based on the equation for mass balance. Rearranging Equation 3.18 permits an estimation of the volume outflow without any thermodynamic assumptions from

$$\dot{m}_{out} = \dot{m}_{in} - \frac{dm}{dt} \quad \textbf{5.4}$$

However, this solution requires measurement of the mass inside the volume which is not possible since no sensor is available. Therefore, the mass has to be estimated from the ideal gas law given by Equation 3.20. An accurate estimate of the mass inside the volume relies on accurate measurement of pressure and temperature [43]. Unfortunately, accurate measurement of a dynamic temperature is difficult due to the response delay of the thermocouple [43]. For this reason, it needs to be clarified whether the mass based observer is more accurate than the isothermal observer or if sensor response delays cause the mass based observer to be less accurate than the isothermal observer.

Substituting the equation for the response delay of the thermocouple from Equation 5.20 into Equations 5.2 and 5.4, it can be shown that the error in outflow estimation including the response delay of the thermocouple is given by Equation 5.5 for the isothermal observer

$$e_{ISO,M} = \frac{dP}{dt}\frac{V}{R}\left(\frac{1}{T} - \frac{1}{T_m}\right) - \frac{PV}{RT^2}\frac{dT}{dt} \quad \textbf{5.5}$$

and Equation 5.6 gives the error for the mass based observer.

$$e_{m,M} = \frac{dP}{dt}\frac{V}{R}\left(\frac{1}{T} - \frac{1}{T_m}\right) - \frac{PV}{R}\left(\frac{dT_m}{dt}\frac{1}{T_m^2} - \frac{dT}{dt}\frac{1}{T^2}\right) \quad \textbf{5.6}$$

Let the time constant τ of the thermocouple go to infinity. Then for $\tau \to \infty$ if follows that $\frac{dT_m}{dt} \to 0$ and consequently, $e_{m,M} = e_{ISO,M}$. This proves that using mass as the observer state can only increase the accuracy but not decrease. The larger the time constant of the thermocouple, the smaller the benefit of using the mass observer. Consequently, the time constant of the thermocouple should be as small as possible. An alternative to an ultra-fast responsive thermocouple is to make use of input reconstruction, which allows compensation for the response delay of the thermocouple as shown in Section 5.4.

5.2 Air-Path Observer for Offline Applications

The UIE based air-path observer presented in this section can be used for all applications where the measurement data are noise free. This may be the case if offline applications where an appropriate filter can be used. Applying the UIE method in form of direct model inversion to the intake volume, intercooler and the intake manifold leads to the following three observers:

- **Intake Volume**

$$\hat{\dot{m}}_c = \dot{m}_{maf} - \frac{dm_{IV}}{dt} \quad \textbf{5.7}$$

$$m_{IV} = \frac{P_{IV}V_{IV}}{RT_{IV}} \quad \textbf{5.8}$$

- **Intercooler**

$$\hat{\dot{m}}_{th} = \hat{\dot{m}}_c - \frac{dm_{IC}}{dt} \quad \textbf{5.9}$$

$$m_{IC} = \frac{P_{IC}V_{IC}}{RT_{IC}} \quad \textbf{5.10}$$

- **Intake Manifold**

$$\hat{\dot{m}}_{iv} = \hat{\dot{m}}_{th} - \frac{dm_{IM}}{dt} \quad \textbf{5.11}$$

$$m_{IM} = \frac{P_{IM}V_{IM}}{RT_{IM}} \quad \textbf{5.12}$$

The derivative of the mass in each volume is approximated with the Euler backwards method described by Equation 4.6. Combining the three observers above allows observation of the actual air mass flow through the intake valve $\hat{\dot{m}}_{iv}$ on a cycle average basis. The observers require the measured air mass flow $\dot{m}_{maf}$ at the location of the MAF sensor as well as measured pressure and temperature inside the intake volume, intercooler, and the intake manifold.

The volumetric efficiency is finally estimated from the observed air mass flow through the intake valve as shown by Equation 5.13.

$$\hat{\eta}_v = \frac{\hat{\dot{m}}_{iv} 120 R T_{IM}}{P_{IM} V_d N_e} \tag{5.13}$$

5.3 Air-Path Observer for Online Applications

The JSPE based air-path observer presented in this section can be used for all applications where the measurement data are corrupted with noise. This solution is particularly suitable for online applications. Applying the JSPE method in form of the AEKF to the intake volume, intercooler and the intake manifold leads to the following three observers:

- **Intake Volume**: The outflow of the intake volume is the compressor mass flow $\dot{m}_c$. As shown in Subsection 3.2.1, accurate modelling of the compressor requires a regression model based on the compressor map, which is provided from the manufacturer. However, due to the characteristic of the map it might be impossible to express the mass flow directly as a function of the pressure ratio and turbine speed. Therefore, it was decided to treat the entire outflow of the intake volume as the adaptive parameter which leads to the following observer.

$$\hat{X}_{IV}(k) \begin{bmatrix} \hat{m}_{IV}(k) \\ \hat{\dot{m}}_c(k) \end{bmatrix} = \begin{bmatrix} \hat{m}_{IV}(k-1) + T_k\left[\dot{m}_{maf}(k-1) - \hat{\dot{m}}_c(k-1)\right] \\ \hat{\dot{m}}_c(k-1) \end{bmatrix} \tag{5.14}$$

$$g(k) = \frac{\hat{m}_{IV} R T_{IV}(k)}{V_{IV}} \tag{5.15}$$

- **Intercooler**: The outflow of the intercooler is the throttle air mass flow. The air mass flow across the throttle plate can be modelled using the compressible flow equation from Equation 3.3. As described in Section 3.1, the equation requires an accurate model of the physical open area

and the discharge coefficient. These two parameters can be combined into one parameter $A_{e,th}$ which now represents the effective throttle open area. This parameter can be used as the adaptive parameter in the AEKF. This leads to the following observer for the intercooler volume.

$$\hat{X}_{IC}(k)\begin{bmatrix}\hat{m}_{IC}(k)\\ \hat{A}_{e,th}(k)\end{bmatrix} = \begin{bmatrix}\hat{m}_{IC}(k-1)+T_k\left[\dot{\hat{m}}_c(k-1)-\hat{A}_{e,th}(k-1)\dfrac{P_{IC}(k)}{\sqrt{RT_{IC}(k)}}\phi\left(\dfrac{P_{IM}(k)}{P_{IC}(k)}\right)\right]\\ \hat{A}_{e,th}(k-1)\end{bmatrix} \quad \textbf{5.16}$$

$$g(k)=\frac{\hat{m}_{IC}RT_{IC}(k)}{V_{IC}} \quad \textbf{5.17}$$

- **Intake Manifold**: The outflow of the intake manifold is the air mass flow through the intake valve. Since it was decided to use a cycle average based air-path model, the air mass flow through the intake valve is given by Equation 3.43. The adaptive parameter for the AEKF is the volumetric efficiency. The observer for the intake manifold is given by Equations 5.18 and 5.19.

$$\hat{X}_{IM}(k)\begin{bmatrix}\hat{m}_{IM}(k)\\ \hat{\eta}_v(k)\end{bmatrix} = \begin{bmatrix}\hat{m}_{IM}(k)+T_k\left[\dot{\hat{m}}_{th}(k-1)-\hat{\eta}_v(k-1)\dfrac{\hat{m}_{IM}(k-1)V_dN_e}{120V_{IM}}\right]\\ \hat{\eta}_v(k-1)\end{bmatrix} \quad \textbf{5.18}$$

$$g(k)=\frac{\hat{m}_{IM}RT_{IM}(k)}{V_{IM}} \quad \textbf{5.19}$$

5.4 Input Reconstruction

As mentioned is Subsection 2.2.3, input reconstruction can be used to compensate for the sensor response delay. Subsection 5.1.3 clarified the importance of fast and accurate temperature measurement. Since any response delay of the thermocouple has a direct impact on the accuracy of the observed outflow, it is essential to provide a temperature measurement signal which is as accurate as possible. Input reconstruction for the measurement signal is almost

identical to the principle of the air-path observer. A dynamic model is used which describes the dynamic response of the measured temperature T_m to a change in the real gas temperature, T_g. Either the UIE method or the JSPE method can be applied to this model in order to estimate / reconstruct the real gas temperature.

As shown by Schaal *et al* [53] the response delay of a thermocouple can be represented by the following first order differential equation.

$$\frac{dT_m}{dt} = \frac{1}{\tau}\left(T_g - T_m\right) \qquad \textbf{5.20}$$

where τ is the time constant of the thermocouple. In fact, the time constant is not a simple constant as demonstrated by Forney and Farlick [55], but depends on geometrical details of the thermocouple as well as on the flow conditions. The two most dominant factors for the time constant of a thermocouple with a specific geometry are the velocity of the gas and the density of the gas at the location of the sensor. As suggested by [55] and [44] the time constant of the sensor can be modelled as a function of air mass flow. Consequently, the time constant of the sensor has to be identified as a function of air mass flow. The reader is referred to Schaal *et al* [53] for a detailed description of the time constant identification process which requires two thermocouple with different diameters. The following two subsections present two solutions for input reconstruction. As for the air-path observer, the UIE method can be used for noise-free data due to its simplicity and the JSPE method in form of the AEKF should be used for applications where the measurement signal is corrupted with noise.

5.4.1 Offline Applications

The unknown input estimation based input reconstruction is achieved by simply inverting the dynamic model of the thermocouple ash shown in Equation 5.21 [44].

$$\hat{T}_g = T_m + \frac{dT_m}{dt}\tau \qquad \textbf{5.21}$$

The derivative of the measured temperature $\frac{dT_m}{dt}$ is approximated using the Euler backwards method given by Equation 4.6.

5.4.2 Online Applications

Equation 5.20 can be discretised using the zero-order hold method [44]. This leads to

$$T_m(k) = a(\dot{m})T_m(k-1) + b(\dot{m})T_g(k-1) \tag{5.22}$$

with the parameters a and b given by

$$a(\dot{m}) = e^{-\frac{T_S}{\tau(\dot{m})}} \quad \text{and} \quad b(\dot{m}) = 1 - a \tag{5.23}$$

Applying the AEKF to Equation 5.22, where the true gas temperate $\hat{T}_g$ is the adaptive parameter lead to Equation 5.24 [44].

$$\hat{X}_{IV}(k)\begin{bmatrix}\hat{T}_m(k)\\ \hat{T}_g(k)\end{bmatrix} = \begin{bmatrix}a(\dot{m})T_m(k-1) + b(\dot{m})T_g(k-1)\\ \hat{T}_g(k-1)\end{bmatrix} \tag{5.24}$$

In case the JSPE based reconstruction is combined with the JSPE based air-path observer, it is possible to combine the states and adaptive parameters in one vector.

5.5 Summary

Section 5.1 shows that a cycle average air-path model based on lumped volumes is sufficient to establish the air-path model. This allows compensation of filling and emptying dynamics along the air-path. The air-path is divided into three major volumes (intake volume, intercooler and intake manifold) which are separated from each other by the compressor and the throttle plate. Using mass as the observed state allows estimation of the outflow of a volume without making any major thermodynamic assumptions, which increases the accuracy if fast temperature measurement is available. The UIE based observer is preferred for applications to noise-free data due to its simplicity. The JSPE based observer, which is much more complex, should be used for applications where the measurement data are corrupted with noise. In the case that no fast responsive temperature sensor is available, input reconstruction can be used to compensate for the response delay of the thermocouple. The process of input reconstruction is very similar to the air path observation. The real gas temperature can be reconstructed by applying the UIE or the JSPE method to a dynamic model of the thermocouple.

Chapter 6 Implementation

This chapter focuses on the practical implementation of the air-path observer in an engine testbed environment. In Section 6.1, the nature of the relationship between volumetric efficiency and various state and static variables is defined. This is followed in Section 6.2 by an overview of the data collection process, whereas Section 6.3 describes how the observer is tuned for a specific engine. Section 6.4 provides details of the test identification signals, which involves ramping manifold pressure over its full operating range from low to high and *vice versa*. Section 6.5 provides details of two approaches to practically implement the desired intake manifold pressure trajectory required by test methodology. The first approach is a simple open loop method, but this possesses several disadvantages. To mitigate these, a closed loop trajectory tracking method is proposed. The necessary data pre-processing tasks are defined in Section 6.6, and finally in Section 6.7 a so-called *dual ramp averaging* technique is discussed. This process accounts for the observed hysteresis in the up and down ramps.

6.1 Characterisation Details

As shown in Subsection 3.4.2, engine speed, intake manifold pressure (P_{IM}), exhaust manifold pressure (P_{EM}), intake opening (IVO) and exhaust valve closing (EVC) event timing, intake manifold temperature (T_{IM}), and exhaust gas temperature (T_{EM}) influence the volumetric efficiency of the engine. To simplify matters, in this work η_v is characterised as: $\eta_v(N, P_{IM}, IVO, EVC)$. To account for the influence of the remaining parameters, suitable correction factors and compensators are subsequently applied. The form of these is discussed in the following:

- **Intake manifold temperature**: As shown by Heywood [59], the change of volumetric efficiency to a change in intake manifold temperature and engine coolant temperature can be approximated with a square root function. Consequently, the characterisation can be performed with constant reference temperatures $T_{IM,ref}$. A correction factor is then used to account for any changes in volumetric efficiency due to a change in T_{man} as shown by Equation 6.1 [59].

$$C_{\eta v} = \frac{\eta_{v,ref}}{\eta_v} = \left(\frac{T_{IM,ref}}{T_{IM}}\right)^{\frac{1}{2}} \quad \textbf{6.1}$$

- **Exhaust manifold pressure**: Variation of the volumetric efficiency due to changes in exhaust manifold pressure can be handled using compensation. The compensator takes the form of an empirically derived model describing how exhaust manifold (P_{EM}) and exhaust back pressure (P_{BP}) influence η_v. The exact formulation was taken from the current Ford ECU air charge strategy feature and as such the details must remain proprietary; however the compensator takes the form $f_c(P_{EM}, P_{BP}) \times \eta_v$. Throughout, $f_c(P_{EM}, P_{BP})$ is considered to be known *a priori*.
- **Exhaust Manifold Gas Temperature**: Exhaust gas temperature mainly depends on air mass flow and spark retard from MBT, IVO, EVC and AFR. Since modern control strategies aim to operate with MBT and $\lambda \approx 1$, it is sufficient to characterise the volumetric efficiency with spark advance at MBT and $\lambda = 1$. Therefore, exhaust gas temperature can be neglected as an independent input for the volumetric efficiency.

The process described in the following can be used to characterise the volumetric efficiency as a function of intake manifold pressure, engine speed, IVO and EVC using any of the air-path observers presented in Chapter 5.

6.2 Process Overview

An overview of the air charge characterisation process is presented in Figure 6.1.

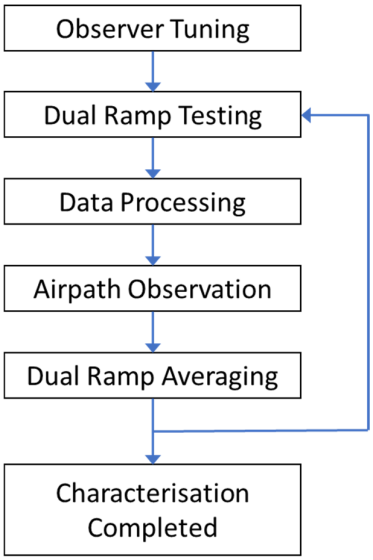

Figure 6.1: Process overview – Rapid observer based engine air charge characterisation

The first step in the procedure is observer tuning. The observer requires tuning for each new engine application. Once tuning is complete, the engine is tested using the dual ramp testing procedure. Upon test completion, the recorded test data is filtered to eliminate the majority of the measurement noise. The air-path observer is then applied to the filtered data to compensate for the filling and emptying dynamics along the air-path, resulting in a prediction of the actual air mass flow through the intake valve. Finally, the Dual Ramp Average method (DRA) is employed to average the identified volumetric efficiency over the up-ramp and the down-ramp, thus mitigating hysteresis effects. It should be noted that the identification process is an offline process.

6.3 Observer Tuning

Before the developed air-path observer is applied to a specific engine, the parameters of the observer have to be tuned. Subsection 6.3.1 is focused on tuning the observer gains and Subsection 6.3.2 if focused on tuning the volume sizes of the observer.

6.3.1 Observer Gains

If a JSPE-based observer is used, it is necessary to tune the process covariance matrix of the observer, since it affects the computation of the Kalman gains. As shown by Equation 4.19, the process covariance matrix contains the process

covariance of the system σ_x^2 and the process covariance of the adaptive parameter σ_ϑ^2. The significance of process covariance is that it describes the accuracy of the model used to observe the system state. Given the mass based observer presented in Subsection 5.1.3 is a very accurate representation of the filling and emptying dynamics of a volume, this suggest the process noise covariance can be neglected; *i.e.* assume $\sigma_x^2 \approx 0$.

The covariance σ_ϑ^2 controls the convergence rate of the adaptive parameter. A large σ_ϑ^2 facilitates fast adaption of $\hat{\vartheta}$, and $\hat{\vartheta}$ converges to the actual value ϑ rapidly. However, as σ_ϑ^2 increases, the greater the influence of the measurement noise on the measurement state and therefore the greater the variation in the adaptive parameter. Therefore, the selection of σ_ϑ^2 is always a trade-off between response time and noise amplification.

Unfortunately, the selected value of σ_ϑ^2 does not directly represent the true value of the covariance of the identified parameter $\hat{\vartheta}$. It is only a measure of how fast the parameter can adapt. Consequently, most authors select a value for σ_ϑ^2 which results in an acceptable compromise between fast response and noise amplification as shown in, among others, [44]. This trial and error method is obviously time consuming and may not lead to the best results.

To simplify the tuning process, an automatic tuning algorithm is proposed. This allows σ_ϑ^2 to be selected automatically from any available steady-state data. The principle is to select a desired covariance $\sigma_{\vartheta,des}^2$ for the adaptive parameter $\hat{\vartheta}$, and to employ an optimisation algorithm to tune σ_ϑ^2 in order to ensure that the real covariance of $\hat{\vartheta}$, denoted by $\sigma_{\vartheta,m}^2$, is identical to the desired covariance $\sigma_{\vartheta,des}^2$. The algorithm is summarised in Figure 6.2.

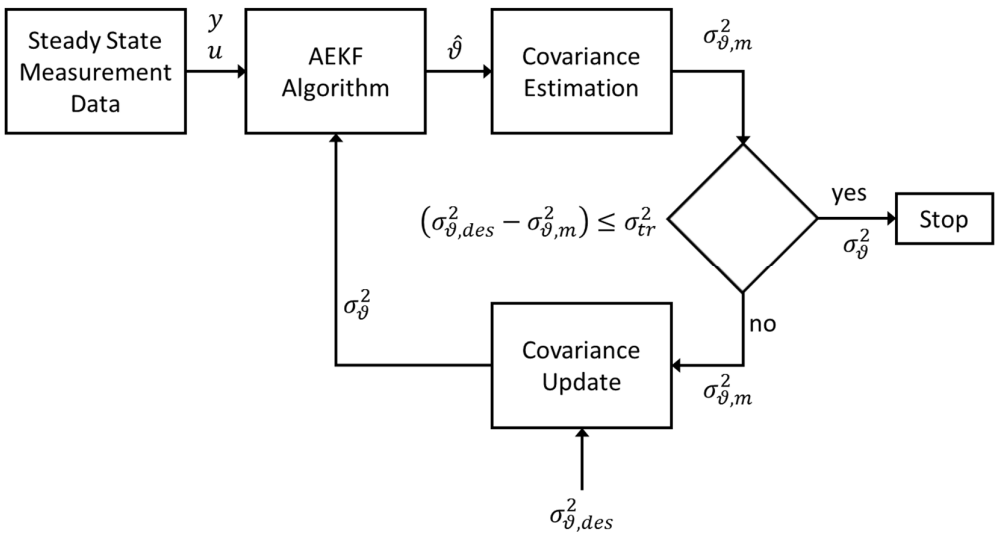

Figure 6.2: AEKF covariance tuning algorithm

A set of steady-state measurement data with N samples is used to feed the AEKF algorithm in order to identify the adaptive parameter. Steady-state data guarantee that the adaptive parameter is constant throughout the dataset. The true covariance of the adaptive parameter $\sigma^2_{\vartheta,m}$ is then estimated from the identified parameter $\hat{\vartheta}$ using Equation 6.2.

$$\sigma^2_{\vartheta,m} = \frac{1}{N}\sum_{i=1}^{N}\left(\hat{\vartheta}_i - \frac{1}{N}\sum_{i=1}^{n}\hat{\vartheta}_i\right)^2 \qquad \textbf{6.2}$$

The covariance σ^2_{ϑ} is dynamically updated using Equation 6.3.

$$\sigma^2_{\vartheta}(k) = \sigma^2_{\vartheta}(k-1) + k_{cov}\left(\sigma^2_{\vartheta,des} - \sigma^2_{\vartheta,m}\right) \qquad \textbf{6.3}$$

Equation 6.3 aims to drive the error between the desired and true covariance to zero. Convergence is signalled when $\left|\sigma^2_{\vartheta}(k) - \sigma^2_{\vartheta}(k-1)\right| \leq \sigma^2_{tr}$. The convergence threshold is specified by the user. This approach eliminates the necessity for trial and error. However, it should be noted that the true covariance of the parameter $\sigma^2_{\vartheta,m}$ will vary once the AEKF is applied to measurement data. It should be noted that any observed variation in $\sigma^2_{\vartheta,m}$ also depends on the model form used in the corresponding state equation.

6.3.2 Intake System Volumes

As mentioned in Subsection 5.1.3, the accuracy of the observed volume outflow depends on the accuracy of the model used to describe the filling and emptying dynamics inside the volume. It is therefore crucial to know the exact volume size of each volume. In this thesis, the volumes were derived using a CAD model of the intake system.

By definition, being a lumped-capacity model, the observer model assumes no spatial-variation in the state parameters [16]. This implies all thermodynamic states are homogenous throughout a specific volume. In reality, spatial variation exists. For example, standing waves may be present in the volume under specific operating conditions, implying that pressure varies with distance as well as with time. Consequently, the observer predictions generated using the physical volume values may not provide the best quality estimate because the zero-dimensional model does not account for spatial variation in the relevant state variable.

To alleviate this concern, it is proposed to perturb the physical volumes and compare predictions from the perturbed condition to the reference state. To gain some insight into the magnitude of possible improvements, due to tuning the intake volumes, a simulation study has been conducted for a single fast transient, where the observer intercooler and intake manifold volumes have been perturbed $\pm$100% from their physical values. A root mean square air mass flow into the error has been computed for each pair of perturbations and is expressed as a percentage difference from the value obtained using the physical volumes.

The procedure is as follows: Firstly, the engine is tested at several different steady-state points, each with constant intake manifold pressure, engine speed and camshaft timing. These data permit a reference steady state volumetric efficiency model, $\eta_v(P_{IM})$, to be estimated. Given the steady state model, the engine is subsequently exposed to a fast intake manifold pressure ramp, again at fixed engine speed and camshaft timing. The observer is then used to estimate the corresponding volumetric efficiency from the dynamic data. This process is repeated many times over a grid of perturbed intercooler and the intake manifold volumes. In actuality, specific volume pairs are taken from a regular grid formed of perturbed values of up to $\pm$100% of the physical value, in 10% intervals. For each volume pair, the relative RMSE between the observed volumetric efficiency

and the steady-state volumetric efficiency is calculate. The results are summarised in Figure 6.3.

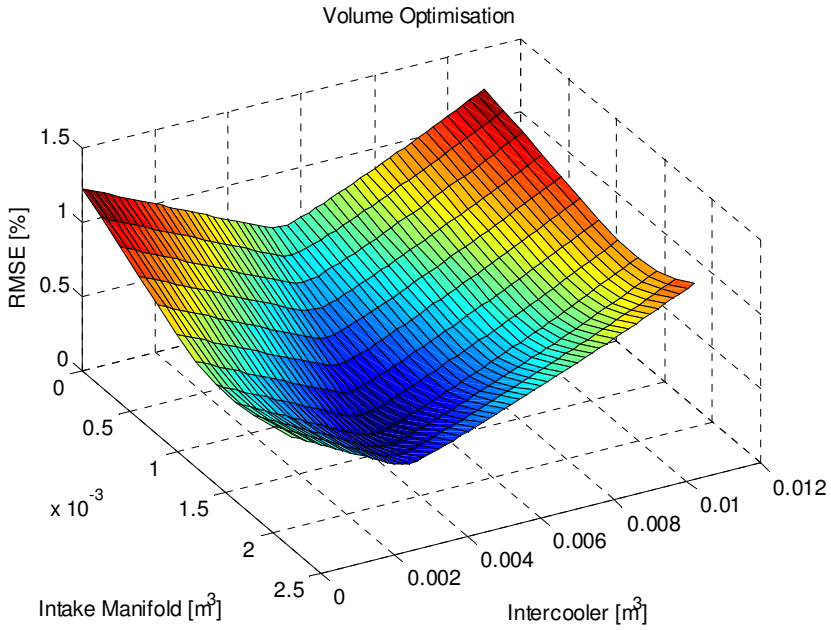

Figure 6.3: Intake volume tuning

Influence of intercooler and intake manifold volume perturbation on percentage root mean square error. Data corresponds to a dual-ramp MAP sweep with 10 seconds ramp time

Using Figure 6.3, it is easy to determine the optimal $(V_{IC}, V_{IM}) = (0.005, 0.00175)$. This compares to the physical values, which are $(V_{IC}, V_{IM}) = (0.006, 0.00125)$. Despite the relatively large difference in the optimal value, the relative RMSE is improved by approximately 0.1%. This modest improvement strongly suggests that tuning the intake volumes away from their physical values is of little practical benefit.

6.4 Test Definition

As mentioned in Section 6.1, the goal is to characterise the volumetric efficiency as $\eta_v(N, P_{IM}, IVO, EVC)$. To identify the model, dual-ramp MAP sweeps were conducted, each at constant engine speed and camshaft timing. The details of the test procedure are given in the following subsections.

6.4.1 Dual-Ramp MAP Sweep

The following graph defines the relevant test parameters for a dual-ramp MAP sweep at constant engine speed and constant camshaft timing.

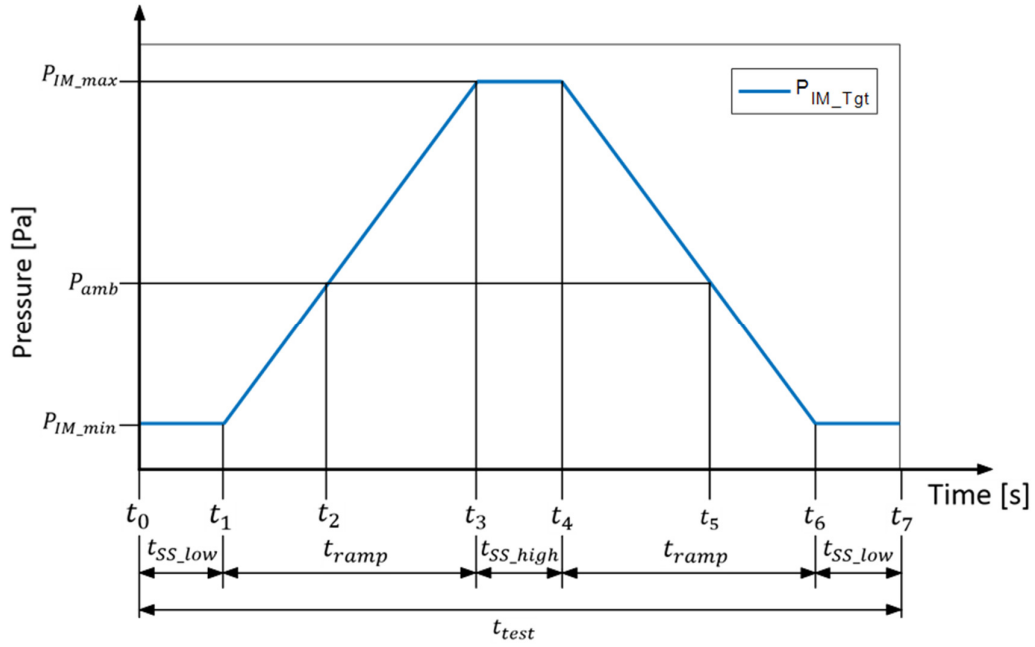

Figure 6.4: Dual-ramp MAP sweep definition

Figure 6.4 shows the target intake manifold pressure P_{IM_Tgt} during the engine test. The engine test specific parameters are defined as follows:

- P_{IM_Tgt}: target intake manifold pressure for dual-ramp MAP sweep
- P_{IM_min}: minimum intake manifold pressure
- P_{IM_max}: maximum intake manifold pressure (engine limit)
- t_{SS_low}: time to stabilize the engine at P_{IM_min}
- t_{ramp}: time to ramp intake manifold pressure up from P_{IM_min} to P_{IM_max} and down from P_{IM_max} to P_{IM_min}
- t_{SS_high}: time to stabilize at P_{IM_max}
- t_{test}: total test time
- Time brake points
    - t_0: start of engine test
    - t_1: start of up-ramp
    - t_2: 1 bar intake manifold pressure (transition from throttled area into boosted operating area)
    - t_3: end of up-ramp

- t_4: start of down-ramp
- t_5: 1 bar intake manifold pressure (transition from boosted area into throttled operating area)
- t_6: end of down-ramp
- t_7: end of test

Letting P_{IM_Tgt} denote the desired instantaneous target P_{IM} value, then

$$P_{IM\_Tgt}(t) = \begin{cases} P_{IM\_min} & for \quad [t_0, t_1] \\ \beta_{P\_IM\_1} t - \beta_{P\_IM\_1} t_1 + P_{IM\_min} & for \quad [t_1, t_3] \\ P_{IM\_max} & for \quad [t_3, t_4] \\ \beta_{P\_IM\_2} - \beta_{\_IM\_2} t_4 + P_{IM\_max} & for \quad [t_4, t_6] \\ P_{IM\_min} & for \quad [t_6, t_7] \end{cases} \tag{6.4}$$

where $\beta_{\_IM\_1}$ is the slope of the up-ramp and $\beta_{P\_IM\_2}$ is the slope of the down ramp. The parameters are calculated from Equations 6.5 and 6.6 respectively.

$$\beta_{P\_IM\_1} = \left(\frac{P_{IM\_max} - P_{IM\_min}}{t_3 - t_1}\right) \tag{6.5}$$

$$\beta_{P\_IM\_2} = \left(\frac{P_{IM\_min} - P_{IM\_max}}{t_6 - t_4}\right) \tag{6.6}$$

6.4.2 Target MAP Signal Smoothing

To avoid undesirable discontinuities in the P_{IM_Tgt} trajectory, the specified path is smoothed by applying a moving average low-pass filter to the specified P_{IM_Tgt} path from Figure 6.4 of the form

$$y_s(k) = \frac{1}{2N+1}[y(k+N) + y(k+N-1) + \cdots + y(k-N)] \tag{6.7}$$

Equation 6.7 is a standard filter in MATLAB where $y_s(k)$ is the smoothed value of $y(k)$, N is the number of neighbouring data points on each side of $y_s(k)$. Therefore, $2N+1$ is the number of data points in the smoothing window, t_{smooth}. For further details of the filter the reader is referred to [153].

A smoothing factor F_{smooth} is defined which is used to set the smoothing time window t_{smooth} for a specific ramp time t_{ramp} as defined by Equation 6.8.

$$t_{smooth} = t_{ramp}\frac{1}{2}F_{smooth} \quad \textbf{6.8}$$

Using the sampling interval, T_s, N can be calculated from Equation 6.9.

$$N = \frac{\frac{t_{smooth}}{T_s} - 1}{2} \quad \textbf{6.9}$$

The smoothing factor has a range from 0 to 1, where 0 means no smoothing at all and 1 represents maximum smoothing in which case the up-ramp and the down-ramp have no linear part.

Applying Equation 6.7 directly to the target MAP signal P_{IM_Tgt} would lead to the problem that the ramp signal would actually start before t_1 and finish after t_3 due to the smoothing window. Therefore, the time breakpoints, t_1, t_3, t_4 and t_6 have to be modified depending on the size of the smoothing time window t_{smooth}. The time breakpoints, t_1, t_3, t_4 and t_6 are modified using t_{smooth} as shown by Equations 6.10, 6.11, 6.12 and 6.13 respectively.

$$t_{1s} = t_1 + \frac{1}{2}t_{smooth} \quad \textbf{6.10}$$

$$t_{3s} = t_3 - \frac{1}{2}t_{smooth} \quad \textbf{6.11}$$

$$t_{4s} = t_4 + \frac{1}{2}t_{smooth} \quad \textbf{6.12}$$

$$t_{6s} = t_6 - \frac{1}{2}t_{smooth} \quad \textbf{6.13}$$

The signal $P_{IM\_Tgt\_s\_in}$, which is passed thorough the moving average filter to produce the smoothened target MAP signal $P_{IM\_Tgt\_s}$ is then calculated from Equation 6.14.

$$P_{IM\_Tgt\_s\_in}(t) = \begin{cases} P_{IM\_min} & for \quad [t_0, t_{1s}] \\ \beta_{P\_IM\_1s}t - \beta_{P\_IM\_1s}t_{1s} + P_{IM\_min} & for \quad [t_{1s}, t_{3s}] \\ P_{IM\_max} & for \quad [t_{3s}, t_{4s}] \\ \beta_{P\_IM\_2s} - \beta_{P\_IM\_2s}t_{4s} + P_{IM\_max} & for \quad [t_{4s}, t_{6s}] \\ P_{IM\_min} & for \quad [t_{6s}, t_7] \end{cases} \quad \textbf{6.14}$$

where β_{1s} is the slope of the up-ramp and β_{2s} is the slope of the down ramp before smoothing $P_{IM\_Tgt\_s}$ with the moving average filter. The parameters $\beta_{P\_IM\_1s}$ and $\beta_{P\_IM\_2s}$ are calculated from Equations 6.15 and 6.16 respectively.

$$\beta_{P\_IM\_1s} = \left(\frac{P_{IM\_max} - P_{IM\_min}}{t_{3s} - t_{1s}}\right) \quad \textbf{6.15}$$

$$\beta_{P\_IM\_2s} = \left(\frac{P_{IM\_min} - P_{IM\_max}}{t_{6s} - t_{4s}}\right) \quad \textbf{6.16}$$

Figure 6.5 compares a linear target MAP signal with different smoothing factors to show how the smoothing factor affects the target MAP signal.

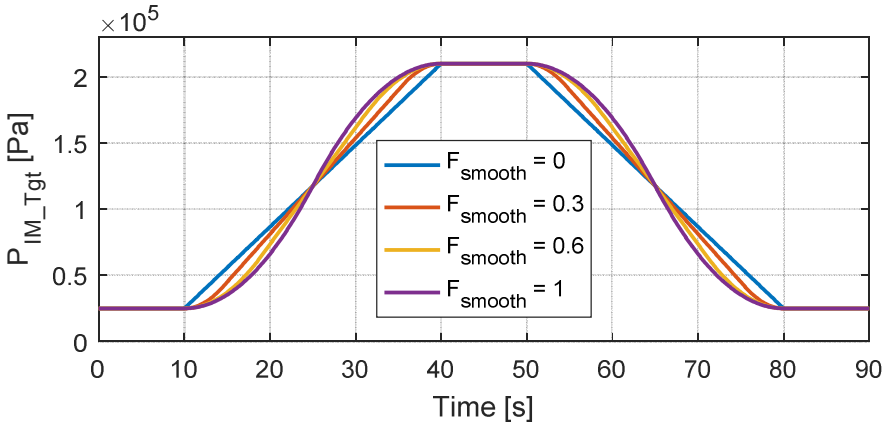

Figure 6.5: Target MAP signal smoothing

Figure 6.5 shows P_{IM_Tgt} for 4 different smoothing factors, F_{smooth}. Note that using the modified time brake points, t_{1s}, t_{3s}, t_{4s} and t_{6s} finally lead to a smoothened target MAP signal in which the up-ramp and the down-ramp start and finish exactly where the ramps of the linear signal start and finish.

6.4.3 Engine Test Summary

For a complete engine air charge characterisation dependent on intake manifold pressure, engine speed and camshaft timing, a dual-ramp MAP sweep is required for each engine speed at each camshaft position. How many engine speeds are used at each camshaft position depends on how sensitive the engine air charge characteristic is to engine speed. Approximately 20 engine speeds are required for each camshaft position. The number of camshaft positions (intake and exhaust) also depends on how sensitive the engine air charge characteristic is to camshaft timing. Common values are approximately 15 to 20 fixed IVO – EVC combinations. However, these numbers vary from engine to engine and each

manufacturer has to decide how many engine speed and camshaft combinations are required to produce a sufficient engine air charge model for the control strategy used. Control strategies which have a MAF sensor probably require a smaller number of MAP sweeps since the MAF sensor can be used to determine the cylinder air charge. In this case the air charge model is only required for the feed-forward torque control. Control strategies which only use a MAP sensor require a highly accurate characterisation over the entire engine speed and camshaft position range since the air charge estimation in this case is solely based on intake manifold conditions.

6.5 Engine Control

In order to achieve the desired target MAP during the dual-ramp MAP sweep, an air-path controller is required, which controls the throttle position and the waste gate accordingly. As mentioned in the introduction, there are three popular control strategies to control the intake manifold pressure in turbocharged gasoline engines. In literature, those are known as optimal fuel economy, optimal response and the boost buffer strategy as described by Eriksson *et al* [18], Gorzelic *et al* [19] and Beckman *et al* [20]. The main difference between these control strategies is how much delta pressure across the throttle is used. An optimal fuel economy strategy runs with wide open throttle in the boosted region to avoid any penalties in fuel economy. The optimal response strategy always controls the boost pressure to its maximum value and the throttle is used to control the intake manifold pressure. The boost-buffer strategy uses a desired delta pressure across the throttle to find a good compromise between fuel economy and drivability. However, the propagation of the pressure waves depends on the throttle position. Therefore, the delta pressure across the throttle affects volumetric efficiency. In other words, the volumetric efficiency at *e.g.* 1.2 bar intake manifold pressure and 1.2 bar intercooler outlet pressure is not identical to the volumetric efficiency at 1.2 bar intake manifold pressure and 1.4 bar intercooler outlet pressure.

To ensure that the characterised volumetric efficiency captures the tuning effects of the intake system, it is important to use the same control strategy during the characterisation as the one implemented on the ECU. The following subsections present a simple open-loop and a more advanced closed-loop controller. The open-loop controller can be used to characterise control strategies, which do not

use any boost-buffer (optimal fuel economy strategy). For strategies, which use a specific or even engine operating dependent boost-buffer, the closed loop controller must be used. Both controllers are evaluated later in Section 7.3.

6.5.1 Open-Loop Air-Path Controller

The simplest way to ramp the intake manifold pressure up and down at constant engine speed is to use an open loop feed forward controller. Throttle position and waste gate are controlled as a linear function of target intake manifold pressure, P_{IM_Tgt}.

$$\alpha_{th}(t) = \begin{cases} \beta_{th}P_{IM\_Tgt} - \beta_{th}P_{IM\_min} + \alpha_{th\_min} & for \quad P_{IM\_Tgt} < P_{amb} \\ \alpha_{th\_max} & for \quad P_{IM\_Tgt} > P_{amb} \end{cases} \quad \textbf{6.17}$$

where β_{th_1} is the slope of the up-ramp and β_{th_2} is the slope of the down ramp. β_{th_1} and β_{th_2} are calculated from Equations 6.5 and 6.6 respectively.

$$\beta_{th} = \left(\frac{\alpha_{th\_max} - \alpha_{th\_min}}{P_{amb} - P_{IM\_min}}\right) \quad \textbf{6.18}$$

and the waste gate open area

$$A_{wg}(t) = \begin{cases} A_{WG\_max} & for \quad P_{IM\_Tgt} < P_{amb} \\ \beta_{wg}P_{IM\_Tgt} - \beta_{wg}P_{amb} + A_{WG\_max} & for \quad P_{IM\_Tgt} > P_{amb} \end{cases} \quad \textbf{6.19}$$

where β_{wg_1} is the slope of the up-ramp and β_{wg_2} is the slope of the down ramp. β_{wg_1} and β_{wg_2} are calculated from Equations 6.5 and 6.6 respectively.

$$\beta_{wg\_1} = \left(\frac{A_{wg\_min} - A_{wg\_max}}{P_{IM\_max} - P_{amb}}\right) \quad \textbf{6.20}$$

Figure 6.6 shows the resulting throttle and waste gate actuator input signals.

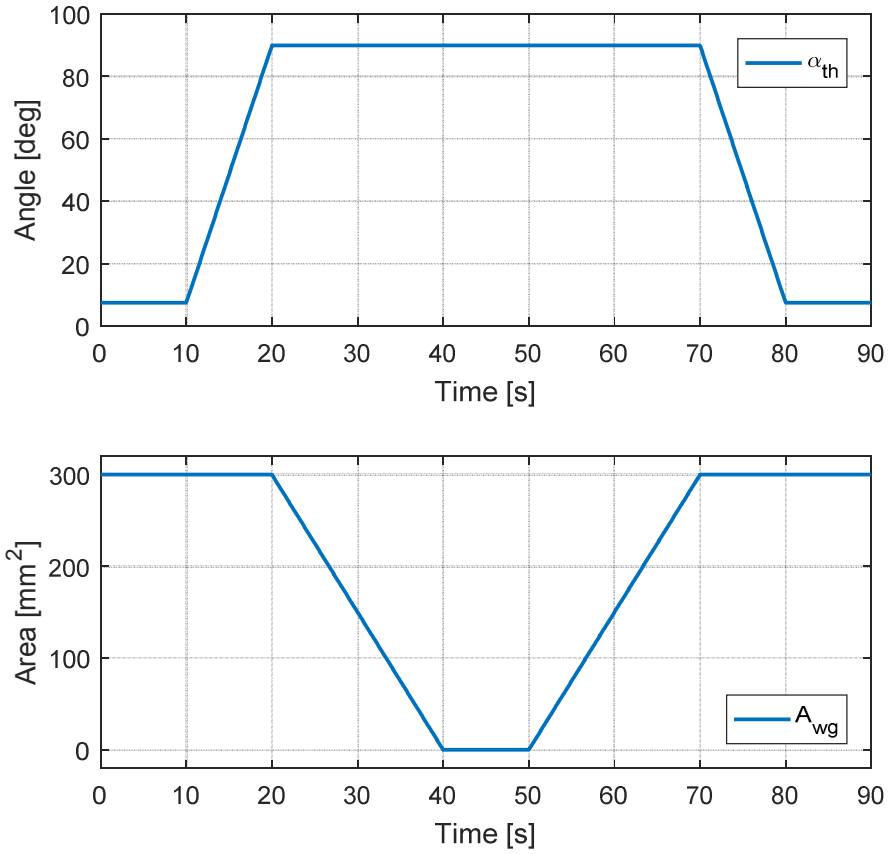

Figure 6.6: Open-loop controller: Throttle and waste gate input signals

The advantage of this controller is its simple implementation. This solution does not require any tuning of PID controllers. However, this solution has two major disadvantages:

1. **Throttle delta pressure**: Since no PID controllers are involved for throttle and waste gate position, it is not possible to characterise the volumetric efficiency with a specific delta pressure across the throttle. Therefore, the solution is only suitable for optimum fuel economy strategies.
2. **Linearity of intake manifold pressure response**: Intake manifold pressure responds very nonlinearly to changes in throttle and waste gate position. As a consequence, the resulting intake manifold pressure will not be linear during the up-ramp and the down-ramp.

6.5.2 Closed-Loop Air-Path Controller

A more advanced solution to achieve a desired target MAP during the engine test is to use a closed loop controller for throttle and waste gate position. This allows ramping the intake manifold pressure with a desired target MAP and allows

performing the air charge characterisation with a desired delta pressure across the throttle by controlling boost pressure and intake manifold pressure. In case some experimental data are already available from previous engine tests, the PID controllers can be combined with a feed-forward model for throttle and waste gate positions which allows more accurate control during fast ramps with significantly lower gains in the PID controllers.

The target MAP signal is controlled by the throttle and a target boost signal is defined which is then controlled by the waste gate. Equation 6.21 defines the target boost signal or target intercooler outlet pressure.

$$P_{IC\_Tgt} = P_{IM\_Tgt} + TP_{DP} \tag{6.21}$$

where TP_{DP} is the desired delta pressure across the throttle plate. However, Equation 6.21 only applies to the engine operating areas where $(P_{IM\_Tgt} + TP_{DP}) > 1bar$ since the compressor outlet pressure is always greater than or equal to ambient pressure. Therefore, the target boost signal is generated by Equation 6.22.

$$P_{IC\_Tgt}(t) = \begin{cases} 1\,[bar] & for \quad (P_{IM\_Tgt} + TP_{DP}) < 1bar \\ P_{IM\_Tgt} + TP_{DP} & for \quad (P_{IM\_Tgt} + TP_{DP}) > 1bar \end{cases} \tag{6.22}$$

Figure 6.7 illustrates $P_{IM\_Tgt}(t)$ and $P_{IC\_Tgt}(t)$ for a TP_{DP} of 0.1 bar and a ramp time of 30 seconds.

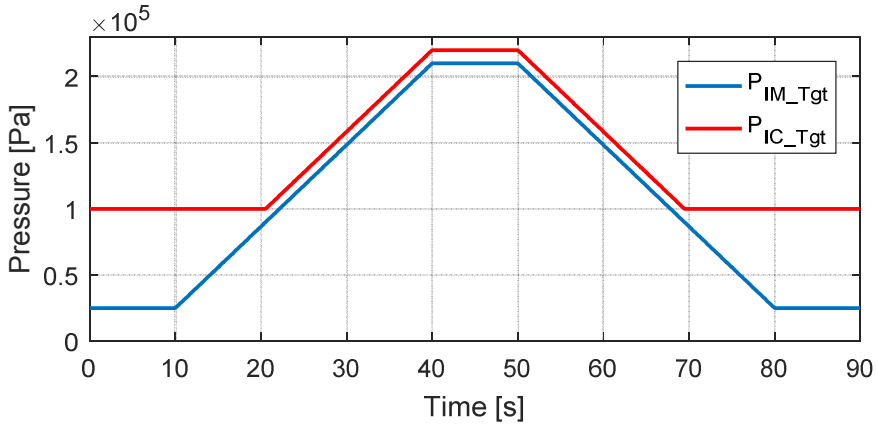

Figure 6.7: Target MAP and Target BOOST signals for a dual-ramp MAP sweep with 30 seconds ramp time

The closed-loop throttle and waste gate controller are then used to control intake manifold pressure and intercooler outlet pressure to P_{IM_Tgt} and P_{IC_Tgt} respectively. The details of the throttle and waste gate controller are provided below.

a) Throttle Controller

The combination of the PID controller with a feed-forward controller for throttle position is illustrated in Figure 6.8.

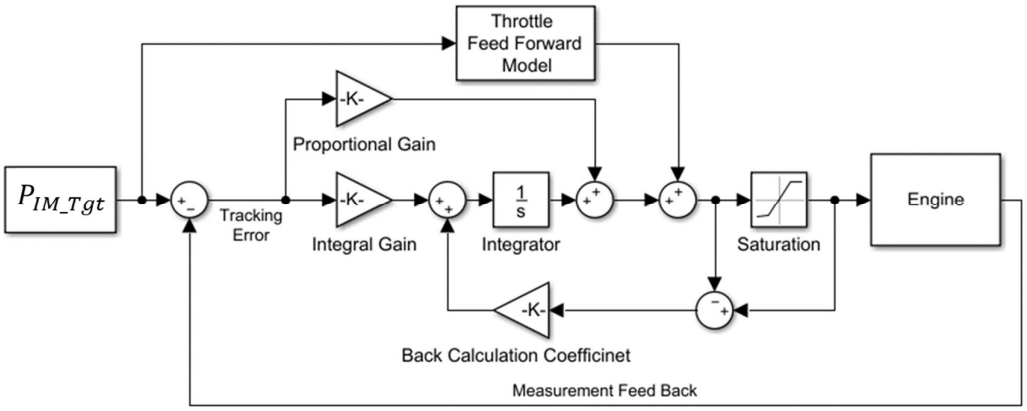

Figure 6.8: Control diagram for closed loop throttle controller

The feed-forward controller requires a model, which approximates the required throttle position in order to achieve a desired intake manifold pressure. If experimental test data from previous engine tests are available, the throttle position can be mapped in a table as a function of engine speed and intake manifold pressure. Figure 6.9 shows an example of the feed-forward throttle model.

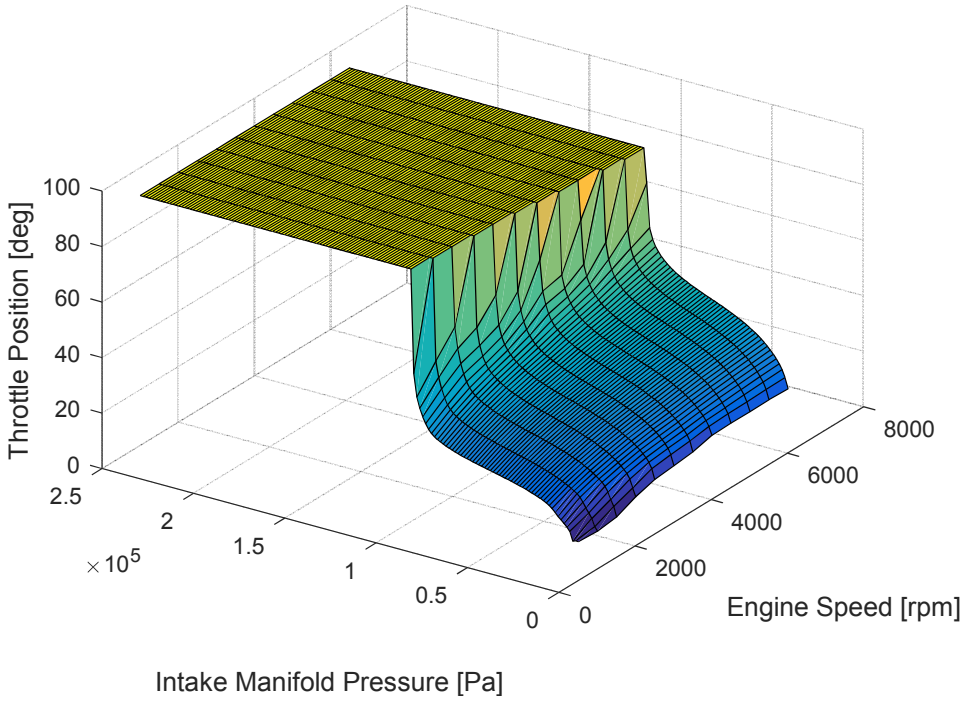

Figure 6.9: Throttle feed-forward model

The feed-forward throttle model in Figure 6.9 was generated using simulation results from the engine model presented in Subsection 7.1.1. Note that the model was generated for a throttle delta pressure of 0kPa, which is why the throttle position is 90 degrees for any intake manifold pressures greater than 1bar.

Since the throttle position has physical actuator limits, the output of the PID controller has to be limited so that the combined signal of the feed-forward controller and the PID controller do not exceed the physical limitations. However, if the output of the PID controller is limited, an anti-windup method is required. In this work, the back-calculation method [154] was implemented. Tuning of the controller and back-calculation gain is treated in Subsection 7.3.2.

b) Waste Gate Controller

The combination of the PID controller and the feed-forward controller for waste gate position are illustrated in Figure 6.10.

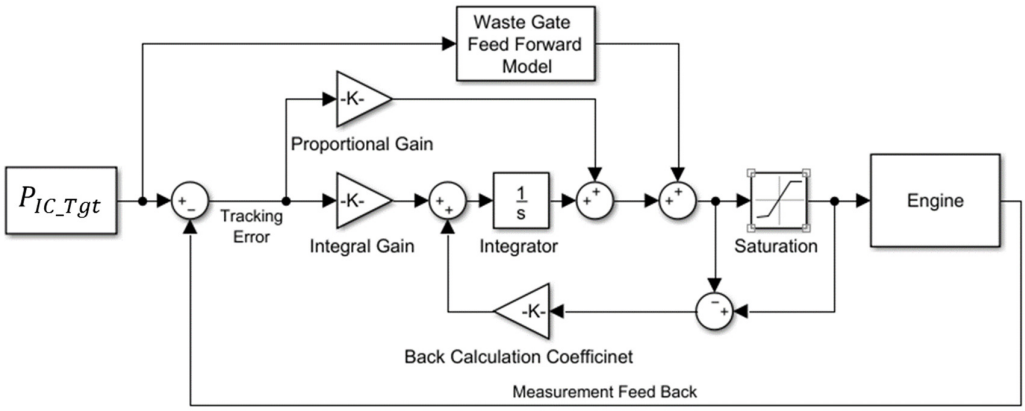

Figure 6.10: Control diagram for waste gate controller

The feed forward controller requires a model, which approximates the required waste gate position in order to achieve a desired intercooler outlet pressure. If experimental test data from previous engine tests are available, the waste gate position can be mapped in a table as a function of engine speed and intercooler outlet pressure. Figure 6.11 shows an example of the feed-forward waste gate model.

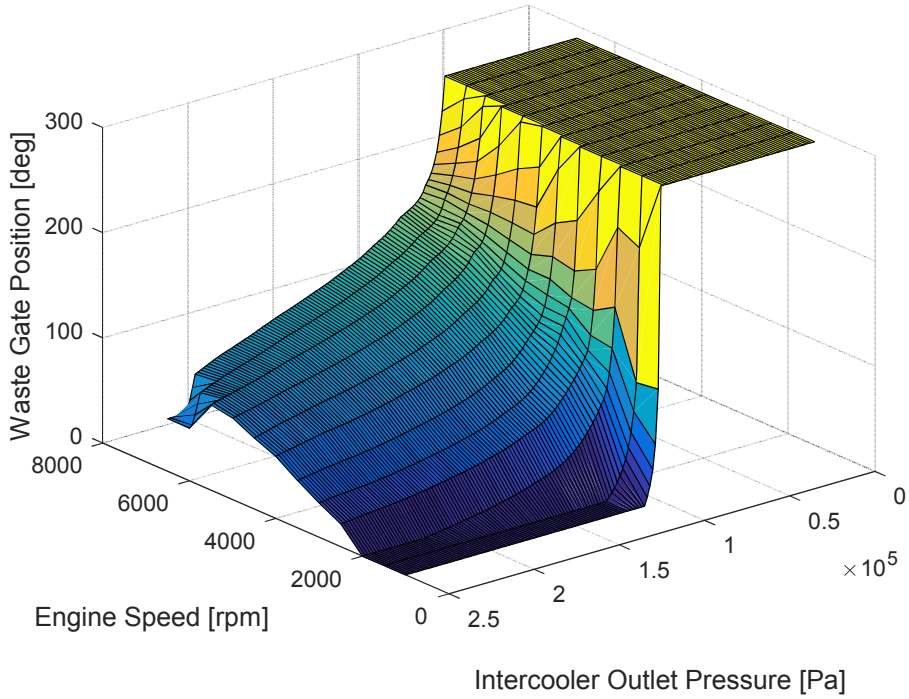

Figure 6.11: Waste gate feed-forward model

The feed-forward waste gate model in Figure 6.11 was generated using simulation results from the engine model presented in Subsection 7.1.1. For all intercooler outlet pressures smaller than 1bar, the waste gate position is fully

open. It should be noted that in the simulation, it is possible to directly control the waste gate open area. This is not possible on a real engine. If the engine under test has an electronic waste gate position actuator, the position of the waste gate can be controlled similarly to the throttle position. However, most engines have either a pressure or vacuum activated waste gate controller which use a solenoid valve to control the pressure / vacuum inside the waste gate canister. In this case, the feed-forward model has to model the required solenoid duty cycle to achieve a desired intercooler outlet pressure.

6.6 Data Processing

To filter the measurement data from measurement noise and cyclic variations a filter is applied. Since the characterisation can be performed offline, a zero-distortion filter can be used which avoids the introduction of a phase shift. A digital first-order low pass filter is used which is represented by Equation 6.23.

$$y_f(k) = Ay(k) + (1 - A)y_f(k - 1) \quad \textbf{6.23}$$

$$A = \frac{T_s}{\tau_f + T_s} \quad \textbf{6.24}$$

where y is the measured signal, y_f is the filtered signal and τ_f is the time constant of the first-order low pass filter which is given by Equation 6.25.

$$\tau_f = \frac{1}{2\pi f_c} \quad \textbf{6.25}$$

where f_c is the of the filter cut-off frequency in [Hz]. However, applying the digital filter from Equation 6.23 to a set of dynamic measurement data leads to a phase shift in the filtered data. To avoid the phase shift, the measurement data have to be filtered forwards and backwards. For an array of measurement data with N samples, *e.g.* $\underline{y} = [y_1; y_2; \dots; y_N]$, zero-distortion filtering is achieved by the following algorithm:

1. Filter $\underline{y}$ with Equation 6.23. this produces $\underline{y_f} = [y_{f,1}; y_{f,2}; \dots; y_{f,N}]$
2. Flip the filtered array so that $\underline{y_f}$ becomes $\underline{y_f} = [y_{f,N}; y_{f,N-1}; \dots; y_{f,1}]$
3. Filter the flipped array again. This produces $\underline{y_{ff}} = [y_{ff,N}; y_{ff,N-1}; \dots; y_{ff,1}]$
4. Flip the array again to return to $\underline{y_{ff}} = [y_{ff,1}; y_{ff,2}; \dots; y_{ff,N}]$

The resulting filter is a second order filter. The output of the filter y_{ff} has precisely zero phase distortion and a magnitude modified by the square of the filter's magnitude response [155].

6.7 Dual Ramp Averaging

The main reason for testing the engine with an up-ramp and a down-ramp is to make use of the Dual Ramp Averaging method, which is reviewed in Subsection 2.2.1. The idea behind this dynamic compensation tool is to excite the system dynamics identically on the up-ramp and the down-ramp. This cancels out the dynamic effects by averaging the results over the up-ramp and the down-ramp. Fast ramps may cause the excitation of thermal dynamics for which the observer does not compensate. Therefore, the DRA method is applied to cancel out any excited dynamics which remain after applying the observer.

The first step of the DRA-method is to split the measurement data set into an up-ramp and a down-ramp. The split point which separates the ramps is defined by the maximum value of intake manifold pressure in the dataset as illustrated in Figure 6.12.

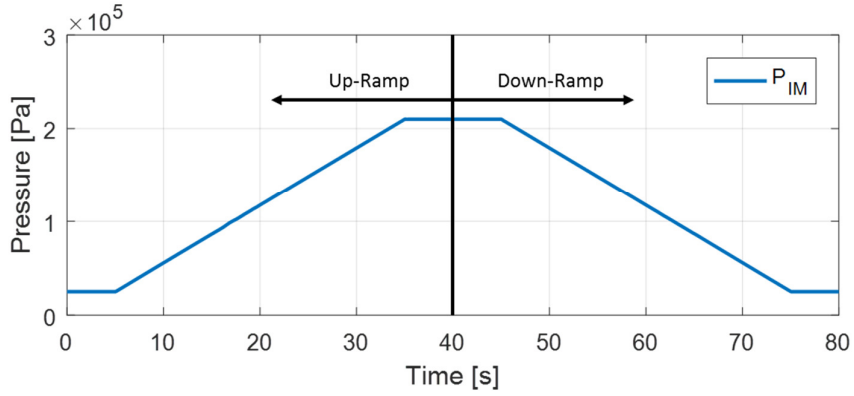

Figure 6.12: Ramp splitting for dual ramp averaging

Once the dataset is separated, it is possible to plot the identified volumetric efficiency from the up-ramp and the down-ramp over intake manifold pressure, which leads to Figure 6.13.

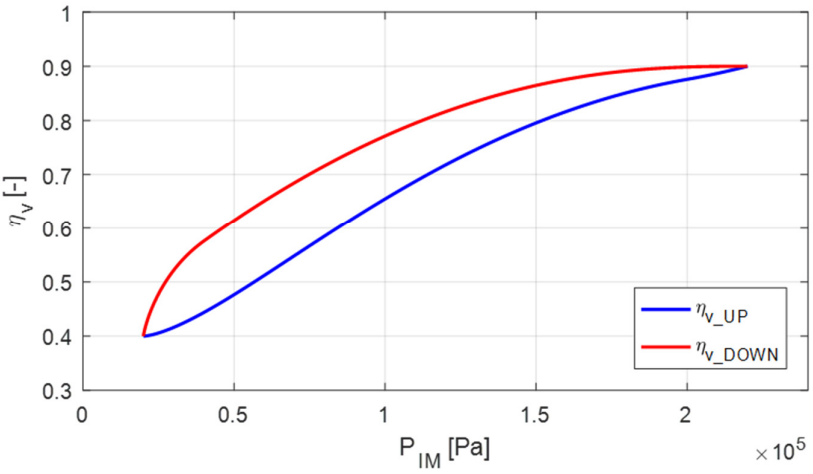

Figure 6.13: Hysteresis caused by a fast dual-ramp sweep

The next step is to interpolate the observed volumetric efficiency in the up-ramp and the down-ramp for specific values of intake manifold pressure. This is necessary in order to be able to average the volumetric efficiency over the up-ramp and the down-ramp. The interpolation is illustrated in Figure 6.14.

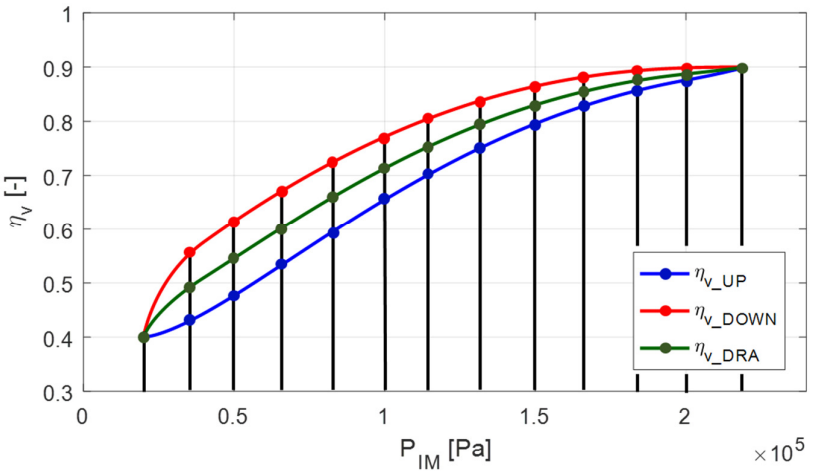

Figure 6.14: Dual ramp averaged volumetric efficiency

The final step is to average the volumetric efficiency over the up-ramp and the down-ramp at each interpolated intake manifold pressure point. The DRA method applied in this work can be summarised by the following three executive steps:

1. Split the measurement dataset into an up-ramp and a down-ramp
2. Re-sample the up-ramp and the down-ramp for specific intake manifold pressure values
3. Average the volumetric efficiency over the up-ramp and the down-ramp

6.8 Summary

Section 6.1 shows that it is sufficient to characterise the volumetric efficiency using intake manifold pressure, engine speed and camshaft timing. This is possible by making use of correction factors and compensators which account for the other inputs that influence the volumetric efficiency. The process overview given in Section 6.2 illustrated that the major steps of the entire process are observer tuning, dual-ramp engine testing, data processing, air-path observation and dual ramp averaging. The tuning algorithm presented in Section 6.3 automatically tunes the observer gains to a desired covariance on the adaptive parameter. The tuning the volume sizes away from their physical values is of little practical benefit. To produce the required ramp in intake manifold pressure, the throttle and the waste gate must be controlled with a suitable controller. Section 6.6 presents a zero-distortion filter which is applied to the measurement data to clear the data from measurement noise and cyclic variations. The dual ramp averaging method in Section 6.7 shows how the observed volumetric efficiency is finally averaged over the up-ramp and the down-ramp in order to cancel out any dynamic effects which may remain after applying the observer.

Chapter 7 Simulation Platform

In this chapter, a simulation platform is developed which is used in Chapter 8 to validate the accuracy of the observer based air charge characterisation methodology. The virtual engine test bed is described in Section 7.1 including the engine simulation model and the implementation of the proposed air-path controllers in MATLAB Simulink. The model is validated in Section 7.2 for its accuracy in air charge prediction to ensure that the model is a valid platform for the validation of the methodology. Section 7.3 evaluates the performance of the air-path controllers which were presented in Section 6.5.

7.1 Virtual Engine Test Bed

The core of the virtual engine test bed is a 1D crank angle resolved engine model, which is developed in Ricardo WAVE. Details of the model are given in Subsection 7.1.1. A Co-Simulation is established in the MATLAB Simulink environment to link the characterisation process with the engine model as described in Subsection 7.1.2.

7.1.1 Ricardo WAVE Engine Model

Ricardo WAVE is a software package for engine simulation. The software allows development of a 1D crank angle resolved engine model using the physical dimensions of the engine. Consequently, the model can be regarded as a white-box model. To increase the prediction accuracy of the model, Ricardo WAVE allows tuning certain model parameters such as flow coefficients of valves and restrictions. The model used in this work was tuned for a number of operating points to achieve a $\pm$5% accuracy for air charge predictions. The top layer of this model is shown in Figure 7.1.

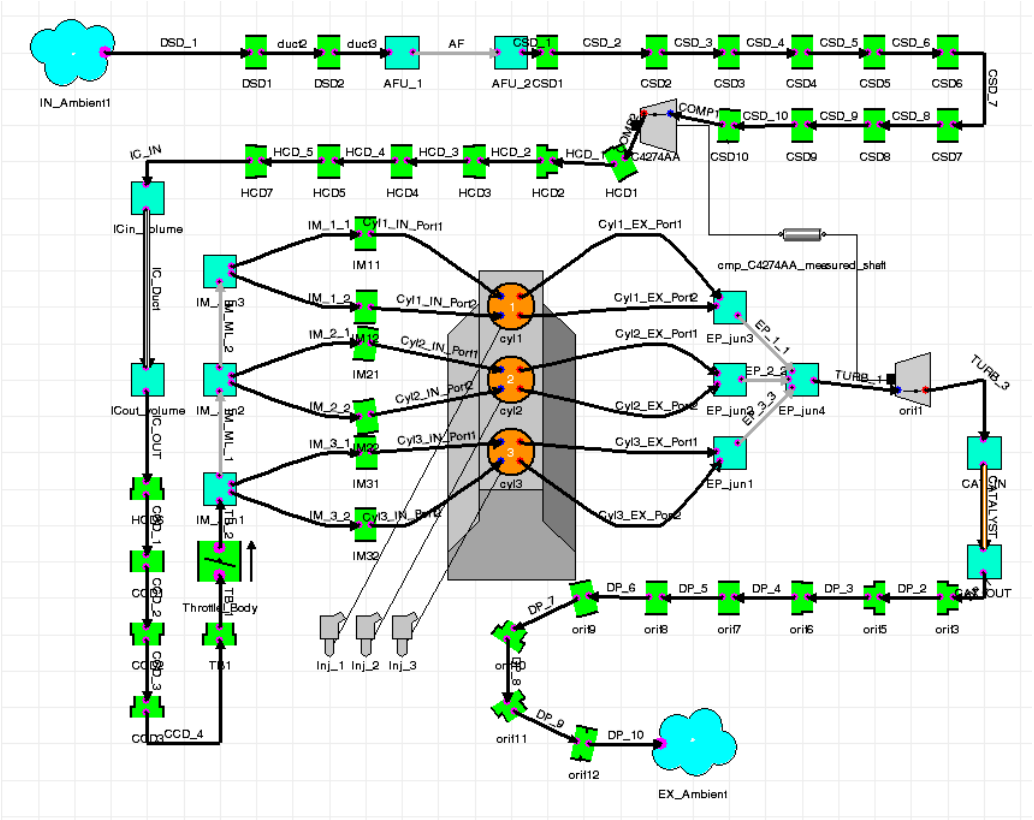

Figure 7.1: Ricardo WAVE engine model

The model has the following inputs and outputs:

- **Inputs**
  - Actuator Positions: N_e, α_{th}, A_{wg}, α_{IVO}, α_{EVC}
  - Additional Inputs: $T_{IC,w}$, P_{amb}, T_{amb}, AFR, $mfb50$,$comb\_dur$
- **Outputs**
  - Mass flows: $\dot{m}_{maf}$, $\dot{m}_c$, $\dot{m}_{th}$, $\dot{m}_{iv}$
  - Pressures: P_{IV}, P_{IC}, P_{IM}
  - Temperatures: T_{IV}, T_{IC}, T_{IM}

All outputs are available as crank angle resolved signals or as cycle average signals.

7.1.2 Co-Simulation with MATLAB Simulink

A Co-Simulation between the Ricardo WAVE engine model and MATLAB Simulink was established to integrate the engine model into the overall characterisation process which is implemented in MATLAB. Figure 7.2 shows the top layer of the Simulink model, which contains the engine model.

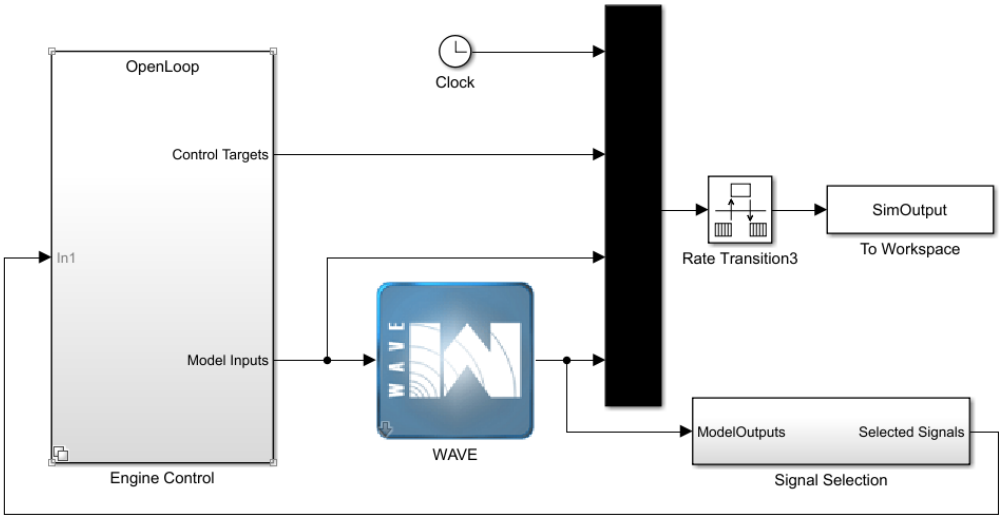

Figure 7.2: Top layer of simulation platform in Simulink

As shown in Figure 7.2, the Simulink model has three major subsystems. The engine control subsystem contains all the control logic presented in Section 6.5. The subsystem can either run in open-loop mode, in which case the controller from Subsection 6.5.1 is used, or in closed-loop mode, in which case the controller from Subsection 6.5.2 is used. The subsystem outputs the model inputs, which are then fed into the WAVE model block. This block communicates with the WAVE engine model at every iteration of the Simulink solver and outputs all the model outputs listed above. The signal selection block selects the measurement signals which are required for the closed-loop controllers. Finally, simulation time, control target signals, model inputs and model outputs are all logged with a constant sampling rate.

Since the WAVE model requires a variable step solver, an ode45 (Dorman-Price) solver was used in the Simulink model. The maximum step size of the solver is set to the sampling interval of the data logging system to avoid any interpolation. The rate transition block shown in Figure 7.2 ensures that the model output data are sampled with the specified sampling interval.

7.2 Engine Model Validation

The engine model was validated against a steady-state data set from a real engine. The details of the engine used to generate the experimental data can be found in Section 9.1. Experimental data were collected at twelve different engine speeds, all at one specific intake and exhaust camshaft position. At each engine

speed, twenty steady-state data points were collected ranging from minimum to maximum intake manifold pressure. A regular grid based DoE was used for validation with engine speed and intake manifold pressure as inputs:

- **Intake manifold pressure**: 0.2 bar to 2.1 bar in 0.1 bar increments
- **Engine speed**: 1000 rpm to 6500 rpm in 500 rpm increments

Figure 7.3 plots the predicted volumetric efficiency of the engine model against the measured volumetric efficiency of the real engine.

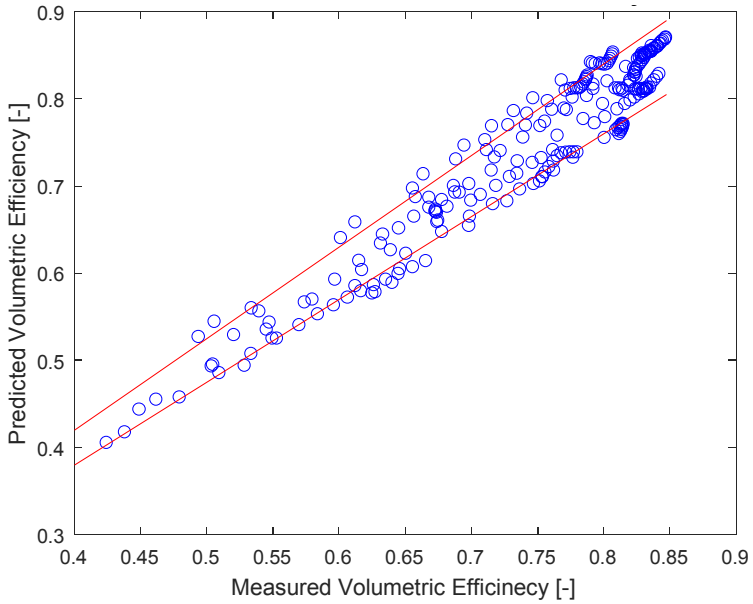

Figure 7.3: WAVE engine model validation: Predicted versus measured volumetric efficiency

The two red lines in Figure 7.3 represent a $\pm$5% error band. Figure 7.4 shows the error in volumetric efficiency over measured volumetric efficiency.

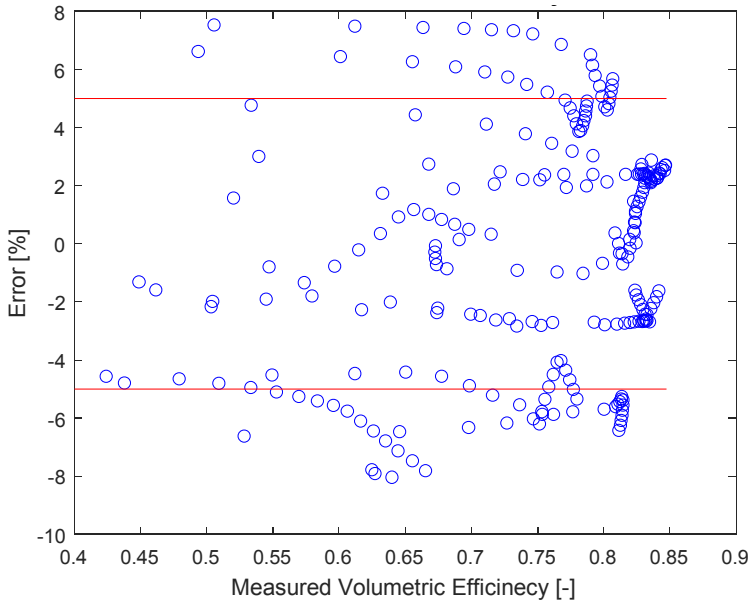

Figure 7.4: WAVE engine model validation: Error in volumetric efficiency

The results from Figure 7.3 and Figure 7.4 show that for most of the validated data points, the predicted volumetric efficiency is within the ±5% error band. The maximum prediction error is approximately 8%. The accuracy of the model can be regarded as sufficient for the following validation of the entire methodology in Chapter 8.

7.3 Evaluation of Air-Path Controllers

In Section 6.5, two different air-path controllers were presented which allow controlling the intake manifold pressure of the engine during a dual-ramp MAP sweep. The purpose of this section is to demonstrate the performance and accuracy of the proposed controllers using the WAVE engine model. The performance of the simple open-loop controller is evaluated in Subsection 7.3.1 and the more advanced closed-loop controller is evaluated in Subsection 7.3.2.

7.3.1 Open-Loop Controller Evaluation

To evaluate the performance of the open-loop controller presented in Subsection 6.5.1 a duel-ramp MAP sweep is simulated with a ramp time of 30 seconds at 3000 rpm engine speed. Using the test definitions from Section 6.4 for a dual-ramp MAP sweep generates the following target MAP signal, shown in Figure 7.5.

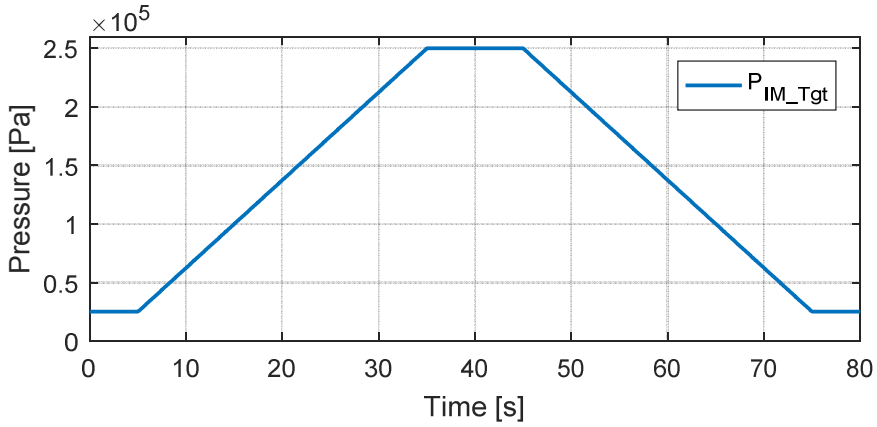

Figure 7.5: Target MAP signal

As described in Subsection 6.5.1, the open-loop controller uses a linear throttle input signal to control the intake manifold pressure during the target MAP range $[P_{im,min}, 1bar]$ and a linear waste gate input signal to control the intake manifold pressure during the target MAP range $[1bar, P_{IM,max}]$. Figure 7.6, Figure 7.7 and Figure 7.8 show the linear input signals for throttle position, waste gate open area and the resulting response of intake manifold pressure respectively.

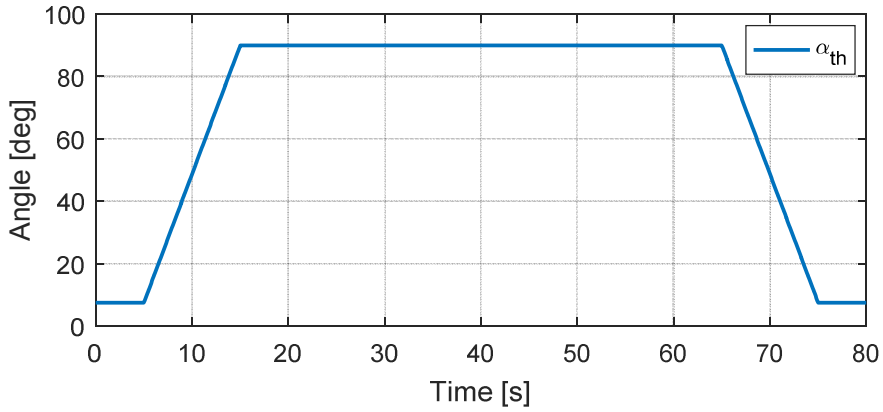

Figure 7.6: Open-loop throttle input signal

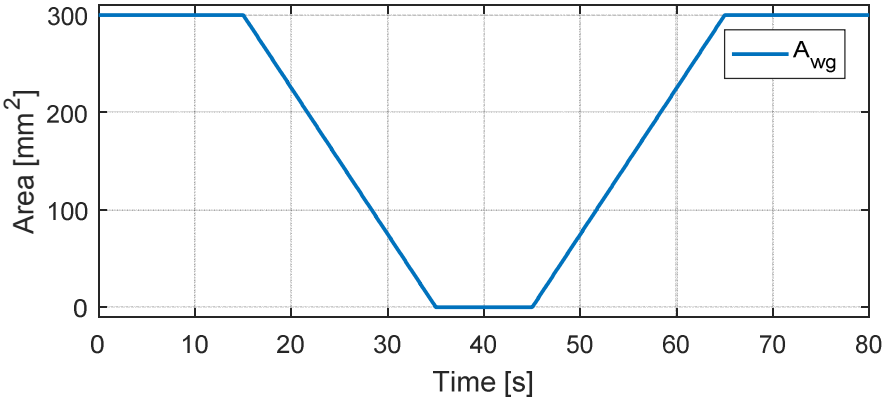

Figure 7.7: Open-loop waste gate input signal

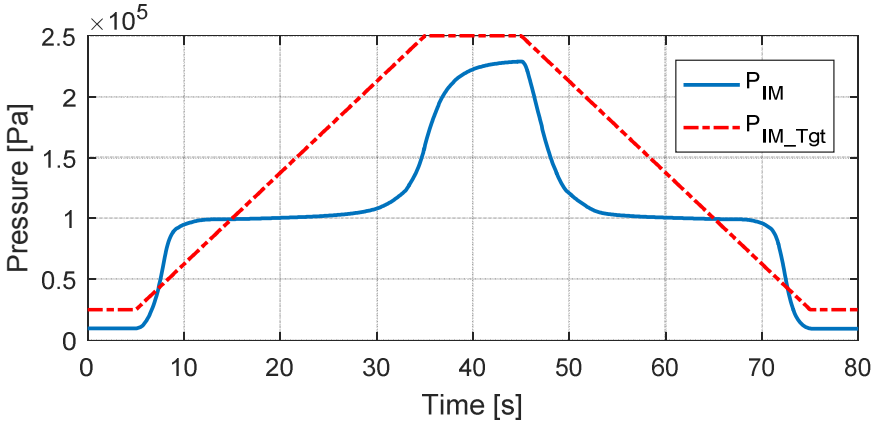

Figure 7.8: Open-loop controller: Intake manifold pressure response

Figure 7.8 shows that linear actuator input signals for throttle position and waste gate are not very suitable for generating a linear ramp in intake manifold pressure. The intake manifold pressure shows a very nonlinear response to the input signals. Consequently, more than 30% of the total test time T_{test} is wasted during the transition from throttled into the boosted region. Additionally, the ramp rate of

intake manifold pressure at the beginning and at the end of the ramp is much higher than desired in the P_{IM_Tgt} signal.

The advantage of this controller is that it is simple and does not involve any closed loop control. The fact that there is a significant difference between the target MAP signal and the resulting intake manifold pressure is not a major issue. For the characterisation, it is important that the engine is tested throughout the entire intake manifold pressure range at each speed, which is definitely achieved with the proposed control strategy. However, the nonlinearity of the ramp rate and the fact that more than 30% of the total test time is effectively wasted clarifies that the open-loop controller is not ideal for dual-ramp MAP sweeps. Additionally, the controller is not suitable to characterise engine control strategies which use a delta pressure across the throttle in the boosted operating range. Boost pressure and intake manifold pressure cannot be controlled separately with this methodology.

7.3.2 Closed-Loop Controller Evaluation

The closed-loop controller presented in Subsection 6.5.2 is evaluated in this subsection. At first, the performance is evaluated using only a PID controller for throttle and waste gate control without a feed-forward model. After that, the performance is evaluated including a feed-forward model to highlight the advantages.

a) Closed-Loop PID control

The PID controllers for throttle position and waste gate open area were tuned using the following *ad-hoc* values:

- **Throttle Controller**: $P = 0.001$, $I = 0.01$, $D = 0$
- **Waste Gate Controller**: $P = 0.002$, $I = 0.03$, $D = 0$

Figure 7.9 shows the intake manifold pressure response for a duel-ramp MAP sweep with a ramp time of 30 seconds at 2000 rpm engine speed.

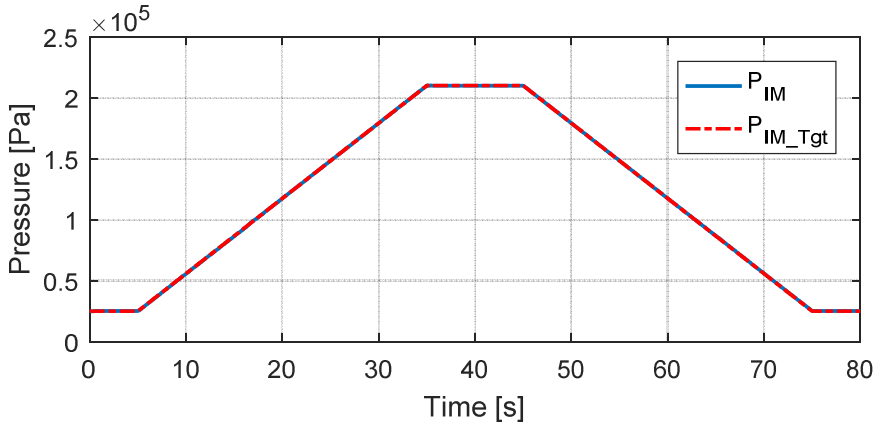

Figure 7.9: Closed-loop controller: intake manifold pressure response for 30 seconds ramp time

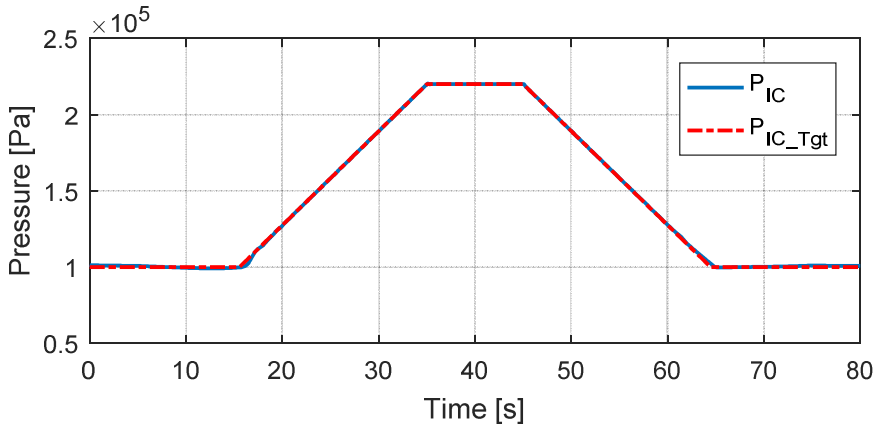

Figure 7.10: Closed-loop controller: Intercooler outlet pressure response for 30 seconds ramp time

Figure 7.9 and Figure 7.10 show that the PID controllers manage to control the intake manifold pressure and intercooler outlet pressure with high accuracy to the desired values P_{IM_Tgt} and P_{IC_Tgt}.

To investigate if the controller achieves a similar accuracy for fast ramps, the simulation was repeated with a ramp time of 3 seconds. Figure 7.11 and Figure 7.12 show the response of intake manifold pressure and intercooler outlet pressure respectively.

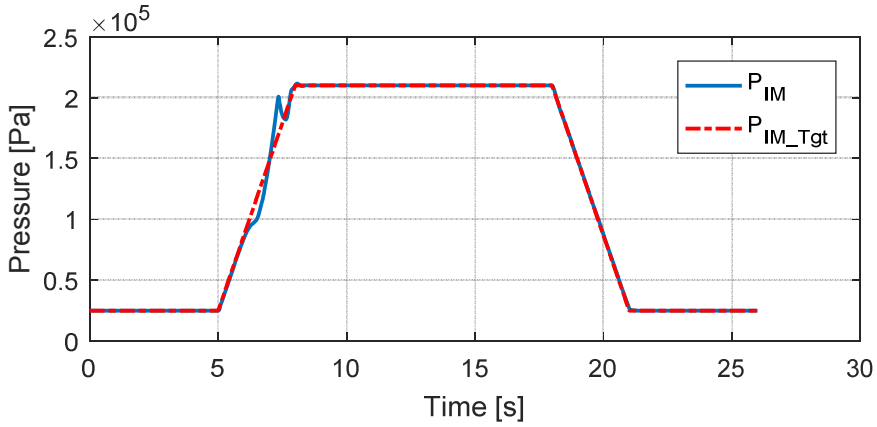

Figure 7.11: Closed-loop controller: Intake manifold pressure response for 3 seconds ramp time

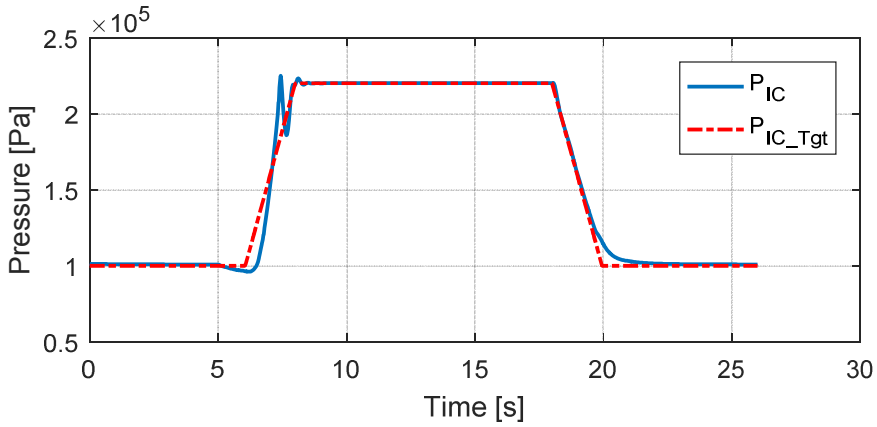

Figure 7.12: Closed-loop controller: Intercooler outlet pressure response for 3 seconds ramp time

Figure 7.11 and Figure 7.12 highlight that the accuracy of the closed loop controller using only a PID controller has its limitations. The results show that the tracking accuracy is significantly reduced compared to the simulation results with a ramp time of 30 seconds. It might be possible to improve the tracking accuracy by tuning the PID controllers with a more advanced method. However, higher gains in the controllers will result in overshoots and fluctuations, which are not desirable since this causes excitation of the gas dynamics.

As mentioned in Subsection 6.5.2, it is possible to improve the tracking accuracy of the controller by combining the PID controllers with a feed-forward model for throttle and waste gate position.

b) Closed-Loop PID control with Feed-Forward Model

For this part of the evaluation of the proposed air-path controller, a feed-forward model was generated for throttle position and waste gate open area. The models

were identified using steady-state simulation data. Throttle position and waste gate open area are modelled as a function of intake manifold pressure and engine speed. The use of perfect models eliminates the need for the PID controllers. Therefore, the steady-state data used to generate the models were simulated with a delta pressure of 0kPa. The simulation results to follow were generated with a desired delta pressure of 10kPa to ensure that the PID controllers have some work to do in order to correct for the errors in the feed-forward models. The models are finally implemented as 2D lookup tables. The reader is referred to Figure 6.9 and Figure 6.11 in Subsection 6.5.2 for an example of the implemented feed-forward models.

Figure 7.13 and Figure 7.14 show the response of intake manifold pressure and intercooler outlet pressure for a ramp time of 3 seconds.

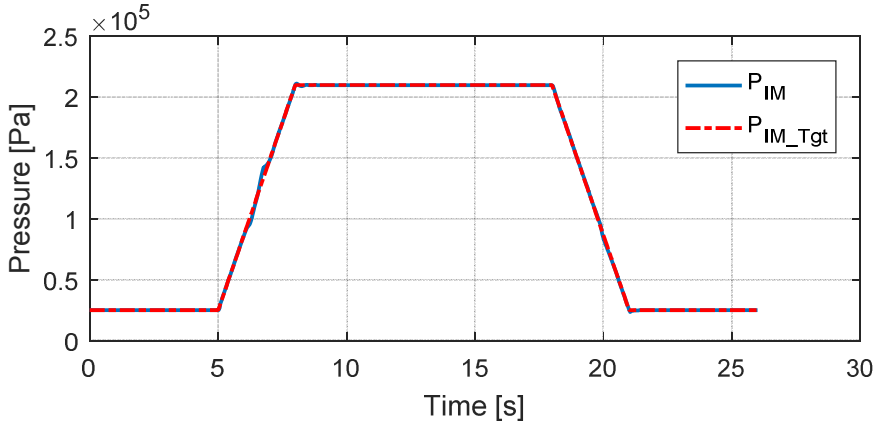

Figure 7.13: Closed-loop controller with feed-forward model: Intake manifold pressure response for 3 seconds ramp time

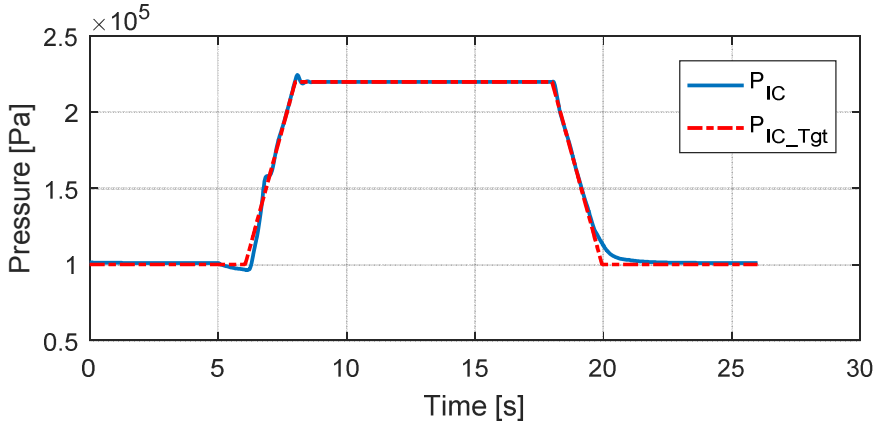

Figure 7.14: Closed-loop controller with feed-forward model: Intercooler outlet pressure response for 3 seconds ramp time

The results show a significant improvement in the tracking accuracy of P_{IM_Tgt} and P_{IC_Tgt}. Dual-ramp MAP sweeps with a ramp time smaller than 3 seconds are definitely not required. Therefore, it can be concluded that the closed-loop controller with feed-forward models for throttle position and waste gate open area is a suitable control solution.

7.4 Summary

A virtual engine test bed was presented in Section 7.1. The core of the simulation platform is a 1D crank angle resolved engine model which was developed in Ricardo WAVE software. A co-simulation between the engine model in MATLAB Simulink permits implementation and switching between different engine air-path controllers. Additionally, the implementation in Simulink allows an easy and direct use of the simulation data in MATLAB. The prediction accuracy of the model for air charge was validated in Section 7.2 and achieved a $\pm$5% accuracy in volumetric efficiency for 80% of the validation points. The maximum prediction error was 8%. The evaluation of the different air-path controllers in Section 7.3 clarified that the open-loop solution is not the ideal control solution for a dual-ramp MAP sweep. Due to the strongly nonlinear response of intake manifold pressure to throttle angle and waste gate open area, over 30% of the total test time is wasted with this control method. Furthermore, the applicability is limited to engine control strategies, which do not use a delta pressure across the throttle in the boosted operating range. The closed-loop controller provides a much more advanced control solution for a dual-ramp MAP sweep. Only using a PID controller to control intake manifold pressure and intercooler outlet pressure is suitable for ramp times down to 30 seconds. For ramp times faster than 30 seconds, the PID controllers have to be combined with a feed-forward model for throttle position and waste gate open area to achieve a good tracking of the target intake manifold pressure and target boost pressure.

Chapter 8 Simulation based Methodology Validation

This chapter is focused on the validation of the developed dynamic engine air charge characterisation methodology. For this task, the simulation platform from Chapter 7 is used. Section 8.1 describes how the simulation results were produced and defines a number of statistical measures used to judge the accuracy of the developed methodology. In Section 8.2, the validity of steady-state volumetric efficiency during transient engine operation is investigated to prove that it is possible to characterise the volumetric efficiency from dynamic engine test data. Section 8.3 investigates the accuracy of the proposed air-path observer. Special attention is paid to the impact of gas dynamic effects upon the observation accuracy of the volume outflow. Finally, the accuracy of the complete methodology is validated in Section 8.4.

8.1 Validation Details

This section provides the details required to validate the developed methodology. Subsection 8.1.1 describes the details of the simulation based data collection. Subsection 8.1.2 defines different volumetric efficiencies, which are validated against each other. Subsection 8.1.3 defines a number of statistical measures used to judge the accuracy of the developed methodology.

8.1.1 Simulation Data

This subsection clarifies how the steady-state reference data and the dynamic data were produced using the simulation platform from Chapter 7.

- **Steady-State Data**: To produce the steady-state reference data at any specific engine speed and camshaft position, the model was simulated at 200 steady-state points equally spaced between 0.3 bar and 2.3 bar intake manifold pressure. To ensure that all variables have reached steady-state conditions, the model was simulated for two minutes at each test point. All model output signals were set to cycle average to ignore any cyclic variations in the measured variables. All signals were logged with a sampling interval of one millisecond. Finally, the last data point at t = 2 minutes was selected to estimate the volumetric efficiency at steady-state.
- **Dynamic Data**: All dynamic data were produced using the closed-loop air-path controller, which was presented in Subsection 6.5.2 and validated in

7.3.2. All model output signals were set to cycle average to ignore any cyclic variations in the measured variables. All signals were logged with a sampling interval of one millisecond.

8.1.2 Definition of Volumetric Efficiency

In the following sections of this chapter, different volumetric efficiencies are compared and validated against each other. A clear definition of each volumetric efficiency is listed below to avoid any confusion:

- **Actual Volumetric Efficiency**: Actual volumetric efficiency, η_v, which is given by Equation 8.1, is the actual volumetric efficiency at any time t and is estimated from Equation 8.1.

$$\eta_v(t) = \frac{\dot{m}_{iv}(t)120RT_{IM}(t)}{P_{IM}(t)V_dN_e} \quad \textbf{8.1}$$

  where $\dot{m}_{iv}(t)$ is the actual air mass flow into the cylinder. All variables are cycle average data.

- **Steady-State Volumetric Efficiency**: Steady-state volumetric efficiency, η_{v_SS}, which is given by Equation 8.2, refers to the volumetric efficiency of the engine at time t_{ss} when all system states have settled.

$$\eta_{v\_SS} = \eta_v(t_{ss}) = \frac{\dot{m}_{iv}(t_{ss})120RT_{IM}(t_{ss})}{P_{IM}(t_{ss})V_dN_e} \quad \textbf{8.2}$$

  As mentioned in Subsection 8.1.1, a settling time of 2 minutes was used for the steady-state simulation results to ensure that all system states have settled. Therefore, $\dot{m}_{iv}(t_{ss})$, $T_{IM}(t_{ss})$ and $P_{IM}(t_{ss})$ represent the cycle average air mass flow into the cylinder, intake manifold temperature and intake manifold pressure after a settling time of $t_{ss} = 2$ minutes, during which all engine actuators were held constant.

- **Observed Volumetric Efficiency**: Observed volumetric efficiency, which is defined by Equation 8.3, is the volumetric efficiency estimated from the observed air mass flow into the cylinder, $\hat{\dot{m}}_{iv}$. The reader is referred to Section 5.2 for all equations that lead to the observation, $\hat{\dot{m}}_{iv}$.

$$\eta_{v\_OBS}(t) = \frac{\hat{\dot{m}}_{iv}(t)120RT_{IM}(t)}{P_{IM}(t)V_dN_e} \quad \textbf{8.3}$$

- **MAF-based Volumetric Efficiency**: MAF-based volumetric efficiency, which is given by Equation 8.4, is the volumetric efficiency estimated from the air mass flow, $\dot{m}_{maf}$, which is measured at the location of the MAF sensor.

$$\eta_{v\_MAF}(t) = \frac{\dot{m}_{MAF}(t)120RT_{IM}(t)}{P_{IM}(t)V_d N_e} \quad \textbf{8.4}$$

8.1.3 Statistical Measures for Validation

To investigate the difference between steady-state and dynamic test data and to analyse the performance of the air-path observer this subsection defines three different error measures:

- **Error in percent**: The error in percent between a signal S and a reference signal S_{ref} is estimated from Equation 8.5.

$$e(k) = \frac{\left(S(k) - S_{ref}(k)\right)}{S_{ref}(k)} 100 \quad \textbf{8.5}$$

- **Percentage of Root Mean Square Error**: The Root Mean Square Value of an error e is the Root Mean Square Error (RMSE). Equation 8.6. gives the RMS value for an error between two signals with N samples.

$$RMSE = \sqrt{\left(\frac{1}{N}\right)\sum_{k=1}^{N}\left(e(k)\right)^2} \quad \textbf{8.6}$$

- **Percentage of Maximum Absolute Error**: The maximum absolute value of an error e is the Maximum Absolute Error (MAE). Equation 8.7 gives maximum absolute values of an error $e(t)$ with N samples.

$$MAE = max[|e(k)|] \quad \textbf{8.7}$$

8.2 Steady-State versus Transient Volumetric Efficiency

The validity of steady-state volumetric efficiency under transient engine operation was investigated by Chevalier [91] and Smith [109]. Both authors concluded that steady-state volumetric efficiency is entirely valid during transient operation. In

fact, Chevalier and Smith state that there is no noticeable difference irrespective of how transient the engine is behaving. However, both authors used a naturally aspirated engine in their investigations. Additionally, the simulation tools used in both studies were state of the art at the time when the work was carried out; however, 1D crank angle resolved engine models have developed significantly since then. Consequently, the published results require verification for a turbocharged engine using a state of the art engine model.

The purpose of this section is to provide a detailed investigation into the difference between steady-state and transient volumetric efficiency. The 1D crank angle resolved engine model provides the ideal tool for this investigation since it allows measuring the actual air mass flow into the engine during transient operation, which is not possible on a real engine.

Firstly, the simulation platform is used to produce the steady-state data, which provide the reference for this validation. After that, dual-ramp MAP sweeps are produced with a wide range of different ramp times. Comparing the results of the duel-ramp MAP sweeps with the steady-state data allows firstly to clarify if there is any difference between the volumetric efficiency during steady-state and under transient engine operation. Secondly, the different ramp times allows investigation if the difference depends on the intensity of the transient. In this case a short ramp time represents a more intense transient since the rate of change in the system states such as pressures in the intake and exhaust system are higher. A detailed investigation is provided for one specific engine speed and one specific camshaft timing in Subsection 8.2.1. Subsection 8.2.2 summarises the results for different engine speeds.

This part of the investigation does not involve the air-path observer and only investigates if there is any noticeable difference between the volumetric efficiency at steady-state conditions and under transient operation. The results of this investigation are crucial to prove the validity of the proposed rapid engine air charge characterisation methodology. The use of the proposed air-path observer for engine air charge characterisation would be pointless if there is a significant difference between steady-state and transient volumetric efficiency.

8.2.1 Detailed Investigation

In this subsection, simulation results at 3000 rpm engine speed at one specific intake and exhaust camshaft timing are used for a detailed investigation into the validity of steady-state volumetric efficiency during transient engine operation.

Figure 8.1 compares the actual volumetric efficiency η_v from a dual-ramp MAP sweep with a ramp time of 30 seconds to steady-state volumetric efficiency η_{v_SS} over intake manifold pressure. η_{v_UP} represents the actual volumetric efficiency during the up-ramp and η_{v_DOWN} represents the actual volumetric efficiency during the down-ramp.

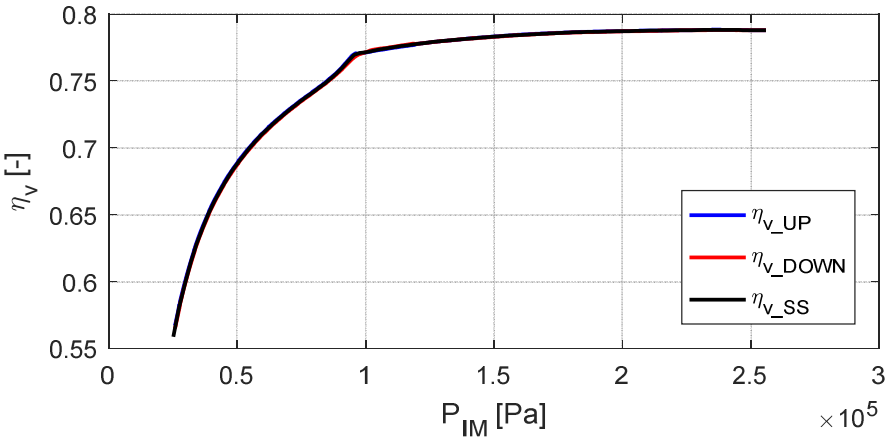

Figure 8.1: Steady-state volumetric efficiency versus actual volumetric efficiency from a dual-ramp MAP sweep with 30 seconds ramp time

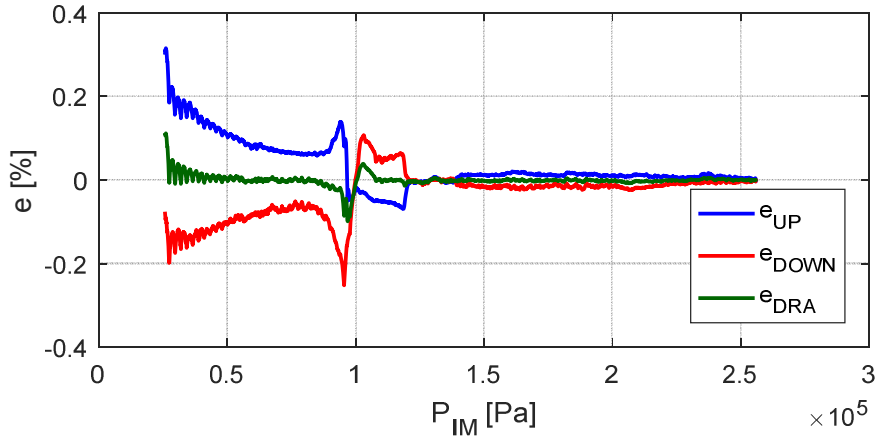

Figure 8.2: Errors between steady-state volumetric efficiency and actual volumetric efficiency from a dual-ramp MAP sweep with 30 seconds ramp time

Figure 8.1 suggests that there is no noticeable difference between steady-state volumetric and transient volumetric efficiency. However, taking a closer look at Figure 8.2 reveals that there is indeed a small error between the steady-state volumetric efficiency and the volumetric efficiency during the up-ramp (blue line) and the down-ramp (red line). The results show an error of up to 0.3% for the error during the up-ramp e_{UP} and the error during the down-ramp e_{DOWN}. Applying the Dual Ramp Averaging (DRA) method from Section 6.7 allows a significant reduction of the remaining error, e_{DRA}, although, a small error of up to 0.1% remains. The fact that there is a small but noticeable difference between the steady-state and the transient volumetric efficiency during a relatively slow ramp of 30 seconds suggests whether the error might increase during more rapid transients. Therefore, the investigation is repeated for 11 different ramp times, ranging from 3 seconds up to 120 seconds. To provide an efficient summary of the 11 separate investigations, the RMSE and MAE values between η_v and η_{v_SS} are plotted over ramp time in Figure 8.5 and Figure 8.6 respectively.

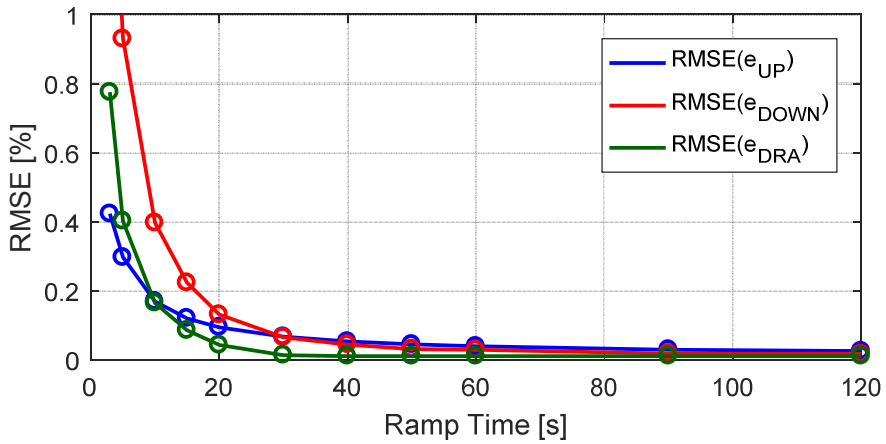

Figure 8.3: RMSE between steady-state volumetric efficiency and actual volumetric efficiency from dual-ramp MAP sweeps with various ramp times

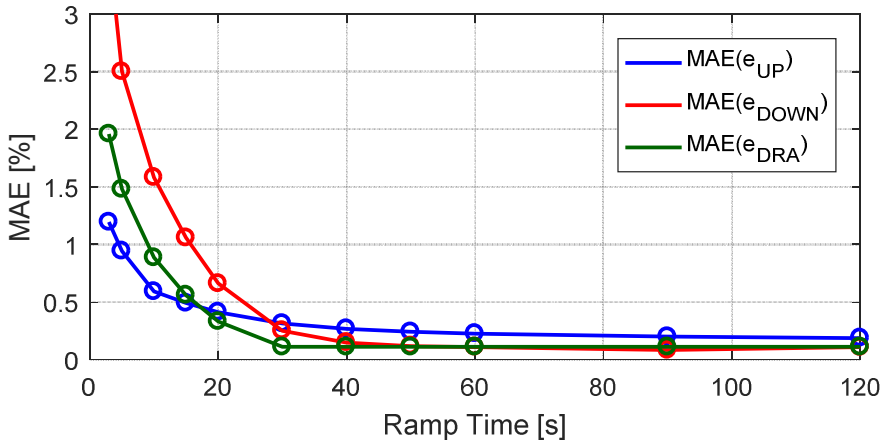

Figure 8.4: MAE between steady-state volumetric efficiency and actual volumetric efficiency from dual-ramp MAP sweeps with various ramp times

Figure 8.3 and Figure 8.4 show a sharp increase in RMSE and maximum error for ramp times shorter than 30 seconds. The results also show that for any ramp times slower than 20 seconds dual-ramp averaging helps significantly in reducing the RMSE. For the MAE, dual-ramp averaging does not lead to a noticeable improvement.

The results show that ramp times faster than 30 seconds lead to a significant difference between steady-state and transient volumetric efficiency. Based on these results it can be concluded that steady-state volumetric efficiency is not entirely valid during transient engine operation. The fact that the difference between the two increases with shorter ramp times indicates that the magnitude of the error depends on the intensity of the transient.

A detailed analysis of the simulation data lead to the following findings:

- **Intake manifold pressure**: P_{IM} is increasing on the up-ramp and decreasing on the down-ramp. The volumetric efficiency is estimated from the cycle average intake manifold pressure. Comparing the crank-angle resolved intake manifold pressures between the steady-state and the dual-ramp MAP sweeps reveals that the mean pressure over the cycle is identical. However, at the time when the intake valve closes, the pressure is not exactly the same due to the slope of the ramp. A difference in intake manifold pressure at the time of intake valve closing will obviously affect the amount of air inside the cylinder, which explains the difference in volumetric efficiency. This theory supports the fact that the difference increases with faster ramps. Faster ramps translate into a higher

difference in intake manifold pressure at intake valve closing due to a steeper slope and, consequently, into a larger difference in volumetric efficiency.

- **Exhaust manifold pressure**: During the ramps exhaust manifold pressure is not identical with the exhaust manifold pressure during steady-state, due to the following two reasons.
    - Exhaust manifold pressure has a slow response time to changes in throttle and waste gate position as compared to intake manifold pressure. Consequently, cycle average exhaust manifold pressures are lower during the up-ramp and higher on the down ramp compared to the steady-state conditions. This difference affects the amount of residuals inside the cylinder at exhaust valve closing and, consequently, affects the amount of air that can be induced during the next intake event, which leads to a difference in volumetric efficiency.
    - Similar to the intake system, crank angle resolved exhaust manifold pressure is affected by the slope of the ramp. Consequently, in addition to the difference in the cycle average pressure there is a difference in the crank-angle resolve exhaust manifold pressure at the time of exhaust valve closing. This again has an effect on the amount of residuals in the cylinder and, therefore, affects the volumetric efficiency.
- **Exhaust gas temperatures**: Temperatures in the exhaust system have long settling times. Therefore, the exhaust gas temperature during the up-ramp is lower compared to the steady-state data and higher on the down-ramp. The difference in temperature affects the amount of residuals since it changes the density of the residuals. This effect on the volumetric efficiency is small compared to the previous two findings but has a noticeable impact.

The ultimate task of this work is to characterise the steady-state volumetric efficiency of the engine as quickly as possible. However, the results presented in this subsection indicate that there is a physical limitation to the ramp time to avoid major errors in the identified volumetric efficiency. As mentioned at the beginning of this subsection, all results from Figure 8.1 to Figure 8.4 are produced at 3000

rpm engine speed. This study was repeated for six different engine speeds to investigate if the RMSE and MAE values are also dependent on engine speed.

8.2.2 Dependency on Engine Speed

Figure 8.5 and Figure 8.6 show the RMSE and MAE of the dual-ramp averaged volumetric efficiency η_{v_DRA} over ramp time for different engine speeds.

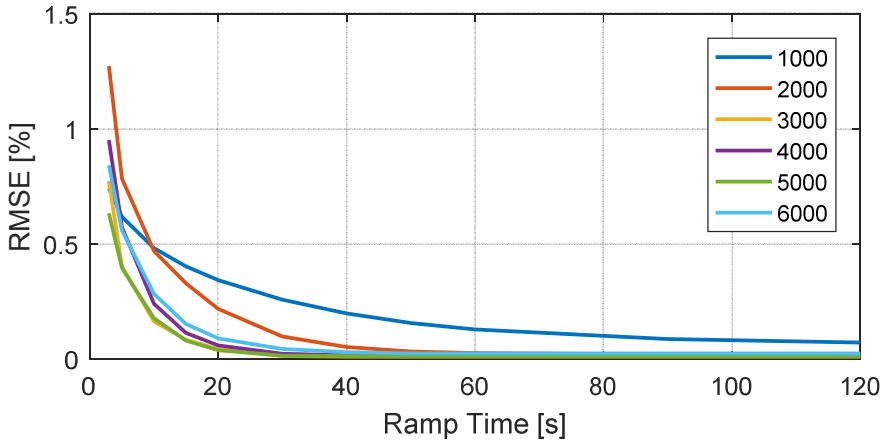

Figure 8.5: RMSE between steady-state volumetric efficiency and actual dual-ramp averaged volumetric efficiency from dual-ramp MAP sweeps with various ramp times for different engine speeds

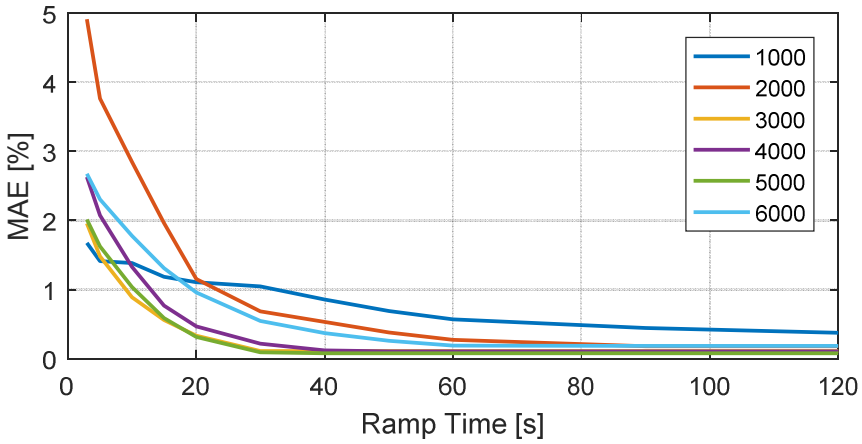

Figure 8.6: MAE between steady-state volumetric efficiency and actual dual-ramp averaged volumetric efficiency from dual-ramp MAP sweeps with various ramp times for different engine speeds

Figure 8.5 and Figure 8.6 show the RMSE and MAE profile for six different engine speeds. The results show that RMSE and MAE tend to be higher at lower engine speeds.

8.2.3 Investigation Summary

The simulation results presented in Section 8.2 revealed that the findings by Chevalier [91] and Smith [109] have to be updated. Clearly, steady-state volumetric efficiency and the volumetric efficiency during transient operation are not identical on a turbocharge engine. The difference depends on the intensity of the transient. The results for RMSE and MAE from Figure 8.5 and Figure 8.6 show that the ramp time has to be limited to avoid significant errors in the identified volumetric efficiency. RMSE and MAE of the identified volumetric efficiency curve also depend on engine speed. Both error measures tend to be higher at low engine speeds.

Even if the air-path observer would allow a 100% accurate observation of the air mass flow into the cylinder during transient operation, the accuracy of the identified volumetric efficiency is still limited by the fact that there is indeed a difference between steady-state and transient volumetric efficiency. However, since the control strategies require steady-state data for the mapping and calibration process, steady-state volumetric efficiency is the measure of success for the validation of the proposed methodology.

The fact that a sufficient accuracy in term of RMSE and MAE can be achieved for ramp times greater than 60 seconds even at low engine speed concludes that it is indeed possible to characterise an accurate volumetric efficiency from dynamic data. A ramp time of 60 seconds would result in a significant time saving compared to traditional steady-state testing. Therefore, the difference is not regarded as a major concern for this work and not further investigated here.

8.3 Observer Accuracy / Impact of Gas Dynamic Effects

As mentioned in Subsection 5.1.1, the air-path observer is based on a mean value engine model. The air-path system is therefore lumped into major volumes, which are modelled using filling and emptying dynamics. Consequently, the observer can only compensate for the filling and emptying dynamics and not for any other gas dynamic effects. It is therefore necessary to investigate the impact of gas dynamic effects upon the accuracy of the observed intake air mass flow. A 1D crank angle resolved engine model is the perfect tool to carry out such an investigation since the model simulates the gas dynamic effects and allows to measure the air mass flow at any location along the air-path. This allows

investigating the accuracy of the entire air-path observer as well as the observers of each volume separately.

8.3.1 Detailed Investigation

Simulation results with a ramp time of three seconds at 3000 rpm are used in this subsection to investigate the accuracy of the air-path observer. Such an aggressive ramp significantly excites the gas dynamics of the air-path. The difference between the measured and the observed intake air mass flow is then used to determine the accuracy of the proposed air-path observer. The volumes of the observer are not tuned for this specific case study to investigate the pure impact of the gas dynamics. The exact physical values of the volumes are therefore used in this case study.

Figure 8.7 shows the simulation results for P_{IV}, P_{IC} and P_{IM} and Figure 8.8 shows the simulation results for $\dot{m}_{maf}$, $\dot{m}_{th}$ and $\dot{m}_{iv}$.

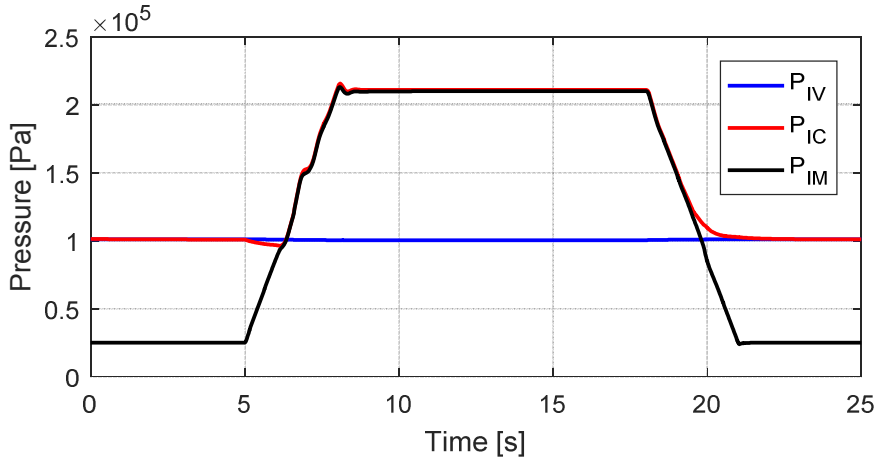

Figure 8.7: Intake system pressure responses for a dual-ramp MAP sweep with 3 seconds ramp time

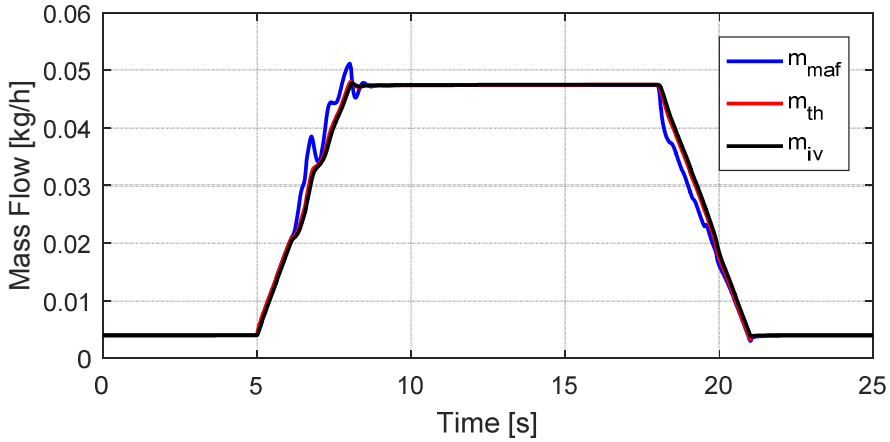

Figure 8.8: Air mass flow responses along the intake system air-path for a dual-ramp MAP sweep with 3 seconds ramp time

Figure 8.8 shows a noticeable difference between the air mass flow which is measured at the location of the MAF sensor $\dot{m}_{maf}$ and the actual air mass flow through the intake valve $\dot{m}_{iv}$ during the up-ramp and the down-ramp. As mentioned in Section 2.5 and Section 3.3, this difference is caused by the excitation of the filing and emptying dynamics and gas dynamics of the air-path system. The task of the developed observer is to observe $\dot{m}_{iv}$ as accurately as possible by compensating for the excited filling and emptying dynamics in each volume.

To judge the accuracy of the observer, two error measures are established in this subsection. The measurement error e_M defines the direct difference between the inflow and the outflow of a volume and is given by Equation 8.8.

$$e_M = \frac{(\dot{m}_{in} - \dot{m}_{out})}{\dot{m}_{out}} 100 \quad \textbf{8.8}$$

The measurement error therefore is a direct measure of the introduced error due to the excited dynamics in the air-path. It can also be seen as the final error if no observer were used. To evaluate the accuracy of the observer the observation error e_{OBS} is used which is given by Equation 8.9.

$$e_{OBS} = \frac{(\hat{\dot{m}}_{out} - \dot{m}_{out})}{\dot{m}_{out}} 100 \quad \textbf{8.9}$$

The observation error gives the difference between the true outflow of a volume and the observed outflow of the volume. Comparing the measurement error with the observation error allows to judge the performance of the observer.

The measurement error and the observation error for the total intake system are shown in Figure 8.9. The errors, e_{M_tot} and e_{OBS_tot} were estimated using Equations 8.10 and 8.11 respectively.

$$e_{M\_tot} = \frac{(\dot{m}_{maf} - \dot{m}_{iv})}{\dot{m}_{iv}} 100 \quad \textbf{8.10}$$

$$e_{OBS\_tot} = \frac{(\hat{\dot{m}}_{iv} - \dot{m}_{iv})}{\dot{m}_{iv}} 100 \quad \textbf{8.11}$$

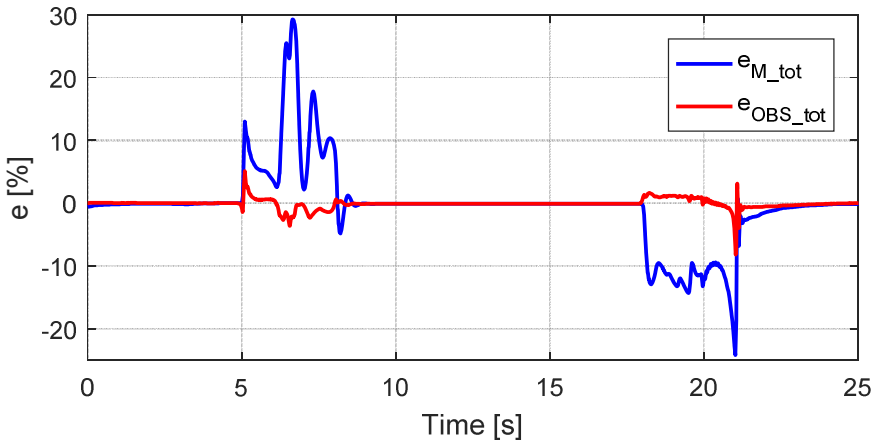

Figure 8.9: Measurement error of the total intake system versus observation error of the total intake system for a dual-ramp MAP sweep with 3 seconds ramp time

Figure 8.9 shows that during the fast ramp, a measurement error between $\dot{m}_{maf}$ and $\dot{m}_{iv}$ of up to 30% is introduced due to the excitation of the air-path dynamics. The results show that the observer can reduce the introduced error significantly.

However, it is also clear that even after applying the observer, an observation error of up to 6% remains. This clearly shows that gas dynamic effects have an impact on the accuracy of the observed intake air mass flow. In the following, each observer is investigated separately to analyse the problem of the observation error in detail.

a) Intake Manifold

Figure 8.10 shows the measurement error and the observation error for the intake manifold volume. The errors, e_{M_IM} and e_{OBS_IM} were estimated using Equations 8.12 and 8.13 respectively.

$$e_{M\_IM} = \frac{(\dot{m}_{th} - \dot{m}_{iv})}{\dot{m}_{iv}} 100 \qquad \textbf{8.12}$$

$$e_{OBS\_IM} = \frac{(\hat{\dot{m}}_{iv} - \dot{m}_{iv})}{\dot{m}_{iv}} 100 \qquad \textbf{8.13}$$

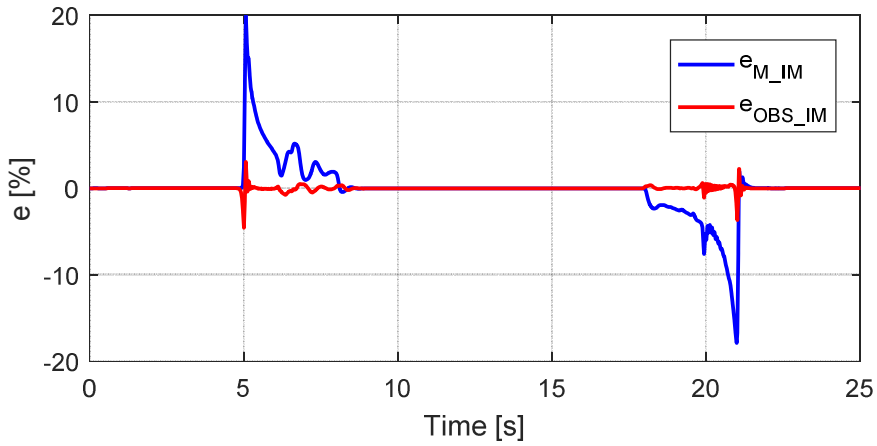

Figure 8.10: Measurement error of the intake manifold versus observation error of the intake manifold for a dual-ramp MAP sweep with 3 seconds ramp time

Although e_{M_IM} reaches up to 18% during the ramp, the observer manages to reduce the error significantly to e_{OBS_IM} < 4%. However, the two spikes at 5 seconds and 22 seconds indicate that there are some dynamics for which the observer cannot compensate. Apart from the two spikes, the results show that the intake manifold observer achieves a very high accuracy even during intensive transients. This can be explained by the fact that the intake manifold volume is very similar to an idealised plenum. Since, in this case, no long pipes are involved, gas dynamics have only a very small impact on the accuracy of the

observed outflow. Filling and emptying is clearly the dominant dynamic effect in the volume and the mean value model based observer compensates well.

b) Intercooler

Figure 8.11 shows the measurement error and the observation error for the intercooler volume. The errors, e_{M_IC} and e_{OBS_IC} were estimated using Equations 8.14 and 8.15 respectively.

$$e_{M\_IC} = \frac{(\dot{m}_c - \dot{m}_{th})}{\dot{m}_{th}} 100 \qquad \textbf{8.14}$$

$$e_{OBS\_IC} = \frac{(\hat{\dot{m}}_{th} - \dot{m}_{th})}{\dot{m}_{th}} 100 \qquad \textbf{8.15}$$

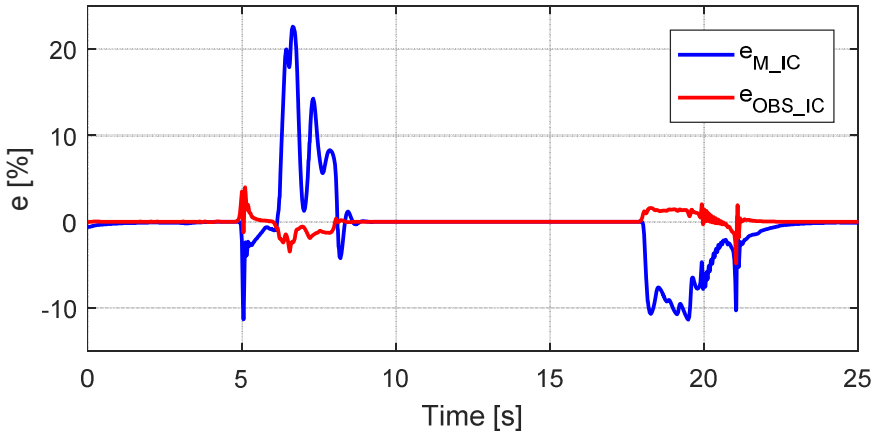

Figure 8.11: Measurement error of the intercooler versus observation error of the intercooler for a dual-ramp MAP sweep with 3 seconds ramp time

Figure 8.11 shows that e_{M_IC} reaches up to 23%. Obviously, e_{OBS_IC} is significantly smaller than e_{M_IC}; however, it is clearly visible that a significant error remains. The significant observation error might be explained by the fact that the intercooler volume consists of a big plenum and two long pipes which connect the intercooler with the compressor and the throttle plate as indicated in Figure 5.2. In the long pipes, gas dynamic effects have a noticeable impact on the spatial variation of gas density, pressure, and velocity. In addition, the fact that the volume is much larger than the intake manifold indicates that the inertia of the gas also has a noticeable impact on the volume inflow and outflow. The investigation results from Figure 8.11 clarify that the volume outflow is not only affected by the filling and emptying dynamics but also by gas dynamic effects. Consequently, the observer of the intercooler volume has a limited accuracy.

c) Intake Volume

Figure 8.12 shows the measurement error and the observation error for the intercooler volume. The errors, $e_{M,IV}$ and $e_{OBS,IV}$ were estimated using Equations 8.16 and 8.17 respectively.

$$e_{M\_IV} = \frac{\left(\dot{m}_{maf} - \dot{m}_c\right)}{\dot{m}_c} 100 \qquad \textbf{8.16}$$

$$e_{OBS\_IV} = \frac{\left(\hat{\dot{m}}_c - \dot{m}_c\right)}{\dot{m}_c} 100 \qquad \textbf{8.17}$$

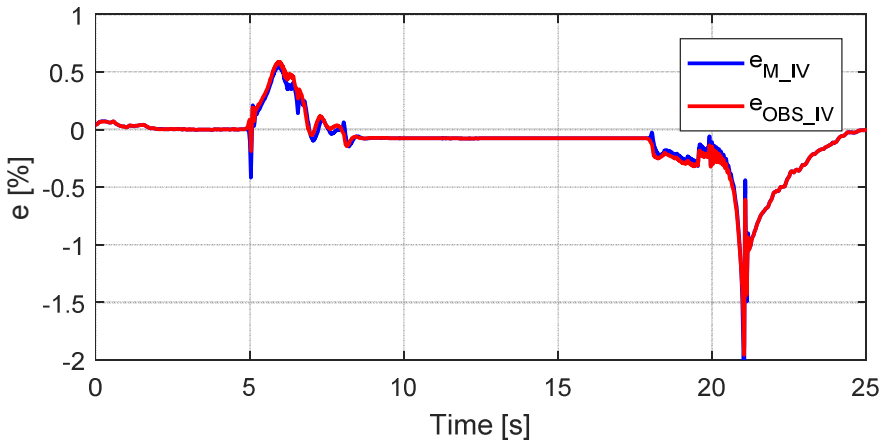

Figure 8.12: Measurement error of the intake volume versus observation error of the intake volume for a dual-ramp MAP sweep with 3 seconds ramp time

Figure 8.12 shows that e_{M_IV} reaches up to 2%. e_{OBS_IV} reveals that the intake volume observer cannot reduce the error at all. This indicates that filling and emptying dynamics are not the dominant dynamic effect in this volume. Studying the engine more closely shows that the volume consists of one long pipe. This indicates that the shape of the volume is vastly different from a plenum where all system states are constant throughout the volume. Consequently, special variation in density, pressure and velocity, as well as the inertia of the gas, have a significant impact on the outflow of the volume. In addition, as shown in Figure 8.7, the pressure in the intake volume P_{IV} changes only very slightly during the entire engine test. If the pressure inside the volume remains almost constant, no significant filling and emptying takes place.

8.3.2 Ramp Time versus Observation Accuracy

Section 8.3 revealed that gas dynamic effects have a significant impact on the accuracy of the observed intake air mass flow during short ramp times.

Consequently, the ramp time has to be limited to a certain value to avoid significant errors in the observed air mass flow into the cylinder. This subsection establishes a trade-off between ramp time and the accuracy of the observed intake air mass flow. For this trade-off, the simulation from Subsection 8.3.1 is repeated for a large range of ramp times. Figure 8.13 and Figure 8.14 show how the RMSE and MAE of the observed air mass flow into the cylinder depends on ramp time.

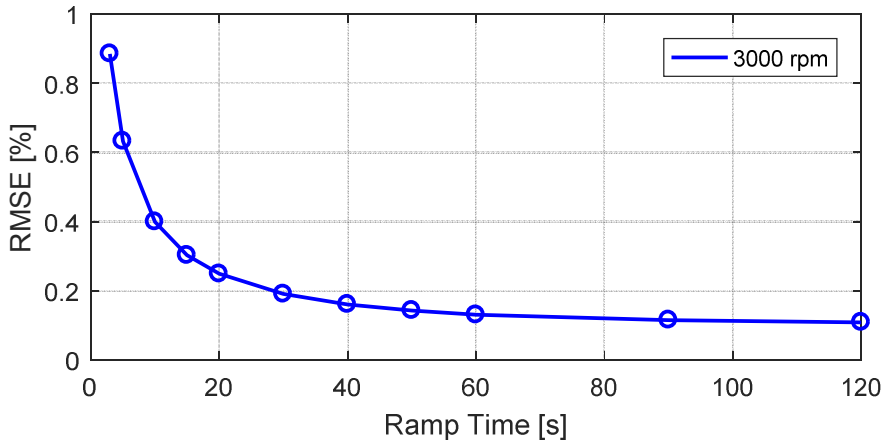

Figure 8.13: RMSE of the total intake system observation error over various ramp times

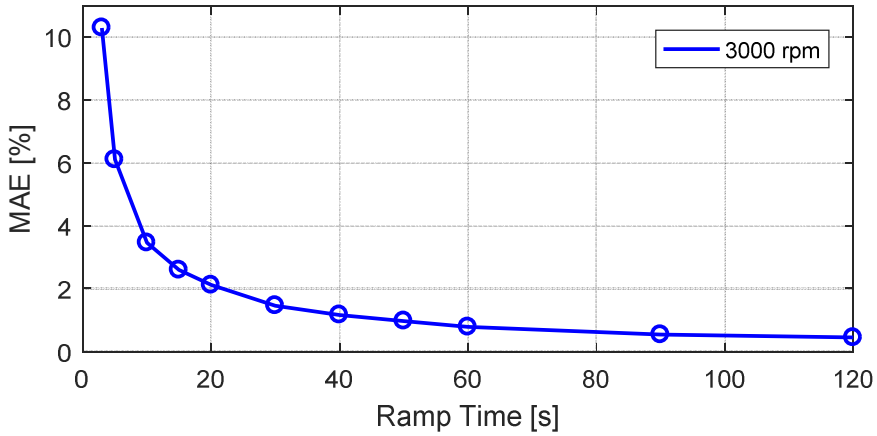

Figure 8.14: MAE of the total intake system observation error over various ramp times

Figure 8.13 and Figure 8.14 show that RMSE and MAE of the observed air mass flow into the cylinder decrease with increasing ramp time. Applying the measure of success of an RMSE < 1% and a maximum error < 2% suggests that a ramp time of 30 seconds is probably the limit that can be used for an accurate engine air charge characterisation.

8.3.3 Observation Error versus Measurement Error

To highlight the benefit of the proposed observer, RMSE and MAE of the observation error are compared to RMSE and MAE of the measurement error in Figure 8.15 and Figure 8.16 respectively.

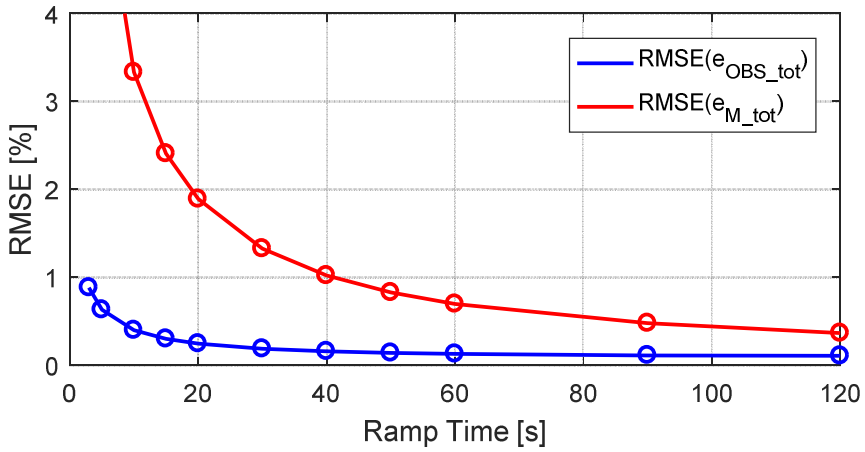

Figure 8.15: RMSE of the total intake system observation error versus RMSE of the total intake system measurement error for various ramp times

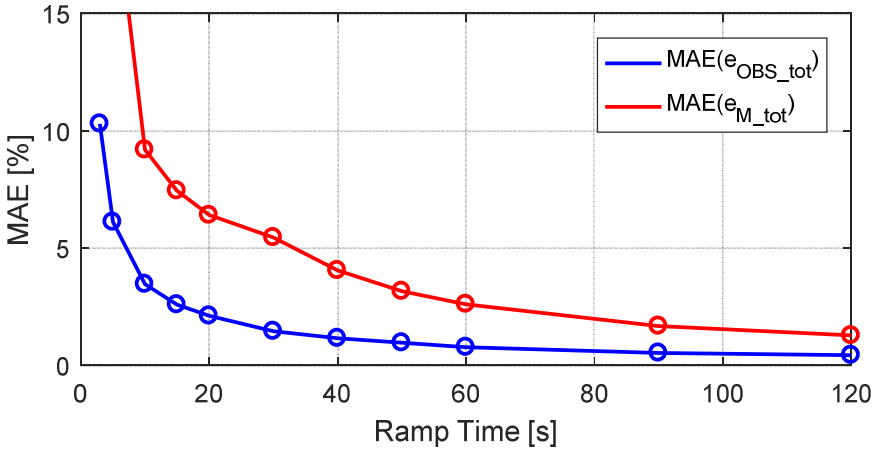

Figure 8.16: MAE of the total intake system observation error versus MAE of the total intake system measurement error for various ramp times

The results show that RMSE and MAE of the observation error are significantly smaller than RMSE and MAE of the measurement error. This shows that the observer achieves a specific measure of success for RMSE and maximum error with a much shorter ramp time. Consequently, the observer is a useful tool to reduce the required test time for engine air charge characterisation.

8.3.4 Dependency on Engine Speed

This subsection repeats the analysis from Subsection 8.3.3 for different engine speeds to investigate if RMSE and MAE of the observed air mass flow into the cylinder is dependent on engine speed. Figure 8.17 and Figure 8.18 show RMSE and MAE of the observation error for six different engine speeds (1000, 2000, 3000, 4000, 5000, and 6000 rpm).

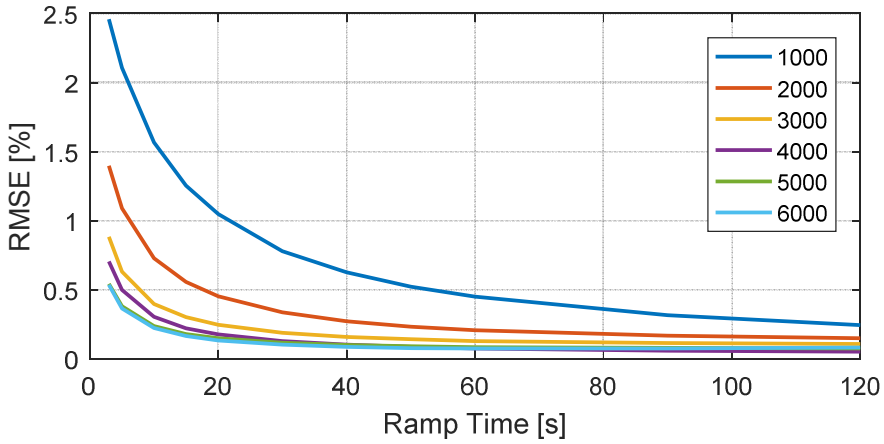

Figure 8.17: RMSE of the total intake system observation error over various ramp times for different engine speeds

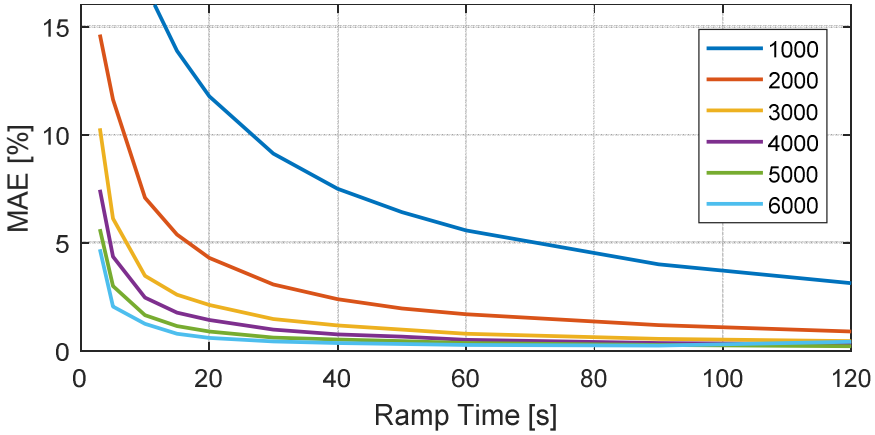

Figure 8.18: MAE of the total intake system observation error over various ramp times for different engine speeds

The results firstly confirm that for all engine speeds RMSE and MAE of the observation error decrease with increasing ramp time. However, the results reveal that the observer works much better on higher engine speeds than it does on the very low engine speeds. Especially for 1000rpm and 2000rpm a significant increase in RMSE and MAE is visible compared to the higher engine speeds. This indicates that the ramp time required to achieve a certain measure of

success in terms of RMSE and MAE has to be a function of engine speed. Clearly, lower engine speeds require longer ramp times while shorter ramp times can be used on the higher engine speeds.

8.3.5 Improvements through Target MAP Signal Smoothing

The results of the detail investigation from Subsection 8.3.1 (Figure 8.9, Figure 8.10, Figure 8.11 and Figure 8.12) show peaks in the observation error at the start and at the end of both ramps (up-ramp and down-ramp). A closer look reveals that the maximum observation error is always located at these peaks. The peaks occur at the time break points T_1 and T_3 on the up-ramp and T_5 and T_6 on the down-ramp which were defined in Section 6.4. This indicates that the observation error is specifically high when the target MAP signal changes the gradient of the ramp. Using a linear ramp results in a step change of the target MAP gradient at the break points T_1, T_3, T_5 and T_6. This leads to the question if it is possible to specifically reduce the maximum observation error by smoothing the target MAP signal with the proposed smoothing algorithm from Subsection 6.4.2. The summary of RMSE and MAE for the observation error for different engine speeds in Subsection 8.3.4 showed particularly high values in the maximum observation error at 2000 rpm. Therefore, in the following, the simulation results from above are repeated at 2000rpm with 6 different smoothing factors (0, 0.2, 0.4, 0.6, 0.8, 1) to investigate if a smoother target MAP signal can help to especially reduce the MAE of the observation error.

Figure 8.19 and Figure 8.20 show RMSE and MAE of the observation error over ramp time for different smoothing factors at 2000 rpm engine speed.

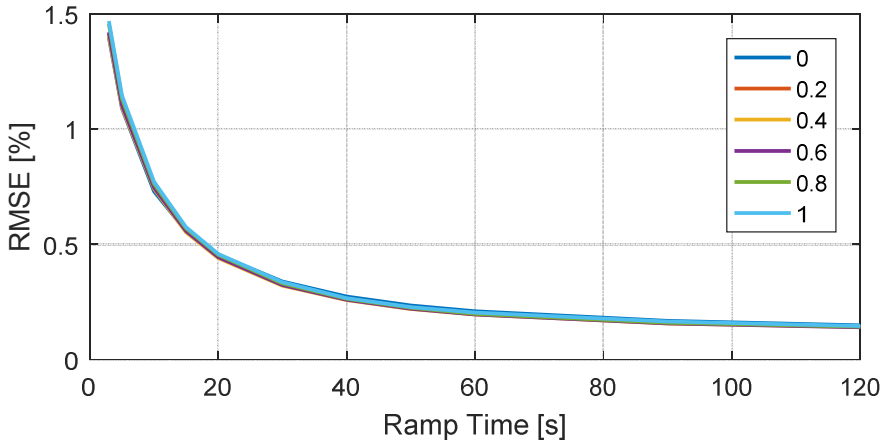

Figure 8.19: RMSE of the total intake system observation error over various ramp times at 2000 rpm engine speed for different smoothing factors

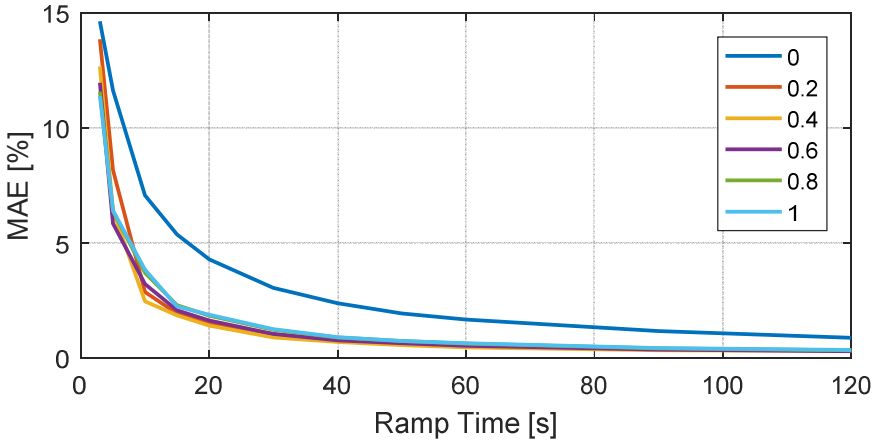

Figure 8.20: MAE of the total intake system observation error over various ramp times at 2000 rpm engine speed for different smoothing factors

The results show a significant reduction in MAE by applying a smoothing factor of 0.2 to the target MAP signal. Using a smoothing factor greater than 0.2 does not lead to any further improvements. Figure 8.19 shows that the smoothing factor has no noticeable impact on the RMSE of the observation error. Therefore, it can be concluded that using a smoothing factor of 0.2 in the target MAP signal P_{IM_Tgt} helps to significantly reduce the MAE of the observation error without any penalties to the RMSE of the observation error.

8.3.6 Investigation Summary

Section 8.3 investigated the accuracy of the developed air-path observer in observing the actual air mass flow into the cylinder during transient engine operation. The detailed investigation in Subsection 8.3.1 showed that the

observer significantly reduces the measurement error caused by excitation of the dynamics in the air-path system. The observer for the intake manifold volume shows a very high accuracy in the observation of the volume outflow. The observer of the intercooler volume shows that the gas dynamics, for which the observer cannot compensate for, have a noticeable impact on the observation accuracy of the volume outflow. The observer of the intake system showed no improvement compared to the measurement error, which indicates that the intake volume is not dominated by filling and emptying dynamics during the dual-ramp MAP sweep. The investigation into ramp time versus observation accuracy in Subsection 8.3.2 showed that RMSE and MAE of the observation error decrease with increasing ramp time. Comparing RMSE and MAE of the observation error with RMSE and MAE of the measurement error in Subsection 8.3.3 highlights the advantage of using the developed air-path observer for rapid engine air charge characterisation. Using the observer achieves a specific measure of success in terms of RMSE and MAE with a much shorter ramp time. Investigating the RMSE and MAE of the observation error for different engine speeds in Subsection 8.3.4 showed that both error measures decrease with increasing ramp time for all engine speeds. However, the results also showed that RMSE and MAE of the observation error are significantly higher at low engine speeds. Subsection 8.3.5 showed that it is possible to significantly reduce the MAE of the observation error by applying a smoothing factor of 0.2 to the target MAP signal without causing any penalties to the RMSE value of the observation error.

8.4 Validation of the Complete Methodology

Using the air-path observer to characterise the volumetric efficiency is a combination of the two problems presented in Sections 8.2 and 8.3. Firstly, the observed air mass flow into the engine is affected by the accuracy of the air-path observer. Secondly, the actual volumetric efficiency identified during the transient operation is not identical to the volumetric efficiency at steady-state conditions. Therefore, comparing the identified volumetric efficiency using the observed air mass flow into the engine with steady-state volumetric efficiency combines the error of the observer with the error in volumetric efficiency during transient operation.

The purpose of this section is to validate the complete methodology. Therefore, the volumetric efficiency is estimated from the observed air mass flow into the

engine during the dual-ramp MAP sweep and finally compared to the volumetric efficiency at steady-state. The achieved accuracy represents the accuracy of the entire methodology. A detailed investigation is provided in Subsection 8.4.1 followed by an investigation into ramp time versus accuracy of observed volumetric efficiency. Subsection 8.4.3 investigates the difference between observation error and measurement error to highlight the advantage of the observer. A summary for different engine speeds is provided in Subsection 8.4.3.

8.4.1 Detailed Investigation

This subsection presents a detailed investigation into the accuracy of the identified volumetric efficiency using the air-path observer. Therefore, results are presented from a dual-ramp MAP sweep with 30 seconds ramp time at 3000 rpm engine speed and constant intake and exhaust camshaft timing.

Figure 8.21 compares the observed volumetric efficiency η_{v_OBS} from a ramp time of 30 seconds with steady-state volumetric efficiency, η_{v_SS}. Figure 8.22 shows the error compared to the steady-state data.

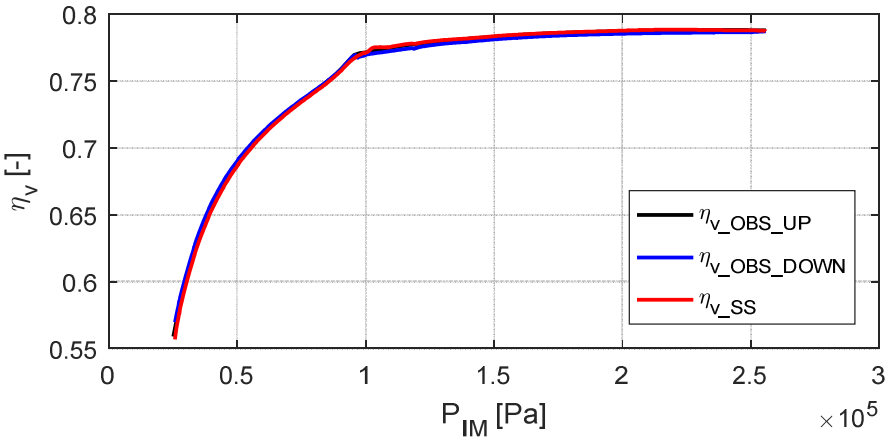

Figure 8.21: Steady-state volumetric efficiency versus observed volumetric efficiency from a dual-ramp MAP sweep with 30 seconds ramp time

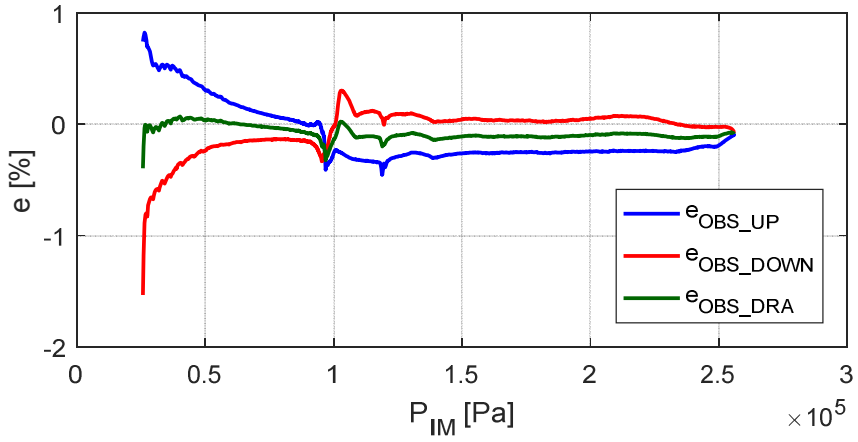

Figure 8.22: Errors between steady-state volumetric efficiency and observed volumetric efficiency from a dual-ramp MAP sweep with 30 seconds ramp time

The results from Figure 8.21 and Figure 8.22 show that a high accuracy is achieved for a ramp time of 30 seconds. The errors during the up-ramp and the down-ramp reach up to a maximum of 1.5%. Applying the dual ramp averaging method reduces the MAE down to 0.4%, which highlights the advantage and importance of DRA.

8.4.2 Ramp Time versus Accuracy of Observed Volumetric Efficiency

This subsection investigates how the ramp time affects the RMSE and MAE of the observed volumetric efficiency. Therefore, the investigation from above is repeated for 11 different ramp times, reaching from three seconds up to 120 seconds. To provide an efficient summary of the investigations, the RMSE and

MAE value between observed volumetric efficiency η_{v_OBS} and steady-state volumetric efficiency η_{v_SS} are analysed. Figure 8.23 and Figure 8.24 plot the RMSE and MAE values over ramp time.

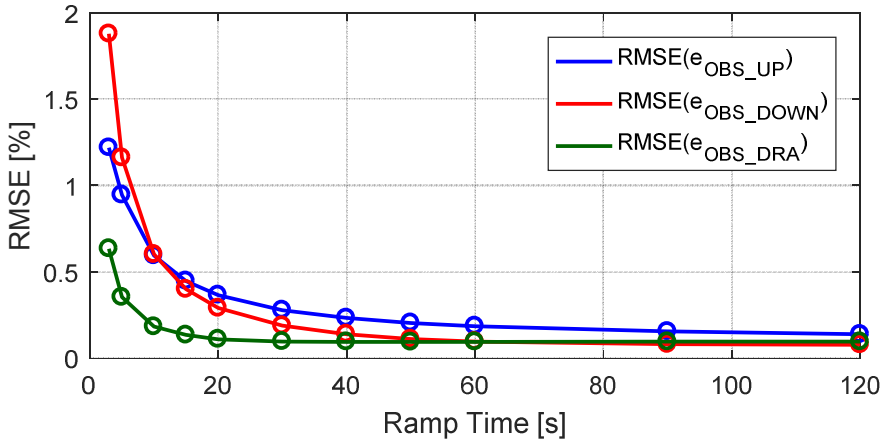

Figure 8.23: RMSE between steady-state volumetric efficiency and observed volumetric efficiency from dual-ramp MAP sweeps with various ramp times

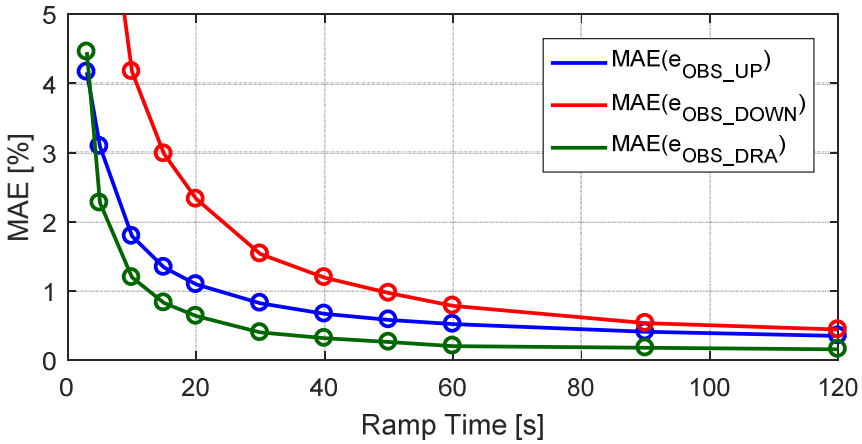

Figure 8.24: MAE between steady-state volumetric efficiency and observed volumetric efficiency from dual-ramp MAP sweeps with various ramp times

The results confirm the findings of Sections 8.2 and 8.3. The RMSE and MAE of the observed volumetric efficiency decrease with increasing ramp time. A sharp rise in both error measures is noticeable for ramp time shorter than 30 seconds. The same results were found for the validity of steady-state volumetric efficiency under transient operation and the observation accuracy of the actual air mass flow into the engine during transient operation. The results above show again the importance of using DRA, specifically in reduction the MAE value. To achieve an identical measure of success in terms of RMSE and maximum errors with the up-ramp or the down-ramp solely would require significantly longer ramp times.

Therefore, it can be concluded that for a specific total engine test time more accurate results are achieved by using the dual-ramp MAP sweep rather than using the entire test time for an up-ramp or a down-ramp only.

8.4.3 Observation Error versus Measurement Error

The advantage of the developed air-path observer is highlighted in this subsection by comparing the observed volumetric efficiency η_{v_OBS} with the MAF-based volumetric efficiency, η_{v_MAF}. Figure 8.25 and Figure 8.26 plot the RMSE and MAE values of the volumetric efficiencies during the up-ramp over ramp time.

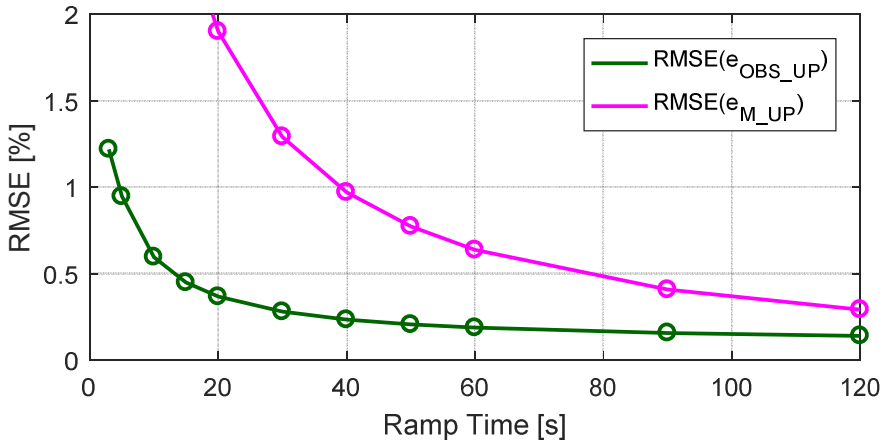

Figure 8.25: RMSE of observed volumetric efficiency versus RMSE of MAF-based volumetric efficiency during the up-ramp of dual-ramp MAP sweeps with various ramp times

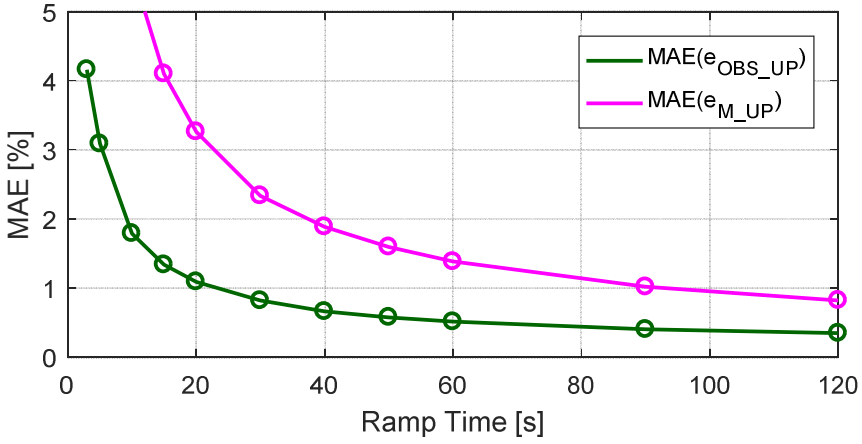

Figure 8.26: MAE of observed volumetric efficiency versus MAE of MAF-based volumetric efficiency during the up-ramp of dual-ramp MAP sweeps with various ramp times

The results in Figure 8.25 and Figure 8.26 show that the observer achieves a significantly lower RMSE and MAE at any ramp time.

Figure 8.27 and Figure 8.28 plot the RMSE and MAE values of the volumetric efficiencies during the down-ramp over ramp time.

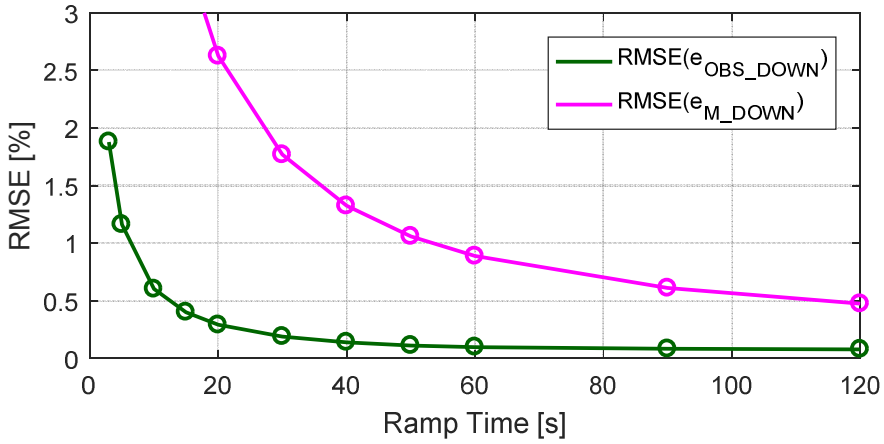

Figure 8.27: RMSE of observed volumetric efficiency versus RMSE of MAF-based volumetric efficiency during the down-ramp of dual-ramp MAP sweeps with various ramp times

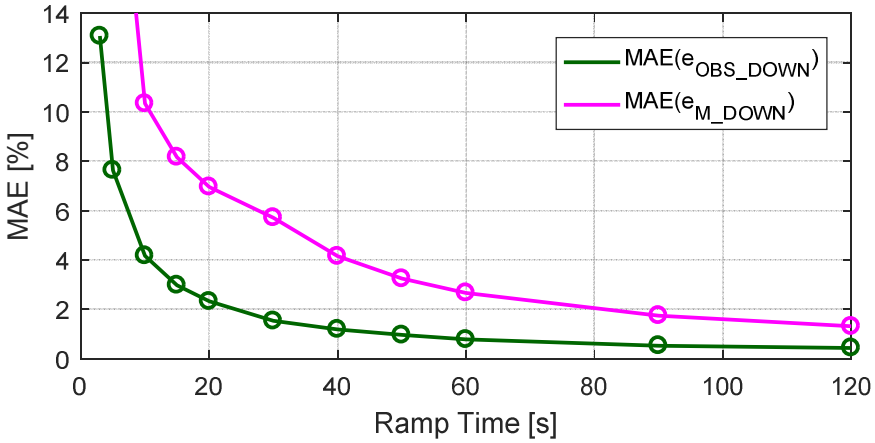

Figure 8.28: MAE of observed volumetric efficiency versus MAE of MAF-based volumetric efficiency during the down-ramp of dual-ramp MAP sweeps with various ramp times

Figure 8.27 and Figure 8.28 show that the observer achieves a significantly lower RMSE and MAE at any ramp time.

Figure 8.29 and Figure 8.30 plot the RMSE and MAE values of the dual ramp averaged volumetric efficiencies over ramp time.

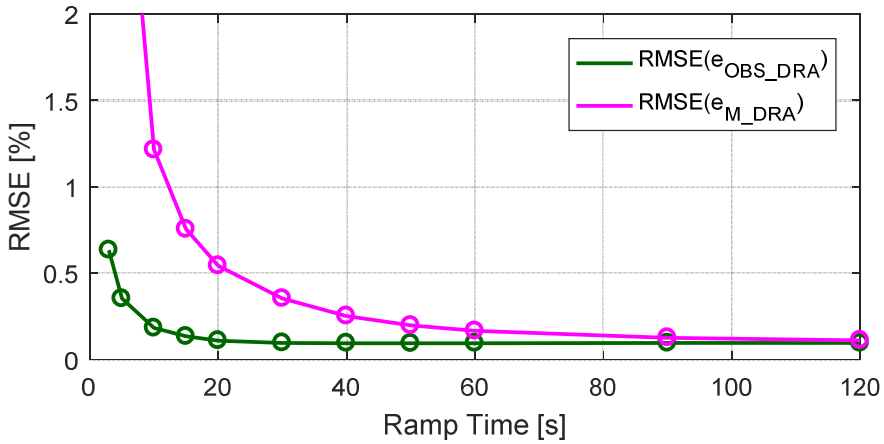

Figure 8.29: RMSE of dual ramp averaged observed volumetric efficiency versus RMSE of dual ramp averaged MAF-based volumetric efficiency over various ramp times

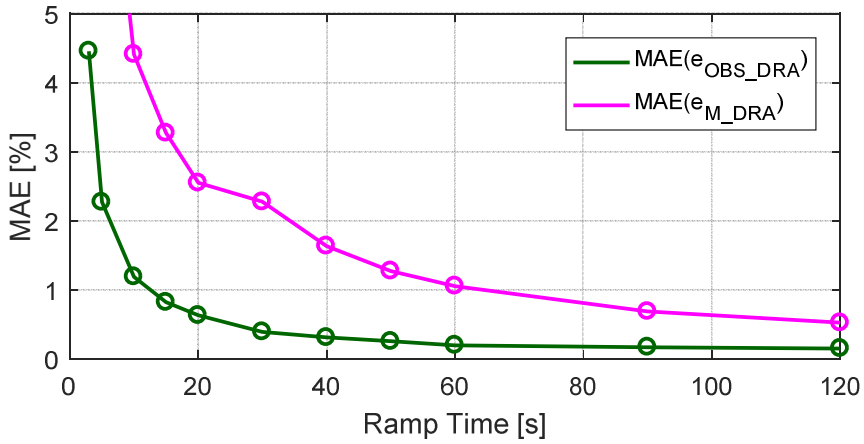

Figure 8.30: MAE of dual ramp averaged observed volumetric efficiency versus RMSE of dual ramp averaged MAF-based volumetric efficiency over various ramp times

Figure 8.29 and Figure 8.30 highlight the significant advantage of using the observer for the air charge characterisation for ramp times shorter than 120 seconds. Figure 8.29 shows an identical RMSE value for a ramp time of 120 seconds. This suggests that for ramp times greater than 120 seconds an identical RMSE performance can be achieved without the observer. However, Figure 8.30 shows that the MAE value for a ramp time of 120 seconds is still significantly lower if the observer is used.

This leads to the conclusion that the observer allows a more accurate characterisation of the volumetric efficiency even for ramp times greater than 120

seconds. For ramp times shorter than 120 seconds the observer leads to a significant improvement of the results.

8.4.4 Dependency on Engine Speed

The investigation into the accuracy of the observed volumetric efficiency compared to steady-state data is repeated for six different engine speeds, reaching from 1000 rpm to 6000 rpm.

Figure 8.31 and Figure 8.32 show the results for RMSE and MAE of dual-ramp averaged observed volumetric efficiency for six different engine speeds.

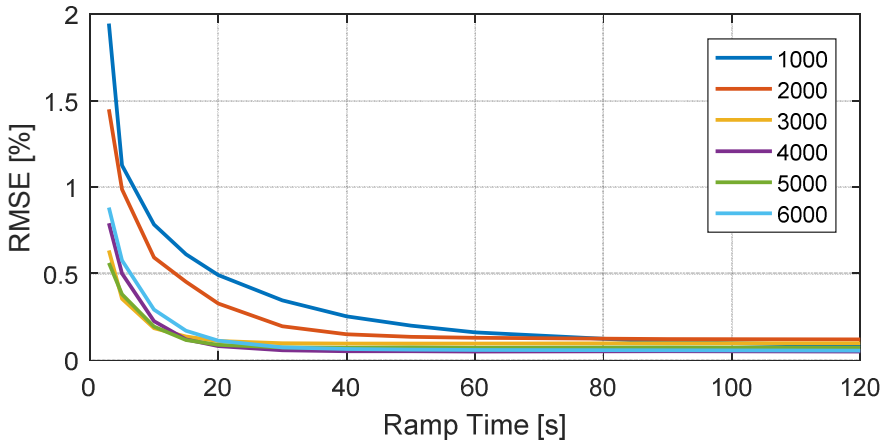

Figure 8.31: RMSE of dual ramp averaged observed volumetric efficiency over various ramp times for different engine speeds

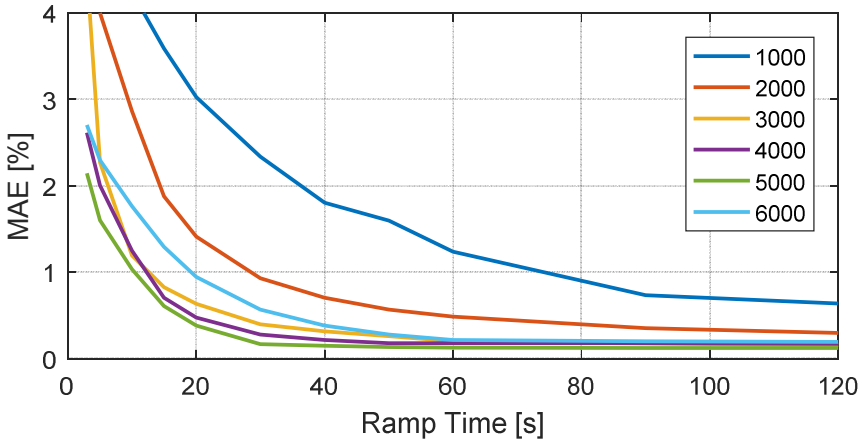

Figure 8.32: MAE of dual ramp averaged observed volumetric efficiency over various ramp times for different engine speeds

Figure 8.31 and Figure 8.32 confirm that RMSE and MAE of the observed volumetric efficiency decrease with increasing ramp time for every engine speed. However, the results reveal that both error measures show a significant increase

for lower engine speeds. While there is almost no difference in RMSE and MAE between 3000 rpm to 6000 rpm, the errors for 2000 rpm and in particular for 1000 rpm are significantly higher. Consequently, the ramp time required to achieve a specific measure of success in terms of RMSE and MAE depends on engine speed. The results show that engine speeds below 2000 rpm require a significantly longer ramp time specifically to eliminate high values in MAE.

8.4.5 Investigation Summary

The accuracy of the entire methodology was considered in Section 8.4. Therefore, the volumetric efficiency identified from the observed air mass flow into the engine during a dual-ramp MAP sweep was compared to steady-state data. The results from Subsection 8.4.1 showed that the RMSE and the MAE of the identified volumetric efficiency rise sharply for ramp times shorter than 30 seconds. The results in Subsection 8.4.2 also highlighted that dual ramp averaging significantly reduces the remaining error compared to the error on the up-ramp and the down-ramp. A dual-ramp MAP sweep with a specific ramp time takes a total test time of x-seconds. If these x-seconds were used to only ramp intake manifold pressure up or down, this would result in a significantly higher RMSE and MAE compared to the dual-ramp MAP sweep with DRA. Therefore, it can be concluded that DRA also helps to reduce the required test time to achieve a specific measure of success in terms of RMSE and MAE. The investigation into observation versus measurement accuracy in Subsection 8.4.3 highlighted the advantage of the developed observer. Identifying the volumetric efficiency from the observed air mass flow into the engine is by far more accurate than estimating the volumetric efficiency directly from the measured air mass flow at the location of the MAF sensor. A specific measure of success in terms of RMSE and maximum error can be achieved with a much shorter ramp time if the observer is used. The results showed that very long ramp times would be required to achieve a good measure of success in case no observer is used.

8.5 Summary

Chapter 8 provides a deep investigation into the accuracy of the entire methodology. The investigation into steady-state versus transient volumetric efficiency in Section 8.2 showed that it is possible to achieve a sufficiently accurate identification of the volumetric efficiency using dynamic engine test

results. However, the results revealed that there is a physical limitation to the ramp time since steady-state and transient volumetric efficiency are not entirely identical. In fact, it was shown that the difference depends on the intensity of the dynamic excitation. Section 8.3 investigated the accuracy of the observer in observing the air mass flow into the cylinder during transient engine operation. The results showed that a highly accurate observation is achievable for ramp times down to 30 seconds. For even faster ramps, the RMSE and MAE of the observed air mass flow into the cylinder increase sharply. A summary for different engine speeds show that the observer is more accurate at higher engine speeds than it is at low engine speeds. Observation errors are significantly higher for engine speeds smaller than 2000 rpm. Finally, the entire methodology was validated in Section 8.4. The results confirm the findings from Sections 8.2 and 8.3. A sharp rise in the error of the identified volumetric efficiency is noticeable for ramp times shorter than 30 seconds. The results also highlighted the advantage of dual-ramp averaging the volumetric efficiency identified over the up-ramp and the down-ramp, which significantly reduces the remaining error. In addition, it was shown that using the observer achieves a much higher accuracy compared to estimating the volumetric efficiency directly from the measured air mass flow. A summary for six different engine speeds shows that for engine speeds below 2000 rpm, a significantly longer ramp time is required to achieve a specific measure of success in terms of RMSE and maximum error.

Chapter 9 Experimental Validation

In this chapter, the developed methodology is validated using experimental data from a real engine. The test rig including all components is introduced in Section 9.1. The details of the experimental data collection are discussed in Section 9.2. A measure of success is established based on the repeatability of conventional steady-state data in Section 9.3. Section 9.4 validates the complete methodology. The observed volumetric efficiency is compared to the steady-state reference data. This includes a detailed investigation into a trade-off between ramp time and accuracy followed by a summary for different engine speeds with a constant ramp time. Section 9.5 is specifically focused on the time saving achieved with the developed methodology compared to conventional steady-state testing and quasi stead-state testing.

9.1 Test Rig

This section presents the details of the experimental test rig. Subsection 9.1.1 gives an overview over the entire test cell. Subsection 9.1.2 includes all technical specifications of the engine used to produce the experimental results. Subsection 9.1.3 presents the measurement equipment which includes all sensors and the data acquisition system.

9.1.1 Engine Test Cell

Figure 9.1 shows the engine test cell at Loughborough University.

Figure 9.1: Engine test cell at Loughborough University

The core of the test cell is the transient engine dynamometer, which is controlled by AVL Puma software. The engine on the dyno is controlled through the ATI Vision software which allows a direct interface into the ECU to control all engine actuators. Figure 9.2 shows the control panels.

Figure 9.2: Engine test cell control panel

The ATI software is connected to AutoTEST which is software developed by Ford to control the engine actuators and protect the engine during the test. The entire

code of the developed methodology for rapid air charge characterisation is implemented in MATLAB. The AutoTEST software communicates with MATLAB through Microsoft Messaging Queues (MSMQ) to run the analysis directly after the data collection for a specific sweep is finished. This allows a very high level of automation for the entire testing process and maximises the efficiency of the data collection process.

Figure 9.3 shows the data acquisition system in the test room.

Figure 9.3: ATI EMX data acquisition modules

All measurement signals are recorded through the ATI EMX modules [156]. Using only one data acquisition system to record all measurement signals is crucial for dynamic engine testing to avoid any errors in data time alignment between different acquisition systems. All analogue signals are plugged into the EMX IOM.SPS16 module and all thermocouples are plugged into the EMX IOM.TC30 module. Both modules are connected to ATI software, which triggers the recorder.

9.1.2 Engine

Figure 9.4 shows the engine used for the experimental results.

Figure 9.4: Ford 1 litre GTDI engine

The engine is a Ford 1.0 litre Gasoline Turbocharged Direct Injection engine. The technical specifications of the engine are tabulated in Table 9.1.

Table 9.1: Engine technical specifications

Parameter	Value	Unit
Engine Capacity	998	Cc
Compression Ratio	10.5:1	-
Number of Cylinders	3	-
Cylinder Bore	71.9	mm
Cylinder Stroke	81.88	mm
Maximum Power	92	KW
Maximum Torque	200	Nm

9.1.3 Measurement Equipment

This subsection provides all the details of test cell measurement equipment. This includes the air mass flow meter, the pressure sensors and the temperature sensors.

a) Air Mass Flow Meter – AVL FLOWSONIC

Figure 9.4 shows the AVL FLOWSONIX [32] air mass flow meter.

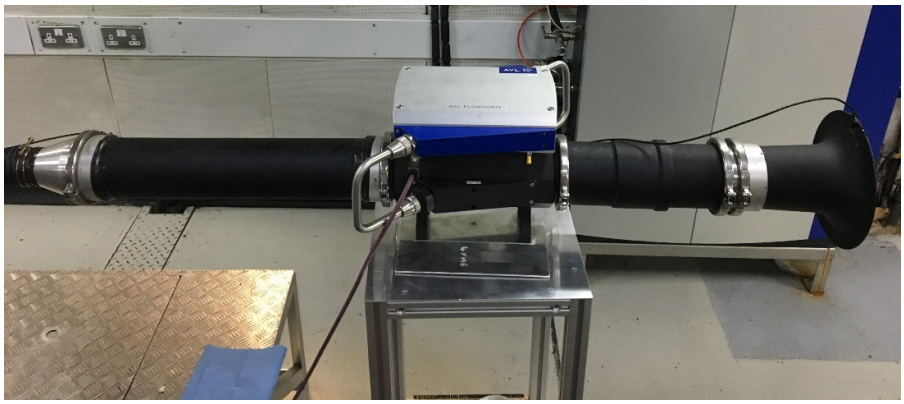

Figure 9.5: AVL FLOWSONIX air mass flow meter in test cell

The measurement device has a laminar flow element in the middle of the tube. An ultrasonic principle is used to measure the velocity of the air through the laminar flow element. A pressure and a temperature sensor are used to measure the density of the air. The air mass flow is then calculated by combining the measurements of velocity and density. The technical specifications of the air flow meter are given in Table 9.2.

Table 9.2: AVL FLOWSONIX air mass flow metre technical specifications

Parameter	Value	Unit
Measurement Range	1400	kg/h
Response Time	T_{90} < 10	ms
Reproducibility	$\pm$0.25	%
Measurement Accuracy	$\pm$1	%

The major advantage of this air mass flow meter is the negligible response time. Consequently, the measurement device allows an instantaneous measurement of the actual air mass flow at the location of the sensor. This is crucial for dynamic engine testing to avoid any measurement errors caused by sensor response delays.

b) Pressure Sensors

Figure 9.6 shows one of the pressure sensors used to measure the pressure along the engine air-path.

Figure 9.6: DRUCK pressure transducer

Two different DRUCK sensors are used with different measurement ranges. The table below gives the technical specifications of both sensors.

Table 9.3: DRUCK pressure transducer technical specifications

Parameter	High Range	Low Range	Unit
Measurement Range	0 to 700	0 to 25	kPa
Response Time	±0.15	±0.15	%

All pressure sensors are gauge sensors. An absolute ambient pressure sensor is installed in the test cell to estimate the absolute pressures at each measurement location.

c) Temperature Sensors

For temperature measurement, two different types of thermocouples are used. Shielded thermocouples are used in locations such as ambient temperature, since no rapid change in temperature is expected.

Figure 9.7 shows the shielded thermocouple.

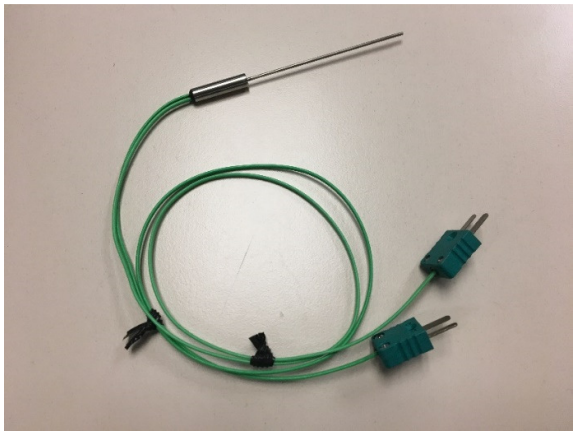

Figure 9.7: Standard shielded thermocouple

The shielded thermocouples have a diameter of 1.5 mm.

For temperature measurement along the intake system, custom-made bare wire thermocouples are used, as shown in Figure 9.8.

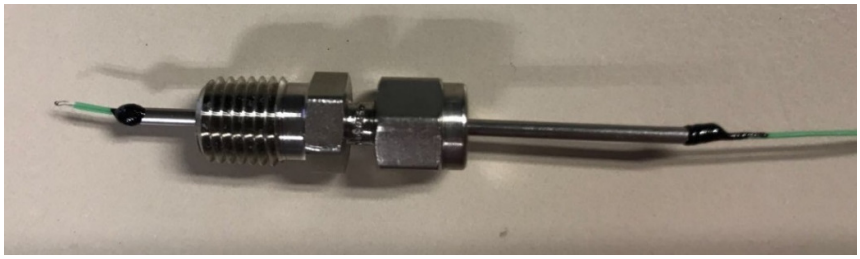

Figure 9.8: Ultra-fast responding bare wire thermocouple

The bare wire of the thermocouple has a diameter of only 0.08 mm. Shielded thermocouples are not suitable for temperature measurement along the air-path during dynamic engine testing since they have a significant response delay. As shown by Schaal [53], the bare wire thermocouples have an ultra fast response time of approximately 0.1 seconds. The bare wire thermocouples are installed at the compressor inlet, compressor outlet, intercooler outlet and in the intake manifold.

9.1.4 Engine Air-Path Controller

Section 6.5 presents two different engine control strategies, which allow controlling the intake manifold pressure during a dual-ramp MAP sweep. However, the experimental data presented in the following were collected during the development phase of this work. Unfortunately, the closed-loop controller was not implemented in the engine test cell by the time of the data collection. However, the engine under test was already fully calibrated; therefore, accurate feed-forward models for throttle and waste gate were available. The open loop-control strategy used to collect the data is illustrated in Figure 9.9.

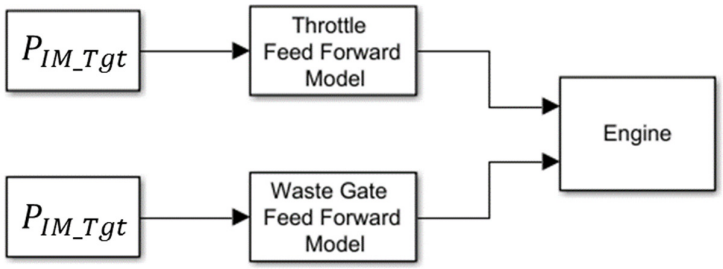

Figure 9.9: Engine air-path controller used for experimental data collection

The target MAP signal P_{IM_Tgt} is generated using Equation 6.14 and the throttle and waste-gate position are directly set using the feed-forward models. Since the feed-forward models are not 100% accurate, the resulting ramps are not perfectly linear. However, this does not affect the accuracy of the data since linearity of the ramps is not important. It is only required that the up-ramp and the down-ramp are symmetrical in order to apply the dual-ramp averaging method presented in Section 6.7. This is certainly achieved with this air-path controller since identical actuator settings are used over the up-ramp and on the down-ramp.

It should be noted that in order to apply the developed methodology to a completely new engine where no feed-forward models are available, the use of the closed-loop air-path controller presented in Subsection 6.5.2 is required. Experimental results using the closed-loop control strategy will be published as soon as the implementation of the project is finished.

9.2 Experimental Data Collection

This section provides the details of the experimental data collection. Subsection 9.2.1 is focused on conventional steady-state data. Quasi steady-state data are treated in Subsection 9.2.2. Subsection 9.2.3 covers the dynamic test data. All three subsections investigate the repeatability of each engine testing method. Based on the results of the repeatability study, a measure of success is established in Section 9.3 to judge the accuracy of the developed methodology.

As mentioned in Subsection 2.1.1, conventional steady-state data are produced by holding all actuator settings constant for a specific amount of time until the engine is at steady-state. After that, data are recorded and then averaged over the recording period. However, the simulation results from Section 8.4 indicate that if the ramp rate is long enough, volumetric efficiency during the dual-ramp MAP sweep is identical to steady-state volumetric efficiency. This theory is known as Slow Dynamic Slope testing (SDS) which is reviewed in Subsection 2.1.2. In Subsection 9.2.2, the repeatability and accuracy of the SDS method is compared to conventional steady-state testing to decide which method is more suitable for the collection of the steady-state reference data which will be used in Section 9.4 to validate the developed methodology.

9.2.1 Conventional Steady-State Data

The conventional steady-state data were collected as described in Subsection 2.1.1. For the first 30 seconds throttle and waste gate position are adjusted to set the test point. After that, all actuator settings are held constant for 60 seconds to ensure all engine parameters have settled. Finally, data are recorded over 30 seconds and averaged over the recording time to eliminate the effect of measurement noise.

To investigate the repeatability of steady-state data, an air charge curve at 2905 rpm engine speed was repeated three times. Figure 9.10 shows η_v for the three repeated sweeps.

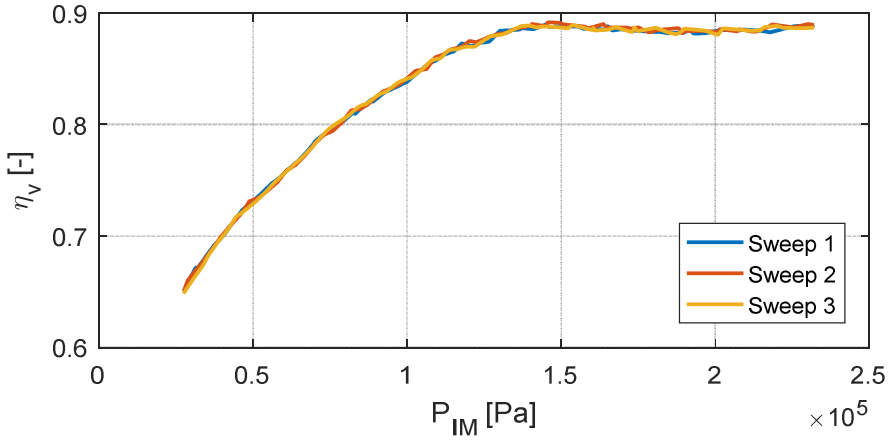

Figure 9.10: Repeatability of conventional steady-state data

To judge the repeatability of conventional steady-state data some statistical measures are required. Repeated measures would be the correct statistical theory to use since three independent datasets were collected. However, repeated measures is a very complex statistical analysis. To simplify the statistical analysis, a simpler approach is used here to get an approximation of the data repeatability. Since only three repeated data sets are available, robust statistics are required to minimise the effect of any data outliers. Therefore, the Median Absolut Deviation (MAD) is used to judge the repeatability. At first, the MAD of the three data sets is estimated. Using the maximum value and the mean value of the estimated MAD establishes a maximum and a mean variance of conventional steady-state data. The data presented in Figure 9.10 lead to the following values:

- $maxMAD_{CSS}$ = 0.0024

- $meanMAD_{CSS}$ = 0.0012

9.2.2 Slow Dynamic Slope Data

The SDS data were collected using the engine control strategy presented in Subsection 9.1.4. A ramp time of 15 minutes was used to ensure that the engine is in quasi steady-state. Figure 9.11 shows P_{IM} during the dual-ramp MAP sweep with 2905 rpm engine speed.

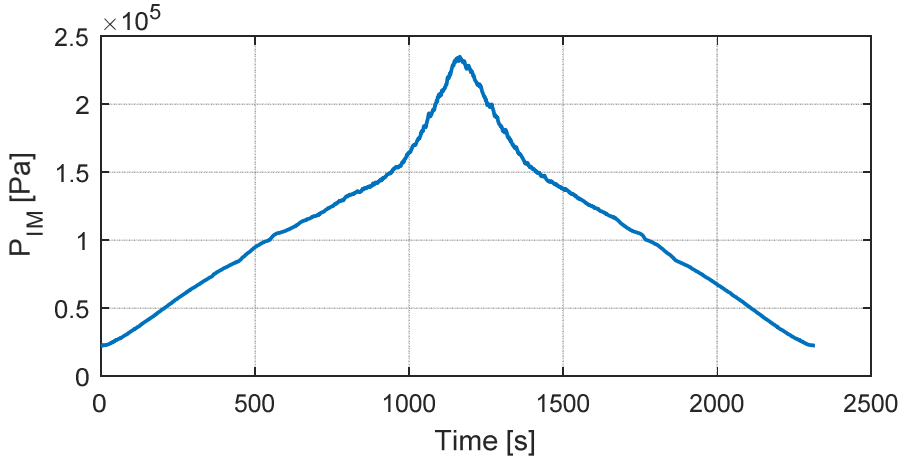

Figure 9.11: Dual-Ramp MAP sweep using SDS testing method

To investigate the repeatability of slow dynamic slope data, an air charge curve at 2905 rpm engine speed was repeated three times. Figure 9.12 shows dual ramp averaged η_v for the three repeated sweeps.

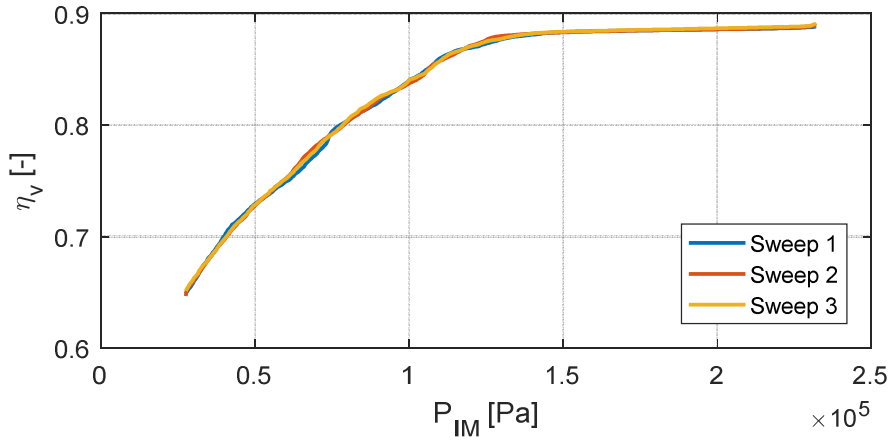

Figure 9.12: Repeatability of slow dynamic slope data

The data from Figure 9.12 lead to the following values for repeatability:

- $maxMAD_{SDS}$ = 0.0038
- $meanMAD_{SDS}$ = 0.00105

The repeatability analysis shows that the SDS data have a smaller mean value of the MAD compared to the conventional steady-state data. This suggests that on average SDS data are more repeatable than conventional steady-state data. However, the data also show that the maximum MAD of the SDS data is slightly higher than the maximum MAD value of the conventional steady-state data. In the following, the accuracy of SDS data is compared to conventional steady-state data.

An important question for slow dynamic slope testing is how slow the ramp has to be in order to guarantee that the engine is indeed in quasi steady-state. To answer this question, a single SDS sweep is investigated. Figure 9.13 plots the η_v of the up-ramp and down-ramp over P_{IM}.

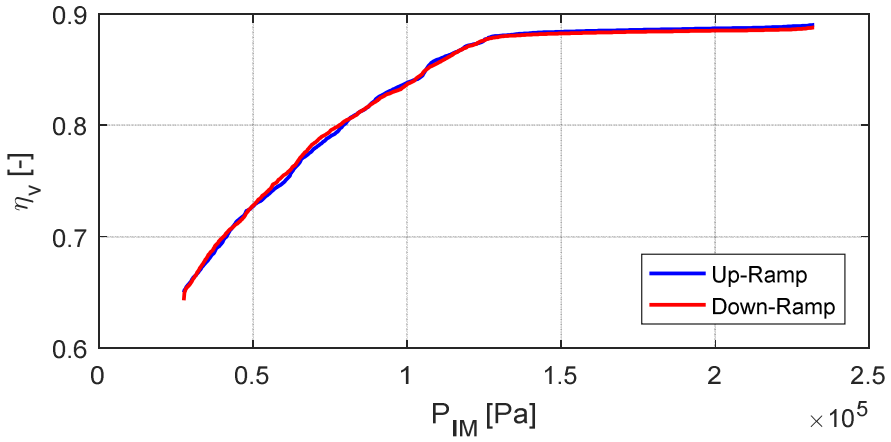

Figure 9.13: Volumetric efficiency from a dual-ramp MAP sweep using SDS testing

The data in Figure 9.13 show an extremely small hysteresis between the up-ramp and the down-ramp. Computing the mean and maximum MAD between the data for the up-ramp and the down-ramp gives the following values:

- $maxMAD_{SDS,up/down}$ = 0.0036
- $meanMAD_{SDS,up/down}$ = 0.00132

The maximum MAD and mean MAD between the up-ramp and the down-ramp show a similar magnitude as the maximum MAD and mean MAD of the SDS repeatability study. This means that the engine is in quasi steady-state during the SDS test since the mean deviation between the up-ramp and the down-ramp has a similar value to the mean deviation between repeated sweeps. This study was repeated with a few different ramp times and the results showed that a ramp time

of approximately 15 minutes is required to end up with a small enough hysteresis which agrees with the conclusion stated above.

To compare the accuracy of SDS data with conventional steady-state data, the median η_v over the three SDS sweeps is compared to the median η_v over the three conventional steady-state sweeps. Figure 9.14 shows η_v over P_{IM} for SDS and convention steady-state data.

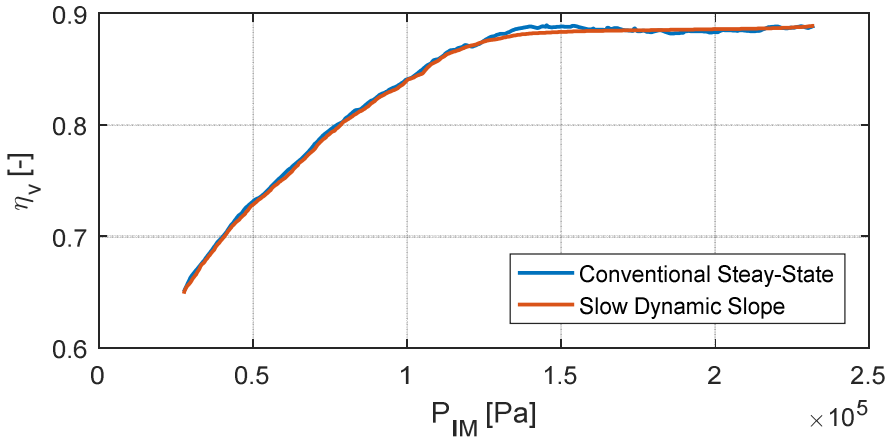

Figure 9.14: Conventional steady-state testing versus SDS testing

Computing the MAD value for the two curves gives the following results:

- $maxMAD_{CSS,SDS}$ = 0.0033
- $meanMAD_{CSS,SDS}$ = 0.00156

The results of the MAD values between the conventional steady-state data and the SDS data are only slightly higher than the MAD values of the conventional steady-state repeatability. Therefore, it can be concluded that there is no noticeable difference in terms of accuracy between SDS data and conventional steady-state data. The MAD values of the SDS repeatability indicate that SDS testing is slightly more repeatable than conventional steady-state testing.

Based on these results, the decision was made to collect the steady-state reference data with the SDS testing method. This has two main reasons.

1. **Data Quality**: The results above showed that the SDS testing method provides a slightly higher repeatability than the traditional steady-state data. Therefore, using the SDS method to produce the steady-state reference data will provide a more solid reference since the results are more repeatable.

2. **Time Saving**: Using the SDS testing method instead of the traditional steady-state method allows to save approximately 66% of time in the data collection process. The reader is referred to Section 9.5 for details of this approximation.

9.2.3 Dynamic Data

Before the experimental results of the fast dual-ramp MAP sweeps can be compared to steady-state data, it is necessary to prove that also the dynamic data have a high repeatability. The dynamic data were collected using the engine control strategy presented in Subsection 9.1.4. A ramp time of 120 seconds was used for the repeatability study. Figure 9.15 shows P_{IM} during the dual-ramp MAP sweep with 2905 rpm engine speed.

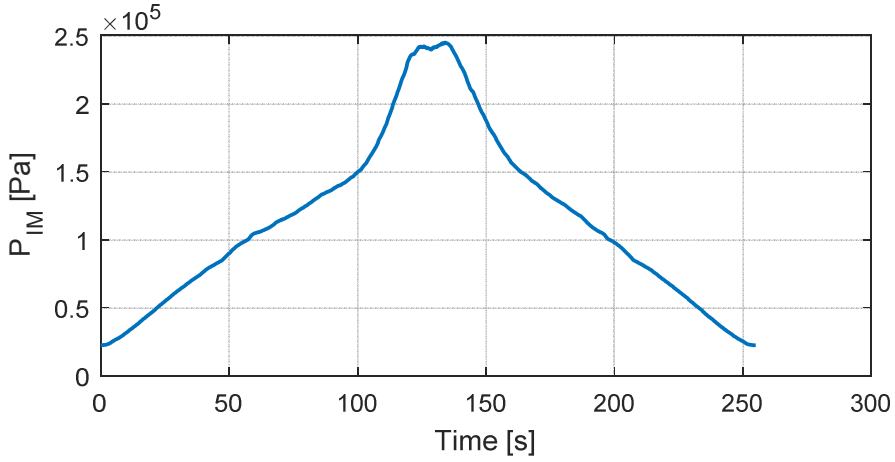

Figure 9.15: Dual-Ramp MAP sweep using dynamic testing method

To investigate the repeatability of slow dynamic slope data, an air charge curve at 2905 rpm engine speed was repeated three times. Figure 9.16 shows dual ramp averaged η_v for the three repeated sweeps.

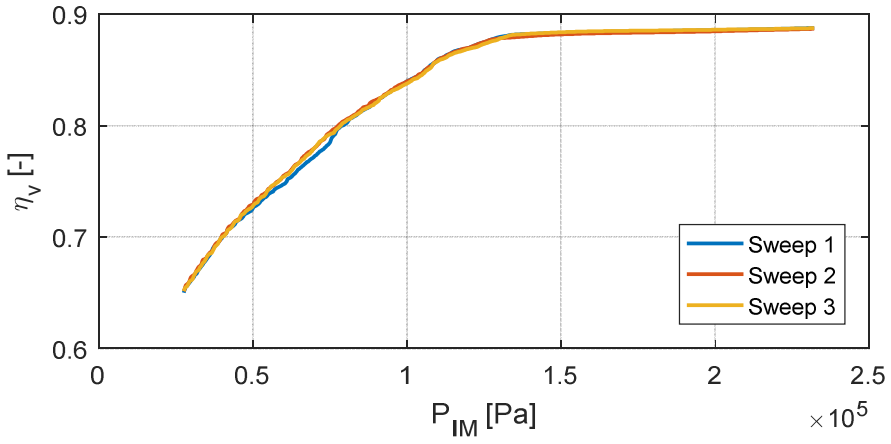

Figure 9.16: Repeatability of dynamic data

The data from Figure 9.16 lead to the following values for repeatability:

- $maxMAD_{DYN}$ = 0.0035
- $meanMAD_{DYN}$ = 0.00112

The fact that the dynamic data achieve a lower Mean MAD suggests that that on average, the dynamic data have a higher repeatability than conventional steady state data. The value is almost identical to the Mean MAD of SDS data. Therefore, it can be concluded that the dynamic data achieve a high repeatability.

9.3 Definition of Measure of Success

To judge if the methodology developed delivers the required data accuracy for the engine mapping process, a measure of success is required. Once a measure of success is available, a trade-off between time saving and accuracy can be established. To establish a measure of success, the repeatability of dynamic data and SDS data has to be considered. The repeatability of quasi steady-state data show $maxMAD_{SDS}$ = 0.0038 and $meanMAD_{SDS}$ = 0.00105. The repeatability of dynamic data show $maxMAD_{DYN}$ = 0.0035 and $meanMAD_{DYN}$ = 0.00112. Since both testing methods have an almost identical maximum and mean MAD values, it can be concluded that both methods have a similar repeatability. Therefore, using the dynamic testing method does not introduce an additional error into the measurement results due to repeatability.

The $maxMAD_{SDS}$ = 0.0038 translates roughly into an $\pm$0.4% to $\pm$1% error in volumetric efficiency depending on the value of volumetric efficiency, which is roughly between 0.4 and 1. Therefore, $\pm$1% is regarded as the standard

deviation. All test data for the repeatability analysis were recorded on one day. To account for day-to-day variability, a $\pm 2\sigma$ is used to define the measure of success. Therefore, the measure of success is defined as $\pm$2% for the maximum error.

The $meanMAD_{SDS}$ = 0.00105 translates roughly into a $\pm$0.1% to $\pm$0.25% RMSE in volumetric efficiency depending on the value of volumetric efficiency. Therefore, $\pm$0.25% RMSE is regarded as the standard deviation. To account for day-to-day variability, a $\pm 2\sigma$ is used, which gives $\pm$0.5%. An additional 0.5% error can be tolerated as trade-off to save as much time as possible. Consequently, the measure of success for RMSE is defined as $\pm$1%.

9.4 Validation of the Complete Methodology

The purpose of this chapter is to validate the accuracy of the complete methodology using experimental test data. The structure of this section is identical to Section 8.4, which investigates the accuracy of the methodology using simulation data. The volumetric efficiency is estimated from the observed air mass flow into the engine during the dual-ramp MAP sweep and finally compared to the volumetric efficiency at steady-state. The achieved accuracy represents the accuracy of the entire methodology. A detailed investigation is provided in Subsection 9.4.1 and followed by the trade-off between ramp time and accuracy in Subsection 9.4.2. Subsection 9.4.3 compares the observation error to the pure measurement error and Subsection 9.4.4 provides a summary for different engine speeds. The entire section uses the error measures defined in Subsection 8.1.3.

9.4.1 Detailed Investigation

A detailed investigation into the accuracy of the identified volumetric efficiency using the air-path observer is provided in this subsection. Therefore, results are presented for a ramp time of 60 seconds at 3000 rpm engine speed and constant intake and exhaust camshaft timing.

Figure 9.17 compares the observed volumetric efficiency η_{v_OBS} from a ramp time of 60 seconds with steady-state volumetric efficiency η_{v_SS}. Figure 9.18 shows the error compared to the steady-state data.

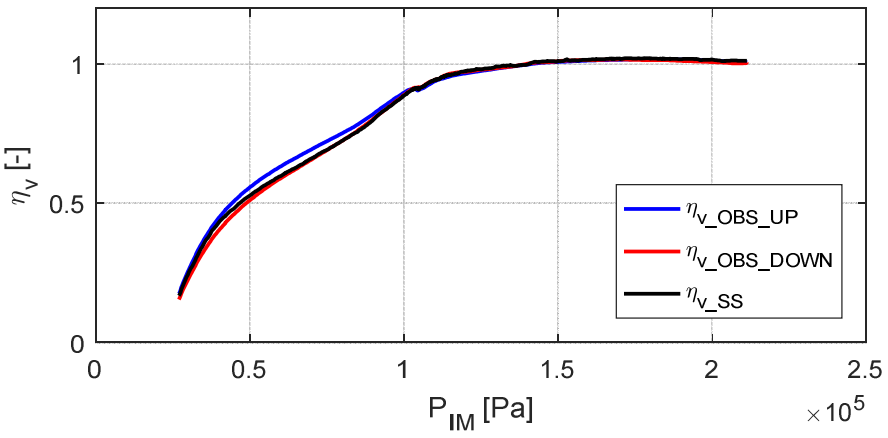

Figure 9.17: Steady-state volumetric efficiency versus observed volumetric efficiency from a dual-ramp MAP sweep with 60 seconds ramp time

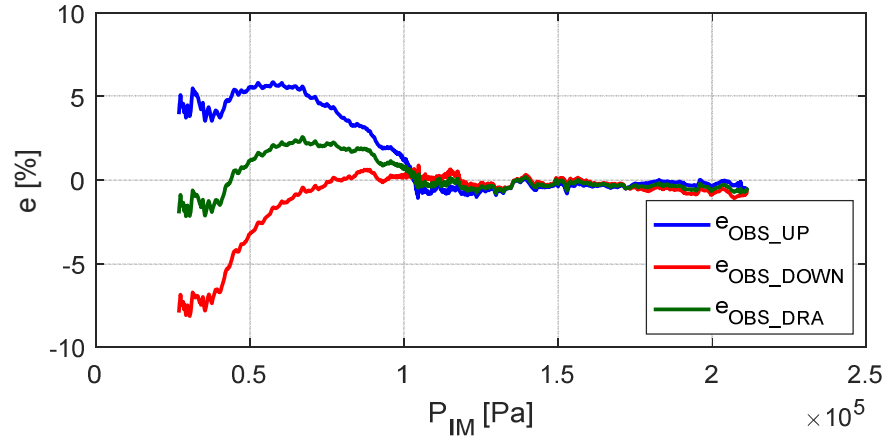

Figure 9.18: Errors between steady-state volumetric efficiency and observed volumetric efficiency from a dual-ramp MAP sweep with 60 seconds ramp time

The results from Figure 9.17 and Figure 9.18 show significant errors in the observed volumetric efficiency during the up-ramp and the down-ramp, especially at low intake manifold pressures. The results demonstrate the efficiency of applying the dual-ramp averaging method which allows to reduce the maximum error to less than 2%.

9.4.2 Ramp Time versus Accuracy of Observed Volumetric Efficiency

This subsection investigates how the ramp time affects the RMSE and MAE of the observed volumetric efficiency. Therefore, the investigation from above is repeated for seven different ramp times, ranging from 10 seconds to 450 seconds. To provide an efficient summary of the investigations, the RMSE and

MAE value between observed volumetric efficiency η_{v_OBS} and steady-state volumetric efficiency η_{v_SS} are analysed. Figure 9.19 and Figure 9.20 plot the RMSE and MAE values over ramp time.

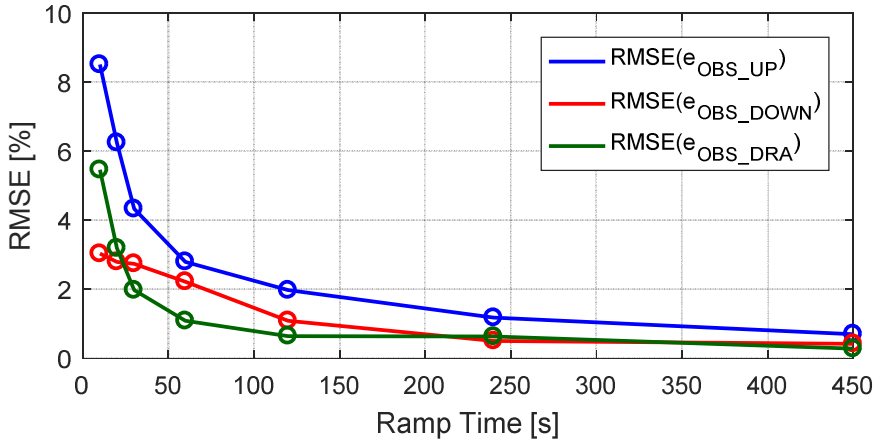

Figure 9.19: RMSE between steady-state volumetric efficiency and observed volumetric efficiency from dual-ramp MAP sweeps with various ramp times

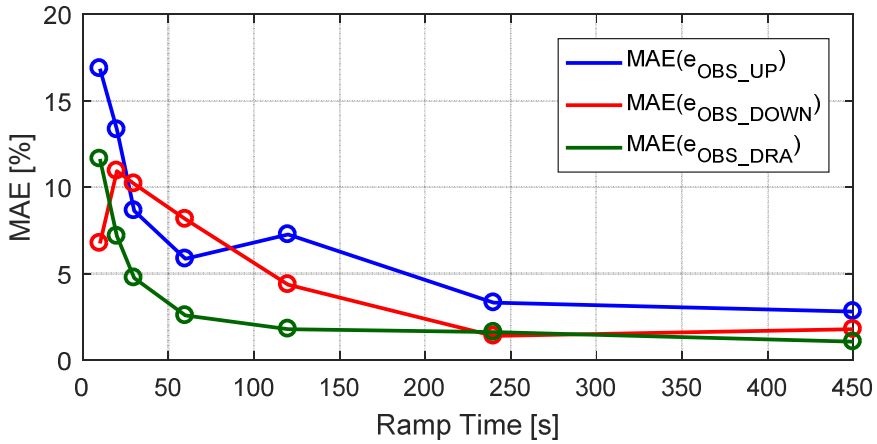

Figure 9.20: MAE between steady-state volumetric efficiency and observed volumetric efficiency from dual-ramp MAP sweeps with various ramp times

The experimental results confirm the findings from the simulation based validation which showed that the RMSE and MAE values decrease with increasing ramp time. However, whilst the simulation data indicated a sharp rise in the values for ramp times faster than 30 seconds, the experimental results suggest a sharp rise in the values for ramp times faster than 60 seconds. The results also confirm the importance of the DRA method, which allows a significant reduction in RMASE and MAE especially for ramp times shorter than 250 seconds.

9.4.3 Observation Error versus Measurement Error

This subsection highlights the advantage of the developed air-path observer by comparing the observed volumetric efficiency η_{v_OBS} with the MAF-based volumetric efficiency η_{v_MAF}. Figure 9.21 and Figure 9.22 plot the RMSE and MAE values of the volumetric efficiencies during the up-ramp over ramp time.

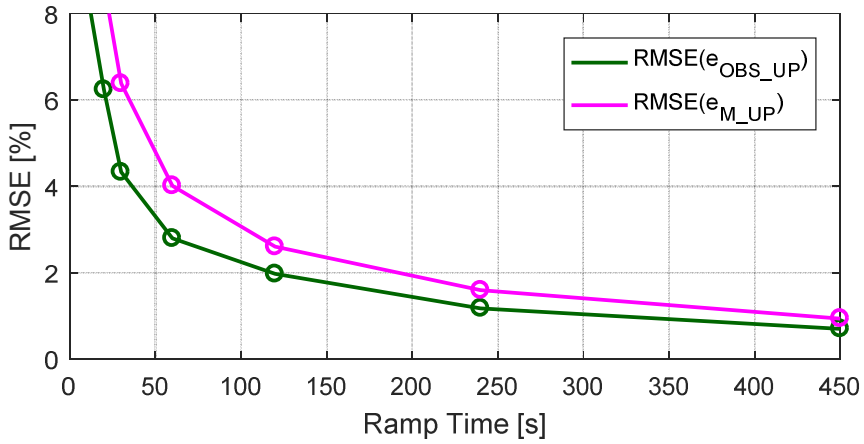

Figure 9.21: RMSE of observed volumetric efficiency versus RMSE of MAF-based volumetric efficiency during the up-ramp of dual-ramp MAP sweeps with various ramp times

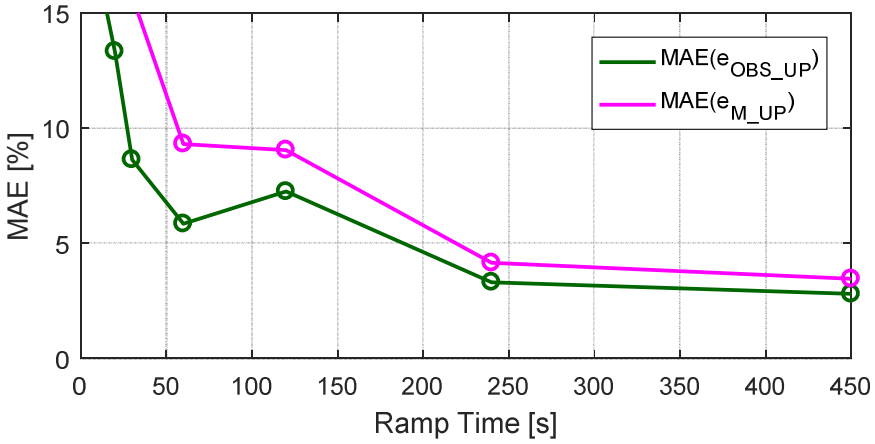

Figure 9.22: MAE of observed volumetric efficiency versus MAE of MAF-based volumetric efficiency during the up-ramp of dual-ramp MAP sweeps with various ramp times

The results in Figure 9.21 and Figure 9.22 show that the observer achieves a significantly lower RMSE and MAE at any ramp time.

Figure 9.23 and Figure 9.24 plot the RMSE and MAE values of the volumetric efficiencies during the down-ramp over ramp time.

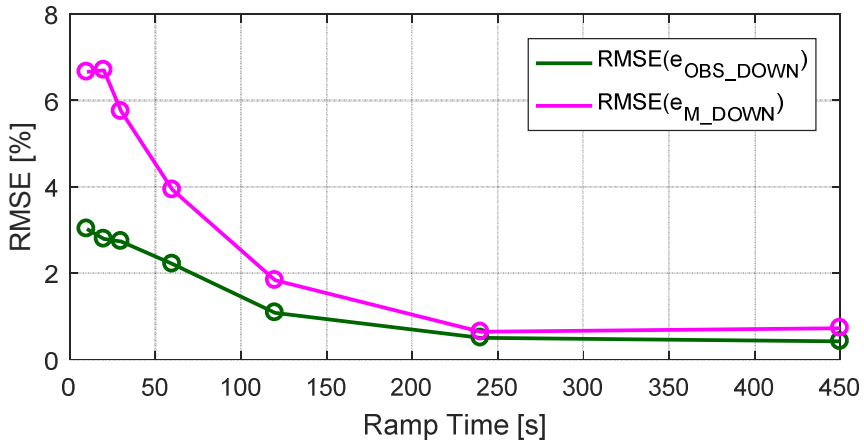

Figure 9.23: RMSE of observed volumetric efficiency versus RMSE of MAF-based volumetric efficiency during the down-ramp of dual-ramp MAP sweeps with various ramp times

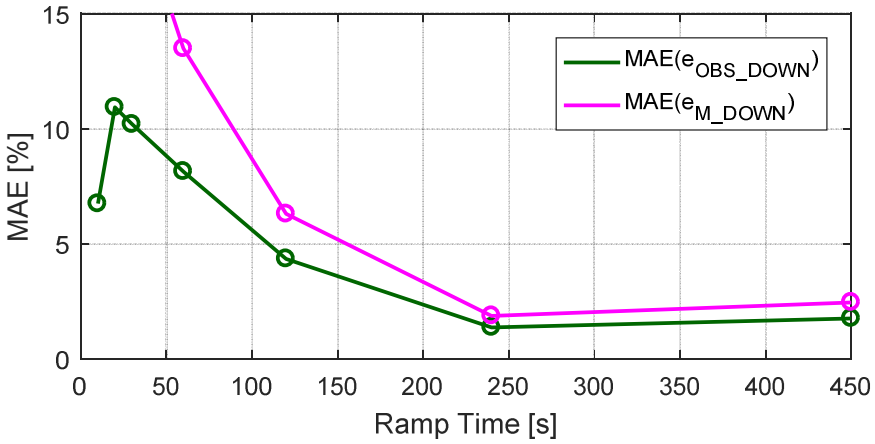

Figure 9.24: MAE of observed volumetric efficiency versus MAE of MAF-based volumetric efficiency during the down-ramp of dual-ramp MAP sweeps with various ramp times

Similarly to the results presented for the up-ramp, Figure 9.23 and Figure 9.24 also show that the observer achieves significantly lower values in RMSE and MAE during the down-ramp.

Figure 9.25 and Figure 9.26 plot the RMSE and MAE values of the dual ramp averaged volumetric efficiencies over ramp time.

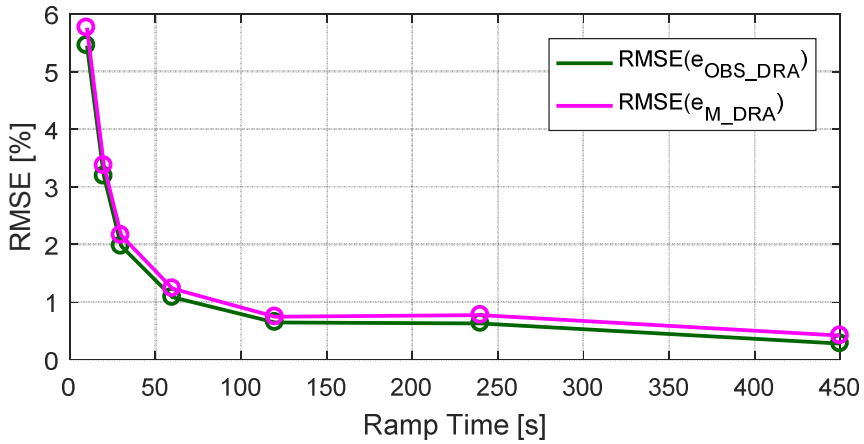

Figure 9.25: RMSE of dual ramp averaged observed volumetric efficiency versus RMSE of dual ramp averaged MAF-based volumetric efficiency over various ramp times

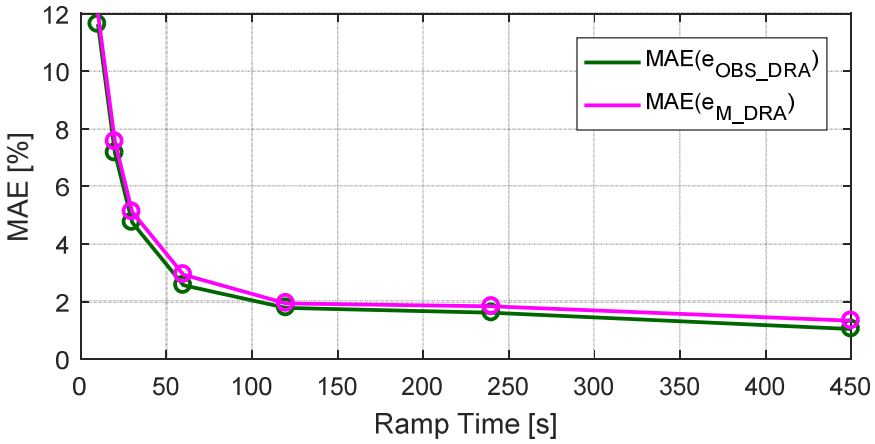

Figure 9.26: MAE of dual ramp averaged observed volumetric efficiency versus RMSE of dual ramp averaged MAF-based volumetric efficiency over various ramp times

Figure 9.25 and Figure 9.26 show that RMSE and MAE of the dual-ramp averaged observed volumetric efficiency $\eta_{v\_OBS\_DRA}$ is only slightly lower than RMSE and MAE of the dual-ramp averaged MAF-based volumetric efficiency, $\eta_{v\_MAF\_DRA}$. This indicates that dual-ramp averaging is a very powerful tool to compensate for dynamic effects during the up-ramp and the down-ramp. To explain the fact that RMSE and MAE of $\eta_{v\_OBS\_DRA}$ are only slightly smaller than RMSE and MAE of $\eta_{v\_MAF\_DRA}$, it is necessary to have a closer look into the test details of the dual-ramp MAP sweep.

Ramping intake manifold pressure with the same rate on the up-ramp and on the down-ramp excites all dynamics to the same level on both ramps. This means

that the filling and emptying dynamics are equally excited during the up-ramp and the down-ramp. Therefore, it is possible to cancel out the dynamics by averaging the results over the up-ramp and the down-ramp. Figure 9.21, Figure 9.22, Figure 9.23 and Figure 9.24 proved that the observer achieves a significantly higher accuracy during the up-ramp and during the down-ramp. This proves that the observer is compensating for the filling and emptying dynamics during both ramps. The remaining error after applying the observer can be explained by thermal transients and a difference in the exhaust back-pressure between the fast ramps and steady-state conditions. Figure 9.25 and Figure 9.26 show that dual-ramp averaging significantly reduces the remaining errors during the up-ramp and the down-ramp.

The results form Figure 9.25 and Figure 9.26 showed that simply dual-ramp averaging the MAF-based volumetric efficiency can achieve almost an identical accuracy as the dual-ramp averaged observed volumetric. However, it should be noted that this only works if the ramp rates of the up-ramp and the down-ramp are identical. If the dynamics during both ramps are unequally excited due to different ramp-rates, dual-ramp averaging will not cancel out the filling and emptying dynamics. In addition, the closed loop control strategy used to control the intake manifold pressure during the dual-ramp MAP sweep might not always lead to a perfectly linear ramp. Due to the high nonlinear response of intake manifold pressure to changes in throttle position and waste gate duty cycle, the closed loop control can cause some fluctuations in intake manifold pressure during the ramps. Rapid changes in pressure cause an excitation of the filling and emptying dynamics, which means that the observer is required to compensate for the excited dynamics. Therefore, the observer does not only achieve a slightly higher accuracy, it also improves the robustness of the entire methodology. The observer can always compensate for filling and emptying caused by the closed loop control. Dual-ramp averaging can only cancel out the dynamics if the dynamic excitation is identical during the up-ramp and the down-ramp.

9.4.4 Dependency on Engine Speed

In this subsection, the investigation into the accuracy of the observed volumetric efficiency compared to steady-state data is repeated for 16 different engine speeds.

Figure 9.27 and Figure 9.28 show the results for RMSE and MAE of dual-ramp averaged observed volumetric efficiency over engine speed. All dual-ramp MAP sweeps were collected with a ramp time of 120 seconds.

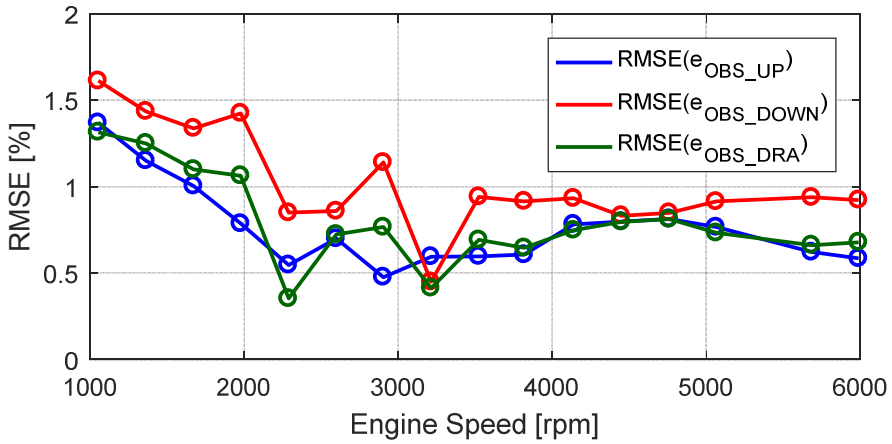

Figure 9.27: RMSE of observed volumetric efficiency over different engine speeds from a dual-ramp MAP sweep with 120 seconds ramp time

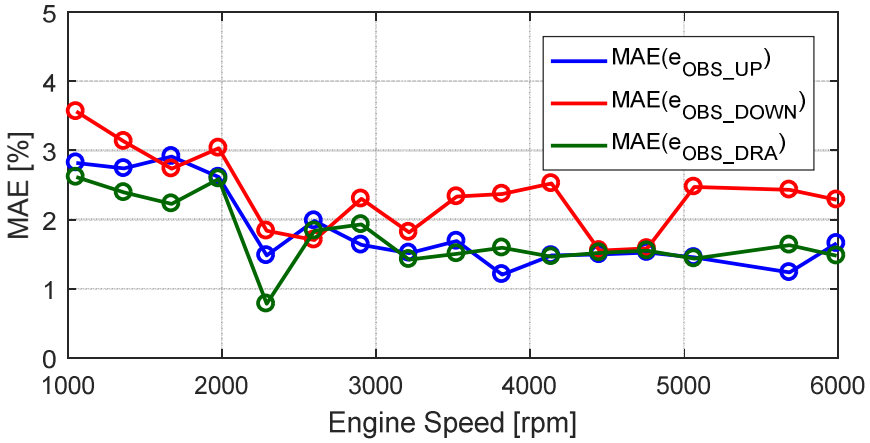

Figure 9.28: RMSE of observed volumetric efficiency over different engine speeds from a dual-ramp MAP sweep with 120 seconds ramp time

Figure 9.27 and Figure 9.28 confirm the finding from Subsection 8.4.4. RMSE and MAE show an increase for engine speeds smaller than 2000 rpm. The results show that for engine speeds greater than 2000 rpm, a ramp time of 120 seconds meets the measure of success which was defined as RMSE $<$ 1% and MAE $<$ 2%. For engine speeds smaller than 2000 rpm, the ramp time has to be increased to achieve the measure of success. Figure 9.27 and Figure 9.28 also confirm that DRA reduces RMSE and MAE.

Figure 9.29 and Figure 9.30 compare the observed volumetric efficiency η_{v_OBS} with the MAF-based volumetric efficiency η_{v_MAF}. RMSE and MAE values of the dual ramp averaged volumetric efficiencies over engine speed.

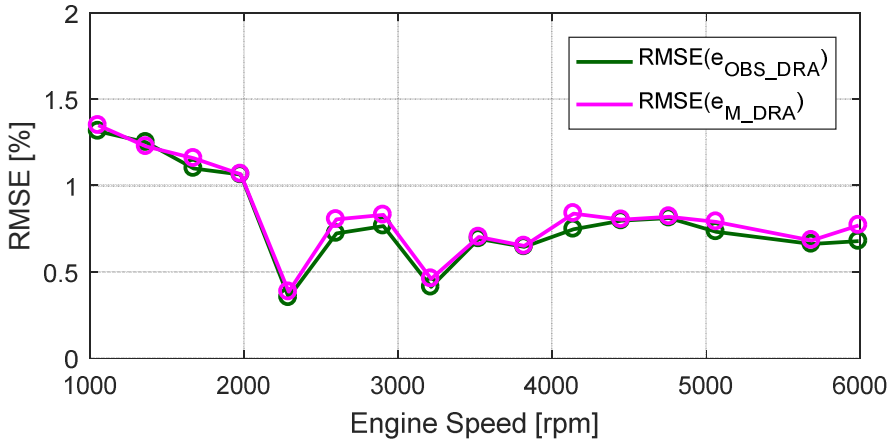

Figure 9.29: RMSE of dual ramp averaged observed volumetric efficiency versus RMSE of dual ramp averaged MAF-based volumetric efficiency over different engine speeds from a dual-ramp MAP sweep with 120 seconds ramp time

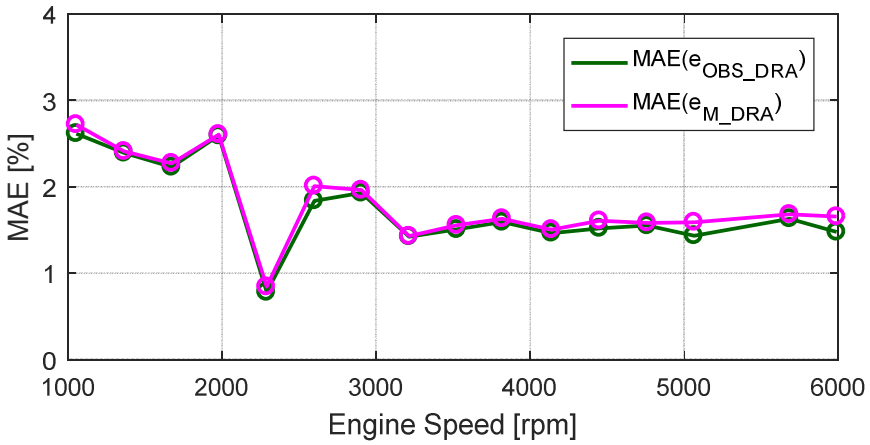

Figure 9.30: MAE of dual ramp averaged observed volumetric efficiency versus RMSE of dual ramp averaged MAF-based volumetric efficiency over different engine speeds from a dual-ramp MAP sweep with 120 seconds ramp time

Figure 9.29 and Figure 9.30 confirm the results of Subsection 9.4.3 for different engine speeds. $\eta_{v\_OBS\_DRA}$ consistently achieves slightly better results in RMSE and MAE than $\eta_{v\_MAF\_DRA}$.

9.5 Time Saving

The results presented in Section 9.4 showed that the developed methodology allows to characterise the engine air charge characteristic using dynamic test data. The experimental test results showed that for engine speeds greater than 2000 rpm a ramp time of 120 seconds is sufficient to achieve the measure of success defined in Section 9.3. For engine speeds below 2000 rpm, it was found that the ramp time has to be increased to achieve the desired accuracy.

To summarise the time saving achieved with the developed methodology, a relation is developed in this section, which allows estimating the time saving per MAP sweep. Equation 9.1 gives the time saving in seconds t_{save} between a steady-state MAP sweep and a dual-ramp MAP sweep.

$$t_{save} = t_{SS} - t_{DYN} \tag{9.1}$$

where t_{SS} is the total test time required for a steady-state MAP sweep and t_{DYN} is the total test time for MAP sweep collected with the dual-ramp MAP sweep method. Equation 9.2 gives the time saving per MAP sweep in percent.

$$PCT_{save} = \left(\frac{t_{SS} - t_{DYN}}{T_{CSS}}\right) 100 \tag{9.2}$$

The total test time for a dynamic dual-ramp MAP sweep is given by Equation 9.3.

$$t_{DYN} = 2t_{ss\_low} + t_{ss\_high} + 2t_{ramp} \tag{9.3}$$

The reader is referred to Subsection 6.4.1 for the details that lead to Equation 9.3.

Time saving per MAP sweep obviously depends on the testing method that is used to collect the steady-state data and on the test details of the used method. Subsection 9.5.1 investigates the time saving compared to conventional steady-state testing and Subsection 9.5.2 investigates the time saving compared to quasi steady-state testing. In both subsections, a realistic case study is presented to get an indication of the time saving.

9.5.1 Time Saving Compared to Conventional Steady-State Testing

Equation 9.4 gives the total test time required for a MAP sweep collected with the conventional steady-state testing method.

$$t_{SS} = N_{pp\_sweep} t_{SS\_TP} \quad \textbf{9.4}$$

For the case study, the following values were chosen:

- $N_{pp_{sweep}}$ = 60
- t_{SS_TP} = 120 seconds
- $t_{ss_{low}}$ = 10 seconds
- $t_{ss_{high}}$ = 10 seconds
- t_{ramp} = 180 seconds

Based on experience inside Ford Motor Company it has been shown that approximately 60 points per MAP sweep are required to deliver an accurate calibration for that specific engine speed. On average, a steady-state test point at Ford takes approximately 120 seconds. This number includes setting the test point, waiting for the engine to stabilize and recording the data over a certain amount of time. As mentioned above, for engine speeds below 2000 rpm, it was found that the ramp time has to be greater than 120 seconds in order to achieve the desired accuracy. Therefore, a ramp time of 180 seconds is used in this case study to account for the fact that not all sweeps that have to be collected for a complete air charge calibration can be run with a ramp time of 120 seconds.

Inserting the values above into Equations 9.1 and 9.2 delivers the following values for time saving:

- $t_{save} \approx$ 113 minutes saving per MAP sweep
- $PCT_{save} \approx$ 95% saving of total test time

The results of the case study show that the developed methodology reduces the total test time for a MAP sweep by more than 95%.

9.5.2 Time Saving Compared to Quasi Steady-State Testing

Subsection 9.2.2 proved that it is possible to collect steady-state data with the quasi steady-state testing method which is significantly faster than conventional steady-state testing. The steady-state reference data used to judge the accuracy

of the developed methodology in Section 9.4 were collected with the dual-ramp MAP sweep testing method to improve the robustness of the reference data. In this case, the test time for the SDS MAP sweep can be calculated from Equation 9.5.

$$t_{SS} = 2t_{ss\_low} + t_{ss\_high} + 2t_{ramp\_SDS} \quad \textbf{9.5}$$

where t_{ramp_SDS} is the ramp time of the dual-ramp MAP sweep.

However, the experimental results from Subsection 9.2.2 indicate that only one of the ramps, either the up-ramp or the down-ramp, are sufficient to produce steady-state data due to the negligible hysteresis between the two ramps. In case the steady-state data are collected with a single-ramp MAP sweep only, the testing time is given by Equation 9.6.

$$t_{SS} = t_{ss\_low} + t_{ramp\_SDS} + t_{ss\_high} \quad \textbf{9.6}$$

For the case study, the following values were chosen:

- t_{ramp_SDS} = 20 minutes
- $t_{ss_{low}}$ = 10 seconds
- $t_{ss_{high}}$ = 10 seconds
- t_{ramp} = 180 seconds

Inserting the values above into Equation 9.1 and 9.2 delivers the following values for a dual-ramp MAP sweep time saving:

- **Dual-Ramp MAP Sweep**:
  - t_{save} ≈ 34 minutes saving per MAP sweep
  - PCT_{save} ≈ 84% saving of total test time
- **Single-Ramp MAP Sweep**:
  - t_{save} ≈ 14 minutes saving per MAP sweep
  - PCT_{save} ≈ 68% saving of total test time

The results presented in this section showed that the developed methodology allows a significant reduction in engine testing time required to produce an engine air charge calibration. Compared to the conventional steady-state data collection method, the dynamic test method reduces the testing time by 95%. Compared to

quasi steady-state testing, the dynamic test method allows to reduce the testing time by 84% if a dual-ramp MAP sweep is used in the SDS testing method and 68% if a single-ramp MAP sweep is used in the SDS testing method. Thus, the conclusion is that the main aim of this thesis, to significantly reduce engine testing time required for air charge characterisation, is achieved through the developed methodology.

9.6 Summary

A state of the art test cell with state of the art measurement equipment has been used to prove the validity of the methodology with experimental data. Section 9.1 introduced the experimental test rig including the engine and the measurement equipment. Section 9.2 investigated the repeatability of steady-state data collection to establish a measure of success for this project. Based on the presented results it was decided that the measure of success is RMSE < 1% and MAE < 2%. In Section 9.4 the method was validated by comparing the observed volumetric efficiency to steady-state volumetric efficiency. The detailed investigation highlighted the advantage of using DRA, which significantly reduces RMSE and MAE. The investigation into different ramp times indicate that a ramp time of 120 seconds is sufficient to deliver data within the measure of success. The summary for different engine speeds confirmed that a ramp time of 120 seconds is sufficient for engine speeds greater than 2000 rpm. However, at lower engine speeds the ramp time has to be increased to achieve the measure of success. The investigation into observation versus measurement error showed that the observer significantly reduces RMSE and MAE during the up-ramp and down-ramp. The results also showed that it is possible to achieve almost a similar accuracy by directly dual ramp averaging the MAF-based volumetric efficiency. However, it has to be pointed out that this is only the case if the dual-ramp MAP sweep has exactly the same ramp rate on the up-ramp and on the down-ramp.

Chapter 10 Summary, Conclusions and Future Work

10.1 Summary

To begin, a short summary of the work undertaken is provided. Section 1.1 highlights the contribution of the road transportation sector on total GHG emissions in the EU. Although electric vehicles are, without any question, the long-term solution to reduce the output of GHG emission caused by road transportation, it is obvious that internal combustion engines will play an important role in light-duty vehicles until 2040 and beyond. Consequently, research which aims to improve the fuel consumption of ICVs can help to significantly reduce GHG emissions in the following decades. Technology, which is already available, has the potential to increase the overall engine efficiency by up to 17%. However, in order to benefit from these technologies, highly advanced control strategies are required which control the actuators of each technology. This task can only be handled with a central torque oriented control strategy, which relies on feed-forward models to achieve fast response and good drivability to the input of the driver. The parameterisation of these models is called engine calibration, which requires a huge amount of steady-state engine test data. With every new engine actuator, the data amount required for calibration increases exponentially. This development has led to a bottleneck, which prohibits the use of new technologies due to the inefficiency of current engine test methodologies. Dynamic engine testing as a replacement for conventional steady-state testing has the potential to reduce the required testing time by more than 90%. The aim of this thesis was to develop a dynamic test methodology specifically for engine air charge characterisation.

The literature review in Chapter 2 provided a detailed revision of available literature on every major topic of the thesis. Section 2.1 was focused on three fundamental different engine testing methods. Conventional steady-state testing is defined by three consecutive steps. At first iterative adjustment of actuator positions is used to transition from the current operating point to the next operating point. Once the desired actuator position is reached, all actuators are held constant, waiting for the engine to settle to steady-state conditions. Finally, data are recorded over a certain time and the measurement results are averaged over the recording time to eliminate measurement noise. Slow dynamic slope

testing changes one or more actuator settings very slowly. The idea behind this testing method is to change the actuator settings slowly enough to keep any dynamic excitation to an unnoticeable level. Consequently, the SDS testing is also known as quasi steady-state testing. Two fundamentally different approaches are available for dynamic engine testing. Dynamic offset testing ramps actuator settings or engine responses at a fast rate, which causes an excitation of the system dynamics. Rapid step testing uses step-inputs into the actuators to excite the system dynamics. However, since the calibration process requires steady-state data, dynamic test data cannot directly be used. Dynamic compensation tools, which were reviewed in Section 2.2 are required to produce steady-state data. Dynamic offset testing requires dynamic offset compensation and rapid step testing requires steady-state prediction. Both methods rely on dynamic engine models. Dynamic engine models are reviewed in Section 2.3. A classification into white-box, black-box and grey-box models determines whether the model is purely physics based, experimental based or a combination of both. Section 2.4 was focused on mean value engine models. This grey-box model type provides an efficient solution for capturing major dynamic effects on a cycle average basis. This model type was later used to develop the air-path observer. Air charge observers, which were reviewed in Section 2.5 allow compensation for filling and emptying dynamics along the air-path. Numerous researchers have used observers to improve transient air charge estimation in MAF based control strategies. However, currently no attempt has been made to use an observer for the purpose of characterising air charge. Based on the literature review the research gap was identified in Section 2.6. The task was to develop an air-path observer that predicts the air mass flow into the engine by compensating for the filling and emptying dynamics along the air-path. To achieve this, a dynamic air-path model was combined with an observer principle and integrated into a dynamic dual-ramp testing procedure which allows the application of DRA to average over unaccounted dynamic effects.

Chapter 3 provided vital background information for dynamic engine air-path modelling of a turbocharged SI engine. A dynamic air-path model is developed by combining three major elements: restrictions, turbocharger and volumes. Equations describing the behaviour of restrictions are subdivided into compressible and incompressible flow regimes. A pressure ratio criteria is used to select the appropriate equation type. Section 3.2 was focused on the

turbocharger. This model requires considerable amounts of performance data from the manufacturer. Section 3.3 considered the various volumes along the air-path. Volumes are subdivided into plenums and pipes. Plenums are modelled using filing and emptying dynamics. This is a lumped-parameter approach and spatial variation through the volume in the relevant states is ignored. Pipes have to be modelled using gas dynamic equations to represent the special variation of pressures and other quantities. However, solving the gas dynamic equations requires a complex iterative solver. A significant simplification can be achieved by lumping pipes and plenum together into lumped volumes. Those can then be modelled using filling and emptying dynamics only. This solution, however, neglects the gas dynamics in the pipes, only considering filling and emptying dynamics. Section 3.4 was focused on cylinder modelling. The cylinder can either be modelled on a crank angle resolved basis or on a cycle average basis. Crank angle resolved modelling requires modelling of the valves as well as the variable volume of the cylinder. Cycle average modelling uses the volumetric efficiency to represent the gas exchange process.

Chapter 4 reviewed and compared two different solutions for the observer principle. The problem of air charge observation can either be treated as an ‘unknown input estimation’ problem, or as ‘joint state and parameter estimation’ problem. Unknown input estimation, which was treated in Section 4.2, can be achieved by directly inverting the dynamic model. This, however, requires approximating the state derivative. This might be difficult in the presence of measurement noise. Alternatively, an unknown input observer can be used which uses a high gain observer to estimate the state derivative. Joint state and parameter estimation was covered in Section 4.3. This method combines a system state observer with an adaptive parameter identification law. A popular implementation of this combination is the Augmented Extended Kalman Filter, which provides an elegant solution to deal with measurement noise. Both solutions were compared in a simplified but representative case study.

Chapter 5 combined the knowledge about dynamic engine modelling from Chapter 3 and observation principles from Chapter 4 to develop the air-path observer. Section 5.1 was focused on the details of the transient engine air charge estimation problem. At first, the most suitable dynamic engine model type was selected to suit the requirements for the air-path observer. The air-path was

then divided and lumped into three major volumes, separated by restrictions. The three main volumes are intake volume, intercooler and the intake manifold. Finally, the system state was chosen with the aim to avoid any thermodynamic assumptions, which might affect the accuracy of the observed outflow. Two different solutions for the air-path observer were presented in Section 5.2 and 5.3. One uses the unknown input estimation method, which is more suitable for offline applications. This method was later used in this project for the simulation based validation and the experimental validation. The other solution uses the joint state and parameter estimation method, which will be used for online applications in future work.

Chapter 6 provided all implementation details to apply the developed air-path observer to a complete engine air charge characterisation. Section 6.1 provided a detailed analysis of parameters, which affect the engine air charge. This lead to the conclusion that it is sufficient to characterise the engine air charge characteristic based on intake manifold pressure, engine speed as well as intake and exhaust valve timing. For engine testing, a dual-ramp MAP sweep was developed in Section 6.4. This specific test allows to apply dual-ramp averaging which cancels out dynamic effects which are not accounted for in the observer. Two engine air-path controllers were developed in Section 6.5 which can be used to control the intake manifold pressure of the engine during the dual-ramp MAP sweep. To filter the measurement data from measurement noise without any phase shift, a zero distortion filter is applied, as shown in Section 6.6. Section 6.7 was focused on dual-ramp averaging. The measurement results of the dual-ramp MAP sweep are split into an up-ramp and a down-ramp. Both ramps are interpolated onto a common range of intake manifold pressures. Finally, the average over the up-ramp and the down-ramp is estimated at each interpolated point.

A simulation platform was developed in Chapter 7 to carry out a detailed analysis into the accuracy and physical limitations of the developed methodology. A 1D crank angle resolved engine model forms the core of the simulation platform. The model includes gas dynamic effects for which the developed observer cannot compensate for. Therefore, the simulation platform allows investigation of the impact of neglecting these effects. In addition, the model allows to measure the air mass flow along the entire engine air-path, which is not possible on a real

engine. This allows a detailed investigation of each individual observer. The engine model was validated in Section 7.2 to ensure that the model is a sufficient representation of the real engine used for the experimental validation in Chapter 9. The air-path controllers used to control the intake manifold pressure during the dual-ramp MAP sweep were evaluated in Section 7.3 to ensure that a sufficient control performance is achieved.

Chapter 8 used the simulation platform to determine the accuracy and physical limitation of the developed methodology. Statistical measures to judge the performance were developed in Section 8.1. Section 8.2 investigated the difference between transient volumetric efficiency and volumetric efficiency at steady-state. A detailed analysis of the accuracy of each observer in observing the volume outflow was carried out in Section 8.3. Finally, the accuracy of the entire methodology was investigated in Section 8.4. Therefore, the observed volumetric efficiency from fast dual-ramp MAP sweeps were compared to steady-state data.

Chapter 9 validated the developed methodology using experimental test results from a real engine. The test rig was introduced in Section 9.1. In Section 9.2 the repeatability of conventional steady-state, quasi steady-state and dynamic test data was investigated. Based on these results a measure of success was established in Section 9.3 which was used to judge the accuracy of the method in the Section 9.4. A trade-off between ramp time and accuracy was provided in Section 9.4, which allows to choose the corresponding ramp time to achieve the desired measure of success. The main aim of the thesis was to reduce engine testing time for air charge characterisation by as much as possible. Therefore, Section 9.5 was dedicated to estimate the savings of the developed methodology compared to conventional steady-state testing and quasi steady state testing.

10.2 Conclusions

This section presents the conclusions of this thesis. At first the key conclusions are presented in Subsection 10.2.1. Subsection 10.2.2 presents the conclusions of each individual chapter.

10.2.1 Key Conclusions / Main Contributions

In the following, the key conclusions and major contribution of this work are listed in hierarchical order:

1. **Time Saving**: The developed methodology allows to reduce the engine testing time required for air charge characterisation by 95% compared to conventional steady-state data (20 times faster). Compared to quasi steady-state testing, the dynamic test method allows the reduction of testing time by 84% if a dual-ramp MAP sweep is used in the SDS testing method and by 68% if a single-ramp MAP sweep is used in the SDS testing method.
2. **Observer accuracy**: The developed air path observer is founded on a mean value air-path model. Therefore, the observer can only compensate for the filling and emptying dynamics along the air-path. Simulation studies demonstrate that fast ramps significantly excite gas dynamic effects, which the observer cannot compensate for. Consequently, maximum error and the RMSE value of the sweep increase with shorter ramp times.
3. **Steady-state versus transient volumetric efficiency**: Existing literature suggests that transient volumetric efficiency is identical to the volumetric efficiency at steady-state conditions. The simulation results from Section 8.2 revealed that this assumption is wrong. A noticeable difference was found for ramp times shorter than 30 seconds. Consequently, a ramp time of 30 seconds is the physical limitation for the developed methodology to avoid significant errors in the identified volumetric efficiency.
4. **Dual ramp averaging**: Dual ramp averaging is a very effective tool in compensating for unaccounted dynamic effects. Symmetry between the up-ramp and the down-ramp allows to excite dynamic effects to a similar level on the up-ramp and on the down-ramp. Consequently, dynamic effects can be cancelled out by averaging over the resulting hysteresis in the measurement data.
5. **Smoothing the target MAP signal**: Smoothing the target MAP signal of the dual-ramp MAP sweep significantly reduces the maximum error without affecting the RMSE values of the sweep. The smoother target signal avoids unnecessary excitation of gas dynamic effects caused by acceleration and deceleration of the gas.

6. **Repeatability**: Dynamic test data collected with the dual-ramp MAP sweep have a slightly higher repeatability than conventional steady-state data. The main reason for this is the fact that DRA helps to average over thermal transients which do not fully settle during conventional steady-state testing.
7. **Observer principles**: Two different observer principles were compared in Chapter 4. The results showed that the joint state and parameter estimation method is significantly better for online and real time applications, since the augmented extended Kalman filter can automatically deal with measurement noise. The unknown input estimation method is more suitable for offline applications where advanced filters can be used to provide noise free measurement data without a phase shift. The method is easier to implement and allows optimal observation performance without tuning the observer.
8. **Mass based observer**: Using mass as the system state of a volume avoids any thermodynamic assumption for modelling the filling and emptying dynamics. This eliminates errors in the observed volume outflow due to the nature of the assumed thermodynamic process.

10.2.2 Conclusions by Chapter

In the following, the conclusions are listed by chapter:

- **Dynamic Engine Air-Path Modelling**
    - Dynamic engine air-path modelling can be divided into restrictions, turbocharger and volumes. Restrictions have to be modelled using equations for incompressible or compressible flow, depending on the pressure drop across the restriction. To model volumes, a distinction has to be made between plenums and pipes. Plenums are modelled using filling and emptying dynamics since the special variation of the system states is negligible. Pipes have to be modelled with 1D gas dynamic equations. A significant reduction in model complexity can be achieved by lumping pipes and plenums together into a volume with equivalent capacity. This neglects the gas dynamic effect, but still accounts for filling and emptying dynamics.
    - The cylinder can either be modelled in the crank angle or cycle average domain. Crank angle resolved models require modelling of any valves

as restrictions with variable flow area. Similarly, the cylinder volume must be considered variable. Cycle average models use the speed-density equation in combination with the volumetric efficiency to represent the gas exchange process of the cylinder.

- **System Observation & Parameter Identification**
  - The problem of observing the outflow of a volume using a dynamic model, which describes the filling and emptying dynamics of the volume, can be approached using two different observer principles. These are *joints state and parameter estimation* and *unknown input estimation*:
    - Joint state and parameter estimation is significantly better for online and real time applications, since the augmented extended Kalman filter automatically accounts for the influence of measurement noise.
    - Unknown input estimation is more suitable for offline applications. Advanced filters can be used to filter out any measurement noise without introducing a phase shift. The UIE solution is much simpler to implement than the JSPE version and allows optimal observation performance without complicated observer tuning. Therefore, the UIE version is also more robust than the JSPE version.
- **Engine Air-Path Observation**
  - An iterative solver is required to solve the equations for 1D gas dynamics. Therefore, 1D gas dynamic equations are not directly invertible. Since an observer requires an invertible model, this rules out the use of 1D gas dynamic equations. A cycle averaged observer cylinder model is the preferred approach, since there is no significant benefit in observing the air mass flow with crank angle resolution.
  - The air-path of a modern GTDI engine can be divided into three major volumes, separated by restrictions. These are the intake volume, intercooler and intake manifold. Consequently, an individual observer is required to compensate for the filling and emptying dynamics in each volume.
  - The unknown input based observer is developed by directly inverting the equation for filling and emptying dynamics. The derivative of the

state can be adequately approximated using the Euler backwards method.

- **Implementation**
  - Intake manifold pressure, engine speed, intake and exhaust valve timing are the four most important parameters that affect the volumetric efficiency of the engine. Other parameters such as intake manifold temperature, engine coolant temperature and exhaust back pressure have a less significant influence. Suitable compensators and correction factors can account for the effect of these less influential factors.
  - From a data collection perspective, the dual-ramp MAP sweep provides a simple and efficient test procedure. The procedure ramps intake manifold pressure from a low value to a high value and back again at a prescribed rate. Camshaft timing and engine speed are held constant throughout. The symmetry of the up-ramp and the down-ramp facilitates the use of dual ramp averaging post-processing techniques, which significantly reduces the effect of unaccounted dynamics.
  - The target MAP signal of the dual-ramp MAP sweep can be smoothened by using a moving average filter. However, the ramp timing has to be modified to make sure that the overall ramp time is not affected by applying the moving average filter.
  - Open and closed loop methods for controlling the intake manifold pressure during the dual-ramp MAP sweep were applied.
    - The open loop method is inappropriate for engines that do not employ a *boost buffer* in the control strategy. (No boosting behind the throttle).
    - The closed loop solution is generally applicable to all control strategies. However, the closed loop controller requires some tuning to achieve accurate tracking of the target MAP signal during the dual-ramp MAP sweep.
- **Simulation Platform**
  - For the evaluation of the open loop air-path controller, throttle angle and waste gate duty cycle were ramped linearly at prescribed rates. The intake manifold pressure showed a highly nonlinear response to the actuator input signals. However, the resulting up and down-ramp characteristics were symmetric. This permits the application of the dual

ramp averaging post processing technique, improving the quality of the volumetric efficiency estimate. The open loop solution is therefore not suitable, as the instantaneous ramp rate is very unpredictable across operating conditions.

- At the lower boundary of the boosted operating region, until the waste gate duty cycle is sufficiently large, the intake manifold pressure remains almost constant for a significant period, due to nonlinearity in the response. Almost 40% of the total test time is wasted in this state.
- The closed-loop control solution facilitates highly accurate tracking of the target MAP signal. Therefore, the closed-loop solution is significantly better than the open-loop solution. It can be used to characterise any air charge control strategy and is more time efficient since it does not waste any test time during the transition from throttled into boosted operating conditions.

- **Simulation based Methodology Validation**
  - *Actual volumetric efficiency* during transients differs from the equivalent *steady state volumetric efficiency*.
    - At 2000 [RPM], for a 3 second ramp, differences in MAE of up to 5% were detected.
    - For 30 second ramps, and above, RMSE and MAE statistics were suitably low, regardless of the operating condition. Consequently, a minimum ramp time of 30 seconds is recommended to ensure accurate measurement.
  - The efficacy of the observer is demonstrated by comparing the observed air mass flow into the engine to the actual air mass flow into the engine. For a 30-second ramp, simulation studies illustrate that the MAE from the observer and MAF sensor estimates differ by a factor of six. Even for a 120-second ramp, the MAE from the observer and MAF sensor estimates differ by a factor of four.
    - The observer of the intake manifold achieves a very high accuracy in observing the volume outflow. This can be explained by the fact that the intake manifold including the ports is very similar to an idealised plenum, which is not affected by gas dynamics and special variation.

        - The observer of the intercooler volume achieves a lower accuracy in observing the volume outflow compared to the intake manifold observer. This can be explained by the fact that the intercooler volume comprises two long pipes, which connect the compressor the intercooler and the intercooler to the throttle plate. As a consequence, spacial variation as well as acceleration and deceleration of the gas have a noticeable impact on the observation accuracy of the outflow.
        - The observer of the intake volume does not provide a significant compensation for the excited dynamics. Consequently, it can be concluded that the intake volume is dominated by gas dynamic effects and not by filling and emptying.
    - For a 30 second ramp, dual ramped average observer estimates were approximately 4 times more accurate in terms of MAE and 3 times more accurate in terms of RSME than their direct MAF sensor equivalents.
    - Smoothing the target MAP signal significantly reduces the maximum error of the identified volumetric efficiency by a factor of three, without affecting the corresponding RMSE value. Smooth transition into and out of the ramp avoids discontinuous changes in instantaneous intake manifold pressure rise or fall rate. This yields a smoother acceleration and deceleration of the gas, which minimises the excitation of gas dynamics effects.
    - Engine speed affects both MAE and RMSE of the volumetric efficiency estimate. For a given ramp rate, both error measures increase with decreasing engine speed. Consequently, the ramp time used at engine speeds below 2000rpm must be reduced to the specified accuracy requirements of RMSE < 1% and MAE < 2%.
- **Experimental Validation**
    - The experimental validation largely confirmed the findings of the simulation based validation.
    - The major difference between the simulation and experimental results is the comparison between *measurement accura*cy and *observation accuracy*. For symmetrical up and down-ramps, estimates generated by simply applying the DRA algorithm to MAF based volumetric

efficiency measures were very close to corresponding estimates from the observer.

- Volumetric efficiency estimates from the observer are inherently more robust to asymmetry in the up and down-ramp rates and controller actuator fluctuations. For example, controlling the engine speed as well as throttle and waste gate actuators on a real engine, often result in either localised changes in the ramp rate or fluctuations in intake manifold pressure during the ramp. In this case simply dual ramp averaging the MAF based volumetric efficiency estimates for both ramps is not sufficient, given it is very unlikely that the ramps will remain symmetrical under these conditions.
- The results show that for engine speed greater than 2000 rpm, a ramp rate of 120 seconds is sufficient to meet the measure of success, which was defined as $\pm$2% for the maximum error and $\pm$1% for the RMSE value.
- For engine speed lower than 2000 rpm, larger ramp times have to be used to meet the same measure of success. For example, at 1000 rpm, ramp times of 300 seconds are recommended.

10.3 Further work

This section presents suggestions for future work. This includes possible improvements in the developed methodology and its application to different areas.

- **Implementation of closed-loop air-path controller**: As mentioned in Subsection 9.1.4, the experimental test data were collected with an open-loop control strategy. In order to be able to characterise the engine air charge characteristic with a specific delta pressure across the throttle, a closed-loop control strategy as shown in Subsection 6.5.2 is required. However, the implementation of such a controller is not as straightforward as in the simulation platform. The following steps are required for a successful implementation:
  - Develop a real time platform which incorporates the intake manifold pressure controller and the boost controller. Either MATLAB or LabView are suitable platforms to implement the controllers.

- Establish a real time communication between the real time platform and the existing engine control software (AutoTEST, AVL Puma, ATI Vision).
- Develop a method which automatically tunes the gains of the PID controllers to optimise the tracking performance of target MAP and target BOOST signal.

- **Adaptive air charge estimation for control applications**: The developed air-path observer cannot only be used for air charge characterisation on an engine test bed but also for control applications on the ECU. The use of the air-path observer on an engine which is equipped with a MAF sensor would allow the following improvements:
  - Significantly improve transient engine air charge estimation which is highly important for accurate AFR control.
  - Online adaptation of the air charge model of the ECU: Correction of the implemented model for variations from engine to engine and changing ambient conditions such as humidity and altitude.
  - Reduce size of the calibrated air charge model: Online adaptation can be used to populate the air charge model of the ECU. This would significantly reduce the size of the model that has to be calibrated, which consequently reduces the testing time required to produce the calibration data.
- **Air-path observer based on a gas dynamic model**: The air-path observer developed is based on a mean value model which lumps pipes and plenums along the air-path into major volumes. This allows to compensate for the filling and emptying dynamics but neglects the gas dynamics. An observer which is based on 1D gas dynamic equations would also compensate for gas dynamics. This would allow to reduce the ramp time even further and, consequently, save even more engine testing time. The following steps are required to successfully implement an air-path observer based on gas dynamic equations:
  - Detailed literature review on gas dynamic modelling and solvers to solve the 1D gas dynamic equations.
  - Study possible model assumptions to develop the observer based on available measurement signals from a state of the art engine test bed.

- Develop a solver which combines the gas dynamic equations with the measurable system states to observe the outflow of a pipe modelled with gas dynamic equations.
- Validate the observer against a 1D crank angle resolve engine model, similar to the study presented in Section 8.3.

Chapter 11 References

[1] Eurostat, “Greenhouse gas emissions, analysis by source sector, EU-28,” 2017. [Online]. Available: http://ec.europa.eu/eurostat/statistics-explained/index.php/File:Greenhouse_gas_emissions,_analysis_by_source_sector,_EU-28,_1990_and_2015_(percentage_of_total)_new.png. [Accessed: 24-Jan-2018].

[2] European Comission, “A European Strategy for low-emission mobility,” 2014. [Online]. Available: https://ec.europa.eu/clima/policies/transport_en. [Accessed: 24-Jan-2018].

[3] European Comission, “Roadmap to a Single European Transort Area - Towards a competitive and resource efficinet transport system,” 2011. [Online]. Available: http://eur-lex.europa.eu/legal-content/EN/TXT/PDF/?uri=CELEX:52011DC0144&from=EN. [Accessed: 18-Feb-2018].

[4] M. Messagie, “Life Cycle Analysis of the Climate Impact of Electric Vehicles,” European Federation for Transport and Environment, Brussels, 2014.

[5] I. Verbeek, M. Bolech, R. Gijlswijk, and J. Spreen, “Energie- en milieu-aspecten van elektrische personenvoertuigen,” TNO-rapport R10386, Earth, Life & Social Sciences, 2015.

[6] European Environment Agency, “Electric vehicles in Europe,” Luxembourg, Publications Office of the European Union, No 20/2016, 2016.

[7] Ford Motor Company, “Ford Fiesta Engine Information.” [Online]. Available: https://www.ford.co.uk/content/dam/guxeu/uk/documents/feature-pdfs/FT-All_New_Fiesta.pdf. [Accessed: 30-Jan-2018].

[8] G. Fontaras, N.-G. Zacharof, and B. Ciuffo, “Fuel consumption and CO2 emissions from passenger cars in Europe Laboratory versus real-world emissions,” *Prog. Energy Combust. Sci.*, vol. 60, pp. 97–131, 2017.

[9] European Comission, “A Roadmap for moving to a competitive low carbon economy in 2050,” Document 52011DC0112, Brussels, 2011.

[10] Bloomberg New Energy Finance, “Electric Vehicle Outlook 2017,” 2017. [Online]. Available: https://about.bnef.com/electric-vehicle-outlook/.

[11] J. B. Heywood, “On the Road toward 2050,” Massachusetts Institute of Technology, 2015.

[12] Ford Motor Company, “Ford EcoBoost.” [Online]. Available: https://www.ford.co.uk/shop/research/technology/performance-and-efficiency/ford-ecoboost. [Accessed: 30-Jan-2018].

[13] R. Isermann, *Engine Modeling and Control*. Heidelberg: Springer, 2014.

[14] T. Fortuna, H. Koegeler, M. Kordon, G. Vitale, and D. R. Rogers, “A paradigm shift in development methodology for powertrain calibration,” in *PMC - 2nd Biennial Conference on Powertrain Mapping and Calibration*, 2014.

[15] Bosch Professional Automotive Invormation, *Gasoline Engine Management - Systems and Components*. Wiesbaden: Springer, 2015.

[16] L. Guzzella and C. H. Onder, *Introduction to Modeling and Control of Internal Combustion Engine Systems*. Heidelberg: Springer, 2010.

[17] G. P. Merker, C. Schwarz, and R. Teichmann, *Combustion Engines Developement*. Wiesbaden: Vieweg & Teubner, 2009.

[18] L. Eriksson, S. Frei, C. Onder, and L. Guzzella, “Control and optimization of turbocharged Spark ignited engines,” *IFAC Proc. Vol.*, vol. 15, no. 1, pp. 283–288, 2002.

[19] P. Gorzelic, E. Hellström, A. Stefanopoulou, L. Jiang, and S. Gopinath, “A coordinated approach for throttle and wastegate control in turbocharged spark ignition engines,” *Proc. 2012 24th Chinese Control Decis. Conf. CCDC 2012*, pp. 1524–1529, 2012.

[20] R. Beckmann, W. Drewelow, B. Lampe, P. Dunow, M. Schultalbers, and N. Weinhold, “Exact air charge feed forward control of a turbocharged SI engine,” in *International Conference on Control Applications*, 2012, pp. 1509–1515.

[21] A. Thomasson, L. Eriksson, O. Leufvén, and P. Andersson, “Wastegate actuator modeling and model-based boost pressure control,” in *IFAC Workshop on Engine and Powertrain Control, Simulation and Modelling*, 2009, pp. 87–94.

[22] R. J. Wakeman and D. O. Wright, “Closed Loop Turbocharger Control with

Transient Wastegate Functions," *SAE Tech. Pap.*, no. 860487, 1986.

[23] G. Colin, Y. Chamaillard, G. Bloch, and G. Corde, "Neural control of fast nonlinear systems - Application to a turbocharged SI engine with VCT," *Ieee Trans. Neural Networks*, vol. 18, no. 4, pp. 1101–1114, 2007.

[24] a. Y. Karnik, J. H. Buckland, and J. S. Freudenberg, "Electronic throttle and wastegate control for turbocharged gasoline engines," in *Proceedings of the American Control Conference*, 2005, pp. 4434–4439.

[25] U. Kalabić, I. Kolmanovsky, J. Buckland, and E. Gilbert, "Reference and extended command governors for control of turbocharged gasoline engines based on linear models," in *Proceedings of the IEEE International Conference on Control Applications*, 2011, pp. 319–325.

[26] P. Moulin, J. Chauvin, and B. Youssef, "Modelling and control of the air system of a turbocharged gasoline engine," in *17th IFAC World Congress*, 2008, pp. 8487–8494.

[27] L. T, C. J, P. N, and C. G, "MOTION PLANNING CONTROL OF THE AIRPATH OF AN S.I. ENGINE WITH VALVE TIMING ACTUATORS," in *Fifth IFAC Symposium on Advances in Automotive Control*, 2007.

[28] D. Cieslar, "Control for transient response of turbocharged engines," PhD Thesis, University of Cambridge, 2013.

[29] G. Colin, Y. Chamaillard, and B. Bellicaud, "Robust control for the air path of a downsized engine," *Proc. Inst. Mech. Eng. Part D J. Automob. Eng.*, vol. 225, no. 7, pp. 930–943, 2011.

[30] M. Sugita, S. Watanabe, A. Ohata, M. Ehara, and K. Kaizawa, "Rapid Measurement for Steady-State Calibration," in *Design of Experiments (DoE) in Engine Development III*, 2007.

[31] H. Jammoussi and I. Makki, "Diagnostics of Oxygen Sensors and Air-Fuel Ratio Adaptive Controls," in *Proceedings of the ASME Internal Combustion Engine Division Fall Technical Conference*, 2015, pp. 1–10.

[32] AVL, "AVL FLOWSONIX." [Online]. Available: https://www.avl.com/-/avl-flowsonix-air. [Accessed: 15-Feb-2018].

[33] B. Berger, "Modeling and Optimization for Stationary Base Engine Calibration," PhD Thesis, Technical University of Munich, 2012.

[34] S. Toepfer, “Approximation nichtlinearer Prozesse mit Hinging Hyperplane Baummodellen - VDI Fortschrittsbericht 2002,” PhD Thesis, TU-Darmstadt, 2002.

[35] M. Fischer and K. Roepke, “Effizient Applikation von Motorsteuerungsfunktionen fuer Ottomotoren.pdf,” *MTZ*, vol. 61, no. 9, pp. 562–570, 2000.

[36] D. Boehme, “Methoden zur effizienten Basisapplikation fuer Luftpfad- und Abgastemperaturmodelle von Ottomotoren,” *VDI Verlag*, no. 767–12, 2013.

[37] E. W. Hislop, “Dynamic Testing of Internal Combustion Engines,” PhD Thesis, Queen Mary College, Univerity of London, 1974.

[38] G. Fehl, “Entwicklung einer Meßstrategie zur kontinuierlichen Erfassung von Kennlinien auf Motorenpruefstaenden,” PhD Thesis, Technische Hochschule Darmstadt, 1992.

[39] D. Boehme, R. Isermann, M. Martiny, J. Kern, and M. Kerkau, “Quasi-stationary measurement method for the ecu-functions of the cylinder charge determination and the torque model,” in *3rd International Symposium on Development Methodology*, 2009.

[40] Y. Murakami, H. Kusuki, and T. Nakagawa, “Slow Dynamic Slopes (SDS) Methodology Applied for a Stratified Gasoline Engine.,” in *Design of Experiments (DoE) in Engine Development*, 2007, pp. 413–423.

[41] N. Keuth, M. Thomas, H. Pfluegl, E. Martini, and S. Bergold, “Utilisation of the Slow Dynamic Slope Methodology for the Calibration of the ECU-Functions. Air Charge Determination and Torque Prediction in the Series Production,” in *Design of Experiments (DoE) in Engine Development, IV*, 2009, pp. 122–136.

[42] R. Leithgoeb, M. Bollig, and F. Henzinger, “Methodology for efficient calibration of model-based ECU structures,” in *1st International Symposium on Development Methodology*, 2005.

[43] A. Stefanopoulou, O. F. Storset, and R. Smith, “Pressure and temperature-based adaptive observer of air charge for turbocharged diesel engines,” *Int. J. Robust Nonlinear Control*, vol. 14, no. 6, pp. 543–560, 2004.

[44] R. Zimmerschied and R. Isermann, “Nonlinear time constant estimation

and dynamic compensation of temperature sensors," *Control Eng. Pract.*, vol. 18, no. 3, pp. 300–310, 2010.

[45] M. C. Ward, C. J. Brace, N. D. Vaughan, T. Hale, and G. Kennedy, "Investigation of ' Sweep ' Mapping Approach on Engine Testbed," *SAE Tech.*, no. 2002-01–0615, 2002.

[46] J. Goulburn, D. Brown, and R. Case, "Computer-controlled non-steady-state engine testing," *Int. J. Veh. Des.*, vol. 12, no. 1, pp. 50–60, 1991.

[47] A. Schwarte, L. Hack, R. Isermann, H. Nitzke, J. Jenschke, and J. Piewek, "Automatisierte Applikation von Motorsteuergeraeten mit kontinuierlicher Motorvermessung," in *AUTOREG*, 2004, pp. 651–663.

[48] M. Sugita, S. Harada, and H. Arakawa, "Transient Measurement for Steady-State Calibration.pdf," *Design of Experiments (DoE) in Engine Development*. 2009.

[49] R. Isermann, *Modellgestuetzte Steuerung, Regelung und Diagnose von Verbrennungsmotoren*. Berlin: Springer, 2003.

[50] M. Hafner, M. Schueler, and O. Nelles, "Dynamical identification and control of combustion engine exhaust," *Proc. Am. Control Conf.*, vol. 1, no. June, pp. 222–226, 1999.

[51] K. Röpke, M. Knaak, A. Nesstler, and S. Schaum, "Rapid Measurement - Grundbedatung eines Motors in einem Tag," *Mtz*, vol. 68. 2007.

[52] A. Neßler, S. Schaum, M. Knaak, and K. Röpke, "Fast Basic Combustion Engine Calibration with 'Rapid Measurement,'" in *Design of Experiments (DoE) in Engine Development III*, 2007.

[53] P. Schaal, B. Mason, S. Filippou, I. Souflas, and M. Cary, "Robust Methodology for Fast Crank Angle Based Temperature Measurement," *SAE Int.*, no. 2016-01–1072, 2016.

[54] M. Tagawa, T. Shimoji, and Y. Ohta, "A two-thermocouple probe technique for estimating thermocouple time constants in flows with combustion: in situ parameter identification of a first-order lag system," *Rev. Sci. Instrum.*, vol. 69, no. 9, pp. 3370–3378, 1998.

[55] L. J. Forney and G. C. Fralick, "Three-wire thermocouple: Frequency response in constant flow," *Rev. Sci. Instrum.*, vol. 66, no. 5, pp. 3331–

3336, 1995.

[56] I. Souflas, “Qualitative Adaptive Identification for Powertrain Systems,” PhD Thesis, University of Bradford, 2015.

[57] J. C. Wurzenberger, R. Heinzle, M.-V. Deregnaucourt, and T. Katrasnik, “A Comprehensive Study on Different System Level Engine Simulation Models,” *SAE Tech.*, no. 2013-01–1116, 2013.

[58] A. Chow and M. L. Wyszynski, “Thermodynamic modelling of complete engine systems—a review,” *Proc. Inst. Mech. Eng. Part D J. Automob. Eng.*, vol. 213, no. 4, pp. 403–415, 1999.

[59] J. B. Heywood, *Internal Combustion Engine Fundamentals*, 1st ed. McGraw-Hill, 1988.

[60] R. Stone, *Introduction to Internal Combustion Engines*, Second Edi. THE MACMILLAN PRESS LTD, 1992.

[61] C. R. Ferguson and A. T. Kirkpatrick, *Internal Combustion Engines - Applied Thermoscience*, Second Edi. John Wiley & Sons, 2001.

[62] A. Pezouvanis, “Engine modelling for virtual mapping,” PhD Thesis, University of Bradford, 2009.

[63] P. Schaal, I. Souflas, S. Filippou, B. Mason, and M. Cary, “SI Engine Airpath: A model builders guide,” *PMC - 2nd Bienn. Conf. Powertrain Mapp. Calibration*, pp. 1–19, 2014.

[64] E. Hendricks *et al.*, “Modelling of the Intake Manifold Filling Dynamics,” *SAE Int.*, no. 960037, 1996.

[65] R. S. Benson, *The Thermodynamics and Gas Dynamics of Internal Combustion Engines*, vol. 2. Clarendon Press, 1986.

[66] R. S. Benson, *The Thermodynamics and Gas Dynamics of Internal Combustion Engines*, vol. 1. Clarendon Press, 1982.

[67] E. Toro, *Riemann Solvers and Numerical Methods for Fluid Dynamics*, 2nd ed., vol. 1. Berlin: Springer-Verlag Berlin Heidelberg, 1999.

[68] P. Andersson, “Air Charge Estimation in Turbocharged Spark Ignition Engines,” PhD Thesis, Linkoeping University, 2005.

[69] M. Mueller, E. Hendricks, and S. Sorenson, “Mean Value Modelling of

Turbocharged Spark Ignition Engines," *SAE Int.*, no. 980784, 1998.

[70] P. Moraal and I. Kolmanovsky, "Turbocharger Modelling for Automotive Control Applications," *SAE Int.*, no. 1999-01–0908, 1999.

[71] J. Macek, J. Buri, and V. Dole, "Comparison of Lumped and Unsteady 1-D Models for Simulation of a Radial Turbine," *SAE Int.*, no. 2009-01–0303, 2009.

[72] J. C. Wurzenberger, R. Heinzle, and A. Schuemie, "Crank-Angle Resolved Real-Time Engine Simulation – Integrated Simulation Tool Chain from Office to Testbed," *SAE Int.*, no. 2009-01–0589, 2009.

[73] J. Galindo, A. Tiseira, R. Navarro, and D. Tarí, "Compressor Efficiency Extrapolation for 0D-1D Engine Simulations," *SAE Tech. Pap.*, no. 2016-01–0554, 2016.

[74] V. De Bellis, F. Bozza, C. Schernus, and T. Uhlmann, "Advanced Numerical and Experimental Techniques for the Extension of a Turbine Mapping," *SAE Int. J. Engines*, vol. 6, no. 3, pp. 1771–1785, 2013.

[75] G. MARTIN, V. TALON, T. PEUCHANT, P. HIGELIN, and A. CHARLET, "Physics based diesel turbocharger model for control purposes," *SAE Int.*, no. 2009-24–0123, 2009.

[76] L. J. Hamilton, J. S. Cowart, and Rozich, "The Effects of Intake Geometry on SI Engine Performance," *SAE Int.*, no. 2009-01–0302, 2009.

[77] F. Piscaglia, A. Montorfano, A. Onorati, G. Ferrari, and P. Milano, "Modeling of Pressure Wave Reflection from Open- Ends in I . C . E . Duct Systems," *SAE Int.*, no. 2010-01–1051, 2010.

[78] P. V Yarsam, A. A. Athawale, and M. D. Peshave, "Simulation and Experimental Analysis In the Induction Gas Dynamics of 2 Cylinder Naturally Aspirated CRDI Diesel Engine," *SAE Int.*, no. 2012-28–20, 2012.

[79] J. C. Wurzenberger, P. Bartsch, and T. Katrašnik, "Crank-angle Resolved Real-time Capable engine and vehicle Simulation - Fule consumption and driving performance," *SAE Int.*, no. 2010-01–0784, 2010.

[80] G. Alix, C. Pera, and J. Bohbot, "Comparison of 0D and 1D duct system modeling for naturally aspirated spark ignition engines," *SAE Int.*, no. 2011-01–1898, 2011.

[81] D. Chalet, P. Chesse, X. Tauzia, and J. Hetet, “Comparison of Different Methods for the Determination of Pressure Wave in the Inlet and Exhaust Systems of Internal Combustion Engine,” *SAE Int.*, no. 2006-01–1542, 2006.

[82] G. Pacitti, S. Amphlett, P. Miller, R. Norris, and A. Truscott, “Real-Time Crank-Resolved Engine Simulation for Testing New Engine Management Systems,” *SAE Int.*, no. 2008-01–1006, 2012.

[83] E. Corti, F. Migliore, D. Moro, and C. S. A, “Development of A Control-Oriented Model of Engine , Transmission and Vehicle Systems for Motor Scooter HIL Testing,” *SAE Int.*, no. 2009-01–1779, 2009.

[84] Y.-Y. Wu, B.-C. Chen, H.-C. Tsai, and F.-C. Hsieh, “New Charging Model Using Variable Valve Train for HIL Simulation,” *SAE Int.*, no. 2011-01–1150, 2011.

[85] B. Chen, Y. Wu, H. Tsai, and B. Chen, “Development of Engine Model Using Modulization Method for EMS Verification through MIL and HIL,” *SAE Int.*, no. 2014-01–1097, 2014.

[86] K. J. Keesman, *System Identification*. London: Springer, 2011.

[87] L. Ljung, *System identification: theory for the user*, 2nd ed. London: Prentice-Hall Inc., 1999.

[88] M. Cary, “A Model Based Engine Calibration Methodology for a Port Fuel Injection, Spark-Ignition Engine,” PhD Thesis, University of Bradford, 2003.

[89] K. Roepke and C. von Essen, “Design and Analysis for the Gaussian Process Model,” *Qual. Reliab. Eng. Int.*, vol. 24, pp. 643–651, 2008.

[90] L. Kocher, E. Koeberlein, D. G. Van Alstine, K. Stricker, and G. Shaver, “Physically based volumetric efficiency model for diesel engines utilizing variable intake valve actuation,” *Int. J. Engine Res.*, vol. 13, no. 2, pp. 169–184, Apr. 2012.

[91] A. Chevalier, M. Müller, and E. Hendricks, “On the Validity of Mean Value Engine Models During Transient Operation,” *SAE Int.*, no. 2000-01–1261, 2000.

[92] B. Lee, Y. Guezennec, and G. Rizzoni, “Model-Based Fault Diagnosis of Spark-Ignition Direct-Injection Engine Using Nonlinear Estimations,” *SAE*

Int., no. 2005-01–0071, 2005.

[93] M. Muller, A. Chevalier, C. Vigild, E. Hendricks, and S. C. Sorenson, “Mean Value Engine Modelling of an SI Engine with EGR,” *SAE Tech.*, no. 1999-01–0909, 1999.

[94] J. El Hadef, G. Colin, Y. Chamaillard, and V. Talon, “Turbocharged SI Engine Models for Control,” *11th Int. Symp. Adv. Veh. Control - AVEC’12*, pp. 1–6, 2012.

[95] E. Hendricks and S. C. Sorenson, “SI Engine Controls and Mean Value Engine Modelling,” *SAE International*, no. 910258. 1991.

[96] E. Hendricks and T. Vesterholm, “The Analysis of Mean Value SI Engine Models,” *SAE Int.*, no. 920682, 1992.

[97] T. Schulze, M. Wiedemeier, and H. Schuette, “Crank Angle - Based Diesel Engine Modeling for Hardware-in-the-Loop Applications with In-Cylinder Pressure Sensors,” *SAE Int.*, no. 2007-01–1303, 2007.

[98] I. Kolmanovsky and A. Stotsky, “Simple Unknown Input Estimation Techniques for Automotive Applications,” in *American Control Conference*, 2001, no. 4, pp. 3312–3317.

[99] C. F. Aquino, “Transient A/F Control Characteristics of the 5 Liter Central Fuel Injection Engine,” *SAE Int.*, no. 810494, 1981.

[100] A. Chevalier, C. W. Vigild, and E. Hendricks, “Predicting the Port Air Mass Flow of SI Engines in Air / Fuel Ratio Control Applications,” *SAE Int.*, no. 2000-01–0260, 2000.

[101] P. B. Jensen, M. B. Olsen, J. Poulsen, E. Hendricks, M. Fons, and C. Jepsen, “A New Family of Nonlinear Observers for SI Engine Air / Fuel Ratio Control & Exposition,” *SAE Int.*, no. 970615, 1997.

[102] B. Chen, Y. Wu, and H. Tsai, “Estimation of Intake Manifold Absolute Pressure Using Kalman Filter,” *SAE Int.*, no. 2013-32–9061, 2013.

[103] H. Wang, Y. Tian, J. Bosche, and A. El Hajjaji, “Modeling and Dynamical Feedback Control of a Vehicle Diesel Engine Speed and Air-Path,” *J. Dyn. Syst. Meas. Control*, vol. 136, no. 6, p. 61010, 2014.

[104] D. Jung, K. Min, Y. Park, S. Pyo, and M. Sunwoo, “Feedforward Controller Design for EGR and VGT Systems based on Cylinder Pressure Information

and Air Path Model," *IFAC*, vol. 49, no. 11, pp. 596–603, 2016.

[105] P. Drews *et al.*, "Fast model predictive control for the air path of a turbocharged diesel engine," *Proc. Eur. Control Conf.*, pp. 3377–3382, 2009.

[106] H. Schuette and M. Ploeger, "Hardware-in-the-Loop Testing of Engine Control Units - A Technical Survey," *SAE Int.*, no. 2007-01–0500, 2007.

[107] I. Papadimitriou, J. Silvestri, M. Warner, and B. Despujols, "Development of Real-Time Capable Engine Plant Models for use in HIL Systems," *SAE Int.*, no. 2008-01–0990, 2008.

[108] A. Gambarotta, G. Lucchetti, P. Fiorani, M. De Cesare, and G. Serra, "A thermodynamic Mean Value Model of the intake and exhaust system of a turbocharged engine for HiL/SiL applications.," *SAE Int.*, no. 2009-24–0121, 2009.

[109] L. a Smith, T. Fickenscher, and R. P. Osborne, "Engine Breathing - Steady Speed Volumetric Efficiency and Its Validity Under Transient Engine Operation," *SAE Int.*, no. 1999-01–0212, 1999.

[110] J. W. Grizzle, J. a. Cook, and W. P. Milam, "Improved cylinder air charge estimation for transient air fuel ratio control," *Proc. 1994 Am. Control Conf. - ACC '94*, pp. 1568–1573, 1994.

[111] J. Deur, D. Hrovat, J. Petri, and Ž. Šitum, "A Control-Oriented Polytropic Model of SI Engine Intake Manifold," in *ASME International Mechanical Engineering Congress & Exposition*, 2003.

[112] J. Deur, S. W. Magner, M. Jankovic, and D. Hrovat, "Influence of Intake Manifold Heat Transfer Effects on Accuracy of SI Engine Air-Charge Prediction," in *ASME International Mechanical Engineering Congress and Exposition*, 2004.

[113] P. Schaal, B. Mason, K. Ebrahimi, and M. Cary, "Adaptive Transient Engine Air Charge Estimation using a Mass State Observer," in *PMC - 3rd Biennial Conference on Powertrain Mapping and Calibration*, 2016, pp. 1–18.

[114] P. Young, "Parameter estimation for continuous-time model - A survey. Young, P. C. (1981)," *Automatica*, vol. 17, pp. 23–29, 1981.

[115] A. Dabroom and H. Khalil, "Numerical differentiation using high-gain

observers," *Proc. 36th IEEE Conf. Decis. Control*, pp. 4790–4795, 1997.

[116] L. K. Vasiljevic and H. K. Khalil, "Differentiation with High-Gain Observers the Presence of Measurement Noise," *Proc. 45th IEEE Conf. Decis. Control*, pp. 4717–4722, 2006.

[117] D. G. Luenberger, "Observing the State of a Linear System," *IEEE Trans. Mil. Electron.*, vol. 8, no. 2, pp. 74–80, 1964.

[118] D. Luenberger, "An introduction to observers," *IEEE Transactions on Automatic Control*, vol. 16, no. 6. pp. 596–602, 1971.

[119] L. Fridman, J. Davila, and A. Levant, "High-order sliding-mode observation for linear systems with unknown inputs," *Nonlinear Anal. Hybrid Syst.*, vol. 5, pp. 189–205, 2011.

[120] A. Stotsky and I. Kolmanovsky, "Application of input estimation techniques to charge estimation and control in automotive engines," *Control Eng. Pract.*, vol. 10, pp. 1371–1383, 2002.

[121] A. Stotsky, *Automotive Engines Control, Estimation, Statistical Detection*. London: Springer, 2009.

[122] C.-S. Liu and P. He, "Unknown input estimation for a class of nonlinear systems and its application to automotive engine controls," in *American Control Conference*, 2009, pp. 1195–1200.

[123] I. Kolmanovsky, M. Druzhinina, and J. Sun, "Charge Control for Direct Injection Spark Ignition Engines with EGR," in *American Control Conference*, 2000, pp. 34–38.

[124] J. Buckland, I. Kolmanovsky, and U. Kalabic, "Multi-Input Observer For Estimation Of Compressor Flow," in *ASME Dynamic Systems and Control Conferece*, 2013, pp. 1–5.

[125] Z. Wang, Q. Zhu, and R. Prucka, "A Review of Spark-Ignition Engine Air Charge Estimation Methods," *SAE Int.*, no. 2016-01–0620, 2016.

[126] P. Andersson and L. Eriksson, "Air-to-Cylinder Observer on a Turbocharged SI-Engine with Wastegate," *SAE Int.*, no. 2001-01–0262, 2001.

[127] G. Reale, P. Ortner, and L. del Re, "Nonlinear observers for closed-loop control of a combustion engine test bench," in *American Control*

Conference, 2009, pp. 4648–4653.

[128] O. Storset, A. Stefanopoulou, and R. Smith, “Air charge estimation for turbocharged diesel engines,” in *American Control Conference*, 2000, pp. 39–44.

[129] O. F. Storset, A. G. Stefanopoulou, and R. Smith, “Adaptive Air Charge Estimation for Turbocharged Diesel Engines Without Exhaust Gas Recirculation,” *J. Dyn. Syst. Meas. Control*, vol. 126, pp. 633–643, 2004.

[130] G. Colin, G. Bloch, Y. Chamaillard, and F. Anstett, “Two air path observers for turbocharged SI engines with VCT,” *Control Eng. Pract.*, vol. 17, pp. 571–578, 2009.

[131] H. Lee, Y. Park, S. Hong, M. Lee, and M. Sunwoo, “EGR Rate Estimation for Cylinder Air Charge in a Turbocharged Diesel Engine using an Adaptive Observer,” *SAE Int.*, no. 2013-01–0246, 2013.

[132] J. Zhao and J. Wang, “OBSERVER BASED OXYGEN FRACTION ESTIMATION FOR A DUAL-LOOP EGR DIESEL ENGINE FUELED WITH BIODISEL BLENDS,” in *ASME Dynamic Systems and Control Conference*, 2013, pp. 1–7.

[133] V. H. Monir, R. Salehi, H. Salarieh, and A. Alasty, “Real-time estimation of the volumetric efficiency in spark ignition engines using an adaptive sliding-mode observer,” *IMECHE Part D - Automob. Eng.*, 2015.

[134] R. E. Kalman and R. S. Bucy, “New results in linear filtering and prediction theory,” *J. Basic Eng.*, vol. 83, pp. 95–108, 1961.

[135] R. Faragher, “Understanding the basis of the kalman filter via a simple and intuitive derivation,” *IEEE Signal Process. Mag.*, vol. 29, no. 5, pp. 128–132, 2012.

[136] J. Hartikainen and S. Särkkä, “Optimal filtering with Kalman filters and smoothers – a Manual for Matlab toolbox EKF / UKF.” Aalto University School of Science - Biomedical Engineering and Computational Science, 2011.

[137] G. Hovland, “Comparison of Different Kalman Filters for Tracking Nonlinear Transmission Torques,” *IFAC Mechatron. Syst.*, 2004.

[138] I. Hassanzadeh and M. A. Fallah, “Design of Augmented Extended Kalman

Filter for Real Time Simulation of Mobile Robots Using Simulink," in *International Symposium on Mechatronics and its Applications (ISMA09)*, 2009, vol. 9, no. 1, pp. 1–6.

[139] T. A. Wenzel, K. J. Burnham, M. V. Blundell, and R. A. Williams, "Dual extended Kalman filter for vehicle state and parameter estimation," *Veh. Syst. Dyn. Int. J. Veh. Mech. Mobil.*, vol. 44, no. 2, pp. 153–171, 2006.

[140] P. Andersson and L. Eriksson, "Mean-Value Observer for a turbocharged SI-Engine," in *Advances in Automotive Control*, 2004, pp. 131–136.

[141] D. Pavković, J. Deur, I. Kolmanovsky, and D. Hrovat, "Application of adaptive kalman filter for estimation of power train variables," *SAE Int.*, no. 2008-01–0585, 2008.

[142] E. Höckerdal, L. Eriksson, and E. Frisk, "Air Mass-Flow Measurement and Estimation in Diesel Engines Equipped with E GR and VGT," *SAE Int.*, no. 2008-01–0992, 2008.

[143] O. Nelles, S. Sinsel, and R. Isermann, "Local basis function networks for identification of a turbocharger," in *International Conference on Control*, 1996, no. 427, pp. 7–12.

[144] F. White, *Fluid Mechanics*. McGraw-Hill, 1979.

[145] P. Carlsson, "Flow Through a Throttle Body : A Comparative Study of Heat Transfer, Wall Surface Roughness and Discharge Coefficient," Master Thesis, Linkoeping University, 2007.

[146] R. Pursifull, A. J. Kotwicki, and F. M. Co, "Reprinted From : Modeling of SI Engines," *SAE Int.*, no. 2000-01–0571, 2000.

[147] D. Broome, "Induction Ram Part one The inertia and wave effects of ram, and a summary of published work," *Automob. Eng.*, vol. April, pp. 130–133, 1969.

[148] D. Broome, "Induction Ram Part two: Inertial aspects of induction ram," *Automo*, vol. May, pp. 180–184, 1969.

[149] D. Broome, "Induction Ram Part three: Wave phenomena and the design of ram intake systems," *Automob. Eng.*, vol. June, pp. 262–267, 1969.

[150] D. Zwillinger, *Handbook of Differential Equations*, Secon Edit. Boston: Academic Press INC, 1992.

[151] X. Hu, “On state observers for nonlinear systems,” *Syst. Control Lett.*, vol. 17, no. 6, pp. 465–473, 1991.

[152] Mathworks, “Recursive Algorithms for Online Parameter Estimation.” [Online]. Available: https://uk.mathworks.com/help/ident/ug/recursive-algorithms-for-online-estimation.html. [Accessed: 25-Jan-2017].

[153] Mathworks, “Moving Average Filter.” [Online]. Available: https://uk.mathworks.com/help/matlab/data_analysis/filtering-data.html. [Accessed: 30-Jan-2018].

[154] Mathworks, “Anti-Windup Control Using a PID Controller.” [Online]. Available: https://uk.mathworks.com/help/simulink/examples/anti-windup-control-using-a-pid-controller.html. [Accessed: 30-Jan-2018].

[155] Mathworks, “Zero-phase digital filtering.” [Online]. Available: https://uk.mathworks.com/help/signal/ref/filtfilt.html. [Accessed: 30-Jan-2018].

[156] Accurate Technologies, “EMX Data Acquisition Devices.” [Online]. Available: https://www.accuratetechnologies.com/DataAcquisition/EMXModules. [Accessed: 15-Feb-2018].

Chapter 12 Appendices

Appendix A Filling and Emptying Dynamics

This section gives a complete and detailed derivation of the filling and emptying dynamics.

A control volume in a mean value engine model is defined as an open thermodynamic system and is assumed to be zero dimensional.

Mass balance for an open system is given by Equation 12.1 [16].

$$\frac{dm}{dt} = \dot{m}_{in} - \dot{m}_{out} \tag{12.1}$$

First law of thermodynamics applied to an open system yield Equation 12.2 [16].

$$\frac{dE}{dt} = \dot{m}_{in} h_{0\_in} - \dot{m}_{out} h_{0\_out} + \dot{Q} - \dot{W}_s - \dot{W}_p \tag{12.2}$$

Shear work and shaft work can be assumed to be zero. Therefor Equation 12.2 becomes

$$\frac{dE}{dt} = \dot{m}_{in} h_{0\_in} - \dot{m}_{out} h_{0\_out} + \dot{Q} \tag{12.3}$$

The stagnation enthalpy at zero velocity is defined as

$$h_0 = c_p T + \frac{u^2}{2} \tag{12.4}$$

and the internal energy is defined by Equation 12.5.

$$E = m c_v T + \frac{m u^2}{2} + mgz \tag{12.5}$$

In order to apply Equation 12.3 to a control volume for a MVEM, a few assumptions have to be made:

- The changes in kinetic energy and therefore in velocity inside the system are neglected. This can be justified by the fact that the proportion of the kinetic energy is small and in addition changes in velocity inside the system are not substantial.

- The change in potential energy inside the system is zero which can be justified by the fact that there is no significant difference in height between the system entrance and exit.

With these assumptions the enthalpy becomes

$$h_0 = c_p T \tag{12.6}$$

and the internal energy becomes

$$E = m c_v T \tag{12.7}$$

Derivation of Equation 12.7 with respect to time gives

$$\frac{dE}{dt} = c_v T \frac{dm}{dt} + c_v m \frac{dT}{dt} \tag{12.8}$$

Substituting the Equations 12.1, 12.6 and 12.8 into 12.3 the energy balance can be represented by Equation 12.9.

$$c_v T(\dot{m}_{in} - \dot{m}_{out}) + c_v m \frac{dT}{dt} = \dot{m}_{in} c_p T_{in} - \dot{m}_{out} c_p T_{out} + \dot{Q} \tag{12.9}$$

To couple the energy and mass balances together and solve the equations for temperature and pressure the ideal gas law and its first derivative are used as in Equations 12.10 and 12.11.

$$m = \frac{PV}{RT} \tag{12.10}$$

Taking the first derivative of the ideal gas law with respect to time

$$\frac{dm}{dt} = \frac{V}{RT}\frac{dP}{dt} - \frac{PV}{RT^2}\frac{dT}{dt} \tag{12.11}$$

Substituting the Equations 12.1,12.10 and 12.11 into 12.9 and assuming that the gas that is leaving the system has the same temperature as the gas inside, the temperature and pressure state inside the control volume can be solved from

$$\frac{dT}{dt} = \left[c_p \dot{m}_{in} T_{in} - c_p \dot{m}_{out} T - c_v T \dot{m}_{in} + c_v T \dot{m}_{out} + \frac{dQ}{dt}\right] \frac{RT}{c_v PV} \tag{12.12}$$

and

$$\frac{dP}{dt} = \left[c_p \dot{m}_{in} T_{in} - c_p \dot{m}_{out} T + \frac{dQ}{dt}\right] \frac{R}{c_v V} \quad \textbf{12.13}$$

Appendix B Compressible gas flow

The stagnation enthalpy along a streamline is constant.

$$h + \frac{1}{2}u^2 + gz = h_0 = constant \quad \textbf{12.14}$$

The enthalpy h is defined as

$$h = c_p T \quad \textbf{12.15}$$

and the stagnation enthalpy at zero velocity is given by Equation 12.16.

$$h_0 = c_p T_0 \quad \textbf{12.16}$$

Combining Equation 12.14 with 12.15 and 12.16 yields Equation 12.17.

$$c_p T + \frac{1}{2}u^2 + gz = c_p T_0 \quad \textbf{12.17}$$

For gases the gz term can be neglected which simplifies Equation 12.16 to

$$c_p T + \frac{1}{2}u^2 = c_p T_0 \quad \textbf{12.18}$$

Introducing the Mach-Number

$$M = \frac{u}{a} \quad \textbf{12.19}$$

where a is the speed of sound and is defined by Equation 12.20.

$$a = \sqrt{\gamma R T} \quad \textbf{12.20}$$

Substituting Equations 12.19 and 12.20 into 12.18 the relation between stagnation temperature, actual temperature and the Mach – Number can be expressed by Equation 12.21.

$$\frac{T_0}{T} = 1 + \frac{(\gamma - 1)}{2} M^2 \qquad \textbf{12.21}$$

Assuming that the flow through the convergent – divergent nozzle is isentropic the isentropic gas law can be applied as shown in Equation 12.22.

$$\frac{P_0}{P} = \left(\frac{T_0}{T}\right)^{\left(\frac{\gamma}{\gamma-1}\right)} \qquad \textbf{12.22}$$

Substituting 12.22 into 12.21, the relationship between stagnation pressure, actual pressure and the Mach – Number is given by Equation 12.23.

$$\frac{P_0}{P} = \left(1 + \frac{(\gamma - 1)}{2} M^2\right)^{\left(\frac{\gamma}{\gamma-1}\right)} \qquad \textbf{12.23}$$

Mass flow through a pipe can be described by Equation 12.24.

$$\dot{m} = \rho A u \qquad \textbf{12.24}$$

and the ideal gas law can be written in the form of Equation 12.25.

$$P = \rho R T \qquad \textbf{12.25}$$

Combining the Equations 12.24 and 12.25 gives

$$P = \frac{\dot{m}}{Au} RT \qquad \textbf{12.26}$$

Substituting Equations 12.19 and 12.20 into 12.26 gives

$$P = \frac{\dot{m}}{AM} \sqrt{\frac{RT}{\gamma}} \qquad \textbf{12.27}$$

Equation 12.21 can be rearranged to

$$T = \frac{T_0}{\left(1 + \frac{\gamma - 1}{2} M^2\right)} \qquad \textbf{12.28}$$

and Equation 12.23 can be rearranged to

$$P = P_0 \left(1 + \frac{\gamma - 1}{2} M^2\right)^{\frac{-\gamma}{\gamma-1}} \qquad \textbf{12.29}$$

Substituting 12.28 and 12.29 into 12.27 the air mass flow through a convergent – divergent nozzle can be represented by Equation 12.30.

$$\dot{m} = \frac{AP_0M\gamma}{\sqrt{RT_0\gamma}}\left(1 + \frac{(\gamma-1)}{2}M^2\right)^{\left(\frac{-(\gamma+1)}{2(\gamma-1)}\right)} \quad \textbf{12.30}$$

In order to get rid of the Mach – Number and in order to represent the mass flow in dependence of upstream and downstream pressure the following steps are necessary:

Equation 12.23 can be rearranged for the Mach – Number

$$M^2 = \frac{2}{(\gamma-1)}\left(\left(\frac{P}{P_0}\right)^{\left(\frac{-(\gamma-1)}{\gamma}\right)} - 1\right) \quad \textbf{12.31}$$

Substituting Equation 12.31 into 12.30, the air mass flow finally can be represented by Equation 12.32.

$$\dot{m} = \frac{\mathrm{A}P_0\sqrt{\gamma}}{\sqrt{RT_0}}\left(\frac{P}{P_0}\right)^{\frac{1}{\gamma}}\left\{\frac{2}{\gamma-1}\left[1 - \left(\frac{\mathrm{P}}{P_0}\right)^{\frac{(\gamma-1)}{\gamma}}\right]\right\}^{\frac{1}{2}} \quad \textbf{12.32}$$

In order to apply Equation 12.32 on an MVEM it has to be assumed that upstream conditions of the restriction are equal to the stagnation condition P_0 and T_0. This means that the upstream conditions equal a large vessel where the velocities inside can be assumed to be zero. And the conditions at minimum throat area have to be assumed to be equal with the downstream conditions. With this assumption the air mass flow is given by Equation 12.33.

$$\dot{m} = \frac{A_{th}P_{t,in}}{\sqrt{RT_{in}}}\left(\frac{P_{t,out}}{P_{t,in}}\right)^{\frac{1}{\gamma}}\left\{\frac{2\gamma}{\gamma-1}\left[1 - \left(\frac{P_{t,out}}{P_{t,in}}\right)^{\frac{(\gamma-1)}{\gamma}}\right]\right\}^{\frac{1}{2}} \quad \textbf{12.33}$$

The critical pressure ratio at which the velocity at the minimum throat area reaches the speed of sound is defined by Equation 12.34.

$$P_{crit} = \left(\frac{2}{\gamma+1}\right)^{\frac{\gamma+1}{2(\gamma-1)}} \approx 0.528 \quad for\ \gamma = 1.4 \quad \textbf{12.34}$$

In this case the Mach – Number is equal to one and Equation 12.30 becomes for the sonic case.

$$\dot{m} = \frac{AP_0\gamma}{\sqrt{RT_0\gamma}}\left(1 + \frac{(\gamma-1)}{2}\right)^{\left(\frac{-(\gamma+1)}{2(\gamma-1)}\right)} \quad \textbf{12.35}$$

With the assumptions mentioned above Equation 12.35 can be rearranged and the mass flow for the sonic case can be estimated from Equation 12.36.

$$\dot{m} = \frac{A_{th}P_{t,in}}{\sqrt{RT_{in}}}\sqrt{\gamma}\left(\frac{2}{\gamma+1}\right)^{\frac{\gamma+1}{2(\gamma-1)}} \quad \textbf{12.36}$$

Appendix C Incompressible gas flow

The Bernoulli's equation for incompressible flow is given by Equation 12.37.

$$P_1 + \frac{1}{2}\rho {u_1}^2 = P_2 + \frac{1}{2}\rho {u_2}^2 \quad \textbf{12.37}$$

The continuity equation for incompressible flow can be represented by Equation 12.38.

$$u_1A_1 = u_2A_2 \quad \textbf{12.38}$$

Combining Equations 12.37 and 12.38 the velocity u_2 can be expressed by Equation 12.39.

$$u_2 = \sqrt{\frac{2(P_1 - P_2)}{\rho\left(1 - \left(\frac{A_2}{A_1}\right)^2\right)}} \quad \textbf{12.39}$$

Air mass flow generally can be calculated from

$$\dot{m} = \rho A u \quad \textbf{12.40}$$

Substituting 12.38 into 12.39, mass flow can be estimated from Equation 12.41.

$$\dot{m} = A_2\sqrt{\frac{2P_1(P_1 - P_2)}{RT_1\left(\frac{A_2}{A_1}\right)^2}} \quad \textbf{12.41}$$

Assuming that the restriction is only a pipe without any change in cross sectional area then $A_1 = A_2$. Therefor Equation 12.41 becomes

$$\dot{m} = A\sqrt{\frac{2P_1(P_1 - P_2)}{RT_1}} \qquad \textbf{12.42}$$

Subscript 1 denotes upstream conditions and 2 denotes downstream conditions.